

Antennas and RF Front Ends for Cognitive Radio

Guest Editors: Mohammed Al-Husseini, Ali El-Hajj, Mario Bkassiny,
Said El-Khamy, and Amor Nafkha





Antennas and RF Front Ends for Cognitive Radio

Antennas and RF Front Ends for Cognitive Radio

Guest Editors: Mohammed Al-Husseini, Ali El-Hajj,
Mario Bkassiny, Said El-Khamy, and Amor Nafkha



Copyright © 2014 Hindawi Publishing Corporation. All rights reserved.

This is a special issue published in “International Journal of Antennas and Propagation.” All articles are open access articles distributed under the Creative Commons Attribution License, which permits unrestricted use, distribution, and reproduction in any medium, provided the original work is properly cited.

Editorial Board

M. Ali, USA
Charles Bunting, USA
Felipe Cátedra, Spain
Dau-Chyrh Chang, Taiwan
Deb Chatterjee, USA
Z. N. Chen, Singapore
Michael Yan Wah Chia, Singapore
Shyh-Jong Chung, Taiwan
Lorenzo Crocco, Italy
Tayeb A. Denidni, Canada
Antonije R. Djordjevic, Serbia
Karu P. Esselle, Australia
Miguel Ferrando, Spain
Vincenzo Galdi, Italy
Wei Hong, China
Hon Tat Hui, Singapore
Tamer S. Ibrahim, USA
Nemai Karmakar, Australia
Se-Yun Kim, Republic of Korea
Ahmed A. Kishk, Canada

Selvan T. Krishnasamy, India
Tribikram Kundu, USA
Francisco Falcone Lanas, Spain
Ju-Hong Lee, Taiwan
Byungje Lee, Republic of Korea
L. Li, Singapore
Yilong Lu, Singapore
Atsushi Mase, Japan
Andrea Massa, Italy
Giuseppe Mazzearella, Italy
Derek McNamara, Canada
C.Mecklenbräuker, Austria
Michele Midrio, Italy
Mark Mirotznik, USA
Ananda Mohan, Australia
P. Mohanan, India
Pavel Nikitin, USA
A. D. Panagopoulos, Greece
Matteo Pastorino, Italy
Massimiliano Pieraccini, Italy

Sadasiva M. Rao, USA
Sembiam R. Rengarajan, USA
Ahmad Safaai-Jazi, USA
Safieddin Safavi-Naeini, Canada
Magdalena Salazar-Palma, Spain
Stefano Selleri, Italy
Zhongxiang Shen, Singapore
John J. Shynk, USA
Mandeep Singh Jit Singh, Malaysia
Seong-Youp Suh, USA
Parveen Wahid, USA
Yuanxun Ethan Wang, USA
Daniel S. Weile, USA
Tat Soon Yeo, Singapore
Young Joong Yoon, Korea
Jong-Won Yu, Republic of Korea
Wenhua Yu, USA
Anping Zhao, China

Contents

Antennas and RF Front Ends for Cognitive Radio, Mohammed Al-Husseini, Ali El-Hajj, Mario Bkassiny, Said El-Khamy, and Amor Nafkha
Volume 2014, Article ID 231027, 2 pages

Passive Switched Capacitor RF Front Ends for Spectrum Sensing in Cognitive Radios, Bodhisatwa Sadhu, Martin Sturm, Brian M. Sadler, and Ramesh Harjani
Volume 2014, Article ID 947373, 20 pages

Implementation of an Optical-Wireless Network with Spectrum Sensing and Dynamic Resource Allocation Using Optically Controlled Reconfigurable Antennas, E. Raimundo-Neto, J. R. G. da Rosa, M. A. F. Casaroli, I. Feliciano da Costa, A. M. Alberti, and Arismar Cerqueira Sodr  Jr.
Volume 2014, Article ID 670930, 11 pages

Optically Controlled Reconfigurable Antenna Array Based on E-Shaped Elements, Arismar Cerqueira Sodr  Junior, Igor Feliciano da Costa, Leandro Tiago Manera, and Jos  Alexandre Diniz
Volume 2014, Article ID 750208, 8 pages

Application of a Channel Estimation Algorithm to Spectrum Sensing in a Cognitive Radio Context, Vincent Savaux, Mo    Djoko-Kouam, Yves Lou   , and Alexandre Skrzypczak
Volume 2014, Article ID 506457, 13 pages

Cognitive Radio Transceivers: RF, Spectrum Sensing, and Learning Algorithms Review, Lise Safatly, Mario Bkassiny, Mohammed Al-Husseini, and Ali El-Hajj
Volume 2014, Article ID 548473, 21 pages

Frequency-Tunable and Pattern Diversity Antennas for Cognitive Radio Applications, A. H. Ramadan, J. Costantine, Y. Tawk, C. G. Christodoulou, and K. Y. Kabalan
Volume 2014, Article ID 638627, 7 pages

A Miniaturize Bandpass Filter with Harmonic Suppression Using Meandered Quarter-Wavelength Resonators, Yun-Long Lu, Shun Wang, Tingting Gu, Ping Cao, and Kai Li
Volume 2014, Article ID 916927, 6 pages

Editorial

Antennas and RF Front Ends for Cognitive Radio

**Mohammed Al-Husseini,¹ Ali El-Hajj,² Mario Bkassiny,³
Said El-Khamy,⁴ and Amor Nafkha⁵**

¹ Beirut Research and Innovation Center, Lebanese Center for Studies and Research, Beirut 2030 8303, Lebanon

² Department of Electrical and Computer Engineering, American University of Beirut, P.O. Box 11-0236, Beirut 1107 2020, Lebanon

³ Department of Electrical and Computer Engineering, State University of New York (SUNY Oswego), Shineman 426, Oswego, NY 13126, USA

⁴ Department of Electrical Engineering, Faculty of Engineering, Alexandria University, 22 Army Street, Alexandria 21526, Egypt

⁵ Signal, Communication & Embedded Electronics Group, Supélec, 35576 Cesson-Sévigné, France

Correspondence should be addressed to Mohammed Al-Husseini; husseini@ieee.org

Received 5 May 2014; Accepted 5 May 2014; Published 4 June 2014

Copyright © 2014 Mohammed Al-Husseini et al. This is an open access article distributed under the Creative Commons Attribution License, which permits unrestricted use, distribution, and reproduction in any medium, provided the original work is properly cited.

The current radio spectrum regulations assign specific bands to particular services and grant licensed bands access to only licensed users. This results in the inefficient use of the frequency spectrum, a problem for which cognitive radio (CR) [1] is thought to provide a suitable solution. CR implements dynamic spectrum allocation policies by allowing unlicensed or secondary users (SUs) to access spectrum bands licensed to primary users (PUs) while avoiding interference with them. This could happen, for example, when an SU's device searches for an unoccupied band, called a white space, and uses it for its transmission. As a result of this mode of operation, significant challenges have to be dealt with when designing the RF components of a CR transceiver, such as the antennas, the filters, the mixers and oscillators, the power amplifiers (PAs), and the analog-to-digital and digital-to-analog converters (ADCs/DACs). This comes in addition to the necessary algorithms for sensing the surrounding environment and adapting to particular situations through a cognitive engine [2].

In CR, ultrawideband (UWB) antennas are usually required for channel sensing and frequency reconfigurable antennas for communicating. The two antennas can be designed in a single- or dual-port configuration. In the dual-port case, one port has UWB frequency response and is used for channel sensing, and the second port, which is frequency reconfigurable/tunable, is used for communicating. In the more challenging single-port design, the same port can have

UWB response for sensing and can be reconfigured for tunable narrowband operation when required to communicate over a white space. In a distinct spectrum sharing approach, the SU device sends its transmission as UWB pulses with nulls in the bands used by PUs. In this case, the antenna should have a UWB response but with the ability to selectively induce frequency notches in the bands used by PUs. The design of UWB antennas normally requires the proper selection of the patch shape, with preferred round shapes and edges, the use of partial or slotted ground planes, the good matching between the feed and the patch, or the employment of fractals. For frequency band notching, the use of split-ring resonators (SRRs) and complementary split-ring resonators (CSRRs) is famous [3]. Frequency reconfiguration in antennas is usually attained by the use of RF and optical switches or varactors that change the paths or electrical lengths seen by the current on the radiator surface [4].

In addition to the CR antenna design challenges, the constraints on the RF front-end design pertain to the ADC/DAC sampling rate, especially when working with wideband signals, to the sensitivity of the circuitry, since the CR system has to deal with very high to very low PU signal strength, to the linearity and bandwidth of amplifiers (LNAs), and to the frequency agility of the mixer and filters [5]. Designs that guarantee the good performance of the RF components in both wideband and narrowband operation modes are required for CR.

Some of the well-known spectrum sensing algorithms are energy detection and cyclostationarity-based detection. However, blind techniques, which detect the presence of a signal without any knowledge of signal or noise parameters, are more robust [6]. The spectrum sensing algorithms should be devised to overcome main sensing challenges such as RF impairments.

We hope that readers of this special issue will find up-to-date information, comprehensive reviews, and robust designs for antennas and RF blocks for use in CR transceivers. We also hope that they gain a good insight into the most practical channel estimation, spectrum sensing, and decision making algorithms for cognitive radio.

Mohammed Al-Husseini

Ali El-Hajj

Mario Bkassiny

Said El-Khamy

Amor Nafkha

References

- [1] J. Mitola III and G. Q. Maguire Jr., "Cognitive radio: making software radios more personal," *IEEE Personal Communications*, vol. 6, no. 4, pp. 13–18, 1999.
- [2] S. Haykin, "Cognitive radio: brain-empowered wireless communications," *IEEE Journal on Selected Areas in Communications*, vol. 23, no. 2, pp. 201–220, 2005.
- [3] M. Al-Husseini, K. Y. Kabalan, A. El-Hajj, and C. G. Christodoulou, "Cognitive radio: UWB integration and related antenna design," in *New Trends in Technologies: Control, Management, Computational Intelligence and Network Systems*, M. Joo Er, Ed., chapter 20, pp. 395–412, InTech, Rijeka, Croatia, 2010.
- [4] M. Al-Husseini, K. Y. Kabalan, A. El-Hajj, and C. G. Christodoulou, "Reconfigurable microstrip antennas for cognitive radio," in *Advancement in Microstrip Antennas with Recent Applications*, A. Kishk, Ed., chapter 14, pp. 337–362, InTech, Rijeka, Croatia, 2013.
- [5] B. Razavi, "Cognitive radio design challenges and techniques," *IEEE Journal of Solid-State Circuits*, vol. 45, no. 8, pp. 1542–1553, 2010.
- [6] Z. Khalaf, A. Nafkha, and J. Palicot, "Blind spectrum detector for cognitive radio using compressed sensing and symmetry property of the second order cyclic autocorrelation," in *Proceedings of the 7th International ICST Conference on Cognitive Radio Oriented Wireless Networks and Communications (CROWN-COM '12)*, pp. 291–296, Stockholm, Sweden, June 2012.

Research Article

Passive Switched Capacitor RF Front Ends for Spectrum Sensing in Cognitive Radios

Bodhisatwa Sadhu,^{1,2} Martin Sturm,¹ Brian M. Sadler,³ and Ramesh Harjani¹

¹ University of Minnesota, Minneapolis, MN 55455, USA

² IBM T. J. Watson Research Center, Yorktown Heights, NY 10598, USA

³ Army Research Laboratory, Adelphi, MD 20783, USA

Correspondence should be addressed to Bodhisatwa Sadhu; sadhu002@umn.edu

Received 16 November 2013; Accepted 22 March 2014; Published 1 June 2014

Academic Editor: Amor Nafkha

Copyright © 2014 Bodhisatwa Sadhu et al. This is an open access article distributed under the Creative Commons Attribution License, which permits unrestricted use, distribution, and reproduction in any medium, provided the original work is properly cited.

This paper explores passive switched capacitor based RF receiver front ends for spectrum sensing. Wideband spectrum sensors remain the most challenging block in the software defined radio hardware design. The use of passive switched capacitors provides a very low power signal conditioning front end that enables parallel digitization and software control and cognitive capabilities in the digital domain. In this paper, existing architectures are reviewed followed by a discussion of high speed passive switched capacitor designs. A passive analog FFT front end design is presented as an example analog conditioning circuit. Design methodology, modeling, and optimization techniques are outlined. Measurements are presented demonstrating a 5 GHz broadband front end that consumes only 4 mW power.

1. Introduction

With the growth of the wireless industry, the spectral congestion caused by wireless user traffic has become a significant concern that threatens further growth of the technology [1, 2]. However, this congestion is a result of suboptimal frequency usage arising from the inflexibility of the spectrum licensing process. This inefficiency in spectrum allocation can be solved by allowing spectrum sharing using the concept of a cognitive radio (CR), an intelligent device that is able to dynamically adapt and negotiate wireless frequencies and communication protocols for efficient communications. For this, each participating device needs to have many capabilities such as determining location, analysing the external communications environment, sensing the spectrum used by its neighboring devices, dynamically changing the frequency and bandwidth of transmission, adjusting the output power level, and even altering transmission parameters and protocols [3].

Figure 1 provides an indication of the growth of cognitive radios as a research area in the recent past. The figure

shows results for the number of publications with different keywords per year in the IEEE. Many of the keywords represent growing research areas in wireless, whereas other popular keywords such as “VLSI” and “DSP” have also been included for comparison. The first cognitive radio paper was published in 1999; however, research in this area was relatively dormant till 2004. Since then, with maturing technology and rising needs, cognitive radios have seen a tremendous growth in research activity and are now one of the most researched areas in wireless.

A cognitive radio can be structurally and functionally separated into (1) a software defined radio (SDR) unit that includes the hardware of the cognitive radio and (2) an intelligence unit, that provides the required software based intelligence (cognition) to the radio. In this paper, the SDR unit and, more specifically, the spectrum sensing receiver front end of the SDR will be discussed.

The driving force behind the cognitive radio concept has been the use of dynamic spectrum access [4, 5]. Dynamic spectrum access relies on dynamic spectrum monitoring

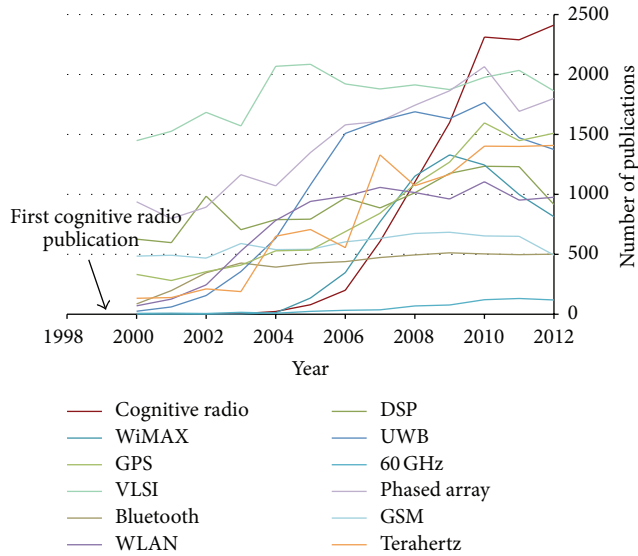


FIGURE 1: Number of publications in different research areas in the last decade.

using a spectrum sensor. Combined with spatial and temporal information, it can be used to perform dynamic spatial [6] or spatio-spectral beamforming [7] to exploit temporal, spatial, and spectral degrees of freedom. In this paper, we focus on the spectrum sensing aspect of the cognitive radio.

Among other features, this continuous monitoring of the spectral environment makes the cognitive radio unique in its hardware. From the hardware perspective, the spectrum sensor remains a challenging aspect of cognitive radio design. Even for narrowband (small frequency range, <100 MHz) spectrum sensors, limiting the power consumption is a challenge. The cognitive radio spectrum sensor needs to detect signals at all frequencies of interest instantaneously. In addition, very high detection sensitivity is desired (perhaps 100 times better than a conventional narrowband radio) to overcome the hidden-terminal problem, shadowing, channel fading, multipath, and so forth lest it causes interference to other users due to incorrect sensing [4].

In this paper, we demonstrate the suitability of passive switched capacitor signal processing techniques for spectrum sensing applications. We present various techniques in passive switched capacitors that allow them to be used in high speed, low power RF applications. As an example, we present a prototype passive charge based FFT design, first presented in [8], that can instantaneously analyze wideband signals (5 GHz bandwidth) with very low power consumption using these techniques. We present previously unpublished details on the FFT design methodology, architecture choice, and optimization techniques. We derive a linear time invariant (LTI) model of the system for use in system level designs. New measurement results are presented to corroborate the suitability of this design for spectrum sensing applications.

2. Review of SDR Spectrum Sensors

The architecture design for the SDR analog/RF is significantly different from that of traditional narrowband radios. In

the original software radio proposal by Joseph Mitola in 1992, he envisioned an architecture that digitized the RF bandwidth (no downconversion) and performed spectrum analysis and demodulation in the digital domain. While providing the maximum amount of flexibility through increased software capability in the digital domain, this architecture imposes impractical requirements on the analog-to-digital and digital-to-analog converters. For example, as discussed in [9], a 12 GHz, 12-bit ADC that might be used for this purpose would dissipate 500 W of power! As a result, the ideal goal of being able to communicate at any desirable frequency, bandwidth, modulation, and data rate by simply digitizing the input and invoking the appropriate software remains far from realizable.

Subsequent proposals for spectrum sensing architectures can be divided into two fundamental categories: a scanner type and a wide bandwidth instantaneous digitizer type.

2.1. Scanner Architecture. In this scheme, a narrowband, wide-tuning receiver scans and digitizes the entire bandwidth (similar to a bench-top spectrum analyzer) for analysis. The digital back end processes each band sequentially and stitches the frequency domain outputs to obtain a spectral map of the environment. An example of architecture is shown in Figure 2. Note, however, that, in order to overcome issues such as multipath, fading, hidden nodes, and interference problems [4], the sensitivity and dynamic range requirements of the architecture are more challenging than a traditional communications receiver. Moreover, sensing may be a blind detection problem, as opposed to traditional reception where *a priori* knowledge of the transmitted signal is available.

Although the scanning architecture is able to reuse some features of a traditional receiver architecture, this detection technique suffers from multiple shortcomings. These systems lack the agility to be able to detect any fast-hopping signals. Frequency domain stitching is power hungry in the digital domain due to the need to correct phase distortion introduced by the analog filters. Moreover, stitching the frequency domain information from several scans is imperfect in the face of multipath; consequently, signals spanning across multiple scan bandwidths are imperfectly reconstructed. Due to these and other reasons, it is desirable to construct a real-time instantaneous bandwidth digitizer (similar to J. Mitola's original software radio idea) in the spectrum sensor.

2.2. Wideband Digitizer Architecture. Unlike the scanning type architecture, a wideband instantaneous digitizer is expected to digitize the entire RF bandwidth simultaneously. Understandably, the wideband digitizer has widely been considered as the bottleneck to the realization of the SDR based cognitive radio. A number of efforts in recent years have focused on wider bandwidths, broadband matching, higher front end linearity, and, most importantly, wideband analog to digital converters.

Several architectures have been proposed for the RF front end. Of these, the most popular is the extension of the traditional receiver architecture as shown in Figure 3 effectively performing an RF to digital (R-to-D) conversion [10].

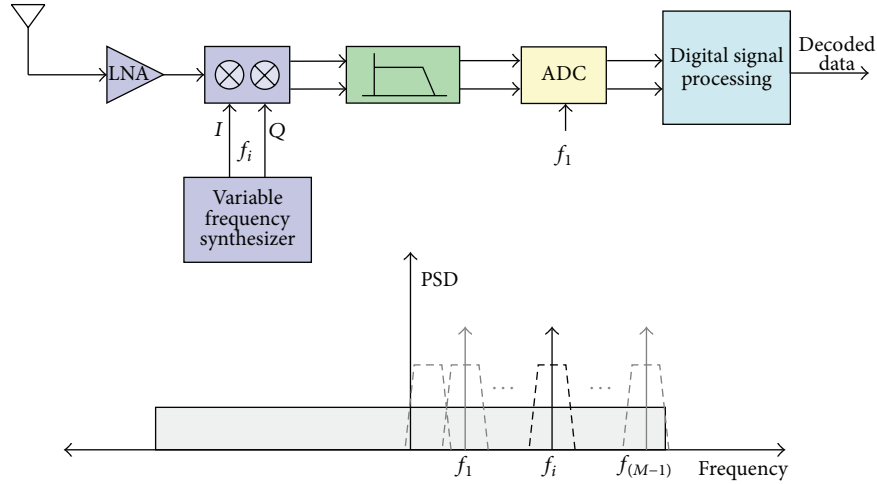


FIGURE 2: A narrowband, wide-tuning scanning approach for signal sensing.

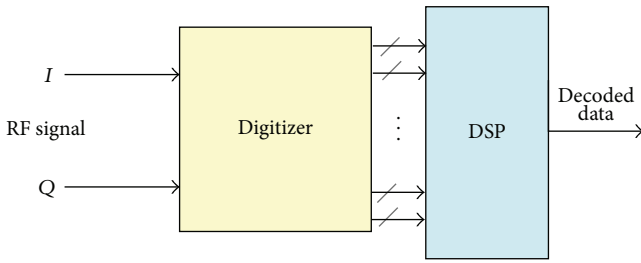


FIGURE 3: A wideband RF to digital conversion architecture for spectrum sensing.

Typically, the front end also requires a wideband low noise amplifier (LNA) prior to the digitizer (not shown). Moreover the front end needs to handle a very large dynamic range due to the generally large peak-to-average power ratio (PAPR) of wideband signals. The increase in PAPR for wide bandwidths is described in Figure 4. As shown, the PAPR for the narrowband signals is only 2, while that for the wideband signal (5 times the bandwidth) with multiple signals, all having similar powers, is 10. As a result of the large PAPR of the wideband inputs, a very linear front end is required. The linearity requirements of the LNA have been addressed in [11]. Another approach using a low noise transconductance amplifier (LNTA) followed by mixers is discussed in [12]. Moreover, passive mixer-first topologies have been proposed for high IIP_3 performance [13].

The digitizer block shown in the figure is essentially an ADC with performance specifications beyond the capability of using state-of-the-art converters. This wideband digitizer can be implemented in multiple ways, all based on some form of multiplexing in order to ease the requirements on the ADCs. A multiplexed broadband approach using time interleaving can be utilized as shown in Figure 5 [10]. This scheme reduces the sampling rate of ADCs. However, all the ADCs still see the full bandwidth and, therefore, still require high dynamic range capability.

In order to reduce the dynamic range requirements on the ADCs, it is possible to transform the signal to a different domain prior to digitization. Specifically, a frequency domain transform is particularly attractive [10]. A frequency domain transform can be approximated in practice using band-pass filters for channelization. This reduces the dynamic range requirements on the ADCs but introduces the problem of designing impractically sharp band-pass filters. Replacing sharp band-pass filters by frequency downconverters followed by sharp low-pass filters eliminates this problem as shown in Figure 6 [10]. However, these are based on PLLs, mixers, and low-pass filters [14] or on injection locked oscillators [15] (note that injection locked oscillators have the advantage of a larger noise suppression bandwidth (\approx lock range) [16] and provide better reciprocal mixing robustness compared to PLLs (assuming that the reference phase noise is better than the VCO phase noise)), and can be power hungry. Moreover, harmonic mixing of signals within the SDR input bandwidth severely corrupts the channelized baseband signals. Additionally, due to overlap between bands and phase issues, signal reconstruction from the digitized filter bank outputs is challenging.

In this paper, we propose a digitizer approach based on analog signal processing using passive switched capacitors to condition the signal prior to digitization by ADCs (Figure 7). The RF discrete time (DT) signal processing, as shown in the second block in Figure 7, eases the dynamic range requirements on the ADCs by prefiltering the signal.

For RF sampled processors, an RF sampler has historically been an inherent bottleneck. However, with the scaling of technology and subsequent improvement in switch performance, RF sampling has become feasible in modern silicon processes. Moreover, it is possible to use charge domain sampling to leverage the inherent benefits of including of a built-in antialias filter into the sampler, robustness to jitter, and the ability to vary the resulting filter notches by simply varying the integration period. This use of RF samplers and subsequent discrete time processing provide a number of advantages in deep submicron CMOS processes [17].

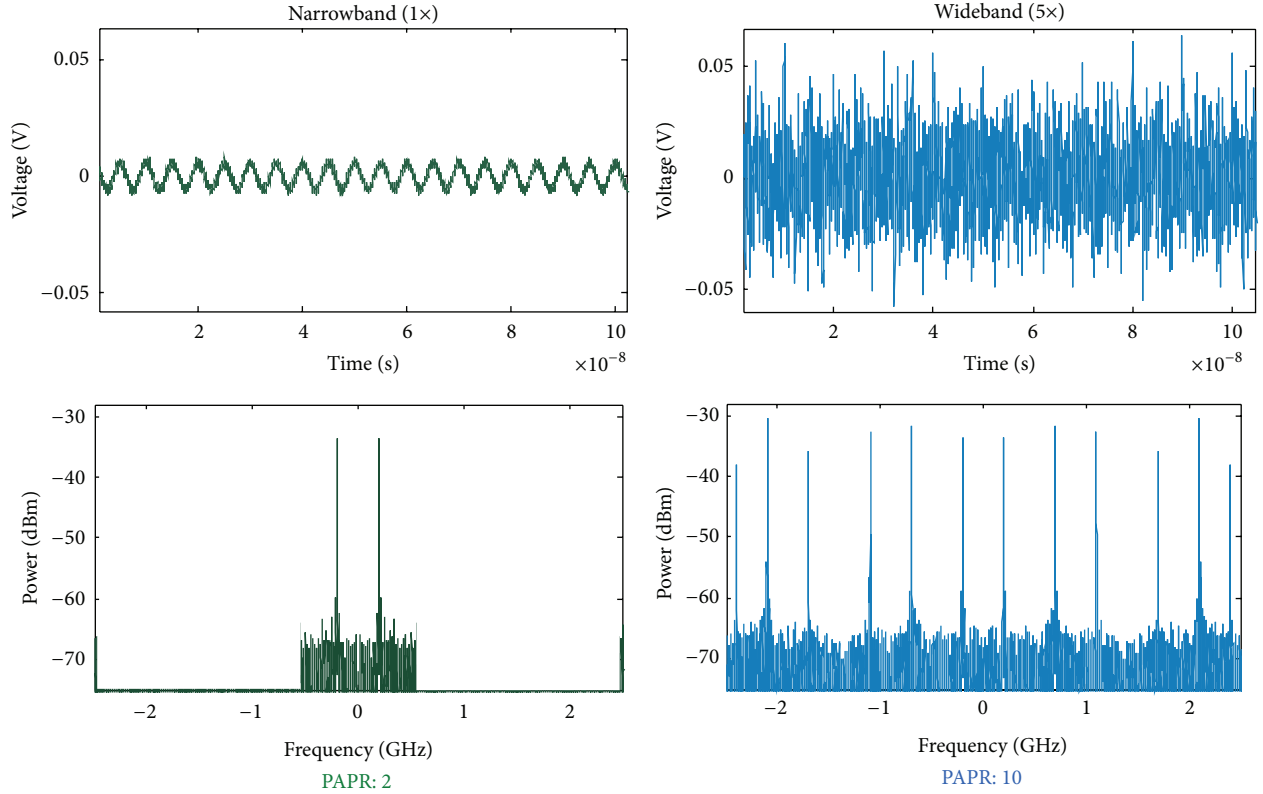


FIGURE 4: PAPR increase in wideband signals compared to narrowband signals.

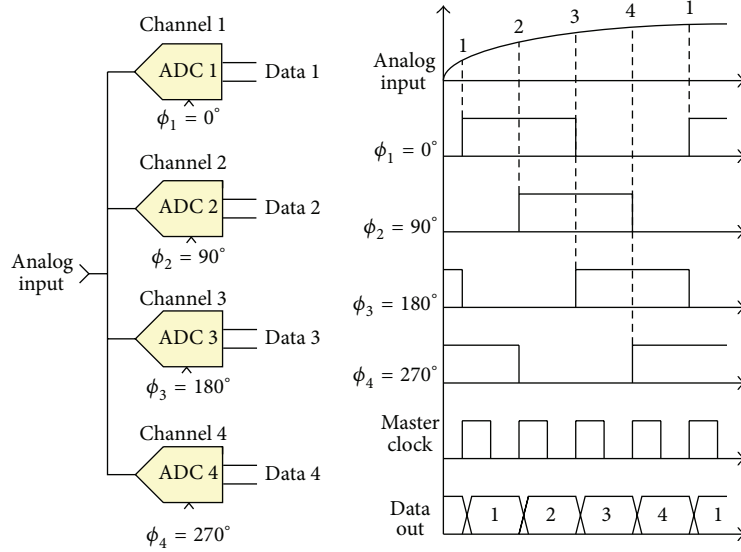


FIGURE 5: Time interleaved ADCs for broadband channelization.

Recently, other discrete time radio receivers using RF sampling have been demonstrated using CMOS technology for Bluetooth [18], GSM/GPRS [19], WLAN [20], and SDR type applications [9, 21].

3. Passive Analog Signal Processing

In this section, we show how signal sampling and variable-rate analog signal processing can be performed in the charge

domain for spectrum sensing applications. Many of the benefits of the discrete time FFT architecture are based on the use of passive discrete time charge based computations. This is best illustrated with the help of an example design. The passive switched capacitor shown in Figure 8 is able to operate at RF sampling speeds [22].

In this circuit the input signal is sampled progressively in time ($\phi_1 - \phi_n$). After N clock periods the averaged output is sampled onto the capacitor C_s , which has previously been

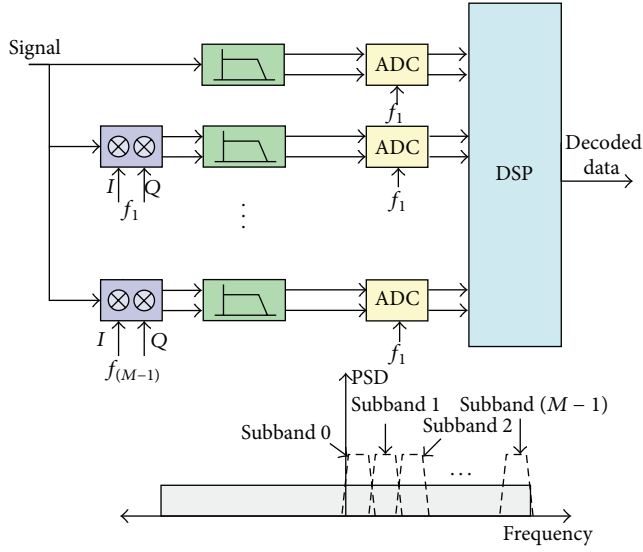


FIGURE 6: Low-pass filter bank approach for channelization.

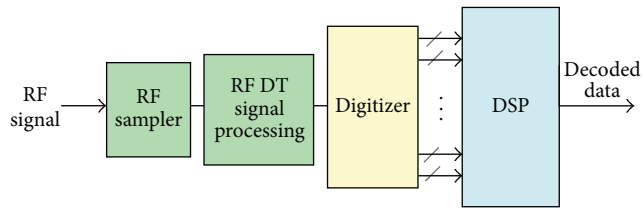


FIGURE 7: An envisioned SDR architecture enabled by passive analog signal processing.

discharged. The complete circuit implements an N -tap FIR filter that is decimated by N . Interestingly, if the capacitor C_s is not discharged between each rotation then the circuit implements an N -tap FIR filter combined with a first-order IIR filter that is decimated by N . Note there is no active element (i.e., amplifier) in this circuit. The circuit consists only of switches and capacitors, so the maximum sampling rate is only dependent on the RC settling times. Additionally, the only power dissipation, other than that required for sampling the signal from the input, is due to the charging and discharging of the switch-transistor gate capacitors in a very digital-like way. As a result, a variety of functions on the sampled signal can be computed very fast and using minimal power.

3.1. Passive Computations. For performing any linear function, addition and multiplication operations need to be performed. Note that all passive switched capacitor operations are destructive in nature. Therefore, once an operation is performed, the input values are lost. For performing multiple operations on a single input, multiple copies of the input need to be maintained. Here we present techniques to perform these operations using passive switched capacitor circuits. In order to select a suitable technique for implementation, it is necessary to compare these techniques based on their

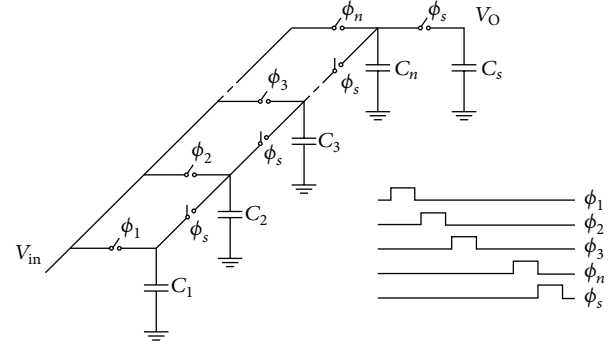
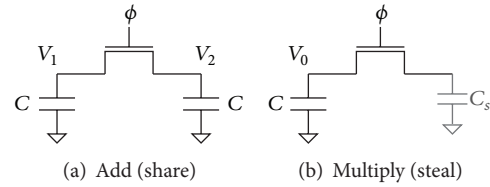
FIGURE 8: Switched capacitor implementation of a passive N -tap FIR with a decimation by N .

FIGURE 9: Techniques for charge domain addition and multiplication operations.

robustness to nonidealities, ease of implementation, power consumption, speed, and so forth.

3.1.1. Addition Operation

(1) *Parallel Connection.* Using passive switched capacitors, voltages may be added by sharing the charges on two participating capacitors by connecting them in parallel as shown in Figure 9. The result of this operation (for capacitors with equal capacitances) is the average value $(V_1 + V_2)/2$ of the input voltages V_1 and V_2 , which is a scaled version of their sum operation. Also note that two copies of the output are obtained and these can be used for two subsequent independent operations as desired. However, the operation inherently attenuates the output by half. From an implementation perspective, use of parallel capacitors allows the sharing of one plate (ground plate) for all the capacitors. This can greatly reduce the parasitic capacitance and resistance of the capacitor and the area of the overall implementation.

(2) *Series Connection.* An alternative technique is to connect the capacitors in series. The result of this operation is the sum $(V_1 + V_2)$ of the input voltages V_1 and V_2 . In this scheme, it is possible to use slightly delayed clock phases in order to make the charge injection independent of the input voltage [23]. However, in the latter technique, switches are required both on the top and bottom plate, thereby increasing the power consumption in this circuit. The two switches placed in series halve the speed of this circuit for identical switch sizes. Moreover, only one output (which can be used for exactly one subsequent

operation) is obtained. Also, both the top and bottom plate parasitics are problematic.

3.1.2. Multiplication

(1) *Charge Stealing.* Multiplication in the charge domain can be performed by scaling the voltage on a capacitor using a share operation with another known capacitor (stealing capacitor). The charge on the stealing capacitor is not utilized later on. The overall operation causes a subunity scaling on the original value. The scaling factor for a capacitor of value C and a stealing capacitor of value C_s is given by $m = C/(C+C_s)$.

Figure 9(b) shows a scaling operation using a stealing capacitor of size C_s with no initial voltage on it. After the sharing operation, the final value on the capacitor with initial value V_0 becomes $V_0 \cdot C/(C+C_s)$. C_s can be chosen appropriately to obtain a particular scaling factor. Note that, although this technique is capable of performing both subunity scaling and multiplication with a known attenuation, at least one of the operands needs to be known in advance for this implementation. In case voltage dependent variable capacitors (i.e., capacitor DACs) are utilized, dynamic operands can also be used.

(2) *Pulse-Width Modulation (PWM).* Another technique to perform multiplication using passive switched capacitors is to modulate the turn on time of the switch and perform an incomplete share operation with a fixed stealing capacitor. The duration of the operation determines the multiplication factor. It is possible to multiply two unknown operands using this technique. Unfortunately, considering the nonlinearity in the resistance and the share operation, the errors caused by this technique make it unusable. However, the concept can be used to devise another PWM scheme which allows complete settling, thereby making it more reliable. In this modified technique, the switch can be turned on using a sequence of randomly placed pulses and sharing the capacitor charge using a small stealing capacitor for each clock cycle. The stealing capacitor is discharged at the end of each cycle. Complete settling is allowed in each cycle. The total number of on-pulses determines the amount of scaling. Maximum scaling is obtained when all the clock cycles have on-pulses, while no scaling is obtained when all the clock cycles have off pulses. Although this technique is relatively accurate and is able to handle dynamic operands, it is slow and consumes more power than the charge stealing technique. Also, depending on the accuracy required, the attenuation is considerable.

(3) *Current Domain.* If the charge is converted to the current domain, a single variable-duration PWM scheme can be used to perform multiplication. Also, multiplication would not entail an inherent attenuation. However, the technique is very power hungry, and the accuracy of the transconductance amplifier that translates from charge to current domain needs to be very high.

Due to their low power, high speed characteristics, we have focused on the parallel connection scheme for addition and the charge stealing scheme for multiplications in our

designs. For many relevant linear algebra problems, multiplication using fixed coefficients is sufficient, and this technique lends itself easily to such applications.

3.2. *Switching Schemes.* To implement these addition and multiplication schemes, a variety of switched capacitor topologies can be used. Note that complex multiplication can be performed using a combination of scalar multiplication operations as discussed in [24]. In this subsection, we discuss the various topologies and their trade-offs. For the addition operation, two capacitors can be shared as shown in Figure 9(a) and represented by Figure 10(a). We can combine a share followed by scaling into a single operation by connecting 3 capacitors (2 with input samples and 1 empty) and sharing their charges. This can be performed in different ways using 2 or 3 switches as shown in Figures 10(b)–10(d). It can be shown that 3 appropriately sized switches in the scheme of Figure 10(d) minimize the settling error [25]. Multiplication by a factor $c + c \cdot j$ is a special case scaling operation that can be performed using a single step operation [25]. Depending on the normalization of the scaling factor, this may be performed using 4 capacitors (Figures 10(e)–10(h)) or using 5 capacitors (Figures 10(i)–10(l)). Moreover, in the case of four input operations (radix-4 operations), these schemes (Figures 10(e)–10(l)) are useful.

While many schemes (Figures 10(a)–10(b), 10(d), 10(e), 10(h), 10(i), and 10(l)) ensure settling symmetry, others (Figures 10(c), 10(f), 10(g), 10(j), and 10(k)) use fewer switches for lower power at the expense of settling performance and mismatch. Some variants (Figures 10(d), 10(h), and 10(l) with equal size switches) provide both settling speed and symmetry at the cost of larger power. When the switches between the operand capacitors are sized differently from those connecting to the stealing capacitor, in (d) and (l), these same configurations can be optimized for an enhanced settling-per-power performance. Finally, when comparing the different schemes, with their appropriate switch sizes, different trade-offs with regard to charge injection, clock feed-through error, and so forth should be considered.

For our design, we chose to use (a) and (d) to perform radix-2 scalar operations, while complex operations are performed by cascading to sets of operations. Configurations (h) and (l) were used to perform single-phase complex multiplication in special cases. In the case of (d) and (l), optimized switch sizing was used to mitigate their extra power demands while still realizing their enhanced settling performance for a net settling-per-power gain versus (b, c) and (i–k), respectively.

3.3. *Nonidealities.* Several nonidealities haunt passive switched capacitor circuits. The problem of nonidealities is aggravated by the absence of a virtual ground node unlike in op-amp based active switched capacitor circuits. The effect of sampling clock jitter in passive switched capacitor circuits has been analyzed [26]. Two important nonidealities, clock feed-through and charge injection, become a nuisance in the absence of a virtual ground node. Consequently, traditional circuit techniques such as bottom plate sampling are difficult

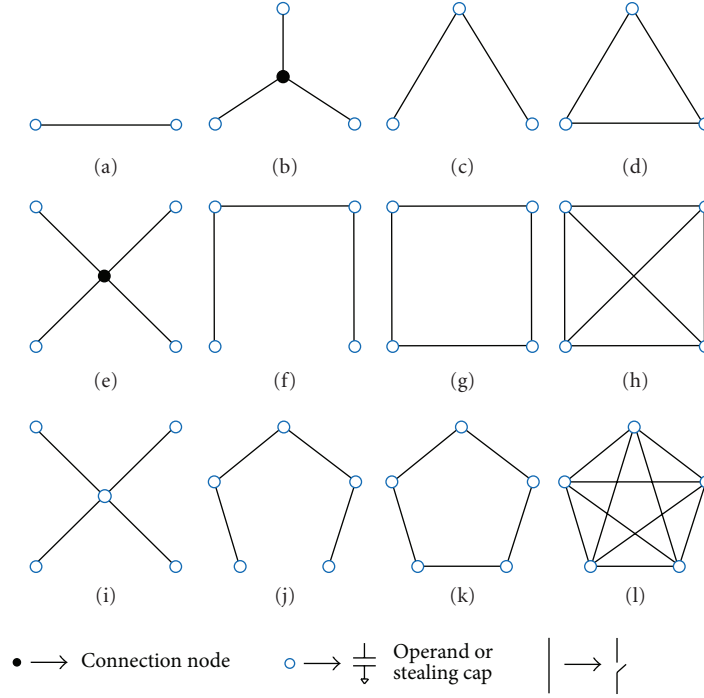


FIGURE 10: Different switching topologies for charge domain operations.

to implement. Also, poor matching between nMOS and pMOS switches and the reducing difference between V_{dd} and V_{th} in scaled technologies make the use of transmission gate switches less effective for mitigating these nonidealities. The noise in the system is dominated by the kT/C noise of the RC filter formed by the switch-capacitor combination. Moreover, for a multistage switched capacitor operation, the sampled noise voltages from one stage recombine in the later stages. These combining noise samples in a particular stage are correlated, and, therefore, the final noise becomes a complicated function of the noise sampled at each stage of the switched capacitor operation. The switch resistance (along with the capacitance of the capacitor) determines the settling time constant. However, the switch resistance is inherently nonlinear and input signal dependent. Consequently, in the case of high speeds of operation, incomplete settling can cause significant signal dependent errors in computations.

Since switched capacitor circuits utilize a clock signal, the accuracy of the clock is critical to performance. Specifically, jitter in clocks reduces the accuracy of the switched capacitor computations by translating timing uncertainty to charge and voltage uncertainty. Fortunately, new techniques based on transconductance linearization can be used to achieve low phase noise clocks in SiGe bipolar [27] and even in scaled CMOS circuits [28]. For increased frequency flexibility, highly optimized switched inductor [29] and switched capacitor [30] based LC VCOs can be utilized to obtain a wide range of frequencies without sacrificing noise performance. Moreover, on-chip self-healing techniques [31] utilizing a digital back end can be used for healing the switched capacitor circuits as well as improving the clock jitter [32].

For high speed designs, it is necessary to accurately model these nonidealities in the circuit simulator. It is also useful to have the ability to individually turn off these nonidealities to trace the effect of each nonideality on the output error. For our designs, we model the nonidealities in MATLAB and include them in system level simulations using MATLAB or Simulink [25]. This allows us to effectively capture the nonidealities and optimize the designs in their presence.

4. An Analog FFT-Based Front End

In this section, as an example of a passive switched capacitor spectrum sensing front end, we introduce a frequency domain divide and conquer approach that can enable wide-band digitization. The architecture comprises an analog domain Fourier transform signal processor (see previous implementations by [33, 34]) that can be followed by multiple ADCs that digitize the input in the frequency domain. In our design, we utilize an RF sampler followed by an analog domain, discrete time, passive switched capacitor FFT engine to perform channelization of the wideband RF input. The circuits are based on the addition and multiplication techniques discussed and selected in Section 3. A description of the design of this charge reuse analog Fourier transform (CRAFT) was presented in [25]. In this paper, we use the CRAFT design as an example of a passive switched capacitor spectrum sensing front end, provide more details on the design methodology and optimization, and develop high level models for system simulations. Although the discussions here pertain to the CRAFT design, the underlying

principles are general and can be easily extended to other passive switched capacitor front end circuits for similar high speed applications, including linear filtering and other transforms.

For spectrum sensing, we use CRAFT as a functionally equivalent linear phase N -path filter (see Figure 11) to perform channelization [35]. This scheme reduces both the required speed and dynamic range of the ADCs and, by virtue of being minimal phase, allows for simple reconstruction in the digital domain using an IFFT without any loss of information.

For dynamic range calculations, signals are assumed to be distributed evenly in frequency. Breaking the input up into equal frequency channels reduces the PAPR as explained earlier in Figure 4. In general, an N -path channelization of spread signals reduces the dynamic range by N times (even in the more general case with multiple signals arbitrarily placed in frequency, this approximation typically holds), causing an N times dynamic range reduction for the ADCs.

The DFT computation to be performed is a time-to-frequency transform defined as

$$\text{DFT: } X(k) = \sum_{n=0}^{N-1} x(n) W^{kn}, \quad (1)$$

where W is defined as $W = e^{-2\pi j/16}$. The desired 16-point DFT ($N = 16$) can also be represented as a linear matrix operation on a vector of length 16 given by

$$\mathbf{X} = \mathbf{F}\mathbf{x}, \quad (2)$$

where the scaling factor due to attenuation inherent in the charge domain operations is absorbed within \mathbf{F} . Expanding (2) for the length 16 case we get

$$\begin{bmatrix} X_0 \\ X_1 \\ X_2 \\ \vdots \\ X_{15} \end{bmatrix} = \frac{1}{k} \begin{bmatrix} 1 & 1 & 1 & \dots & 1 \\ 1 & W & W^2 & \dots & W^{15} \\ 1 & W^2 & W^4 & \dots & W^{30} \\ \vdots & \vdots & \vdots & \ddots & \vdots \\ 1 & W^{15} & W^{30} & \dots & W^{225} \end{bmatrix} \begin{bmatrix} x_0 \\ x_1 \\ x_2 \\ \vdots \\ x_{15} \end{bmatrix}, \quad (3)$$

where x_i are the DFT inputs $x(i)$, X_j are outputs $X(j)$, and k is the scaling factor. The equation can be further simplified by noting the symmetry and periodicity of the powers of W . These properties are utilized to formulate the FFT algorithm as an efficient implementation to calculate the DFT outputs in $N \log_2 N$ operational complexity rather than the N^2 complexity of multiplication by \mathbf{F} .

Figure 12(a) shows the flowchart representation of the radix-2 decimation-in-time FFT algorithm used in CRAFT. As seen in Figure 12(a) and by its definition as a linear operation, the FFT uses only two types of operations: addition (and subtraction) and multiplication by fixed twiddle factors. The twiddle factors are shown as powers of W in Figure 12(a), where $W = e^{-2\pi j/16}$ are equally spaced points on the unit circle in the complex plane as shown in Figure 12(b). As a result, for every scaling factor W^k , $\Re\{W^k\} \leq 1$, $\forall k$ and $\Im\{W^k\} \leq 1$, $\forall k$. Since passive computations discussed above

in Section 3 inherently attenuate the signal, these operations are suitable for subunity scaling.

The CRAFT design is implemented using a number of blocks shown in Figure 13. A brief description of the circuits utilized in the CRAFT design follows. The timing diagram for the various clock phases used to operate the system is shown in Figure 14.

4.1. RF Sampler. An RF nMOS switch based voltage sampler operating at 5 GS/s for both I and Q paths effectively providing 10 GS/s was implemented. An array of 256 samplers was used for providing inputs to CRAFT as shown in Figure 13. The timing of the sampling clock phases is shown in Figure 14. The noise contribution of the sampler is given by kT/C . Therefore, a larger capacitor reduces the noise. However, increasing the size of the capacitor warrants a larger switch transistor to maintain the same sampling bandwidth, increasing the power consumption in the sampler. In CRAFT, the sampling capacitor was selected to be 200 fF so that the noise from the sampler was below -63 dBFS. The switch size was selected to allow sufficient settling such that the output-referred settling error is below -65 dBFS for 5 GS/s operation.

4.2. CRAFT Core Design. The CRAFT core follows the RF sampler and performs an FFT operation as shown in Figure 13. The CRAFT operation, represented in matrix form as shown in (2), can be further broken down into 4 share and 4 multiply operations in the 4 constituent stages leading to $\mathbf{F} = (1/16) \cdot \mathbf{S}_4 \mathbf{S}_3 \mathbf{S}_2 \mathbf{S}_1 \mathbf{I}_{\text{bitrev}} \mathbf{x}$, where each of the 4 stages is denoted by \mathbf{S}_i and i is the stage number. The matrices for each stage are detailed in the appendix. Each stage is implemented using parallel addition and charge stealing techniques outlined in Section 3. Switching schemes are selected to reduce power and improve settling time. Details of the design methodology, circuit design principles, and circuit optimization are discussed in Section 5. Using the optimized design methodologies, only 5 clock phases are used for the entire CRAFT processing operations. These phases have unequal durations to optimize settling and are shown in Figure 14. The total processing time is chosen to be equal to the sampling time in anticipation of an interleave-by-two implementation.

As shown in Figure 12(a), after each operation, half the wires return to their bus while the rest continues on the other buses. Note that the wires in the CRAFT core are permanently connected to the sampling capacitors and their parasitics directly add to the sampling capacitance. Therefore, to equalize the sampler wiring parasitics, the switches are always placed midway between two operand buses. Two example wires, one always returning to its own bus while the other always shifting onto the other operand bus, are highlighted in the layout screenshot in Figure 15. As seen, the two wire lengths (and their associated parasitics) are nominally matched.

4.3. Output Latch. On the far end of the core, CRAFT connects through switches to operational transconductance amplifier (OTA) based analog latches that store the outputs

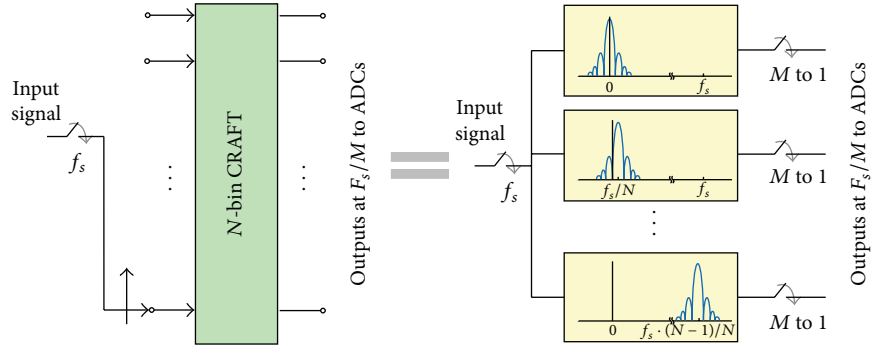


FIGURE 11: The functional equivalence of the DFT with frequency domain outputs and a time-domain N -path complex-bandpass filter bank.

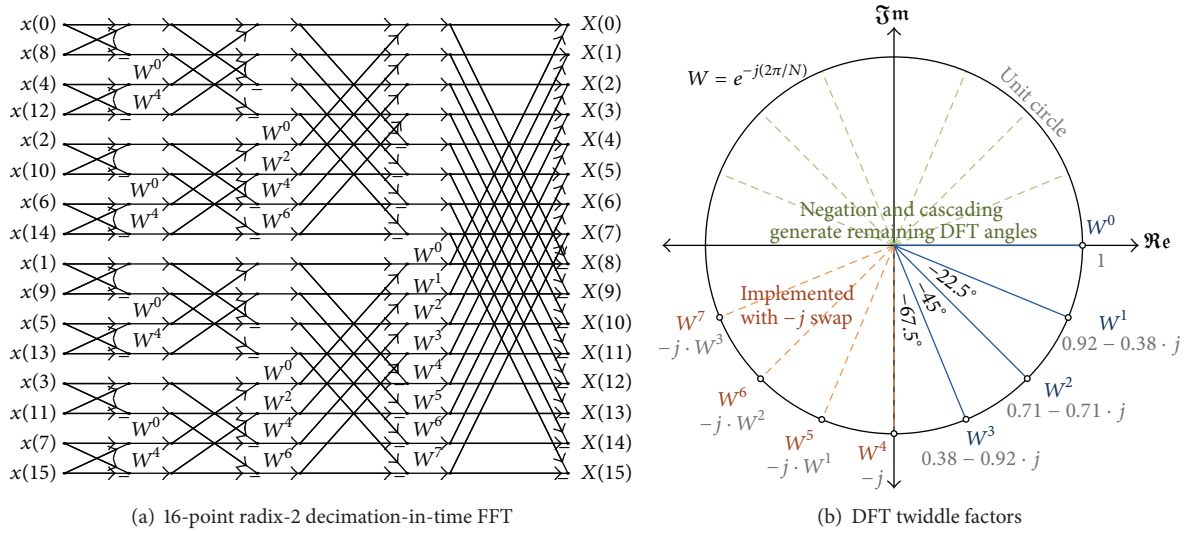


FIGURE 12: A 16-point radix-2 decimation-in-time FFT (a) and DFT twiddle factors coefficients on the unit circle (b).

temporarily prior to being read out (Figure 13). The read-out rate is limited by the speed of the OTA as well as the external amplifiers and ADCs. The OTAs are based on a two-stage, folded cascode, differential architecture and provide 70 dB gain with a 900 MHz unity gain bandwidth (UGB). The OTA is utilized in a differential switched capacitor analog latch configuration. As shown in the timing diagram in Figure 14, the latch performs offset cancellation and OTA common mode feedback during the sampling and processing phases (ϕ_{AZ}) and latches the output with a 10τ settling accuracy (τ is the RC constant of the error settling which is $\propto e^{-t/\tau} = e^{-10}$) during the next 32 clock phases (ϕ_L). The output is then held (ϕ_H) for the external measurement system to read out using an analog multiplexer. As shown in Figure 13, thirty-two latches capture the complex valued FFT output.

4.4. State Machines. The sampling array, CRAFT processing engine, and output latches require multiple clocks to operate and interface with test equipment. These clock phases are shown in Figure 14. The input clock is used to generate all internal signals. The input state machine (labeled state m/c 1 in Figure 13) is externally triggered to initiate a conversion. It

generates 16 sampling clock phases followed by the processing clocks to operate the CRAFT core switches. A second state machine (labeled state m/c 2 in Figure 13) uses handshaking with the first and an external trigger to determine when CRAFT outputs are valid. It subsequently generates the clocks for the analog latch array to save the first CRAFT conversion after being triggered. The latched outputs are then observed sequentially using the integrated low-resistance analog multiplexer (16×4 to 1×4 for differential real and imaginary outputs from one FFT bin). This setup allows asynchronous operation between the conversion and latch triggering.

5. Design Methodology and Optimization

Within the CRAFT processing engine, computational speed, dynamic range, and operating power trade-off with each other. The analysis of design non idealities, discussed in Section 3.3, represents a complex design space with different trade-offs associated with each error source and the particular mitigation techniques utilized. This section outlines a design and optimization methodology used in the CRAFT design to

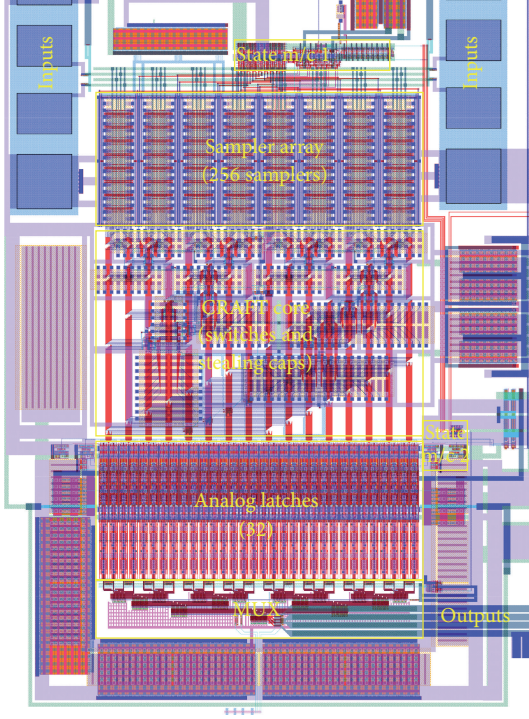


FIGURE 13: Layout of the CRAFT implementation and on-chip test structures.

achieve superior performance. For this implementation, the following specifications and constraints were assumed:

- (1) a 5 GS/s input rate (I and Q) with an interleave-by-two CRAFT engine for processing contiguous windows (this provides a total processing time of $16 \times 1/5 \text{ GHz} = 3.2 \text{ ns}$);
- (2) a 60 dB (10 bit) dynamic range design goal.

Using these goals, the CRAFT engine is optimized for processing power. The design methodology is divided into an architecture choice based on the constraints listed, followed by an energy optimization procedure.

5.1. Design Parameters. To specify the architectural parameters, we initially assume the processing time to be shared equally among the 5 clock phases (unlike in Figure 14). This assumption is revisited during the energy optimization procedure described later on. Also, a nominal V_{dd} for all the stages is assumed as an initial choice and is optimized later on. Based on these assumptions, the following design choices are made.

- (1) *Input Swing.* The maximum input swing, $V_{sig,max}$, for the sampler is chosen to achieve -60 dBFS nonlinearity while running at 5 GS/s. This determines the peak-to-peak input swing to be used as the input full scale. For use with a nMOS switch based processing core the common mode voltage, V_{cm} , is set at $(1/2)V_{sig,max}$.
- (2) *Capacitor Size.* The sampling capacitor size is selected such that the noise floor from the sampling operation

is lower than required for the target SNDR of 60 dB. This dictates a sampling capacitor size of at least 200 fF.

- (3) *Attenuation.* Attenuation degrades FFT performance. Consequently, all techniques that mitigate attenuation are incorporated for improved performance.
- (4) *Dummy Switches.* The effect of clock feed-through and charge injection for each stage on the overall SNDR is simulated. Dummy switches are selected for stages where the overall SNDR is otherwise not met.
- (5) *Additional Settling Switches.* The overall computational settling error is simulated, and additional settling switches are used for stages where their effect is overtly beneficial to SNDR performance.
- (6) *Sampler Switch Size.* The minimum switch size that provides adequate sampler settling and nonlinearity for the required SNDR is determined.
- (7) *Settling.* The minimum per-stage computation settling accuracy required for the overall SNDR is selected. For CRAFT, the following amounts of nominal computational settling were chosen for stages 1–4: 7τ , 4τ , 5τ , and 4τ , respectively.

5.2. Energy Optimization. The exact switch sizing in each stage, as well as the V_{dd} employed, trade-off with the total energy consumption per processing operation. The energy optimization algorithm is outlined below.

5.2.1. Supply Voltage. In short channel devices velocity saturation affects nMOS switches. The triode resistance of a switch in deep triode ($(V_{gs} - V_{tn}) = V_{ov} \gg V_{ds}$) varies proportionally as below and is empirically fit as shown:

$$R_{triode} \propto \left(\frac{1 + U_0 V_{ov}}{V_{ov}} \right) \approx \left(\frac{1}{V_{ov}} \right)^p. \quad (4)$$

For the devices in CRAFT, $p = 0.50$ provided an accurate empirical fit. Using this approximation, the switch resistance is $R_{sw} \propto W^{-1}(V_{ov})^{-p}$. For a constant R_{sw} , $W \propto (V_{ov})^{-p} = (V_{dd} - (V_{tn} + V_{cm}))^{-p}$. In order to calculate the energy per switch operation, we compute $(1/2)C_{gs}V_{dd}^2 \propto W \cdot V_{dd}^2$. Using these equations, we compute the energy per switch operation for a constant switch “on” resistance:

$$E_{sw}|_{const.R_{sw}} \propto \frac{V_{dd}^2}{(V_{dd} - (V_{tn} + V_{cm}))^p}. \quad (5)$$

This is plotted in Figure 16. As seen, this curve has a unique minimum energy that occurs at $V_{dd,opt} = (2/(2-p))(V_{tn} + V_{cm})$. Naturally, this minimum coincides with the typical supply voltage in this technology to optimize digital energy per speed (e.g., consider this nMOS switch as part of an inverter). This optimum V_{dd} is then customized per stage depending on the varying operand voltage swings as a result of attenuation. Note that for the optimization described, it is assumed that 2 different supply domains are available for optimization to cover the general case. The optimization

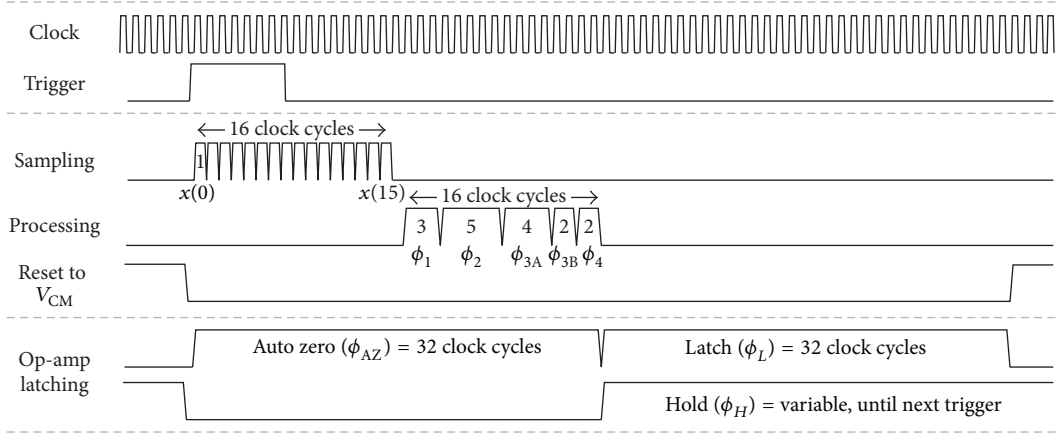


FIGURE 14: Timing diagram showing the clock, trigger, sampling, processing, reset, and output latch clocks.

TABLE 1: Summary of variables in LTI model.

| Variable | Description | Expression |
|---------------------|---------------------------------|---|
| \mathbf{x} | Input (16 samples) | $x(i), \forall i = [0, 15], i \in \mathbb{Z}$ |
| \mathbf{n}_s | Sampler noise | $\sigma_{n_{s,i}}^2 = 2kT/C$ $C = \text{capacitance per copy}$ |
| \mathbf{F} | Ideal FFT | $\frac{1}{16} \mathbf{S}_4 \mathbf{S}_3 \mathbf{S}_2 \mathbf{S}_1$ (see the appendix) |
| $\Delta \mathbf{F}$ | Linear FFT error | See Section 6 |
| \mathbf{F}' | FFT approximation | $\mathbf{F} + \Delta \mathbf{F}$ |
| \mathbf{N}'_p | Processing noise at o/p | See Section 6 |
| \mathbf{N}_q | Quantization noise at ADC i/p | See Section 6 |
| $\hat{\mathbf{H}}$ | Correction matrix | $\mathbf{F}(\hat{\mathbf{F}}')^{-1}$; see Section 6 and [25] |
| \mathbf{Y}' | Digitized o/p | $(\mathbf{F} + \Delta \mathbf{F})(\mathbf{x} + \mathbf{n}_s) + \mathbf{N}'_p + \mathbf{N}_q$; see Section 6 |
| \mathbf{Z}' | Digitized and corrected o/p | $\hat{\mathbf{H}} \mathbf{Y}' = \hat{\mathbf{X}} + \hat{\mathbf{N}}_s + \hat{\mathbf{N}}_p + \hat{\mathbf{H}} \mathbf{N}_q$; see Section 6 |

algorithm can be easily modified for the specific case using single or multiple voltage domains, based on availability. Additionally, if alternate sample rates or time allocations may be used, different V_{dd} settings allow separate optimization for those modes as implemented switch sizes remain fixed.

5.2.2. Switch Size. For calculating the optimal switch width, note that each V_{dd} corresponds to a particular switch width (for a given resistance) on the constant-resistance plot. The maximum allowable nominal resistance can be calculated based on the required settling and allocated time chosen in Section 5.1. Therefore, from the V_{dd} chosen above and the maximum allowable resistance, the optimal switch width W for each stage is calculated.

5.2.3. Time Allocation. The energy per stage is dependent on the required switch resistance and, consequently, the

time allocated per stage. The per-stage time allocated is now considered as the last optimization variable and is redistributed (instead of the equal distribution assumed earlier) to optimize the total energy further. For the new allocated times (as shown in Figure 14), new optimal switch widths are determined.

6. LTI Model

For the purposes of system level simulations to test communication link performance, it is desirable to model the system using a simple but accurate linear model. For this purpose, we have devised an LTI approximation of the entire CRAFT-ADC digitization operation, along with the twiddle factor inaccuracies and noise. Noise disturbances as well as mismatch based nonidealities and digital correction are also included in the LTI model for performance evaluation. The simulated SNDR performance using the LTI model matches the performance obtained through circuit simulations. This makes the LTI model suitable for fast and reliable system level simulations without the need for circuit level modeling. It also allows the simulation of the CRAFT circuitry for a variety of other architectures and applications.

Note that the measurement results (discussed later in Section 7) include the nonidealities of the 8-bit resolution arbitrary waveform generator (AWG) inputs and the output test equipment (these are among the state-of-the-art test equipment available for measuring an RF front end signal processing DUT) that severely limit the observable nonidealities in the CRAFT circuitry. The additional nonidealities due to the test setup are not part of the model (or circuit simulation), so that the model predicts a somewhat better performance (roughly 10 dB) than is measured.

A brief description of the components shown in Figure 17 is tabulated in Table 1. Note that nonlinear effects such as settling error, charge injection and absorption, and clock feed-through have not been included in this model. As discussed earlier, the 16-point FFT ($\mathbf{X} = \mathbf{F}\mathbf{x}$) is implemented as $\mathbf{X} = (1/D)\mathbf{S}_4\mathbf{S}_3\mathbf{S}_2\mathbf{S}_1\mathbf{x}$, where $D = 16$ is the inherent scaling due to charge based operations.

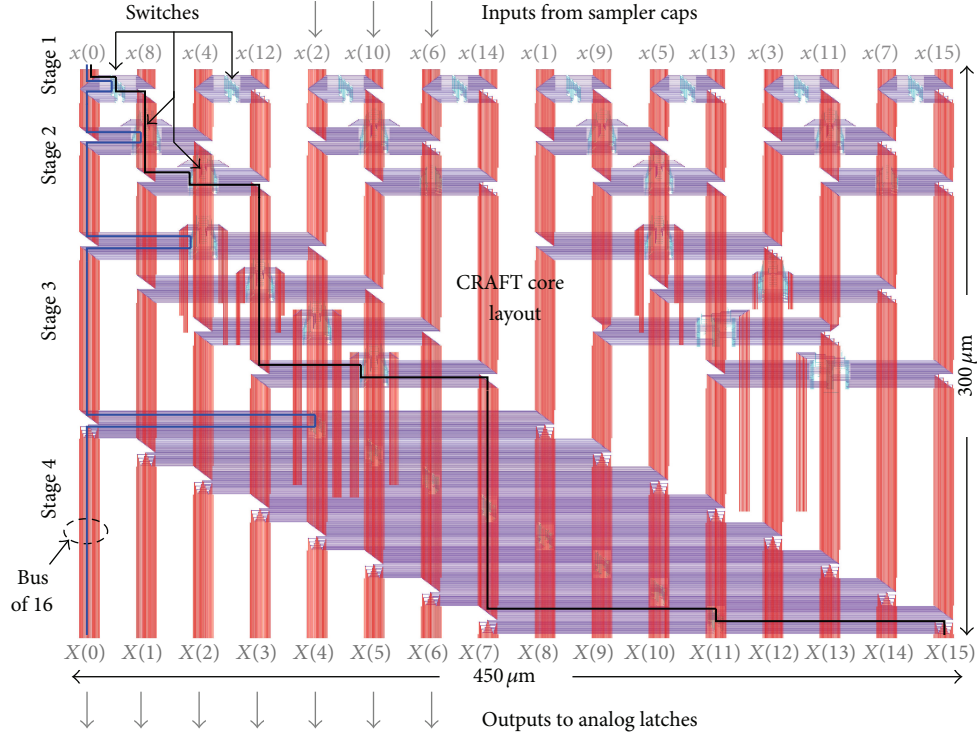


FIGURE 15: Layout of the CRAFT processing core with two highlighted example sampling capacitor distribution cases to be nominally matched for parasitics.

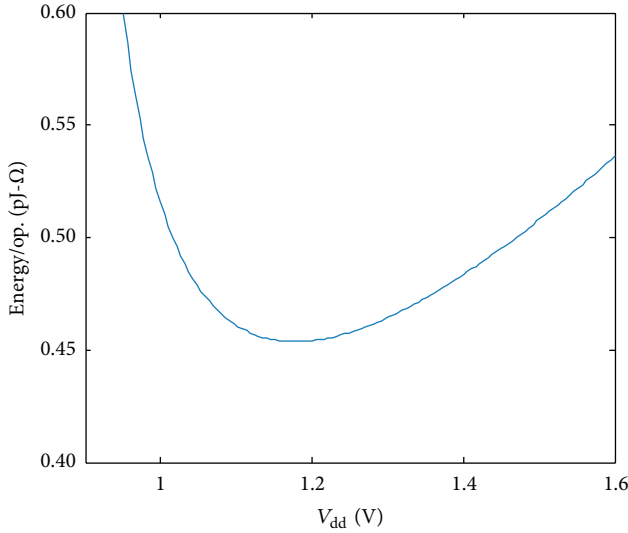


FIGURE 16: Optimization of switch energy per operation (constant R_{sw}).

6.1. Systematic Twiddle Factor Error. The linear errors in the FFT matrix due to systematic capacitor mismatch can be represented using matrix \mathbf{F}' instead of the ideal matrix \mathbf{F} , producing \mathbf{X}' at the output, where

$$\mathbf{X}' = \mathbf{F}' \mathbf{x} = \frac{1}{16} \mathbf{S}'_4 \mathbf{S}'_3 \mathbf{S}'_2 \mathbf{S}'_1 \mathbf{x}. \quad (6)$$

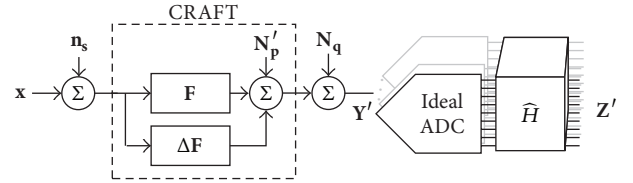


FIGURE 17: An LTI model of the nonideal CRAFT operation followed by digitization and correction.

Expanding each nonideal stage (\mathbf{S}'_i) as an ideal stage (\mathbf{S}_i) plus a systematic error (\mathbf{E}_i),

$$\begin{aligned} \mathbf{X}' &= \frac{1}{16} (\mathbf{S}_4 + \mathbf{E}_4) (\mathbf{S}_3 + \mathbf{E}_3) (\mathbf{S}_2 + \mathbf{E}_2) (\mathbf{S}_1 + \mathbf{E}_1) \mathbf{x} \\ &= (\mathbf{F} + \Delta\mathbf{F}) \mathbf{x}, \end{aligned} \quad (7)$$

where

$$\begin{aligned} \Delta\mathbf{F} &= \frac{1}{16} (\mathbf{E}_4 \mathbf{E}_3 \mathbf{E}_2 \mathbf{E}_1 + \mathbf{E}_4 \mathbf{E}_3 \mathbf{E}_2 \mathbf{S}_1 + \mathbf{E}_4 \mathbf{E}_3 \mathbf{S}_2 \mathbf{E}_1 + \cdots \\ &\quad \mathbf{E}_4 \mathbf{S}_3 \mathbf{E}_2 \mathbf{E}_1 + \mathbf{S}_4 \mathbf{E}_3 \mathbf{E}_2 \mathbf{E}_1 + \mathbf{E}_4 \mathbf{E}_3 \mathbf{S}_2 \mathbf{S}_1 + \cdots \\ &\quad \mathbf{E}_4 \mathbf{S}_3 \mathbf{E}_2 \mathbf{S}_1 + \mathbf{S}_4 \mathbf{E}_3 \mathbf{E}_2 \mathbf{S}_1 + \mathbf{E}_4 \mathbf{S}_3 \mathbf{S}_2 \mathbf{E}_1 + \cdots \\ &\quad \mathbf{S}_4 \mathbf{E}_3 \mathbf{S}_2 \mathbf{E}_1 + \mathbf{S}_4 \mathbf{S}_3 \mathbf{E}_2 \mathbf{E}_1 + \mathbf{E}_4 \mathbf{S}_3 \mathbf{S}_2 \mathbf{S}_1 + \cdots \\ &\quad \mathbf{S}_4 \mathbf{E}_3 \mathbf{S}_2 \mathbf{S}_1 + \mathbf{S}_4 \mathbf{S}_3 \mathbf{E}_2 \mathbf{S}_1 + \mathbf{S}_4 \mathbf{S}_3 \mathbf{S}_2 \mathbf{E}_1). \end{aligned} \quad (8)$$

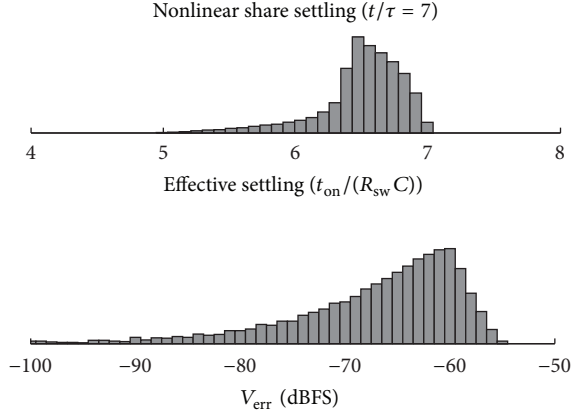


FIGURE 18: Monte Carlo simulations of the settling error in a 2-point share operation with voltage dependent switch resistance.

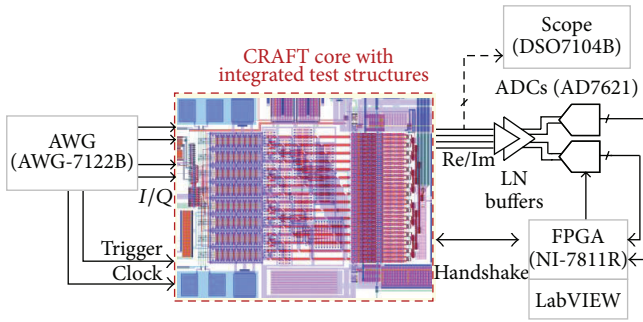


FIGURE 19: Test setup for measuring the CRAFT system.

6.2. Noise. Given that the DFT is a linear operation, the noise in the system can be analyzed using linear superposition of the individual noise sources: noise in the sampler, noise per processing stage, and ADC noise, as shown below.

6.2.1. Sampler Noise

Consider the following:

$$\mathbf{X}' = \mathbf{F}'(\mathbf{x} + \mathbf{n}_s) = \mathbf{F}'\mathbf{x} + \mathbf{N}'_s, \quad (9)$$

where, $\mathbf{N}'_s = (\mathbf{F} + \Delta\mathbf{F})\mathbf{n}_s$.

Note that the outputs of the CRAFT operation are interpreted in the frequency domain. Therefore, any inequality in the gains to the individual outputs will cause the output noise to be colored. This results in (10), where the sampler noise appears at the FFT output as expected white noise terms plus additional colored noise terms due to the unequal gains of $\Delta\mathbf{F}$ to the different bin outputs. Consider the following:

$$\mathbf{X}' = \underbrace{\mathbf{F}(\mathbf{x} + \mathbf{n}_s)}_{\text{white}} + \underbrace{\Delta\mathbf{F}(\mathbf{x} + \mathbf{n}_s)}_{\text{colored}}. \quad (10)$$

6.2.2. Processing Noise. Each stage of processing adds noise in the charge domain and can be expanded as shown:

$$\begin{aligned} \mathbf{X}' &= \frac{1}{2}\mathbf{S}'_4 \left(\frac{1}{2}\mathbf{S}'_3 \left(\frac{1}{2}\mathbf{S}'_2 \left(\frac{1}{2}\mathbf{S}'_1 \mathbf{x} + \mathbf{N}_1 \right) + \mathbf{N}_2 \right) + \mathbf{N}_3 \right) + \mathbf{N}_4 \\ &= (\mathbf{F} + \Delta\mathbf{F})\mathbf{x} + \mathbf{N}'_p, \end{aligned} \quad (11)$$

where

$$\mathbf{N}'_p = \frac{1}{8}\mathbf{S}'_4\mathbf{S}'_3\mathbf{S}'_2\mathbf{N}_1 + \frac{1}{4}\mathbf{S}'_4\mathbf{S}'_3\mathbf{N}_2 + \frac{1}{2}\mathbf{S}'_4\mathbf{N}_3 + \mathbf{N}_4. \quad (12)$$

6.2.3. ADC Noise. The ADC quantizers add noise (\mathbf{N}_q) to the outputs of the CRAFT operation and are interpreted as frequency domain noise perturbations, given by

$$\mathbf{X}' = \mathbf{F}'\mathbf{x} + \mathbf{N}_q. \quad (13)$$

In case all the ADCs have equal gains and the white quantization noise approximation holds, \mathbf{N}_q can be approximated to be white.

6.2.4. All Superposed Noise Sources. Assuming that the noise terms are independent, the total error can be expressed as

$$\mathbf{Y}' = (\mathbf{F} + \Delta\mathbf{F})\mathbf{x} + \mathbf{N}'_s + \mathbf{N}'_p + \mathbf{N}_q. \quad (14)$$

6.3. Digital Correction. Next we consider a linear correction step that can be implemented in the digital domain. The correction matrix is given by $\hat{\mathbf{H}} = \mathbf{F}(\hat{\mathbf{F}}')^{-1} = \mathbf{F}\hat{\mathbf{x}}(\mathbf{X}')^{-1}$, where $\hat{\mathbf{x}}$ is the estimated set of independent input vectors giving uncorrected output responses \mathbf{X}' . Note that $\hat{\mathbf{x}}$ and \mathbf{X}' are matrices comprising N vectors of size N . The output, \mathbf{Z}' , after digital correction, is given by

$$\mathbf{Z}' = \hat{\mathbf{H}}\mathbf{Y}' = \hat{\mathbf{X}} + \hat{\mathbf{N}}_s + \hat{\mathbf{N}}_p + \hat{\mathbf{H}}\mathbf{N}_q, \quad (15)$$

where

$$\begin{aligned} \hat{\mathbf{N}}_s &= \hat{\mathbf{H}}\mathbf{N}'_s = \mathbf{F}(\hat{\mathbf{F}}')^{-1}\mathbf{N}'_s = \mathbf{F}(\hat{\mathbf{F}}')^{-1}\mathbf{F}'\mathbf{n}_s \approx \mathbf{F}\mathbf{n}_s \\ \hat{\mathbf{N}}_p &= \hat{\mathbf{H}}\mathbf{N}'_p = \mathbf{F}(\hat{\mathbf{F}}')^{-1}\mathbf{N}'_p \\ &= \mathbf{F}(\hat{\mathbf{S}}'_4\hat{\mathbf{S}}'_3\hat{\mathbf{S}}'_2\hat{\mathbf{S}}'_1)^{-1} \\ &\quad \times \left[\frac{1}{2}\mathbf{S}'_4 \left(\frac{1}{2}\mathbf{S}'_3 \left(\frac{1}{2}\mathbf{S}'_2\mathbf{N}_1 + \mathbf{N}_2 \right) + \mathbf{N}_3 \right) + \mathbf{N}_4 \right] \\ &\approx \mathbf{F} \left[\mathbf{S}'_1{}^{-1} \left(\frac{1}{8}\mathbf{N}_1 + \mathbf{S}'_2{}^{-1} \right. \right. \\ &\quad \left. \left. \times \left(\frac{1}{4}\mathbf{N}_2 + \mathbf{S}'_3{}^{-1} \left(\frac{1}{2}\mathbf{N}_3 + \mathbf{S}'_4{}^{-1}\mathbf{N}_4 \right) \right) \right) \right]. \end{aligned} \quad (16)$$

This assumes that the correction uses an accurate estimate of the implementation, as represented by the relationships $\hat{\mathbf{F}}' \approx \mathbf{F}'$ and $\hat{\mathbf{S}}'_i \approx \mathbf{S}'_i$.

If the implementation has small error with regard to the ideal transform (so that $\mathbf{S}'_i \approx \mathbf{S}_i$), the approximation below

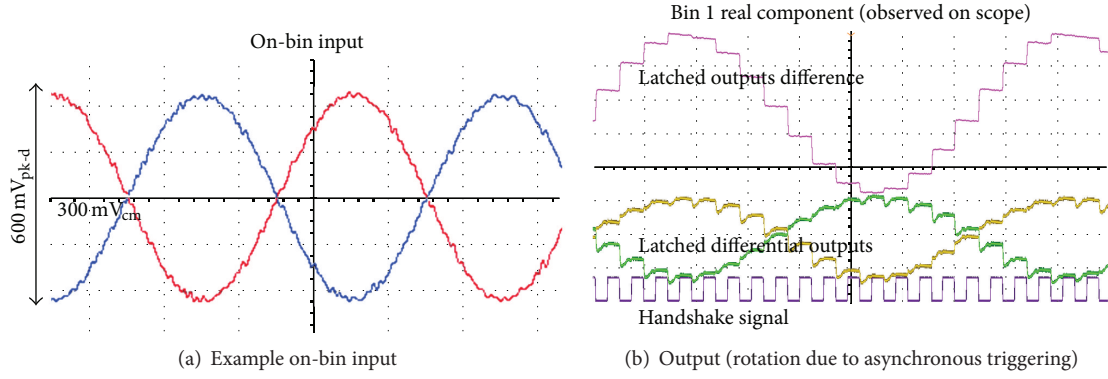


FIGURE 20: Time-domain latched CRAFT outputs and single-bin input, with fractional triggering rate for periodic phase rotation of output.

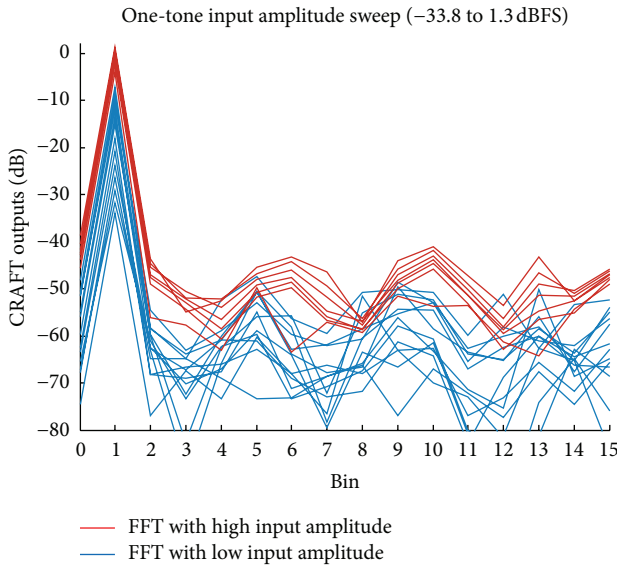


FIGURE 21: Measured frequency domain outputs of the 16 bins with an input on bin 1 at different input amplitudes showing noise in the other bins at low amplitudes (blue, thin) and nonlinearity at higher amplitudes (red, thick).

shows that the processing noise is ideally reduced so that the additive white noise model holds:

$$\begin{aligned} \hat{\mathbf{N}}_p &\approx \mathbf{F} \left[\mathbf{S}_1'^{-1} \left(\frac{1}{8} \mathbf{N}_1 + \mathbf{S}_2'^{-1} \right. \right. \\ &\quad \times \left. \left. \left(\frac{1}{4} \mathbf{N}_2 + \mathbf{S}_3'^{-1} \left(\frac{1}{2} \mathbf{N}_3 + \mathbf{S}_4'^{-1} \mathbf{N}_4 \right) \right) \right) \right] \quad (17) \\ &\Rightarrow \frac{1}{8} \mathbf{S}_4 \mathbf{S}_3 \mathbf{S}_2 \mathbf{N}_1 + \frac{1}{4} \mathbf{S}_4 \mathbf{S}_3 \mathbf{N}_2 + \frac{1}{2} \mathbf{S}_4 \mathbf{N}_3 + \mathbf{N}_4 = \mathbf{N}_p. \end{aligned}$$

In summary, (15) shows that, with small error, digital correction correctly leads to an estimate, $\hat{\mathbf{X}}$, of the desired ideal noiseless transform $\mathbf{X} = \mathbf{F}\mathbf{x}$. Additionally, the colored sampling and processing noise terms are restored to their ideal output-referred values: $\hat{\mathbf{N}}_s \approx \mathbf{F}\mathbf{n}_s$ and $\hat{\mathbf{N}}_p \approx \mathbf{N}_p$. Quantization noise, $\hat{\mathbf{H}}\mathbf{N}_q$, is slightly modified after correction. Rather than being completely independent between output

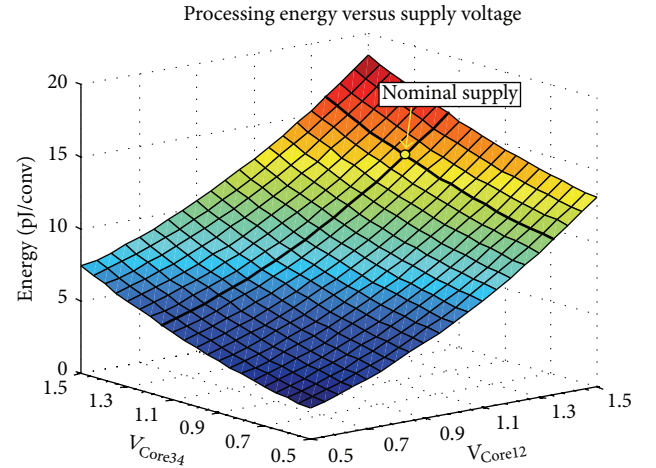


FIGURE 22: Measured energy required per conversion versus CRAFT core supply voltages.

bins, the correction matrix causes some weighted combining of outputs. However, since the implementation is designed to match the desired ideal transform to many bits of accuracy, this effect is minimal.

6.4. Application of the Model. In order to incorporate the nonidealities arising from CRAFT as well as from the rest of the signal path, the appropriate error terms need to be computed and input to the LTI model. For the signal independent computation errors, such as those from uncompensated parasitics or mismatched capacitors, the \mathbf{S}_i matrices can be appropriately modified (i.e., $\mathbf{E}_i \neq 0$). This information is directly available from simulations, chip measurement, or foundry data and can be incorporated as the bit resolution of the matching and the resolution of the parasitic estimation.

In order to model signal dependent nonidealities, the error terms \mathbf{E}_i are computed as a function of the input amplitude. For example, for nonlinear incomplete settling errors, the error is proportional to the input amplitude (by the factor $e^{-t/\tau}$), and the individual errors are made input signal dependent. Note that, in reality, each addition and multiplication operation is dependent on its specific inputs.

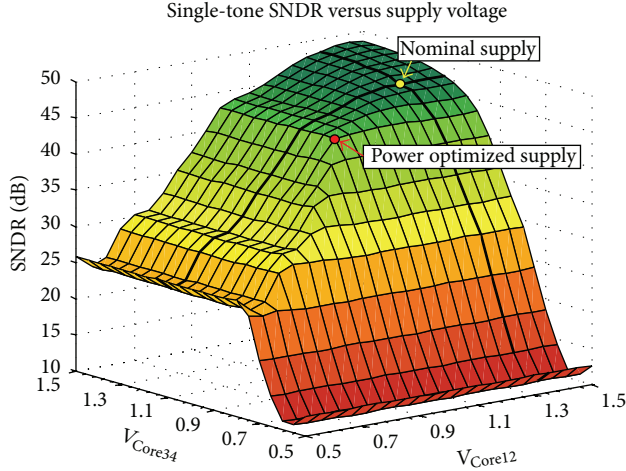


FIGURE 23: Measured SNDR as a function of CRAFT core supply voltages.

In our model, we effectively average out this dependence linearly across all computations such that the resulting error is an approximate function of the input amplitude distribution. For example, Monte Carlo simulations for the effective settling in a 2-point share operation with uniformly distributed input amplitudes are shown in Figure 18. A histogram of the effective settling time is shown on the top, while a histogram of the resulting error with respect to the full-scale signal is shown at the bottom. In this case, the average settling time is 6.5τ while the average error is -62.9 dBFS. The nonlinear settling error can therefore be averaged and incorporated into the LTI system. Note that this average is a strong function of the input amplitude distribution and should be recalculated for the appropriate distribution.

7. Measurement Results

In this section, we present some additional previously unpublished measurements of the CRAFT engine to demonstrate its spectrum sensing capabilities. The test setup for measuring the CRAFT system is shown in Figure 19. As shown in the figure, I and Q inputs from a Tektronix AWG-7122B arbitrary waveform generator are input to the CRAFT sampler. The latched outputs are externally buffered and digitized by external ADCs controlled by an FPGA (NI-7811R) programmed using LabVIEW.

The time-domain input and output characteristics, as observed by the oscilloscope (Agilent DSO7104B, see Figure 19), for a single frequency sinusoidal signal on the first bin are shown in Figure 20. A combination of sine and cosine signals is used to obtain an I/Q input signal. For this measurement, the system is set up such that the input signal is sampled using a progressively shifting phase ($2\pi/16$) upon every FFT conversion causing the bin 1 output to rotate periodically as shown in the figure. Note that this differential peak-to-peak measurement allows us to cancel the fixed DC offset and directly provides the on-bin output magnitude of the CRAFT operation.

TABLE 2: Table of SNDR and SFDR with 1-tone, on-bin, 0 dBFS inputs.

| One-tone bin | 1 GS/s | | 3 GS/s | | 5 GS/s | |
|--------------|-------------|-------------|-------------|-------------|-------------|-------------|
| | SNDR | SFDR | SNDR | SFDR | SNDR | SFDR |
| 1 | 46.6 | 37.7 | 45.8 | 35.8 | 48.1 | 42.6 |
| 2 | 50.9 | 42.8 | 50.7 | 43.8 | 48.4 | 39.7 |
| 3 | 51.5 | 44.7 | 49.8 | 44.8 | 45.8 | 41.8 |
| 4 | 48.9 | 37.9 | 51.4 | 40.2 | 51.1 | 41.1 |
| 5 | 50.2 | 44.4 | 47.7 | 40.7 | 46.2 | 42.5 |
| 6 | 51.4 | 44.8 | 48.0 | 40.1 | 45.0 | 36.3 |
| 7 | 48.1 | 40.2 | 48.2 | 42.6 | 45.1 | 40.1 |
| 8 | 56.5 | 51.2 | 61.2 | 57.2 | 49.9 | 42.8 |
| 9 | 48.5 | 41.3 | 47.5 | 41.2 | 45.2 | 39.6 |
| 10 | 53.7 | 47.8 | 46.6 | 39.6 | 44.5 | 35.6 |
| 11 | 50.3 | 44.9 | 47.6 | 40.0 | 46.6 | 43.3 |
| 12 | 49.2 | 37.9 | 52.2 | 41.4 | 50.9 | 41.6 |
| 13 | 52.0 | 46.2 | 50.0 | 45.5 | 45.0 | 39.9 |
| 14 | 53.8 | 46.6 | 50.9 | 43.0 | 48.5 | 38.8 |
| 15 | 47.1 | 39.0 | 45.4 | 35.9 | 48.9 | 42.3 |
| Minimum | 46.6 | 37.7 | 45.4 | 35.8 | 44.5 | 35.6 |
| Maximum | 56.5 | 47.8 | 61.2 | 45.5 | 51.1 | 43.3 |
| μ | 50.6 | 43.2 | 49.5 | 42.1 | 47.3 | 40.5 |
| σ | 2.7 | 4.1 | 3.8 | 5.0 | 2.3 | 2.3 |

For a signal with frequency exactly aligned with the first DFT bin, the output is expected only at the first bin output for a rectangular window. All other bin outputs are expected to be zero [36]. However, due to nonidealities in the CRAFT operation, outlined earlier in Section 3.3, the other bin outputs contain leaked outputs that rotate similarly over time.

To measure the FFT performance across bins with high resolution, the outputs were digitized using off-chip ADCs and recorded by an FPGA (NI-7811R) programmed using LabVIEW. In order to reduce the output noise so as to observe the design nonlinearities, a large number of outputs were recorded and averaged. Offline calibration was used to cancel the static error due to parasitics as discussed in Section 6.3. For a single-tone input of varying amplitude at a frequency corresponding to bin 1, the outputs across all 16 bins are shown in Figure 21.

As shown in the figure, for low input amplitudes (thin, blue curves), bin 1 shows an output amplitude proportional to the input signal as expected. Noise appears on other bins in a random way as shown in the blue curves. As the amplitude increases (thick, red curves), we see that the bin 1 output increases as expected. However, the leakage onto the other bins now follows a particular nonrandom pattern that also rises with the rising input. This pattern signifies nonlinearity, as opposed to noise in the other bins at lower input amplitudes. It is also noticeable that this leakage rises faster than the rise of the bin 1 output amplitude (in dB scale). This is expected since the higher-order harmonics due to the sampler nonlinearity increase faster with an increase in input

[illegible]

$$\mathbf{F}_4 = \begin{bmatrix} 1 & 0 & 0 & 0 & 0 & 0 & 0 & 0 & 0 & 1 & 0 & 0 & 0 & 0 & 0 & 0 & 0 \\ 0 & 1 & 0 & 0 & 0 & 0 & 0 & 0 & 0 & 0 & 1 & 0 & 0 & 0 & 0 & 0 & 0 \\ 0 & 0 & 1 & 0 & 0 & 0 & 0 & 0 & 0 & 0 & 0 & 1 & 0 & 0 & 0 & 0 & 0 \\ 0 & 0 & 0 & 1 & 0 & 0 & 0 & 0 & 0 & 0 & 0 & 0 & 1 & 0 & 0 & 0 & 0 \\ 0 & 0 & 0 & 0 & 1 & 0 & 0 & 0 & 0 & 0 & 0 & 0 & 0 & 1 & 0 & 0 & 0 \\ 0 & 0 & 0 & 0 & 0 & 1 & 0 & 0 & 0 & 0 & 0 & 0 & 0 & 0 & 1 & 0 & 0 \\ 0 & 0 & 0 & 0 & 0 & 0 & 1 & 0 & 0 & 0 & 0 & 0 & 0 & 0 & 0 & 1 & 0 \\ 0 & 0 & 0 & 0 & 0 & 0 & 0 & 1 & 0 & 0 & 0 & 0 & 0 & 0 & 0 & 0 & 1 \\ 1 & 0 & 0 & 0 & 0 & 0 & 0 & 0 & 0 & -1 & 0 & 0 & 0 & 0 & 0 & 0 & 0 \\ 0 & 1 & 0 & 0 & 0 & 0 & 0 & 0 & 0 & 0 & -1 & 0 & 0 & 0 & 0 & 0 & 0 \\ 0 & 0 & 1 & 0 & 0 & 0 & 0 & 0 & 0 & 0 & 0 & -1 & 0 & 0 & 0 & 0 & 0 \\ 0 & 0 & 0 & 1 & 0 & 0 & 0 & 0 & 0 & 0 & 0 & 0 & -1 & 0 & 0 & 0 & 0 \\ 0 & 0 & 0 & 0 & 1 & 0 & 0 & 0 & 0 & 0 & 0 & 0 & 0 & -1 & 0 & 0 & 0 \\ 0 & 0 & 0 & 0 & 0 & 1 & 0 & 0 & 0 & 0 & 0 & 0 & 0 & 0 & -1 & 0 & 0 \\ 0 & 0 & 0 & 0 & 0 & 0 & 1 & 0 & 0 & 0 & 0 & 0 & 0 & 0 & 0 & -1 & 0 \\ 0 & 0 & 0 & 0 & 0 & 0 & 0 & 1 & 0 & 0 & 0 & 0 & 0 & 0 & 0 & 0 & -1 \end{bmatrix}. \quad (\text{A.2})$$

The radix-2, 16-point, DIT FFT is implemented by CRAFT as a cascade of four stages of in-place processing operations:

$$\text{CRAFT: } \mathbf{X} = \frac{1}{16} \cdot \mathbf{S}_4 \mathbf{S}_3 \mathbf{S}_2 \mathbf{S}_1 \mathbf{I}_{\text{bitrev}} \mathbf{x}, \quad (\text{A.3})$$

where $\mathbf{I}_{\text{bitrev}}$ was shown previously and \mathbf{S}_1 , \mathbf{S}_2 , \mathbf{S}_3 , and \mathbf{S}_4 are shown below. They differ from the FFT matrices due to the attenuation, charge-averaging, and stage scaling factor effects of the implementation. They are rewritten below in a manner that matches the implementation:

$$\begin{aligned} \mathbf{S}_1 &= \mathbf{F}_1, & \mathbf{S}_4 &= \mathbf{F}_4 \\ \mathbf{S}_2 &= k_2 \begin{bmatrix} 1 & 0 & 1 & 0 & 0 & 0 & 0 & 0 & 0 & 0 & 0 & 0 & 0 & 0 & 0 & 0 & 0 \\ 0 & 1 & 0 & 1 & 0 & 0 & 0 & 0 & 0 & 0 & 0 & 0 & 0 & 0 & 0 & 0 & 0 \\ 1 & 0 & -1 & 0 & 0 & 0 & 0 & 0 & 0 & 0 & 0 & 0 & 0 & 0 & 0 & 0 & 0 \\ 0 & 1 & 0 & -1 & 0 & 0 & 0 & 0 & 0 & 0 & 0 & 0 & 0 & 0 & 0 & 0 & 0 \\ 0 & 0 & 0 & 0 & 1 & 0 & 1 & 0 & 0 & 0 & 0 & 0 & 0 & 0 & 0 & 0 & 0 \\ 0 & 0 & 0 & 0 & 0 & W^2 & 0 & W^2 & 0 & 0 & 0 & 0 & 0 & 0 & 0 & 0 & 0 \\ 0 & 0 & 0 & 0 & -j & 0 & j & 0 & 0 & 0 & 0 & 0 & 0 & 0 & 0 & 0 & 0 \\ 0 & 0 & 0 & 0 & 0 & -jW^2 & 0 & jW^2 & 0 & 0 & 0 & 0 & 0 & 0 & 0 & 0 & 0 \\ 0 & 0 & 0 & 0 & 0 & 0 & 0 & 0 & 1 & 0 & 1 & 0 & 0 & 0 & 0 & 0 & 0 \\ 0 & 0 & 0 & 0 & 0 & 0 & 0 & 0 & 0 & 1 & 0 & 1 & 0 & 0 & 0 & 0 & 0 \\ 0 & 0 & 0 & 0 & 0 & 0 & 0 & 0 & 1 & 0 & -1 & 0 & 0 & 0 & 0 & 0 & 0 \\ 0 & 0 & 0 & 0 & 0 & 0 & 0 & 0 & 0 & 1 & 0 & -1 & 0 & 0 & 0 & 0 & 0 \\ 0 & 0 & 0 & 0 & 0 & 0 & 0 & 0 & 0 & 0 & 0 & 0 & 1 & 0 & 0 & 1 & 0 \\ 0 & 0 & 0 & 0 & 0 & 0 & 0 & 0 & 0 & 0 & 0 & 0 & 0 & 0 & W^2 & 0 & W^2 \\ 0 & 0 & 0 & 0 & 0 & 0 & 0 & 0 & 0 & 0 & 0 & 0 & 0 & -j & 0 & j & 0 \\ 0 & 0 & 0 & 0 & 0 & 0 & 0 & 0 & 0 & 0 & 0 & 0 & -jW^2 & 0 & jW^2 \end{bmatrix} \\ \mathbf{S}_3 &= k_3 \begin{bmatrix} 1 & 0 & 0 & 0 & 1 & 0 & 0 & 0 & 0 & 0 & 0 & 0 & 0 & 0 & 0 & 0 & 0 \\ 0 & 1 & 0 & 0 & 0 & 1 & 0 & 0 & 0 & 0 & 0 & 0 & 0 & 0 & 0 & 0 & 0 \\ 0 & 0 & 1 & 0 & 0 & 0 & 1 & 0 & 0 & 0 & 0 & 0 & 0 & 0 & 0 & 0 & 0 \\ 0 & 0 & 0 & 1 & 0 & 0 & 0 & 1 & 0 & 0 & 0 & 0 & 0 & 0 & 0 & 0 & 0 \\ 1 & 0 & 0 & 0 & -1 & 0 & 0 & 0 & 0 & 0 & 0 & 0 & 0 & 0 & 0 & 0 & 0 \\ 0 & 1 & 0 & 0 & 0 & -1 & 0 & 0 & 0 & 0 & 0 & 0 & 0 & 0 & 0 & 0 & 0 \\ 0 & 0 & 1 & 0 & 0 & 0 & -1 & 0 & 0 & 0 & 0 & 0 & 0 & 0 & 0 & 0 & 0 \\ 0 & 0 & 0 & 1 & 0 & 0 & 0 & -1 & 0 & 0 & 0 & 0 & 0 & 0 & 0 & 0 & 0 \\ 0 & 0 & 0 & 0 & 0 & 0 & 0 & 0 & 1 & 0 & 0 & 0 & 1 & 0 & 0 & 0 & 0 \\ 0 & 0 & 0 & 0 & 0 & 0 & 0 & 0 & 0 & W^1 & 0 & 0 & 0 & W^1 & 0 & 0 & 0 \\ 0 & 0 & 0 & 0 & 0 & 0 & 0 & 0 & 0 & 0 & W^2 & 0 & 0 & 0 & W^2 & 0 & 0 \\ 0 & 0 & 0 & 0 & 0 & 0 & 0 & 0 & 0 & 0 & 0 & W^3 & 0 & 0 & 0 & W^3 & 0 \\ 0 & 0 & 0 & 0 & 0 & 0 & 0 & 0 & -1 & 0 & 0 & 0 & j & 0 & 0 & 0 & 0 \\ 0 & 0 & 0 & 0 & 0 & 0 & 0 & 0 & 0 & -jW^1 & 0 & 0 & 0 & jW^1 & 0 & 0 & 0 \\ 0 & 0 & 0 & 0 & 0 & 0 & 0 & 0 & 0 & 0 & -jW^2 & 0 & 0 & 0 & jW^2 & 0 & 0 \\ 0 & 0 & 0 & 0 & 0 & 0 & 0 & 0 & 0 & 0 & 0 & -jW^3 & 0 & 0 & 0 & jW^3 \end{bmatrix}, \quad (\text{A.4}) \end{aligned}$$

where

$$k_2 = \frac{1}{\sqrt{2}}, \quad k_3 = \frac{1}{2} \sec\left(\frac{\pi}{8}\right). \quad (\text{A.5})$$

Conflict of Interests

The authors declare that there is no conflict of interests regarding the publication of this paper.

Acknowledgments

This work was partially supported by DARPA and Center for Circuit and System Solutions (C2S2). The authors are grateful to the members of the UMN analog design lab for discussions and tape-out help.

References

- [1] B. Fette, *Cognitive Radio Technology*, Newnes, 2006.
- [2] B. Sadhu and R. Harjani, *Cognitive Radio Receiver Front-Ends: RF/Analog Circuit Techniques*, Springer, 2014.
- [3] T. Ulversoy, "Software defined radio: challenges and opportunities," *IEEE Communications Surveys and Tutorials*, vol. 12, no. 4, pp. 531–550, 2010.
- [4] D. Cabric, I. D. O'Donnell, M. S.-W. Chen, and R. W. Brodersen, "Spectrum sharing radios," *IEEE Circuits and Systems Magazine*, vol. 6, no. 2, pp. 30–45, 2006.
- [5] Q. Zhao and B. M. Sadler, "A survey of dynamic spectrum access," *IEEE Signal Processing Magazine*, vol. 24, no. 3, pp. 79–89, 2007.
- [6] A. Valdes-Garcia, A. L. Natarajan, L. Duixian et al., "A fully-integrated dual-polarization 16-element W-band phased-array transceiver in SiGe BiCMOS," in *Proceedings of the Radio Frequency Integrated Circuits Symposium (RFIC '13)*, pp. 375–378, 2013.
- [7] S. Kalia, S. A. Patnaik, B. Sadhu et al., "Multi-beam spatio-spectral beamforming receiver for wideband phased arrays," *IEEE Transactions on Circuits and Systems I*, vol. 60, no. 8, pp. 2018–2029, 2013.
- [8] B. Sadhu, M. Sturm, B. M. Sadler, and R. Harjani, "A 5GS/s 12.2pJ/conv. analog charge-domain FFT for a software defined radio receiver front-end in 65nm CMOS," in *Proceedings of the IEEE Radio Frequency Integrated Circuits Symposium*, pp. 39–42, 2012.
- [9] R. Bagheri, A. Mirzaei, S. Chehrizi et al., "An 800-MHz-6-GHz software-defined wireless receiver in 90-nm CMOS," *IEEE Journal of Solid-State Circuits*, vol. 41, no. 12, pp. 2860–2875, 2006.
- [10] B. Sadhu, M. Sturm, B. M. Sadler, and R. Harjani, "Building an on-chip spectrum sensor for cognitive radios," *IEEE Communications Magazine*, vol. 52, no. 4, pp. 92–100, 2014.
- [11] W.-H. Chen, G. Liu, B. Zdravko, and A. M. Niknejad, "A highly linear broadband CMOS LNA employing noise and distortion cancellation," *IEEE Journal of Solid-State Circuits*, vol. 43, no. 5, pp. 1164–1175, 2008.
- [12] Z. Ru, N. A. Moseley, E. A. M. Klumperink, and B. Nauta, "Digitally enhanced software-defined radio receiver robust to out-of-band interference," *IEEE Journal of Solid-State Circuits*, vol. 44, no. 12, pp. 3359–3375, 2009.
- [13] M. C. M. Soer, E. A. M. Klumperink, Z. Ru, F. E. Van Vliet, and B. Nauta, "A 0.2-to-2.0GHz 65nm CMOS receiver without LNA achieving >11dBm IIP3 and <6.5 dB NF," in *Proceedings of the IEEE International Solid-State Circuits Conference (ISSCC '09)*, pp. 222–223, February 2009.
- [14] T.-L. Hsieh, P. Kinget, and R. Gharpurey, "A rapid interference detector for ultra wideband radio systems in 0.13μm CMOS," in *Proceedings of the IEEE Radio Frequency Integrated Circuits Symposium (RFIC '08)*, pp. 347–350, June 2008.
- [15] M. Elbadry, B. Sadhu, J. Qiu, and R. Harjani, "Dual channel injection-locked quadrature LO generation for a 4GHz instantaneous bandwidth receiver at 21GHz center frequency," in *Proceedings of the IEEE Radio Frequency Integrated Circuits Symposium*, pp. 333–336, 2012.
- [16] S. Kalia, M. Elbadry, B. Sadhu, S. Patnaik, J. Qiu, and R. Harjani, "A simple, unified phase noise model for injection-locked oscillators," in *Proceedings of the IEEE Radio Frequency Integrated Circuits Symposium (RFIC '11)*, pp. 1–4, June 2011.
- [17] Z. Ru, E. A. M. Klumperink, and B. Nauta, "On the suitability of discrete-time receivers for software-defined radio," in *Proceedings of the IEEE International Symposium on Circuits and Systems (ISCAS '07)*, pp. 2522–2525, May 2007.
- [18] K. Muhammad, D. Leipold, B. Staszewski et al., "A discrete-time bluetooth receiver in a 0.13μm digital CMOS process," in *Proceedings of the IEEE International Solid-State Circuits Conference*, pp. 267–272, February 2003.
- [19] K. Muhammad, Y.-C. Ho, T. Mayhugh et al., "A discrete time quad-band GSM/GPRS receiver in a 90 nm digital CMOS process," in *Proceedings of the IEEE Custom Integrated Circuits Conference*, pp. 809–812, September 2005.
- [20] D. Jakonis, K. Folkesson, J. Dabrowski, P. Eriksson, and C. Svensson, "A 2.4-GHz RF sampling receiver front-end in 0.18-μm CMOS," *IEEE Journal of Solid-State Circuits*, vol. 40, no. 6, pp. 1265–1277, 2005.
- [21] Z. Ru, E. A. M. Klumperink, and B. Nauta, "Discrete-time mixing receiver architecture for RF-sampling software-defined radio," *IEEE Journal of Solid-State Circuits*, vol. 45, no. 9, pp. 1732–1745, 2010.
- [22] R. Bagheri, A. Mirzaei, M. E. Heidari et al., "Software-defined radio receiver: dream to reality," *IEEE Communications Magazine*, vol. 44, no. 8, pp. 111–118, 2006.
- [23] N. J. Guilar, F. Lau, P. J. Hurst, and S. H. Lewis, "A passive switched-capacitor finite-impulse-response equalizer," *IEEE Journal of Solid-State Circuits*, vol. 42, no. 2, pp. 400–409, 2007.
- [24] K. W. Martin, "Complex signal processing is not complex," *IEEE Transactions on Circuits and Systems I*, vol. 51, no. 9, pp. 1823–1836, 2004.
- [25] B. Sadhu, M. Sturm, B. M. Sadler, and R. Harjani, "Analysis and design of a 5 GS/s analog charge-domain FFT for an SDR front-end in 65 nm CMOS," *IEEE Journal of Solid-State Circuits*, vol. 48, no. 5, pp. 1199–1211, 2013.
- [26] A. Mirzaei, S. Chehrizi, R. Bagheri, and A. A. Abidi, "Analysis of first-order anti-aliasing integration sampler," *IEEE Transactions on Circuits and Systems I*, vol. 55, no. 10, pp. 2994–3005, 2008.
- [27] J.-O. Plouchart, M. Ferriss, B. Sadhu, M. Sanduleanu, B. Parker, and S. Reynolds, "A 73.9–83.5 GHz synthesizer with -111dBc/Hz phase noise at 10MHz offset in a 130nm SiGe BiCMOS technology," in *Proceedings of the Radio Frequency Integrated Circuits Symposium (RFIC '13)*, pp. 123–126, IEEE, 2013.
- [28] B. Sadhu, M. A. Ferriss, J.-O. Plouchart et al., "A 21.8-27.5GHz PLL in 32nm SOI using Gm linearization to achieve -130dBc/Hz

- phase noise at 10MHz offset from a 22GHz carrier,” in *Proceedings of the IEEE Radio Frequency Integrated Circuits Symposium*, pp. 75–78, 2012.
- [29] B. Sadhu, J. Kim, and R. Harjani, “A CMOS 3.3-8.4 GHz wide tuning range, low phase noise LC VCO,” in *Proceedings of the IEEE Custom Integrated Circuits Conference (CICC '09)*, pp. 559–562, September 2009.
 - [30] B. Sadhu and R. Harjani, “Capacitor bank design for wide tuning range LC VCOs: 850MHz-7.1GHz (157%),” in *Proceedings of the IEEE International Symposium on Circuits and Systems (ISCAS '10)*, pp. 1975–1978, June 2010.
 - [31] S. Sun, F. Wang, S. Yaldiz et al., “Indirect performance sensing for on-chip analog selfhealing via Bayesian model fusion,” in *Proceedings of the Custom Integrated Circuits Conference (CICC '13)*, pp. 1–4, 2013.
 - [32] B. Sadhu, M. A. Ferriss, A. S. Natarajan et al., “A linearized, low-phase-noise VCO-based 25-GHz PLL with autonomic biasing,” *IEEE Journal of Solid-State Circuits*, vol. 48, no. 5, pp. 1138–1150, 2013.
 - [33] M. Lehne and S. Raman, “A 0.13-um 1-GS/s CMOS discrete-time FFT processor for ultra-wideband OFDM wireless receivers,” *IEEE Transactions on Microwave Theory and Techniques*, vol. 59, no. 6, pp. 1639–1650, 2011.
 - [34] F. Rivet, Y. Deval, J.-B. Begueret, D. Dallet, P. Cathelin, and D. Belot, “The experimental demonstration of a SASP-based full software radio receiver,” *IEEE Journal Solid-State Circuits*, vol. 45, no. 5, pp. 979–988, 2010.
 - [35] F. J. Harris, C. Dick, and M. Rice, “Digital receivers and transmitters using polyphase filter banks for wireless communications,” *IEEE Transactions on Microwave Theory and Techniques*, vol. 51, no. 4, pp. 1395–1412, 2003.
 - [36] A. V. Oppenheim, R. W. Schaffer, and J. R. Buck, *Discrete-Time Signal Processing*, Prentice Hall, Upper Saddle River, NJ, USA, 2nd edition, 1999.

Research Article

Implementation of an Optical-Wireless Network with Spectrum Sensing and Dynamic Resource Allocation Using Optically Controlled Reconfigurable Antennas

**E. Raimundo-Neto,¹ J. R. G. da Rosa,¹ M. A. F. Casaroli,² I. Feliciano da Costa,^{1,3}
A. M. Alberti,² and Arismar Cerqueira Sodré Jr.¹**

¹ Laboratory WOCA (Wireless and Optical Convergent Access), National Institute of Telecommunications (Inatel),
João de Camargo Avenue 510, 37540-000 Santa Rita do Sapucaí, MG, Brazil

² “NovaGenesis” Project, National Institute of Telecommunications (Inatel), João de Camargo Avenue 510, 37540-000
Santa Rita do Sapucaí, MG, Brazil

³ Federal University of Itajubá (Unifei), Benedito Pereira dos Santos Avenue, 1303, 37500-903 Itajubá, MG, Brazil

Correspondence should be addressed to E Raimundo-Neto; egidio.neto@gee.inatel.br

Received 14 December 2013; Revised 14 February 2014; Accepted 22 February 2014; Published 30 April 2014

Academic Editor: Ali El-Hajj

Copyright © 2014 E. Raimundo-Neto et al. This is an open access article distributed under the Creative Commons Attribution License, which permits unrestricted use, distribution, and reproduction in any medium, provided the original work is properly cited.

This work proposes the concept and reports the implementation of an adaptive and cognitive radio over fiber architecture. It is aimed at dealing with the new demands for convergent networks by means of simultaneously providing the functionalities of multiband radiofrequency spectrum sensing, dynamic resource allocation, and centralized processing capability, as well as the use of optically controlled reconfigurable antennas and radio over fiber technology. The performance of this novel and innovative architecture has been evaluated in a geographically distributed optical-wireless network under real conditions and for different fiber lengths. Experimental results demonstrate reach extension of more than 40 times and an enhancement of more than 30 dB in the carrier to interference plus noise ratio parameter.

1. Introduction

The development of telecommunications systems and networks has increasingly influenced the people's life style and vice versa. People desire to be connected anywhere, anytime, and at high data rate and quality. Social networks, real time video, and photo share applications have been demanding new and tough requirements. While the research in wireless communication systems is mainly focused on providing fast, energy-efficient, and reliable connections to the final users, studies have been developed and applied in all network layers. Among various research areas, two of them have been particularly successful in the last years: radio over fiber (RoF) systems [1] and cognitive radio (CR) [2].

The next generation of telecom systems will require extremely high capacity and reliable mobility. Enabling the convergence of wired and wireless services can satisfy these

two requirements. In this way, it would be practicable to simultaneous delivery voice and data and video services in order to serve the fixed and mobile users in a unified networking platform. The radio over fiber (RoF) technology represents a key solution for taking advantage of both systems in a unique way. In other words, it enables making use of the huge bandwidth offered by optical communications systems with the mobility and flexibility provided by wireless systems.

RoF systems play an important role in the convergence of optical and wireless networks and, additionally, can take advantage of photonics technology in order to efficiently enable the generation and detection of microwave signals in the optical domain [3, 4]. These systems have been considered a key solution to connect base stations to the antenna units not only for the current cellular systems but also for Wi-Fi and 4G networks [5–7]. Other applications include hybrid passive optical network (PON) implementations [8] and transport

sensorial information in wireless sensor networks (WSNs) [9].

Cognitive radio technology is the target of a large number of researches focused on a better frequency spectrum usage, as well as network self-management, self-optimization, and machine learning [10]. Spectrum sensing (SS) techniques and algorithms for multiple access are also being developed for opportunistic spectrum management [11]. CR can be seen as a self-aware, environment-aware, and regulation-aware device. It can estimate the spectrum occupancy by using a SS technique and, consequently, determining opportunities in a frequency range of interest, based on the occupation or not of the channels by licensed users (also known as primary users) [12].

Some researchers have been working on the synergy of cognitive radio and different photonics technologies in the last years. Different applications and system architectures have been proposed in literature, such as cognitive radio over fiber (CRoF) for microcell applications [13], cognitive wireless LAN over fiber (CWLANoF) [14], cognitive front ends using optically pumped reconfigurable antennas (OPRAS) [15], and photonic analog-to-digital converter (Ph-ADC) [16, 17]. The CRoF architecture is based on RoF technology for connecting CRs. Al-Dulaimi et al. have numerically demonstrated that CRoF is able to use local spectrum holes efficiently and provide higher throughput to secondary users if compared to the traditional CR functioning [13]. On the other hand, Attar et al. have reported a WLANoF based on a multiuser MAC with CR capability for multiple cooperating receivers with distributed antennas [14]. It consists of a number of access points without processing capabilities connected via RoF links to a cognitive access point (CogAp). The latter one is responsible for all processing functions and the spectrum sensing is performed based on MAC layer information. In [15], the development of a cognitive front-end based on a UWB antenna and an optically pumped reconfigurable antenna is presented. The latter one is activated by local laser diodes, which had been incorporated to its structure for illuminating a photoconductive switch. The main drawback of this approach is that the laser is only locally controlled, since it is integrated to the antenna rather than using an optical fiber to control the antenna properties. Finally, Llorente et al. have published some articles on the experimental demonstration of a time-stretched photonic analog-to-digital converter with optical amplification applied to sense ultralow power signals for cognitive radio applications [16, 17]. They have indeed demonstrated the feasibility of a Ph-ADC and a bidirectional UWB radio over fiber transmission in a dispersion compensating fiber (DCF). The experiment has confirmed that the proposed Ph-ADC can be used for UWB signal distribution at DCF dispersion values $D_2 \approx -2500$ ps/nm for in-building communications. Higher dispersion values distort severely UWB carrier constellation [16].

This work proposes the concept and reports the implementation of an innovative architecture called ACRoF, which stands for adaptive and cognitive radio over fiber. It is based on a central office with multiband SS and dynamic resource allocation functionalities and simple remote antenna units

composed of previous developed optically controlled reconfigurable antennas for data transmission and a broadband antenna for continuously sensing the frequency spectrum. There are six main contributions of the current work when compared to others previously published in literature. First, ACRoF can be considered innovative and unique, since it takes advantage of RoF and CR technologies in an adaptive way, since the antenna electromagnetic properties are constantly reconfigured as a function of SS information. Secondly, this work presents an implementation in a real optical-wireless network, whereas CRoF has been only analyzed numerically [13]. If compared to [14], our main contribution concerns the cognition in the physical layer and not in medium access control, as well as the possibility of performing multiband SS.

The OPRAS antenna reported in [16] is locally manipulated by a diode laser differently to our optically controlled antenna that is remotely reconfigured by using a dedicated optical link from the central office to the remote antenna unit. Moreover, the current paper presents experimental results on the network performance parameters based on online SS. Finally, [16, 17] report the development and laboratory experiments of a Ph-ADC, whereas this work proposes the use a spectrum analyzer as ADC and RoF links for enabling centralized processing capability in a geographically distributed optical-wireless network.

2. Cognitive Radio and Spectrum Sensing

Software-defined radio (SDR) and cognitive radio (CR) represent two remarkable concepts on the wireless communications evolution, which are frequently attributed to Mitola III [18, 19]. A SDR is a radio in which the physical layer signal processing is software-controlled rather than using a dedicated hardware to handle radio frequency (RF) signals. It is capable of reconfiguring its parameters and even functionalities according to the software controls. On the other hand, a CR is a software-defined wireless communication that provides the functionalities of self-organization, self-management, and self-adaptation as a function of the radio environment, spectrum occupancy and regulation, user requirements, internal capabilities, and operational constraints. Several technologies inspired on human biology have been suggested to achieve these complex objectives. The inspirations typically come from our sensory system (spectrum sensing), somatic nervous system (controllers and actuators), autonomic nervous system (self-management, situation-awareness, and self-management) [20], and human brains (analyzing, correlating, decision making, learning, planning, and experimenting) [10]. A CR must be aware of many aspects, namely, the radio frequency spectrum and channels situation (environment-awareness), its own devices and systems (self-awareness), regulations (regulation-awareness), service requirements (service-awareness), business plans (business-awareness), and etiquettes/policies [21, 22]. It can experiment new configurations and functionalities, correlating the applied plans to the obtained results. Therefore, it can learn

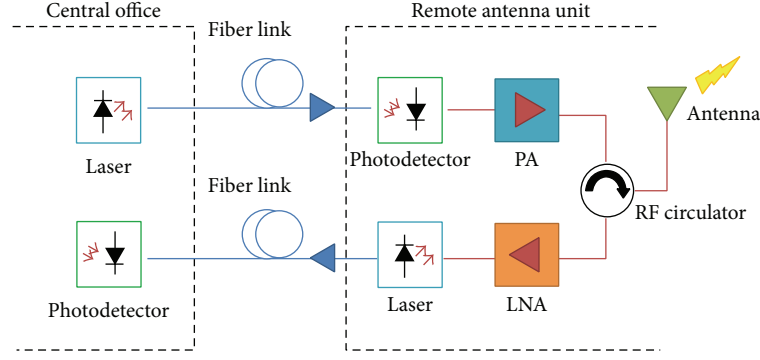


FIGURE 1: RoF system block diagram.

from previous experiences in order to optimize its functionalities. A CR must perform spectrum sensing constantly for finding out new bandwidth opportunities that could be explored by its radio capabilities. Furthermore, it needs to sense and monitor the radio channels to detect primary users' transmissions, as well as secondary users' transmissions (coexistence). If a primary signal is detected, the secondary transmission should immediately stop to avoid interference.

The increasing demand for high data rates in wireless communications has motivated the emergence of CR as a key solution for the limited and underutilized wireless electromagnetic spectrum resources. The licensed spectrum is allocated during long time periods exclusively to licensed users, that is, the primary users. Many studies on spectrum utilization have demonstrated the unused frequency time and space resources of this strategy [23, 24]. CR aims to exploit these opportunities without causing significant interference to primary users [10]. It is aimed at reusing the unused spectrum in an opportunistic way. In order to avoid interference with the primary users, CR must monitor constantly the spectrum usage and determine the possibilities for spectrum occupancy. Transceivers based on this technology are able to sense the frequency spectrum and determine its occupancy by one or more primary users [25].

The spectrum sensing can be simply modeled in deciding whether a slice of spectrum is available or not. It can be discriminated in two hypotheses:

$$\begin{aligned} H_0 : \mathbf{y}[n] &= \mathbf{w}[n], \quad n = 1, 2, \dots, N \\ H_1 : \mathbf{y}[n] &= \mathbf{x}[n] + \mathbf{w}[n], \quad n = 1, 2, \dots, N, \end{aligned} \quad (1)$$

where $\mathbf{x}[n]$ represents a primary user, $\mathbf{w}[n]$ is the noise, and n represents time. The sensed signal $\mathbf{y}[n]$ is a vector with length L .

First, CR needs to perform a test statistic $\Lambda(\mathbf{y})$ using the received data $\mathbf{y}[n]$ and compare it with predetermined values of the threshold λ . If $\Lambda(\mathbf{y}) > \lambda$, CR decides the H_1 hypothesis. Otherwise, if $\Lambda(\mathbf{y}) < \lambda$, CR decides H_0 . The detector performance is quantified by a receiver operating characteristics (ROC) curve, which gives the probability of detection P_D as function of the probability of false alarm P_{FA}

by varying the threshold [26]. The parameters P_D and P_{FA} are defined by the following expressions:

$$\begin{aligned} P_D &= \Pr(H_1 | H_1) \\ P_{FA} &= \Pr(H_1 | H_0). \end{aligned} \quad (2)$$

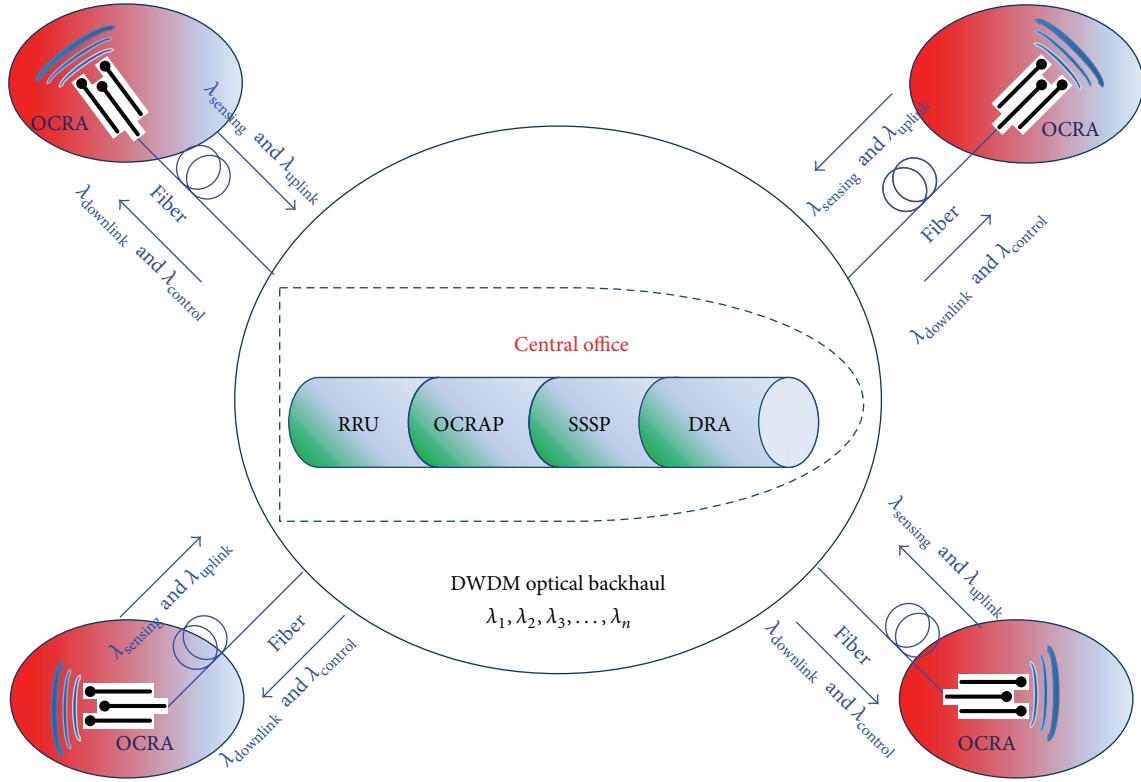
The choices of the optimum number of required samples and threshold λ are very crucial, since they strongly affect the detection performance [27]. Recently, some SS techniques have been proposed and investigated, such as energy detection (ED) [28], cyclostationary detection [29], feature detection, covariance matrix [30, 31], and blind detection [32]. The ED technique has been chosen for the optical-wireless network implementation, which will be subsequently described. In this approach, a CR measures the energy of the received signal over a finite time interval and compares it to a predetermined decision threshold. The test statistic $\Lambda(\mathbf{y})$ is given by

$$\Lambda(\mathbf{y}) = \frac{1}{N} \sum_{i=1}^{N \cdot L} [\mathbf{y}(n)]^2. \quad (3)$$

Note that higher values of the $N \cdot L$ product lead to a more precise estimate of $\Lambda(\mathbf{y})$. However, this is not typically used in practical cases due to the dynamic variations of the spectrum occupancy during long periods of time. Therefore, the parameters N and L need to be properly chosen in order to enable a good and fast sensing performance.

3. Radio over Fiber Technology

The radio over fiber technology consists of a heterogeneous network formed by optical and wireless links. Unlike traditional optical communications networks, in which a baseband signal is transmitted into the optical fibers, in RoF systems one or multiple analog carriers are transported into the fibers [9], as presented in Figure 1. The signal transmission is realized by directly or externally modulating lasers with the analogous radio frequency signals. On the receiver side, the transmitted signal is recuperated by using a photodetector. Moreover, RF amplifiers can be built in the RoF system to further increase its reach. In this way, using fiber-optic links ensures the transmission of RF signals



RRU: remote radio unit
 OCRAP: optically controlled reconfigurable antenna processing
 SSSP: spectrum and spatial sensing processing
 DRA: dynamic resource allocation

FIGURE 2: Adaptive and cognitive radio over fiber architecture.

between a central office (CO) and a given number of RAUs. The final users are commonly mobile devices, which are connected to RAUs via a wireless link.

The integration of optical and wireless broadband infrastructures into the same backhaul network leads to a significant systemic simplification and cost reduction, since all routing, switching, and processing are performed at CO [33]. The signal processing centralization makes possible equipment sharing and dynamic resource allocation. Ideally, a RoF system can be entirely transparent to all signals transmitted in the optical channel, because the transmission is ensured by modulating the optical carrier with the RF signal. RoF links can simultaneously transport several wireless standards, such as Wi-Fi, GSM, UMTS, WiMAX, LTE, and UWB [14]. Furthermore, low attenuation, electromagnetic interference immunity, low energy consumption, and large bandwidth are other advantages of this technology.

4. ACroF-Adaptive and Cognitive Radio over Fiber

The proposed architecture for the implementation of an optical-wireless network and spectrum sensing allocation is called ACroF (adaptive and cognitive radio over fiber) and

is illustrated in Figure 2. It consists of a CO and several RAUs. The CO concentrates the following elements: (i) remote radio unit (RRU), which consists of a radio capable of transmitting and receiving data to/from different RAUs; (ii) optically controlled reconfigurable antenna processing (OCRAP), which is responsible for optically reconfiguring the antenna electromagnetic properties; (iii) spectrum and spatial sensing processing (SSSP), responsible for collecting the spectrum samples of the radio environment and processing and making them available to DRA; and (iv) dynamic resource allocation (DRA), which dynamically performs spectrum resource allocation based on the SSSP information. On the other side, RAU is based on a previously developed optically controlled reconfigurable antenna (OCRA) [34] for data transmission and a broadband antenna for performing SS.

The proposed ACroF architecture has been implemented in an optical-wireless network under real conditions, as reported in Figure 3. The main blocks of our testbed are a CO, a RAU, a bidirectional RoF link, and an optical control link. The RoF modules perform the electrical-optical and optical-electrical signal conversion. The RF signal distribution is carried out using bidirectional RoF links. The antenna control link enables the transmission of an additional optical signal

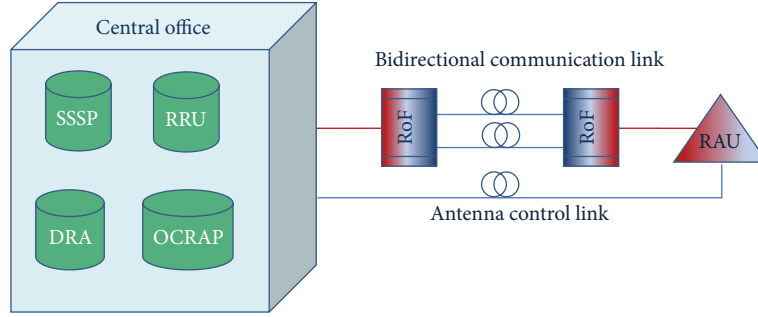


FIGURE 3: Block diagram of the optical-wireless network implementation.

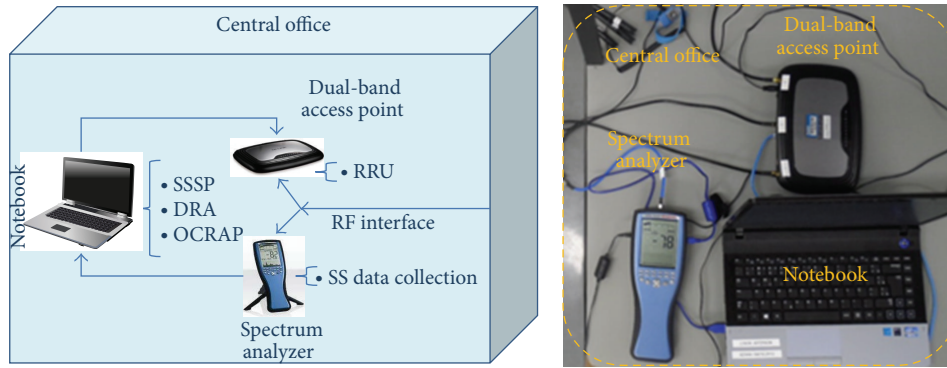


FIGURE 4: Components and functionalities of the central office.

responsible for reconfiguring its electromagnetic characteristics. Finally, an optically reconfigurable antenna and a commercial broadband log-periodic antenna (680 MHz to 10 GHz) compose RAU and are used for data transmission and spectrum sensing, respectively.

The ACRoF operational principle is described as follows:

(i) the frequency spectrum is sensed by RAUs and raw samples are transmitted to CO through the optical links; (ii) the information is extracted and processed using an ED algorithm, with the purpose of choosing the frequency channel and/or band at a lower level of energy; (iii) DRA is conducted by setting the RF parameters (number of the selected channels and the antenna operation bands: 2.4 GHz or 5 GHz); (iv) the system operates at the new allocated channel until the next estimation is performed.

CO integrates a spectrum analyzer, a dual-band access point (AP), and a notebook, as illustrated in Figure 4. It receives the RF signal composed of the uplink and sensed spectrum data. AP processes the uplink data, whereas sensed data is forwarded to a portable spectrum analyzer, which is directly connected to the notebook by using a USB port. The ED algorithm is then online processed by the notebook in order to define the channel and/or band which is going to be used. After taking this decision, it sends a command to AP for setting the best channel, as well as an optical control signal to reconfigure the antenna electromagnetic characteristics. Note that data communication is performed by using a bidirectional optical link and the control signal

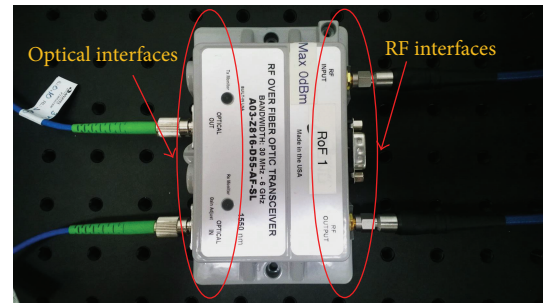


FIGURE 5: RoF transceiver used in the experiments.

uses a dedicated link to adapt the antenna properties, such as bandwidth and radiation pattern.

The broadband RoF modules operate from 30 MHz up to 6 GHz using direct modulation. Figure 5 displays a photograph of a RoF module, including some indications of its optical and electrical interfaces. It operates at different wavelengths for downlink and uplink. Therefore, a unique optical fiber is required to enable bidirectional communication.

Figure 6 shows the antennas used in the RAU. The optically controlled reconfigurable antenna is based on an "E"-shape slot, previously developed by our research group [34]. Its operational bandwidth and radiation pattern can be reconfigured through 2.4 or 5 GHz bands by controlling the optical power launched on its photoconductive switch.

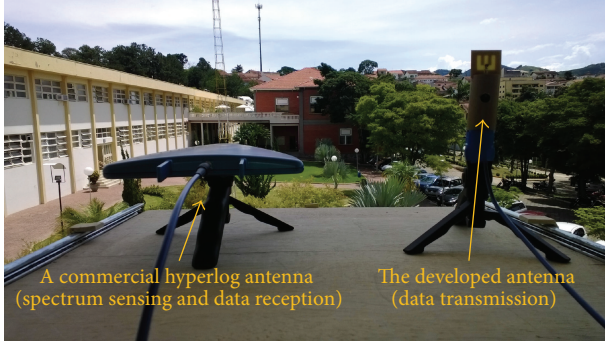


FIGURE 6: “E”-shape and Hyperlog antennas.

5. Optically Controlled Reconfigurable Antenna

Patch antennas have been intensely exploited in the last decades due to their low-profile structure and facility to be embedded in handheld wireless devices. Furthermore, they provide other advantages, such as good radiation efficiency, simple manufacturing, low cost, easy integration with microwave integrated circuits (MIC), light weight, low volume, and the possibility to be made conformal to the host surface.

Khidre et al. have recently reported some results on a circular polarization reconfigurable E-shaped patch antenna using 2 PIN diodes [35]. Our proposed patch antenna is based on E-shape printed slot, as presented in Figure 7(a). It has been fabricated using a low-cost fiberglass dielectric substrate. It is elevated from the ground plane with a sizable air gap to achieve wide bandwidth. Therefore, the electromagnetic coupling is ensured by a printed probe located in the bottom plane of the antenna structure, as shown in Figure 7(b). Its main advantages compared to traditional electrically controlled reconfigurable antennas are easy integration to optical systems, absence of bias lines, linear behavior, and activation without producing harmonics and intermodulation. An intrinsic silicon photoconductive switch has been fixed to the printed probe for enabling us to reconfigure the antenna frequency response as a function of the incident optical power. A fiber has been used to illuminate a silicon dice, as shown in Figure 7(b). Table 1 presents the typical antenna electromagnetic properties for the central frequencies from 2.4 and 5 GHz ISM bands. It operates in the 2.4 GHz band if the photoconductive switch is illuminated (“ON” state), since its reflection coefficient is very low. On the other hand, in the absence of light (“OFF” state), the antenna operation is reconfigured to the 5 GHz band, giving rise to a gain of 5.22 dBi. Therefore, it provides two operational and reconfigurable frequency bands: one from 2.407 to 2.524 GHz and the other from 5.033 GHz up to 6 GHz. Some examples of its radiation pattern are reported in Figures 7(a) and 7(c).

6. Implementation of ACROF Architecture

The proposed ACROF architecture has been implemented in a real geographically distributed optical-wireless network

TABLE 1: Typical reconfigurable antenna parameters for the central frequencies of 2.4 and 5 GHz bands.

| Frequency (GHz) | Switch state | Reflection coefficient (dB) | Gain (dBi) |
|-----------------|--------------|-----------------------------|------------|
| 2.47 GHz | “OFF” | −2.18 | 1.42 |
| | “ON” | −14.37 | 3.28 |
| 5.41 GHz | “OFF” | −17.42 | 5.22 |
| | “ON” | −9.51 | 3.21 |

TABLE 2: System reach in meters.

| Network type/frequency band | 2.4 GHz | 5 GHz |
|-----------------------------|---------|-------|
| Pure wireless | 45 | 25 |
| ACRoF | 1,045 | 1,035 |

located in the campus of the Brazilian National Institute of Telecommunications (Inatel). Figure 8 shows a Google Earth image with indications of the implemented network components. The optical links are composed of two pieces of 1,020 m single-mode fibers, under real conditions of temperature, humidity, and pressure. CO is located in the second floor of the main building and RAU is placed at the Laboratory WOCA (Wireless and Optical Convergent Access), which allows covering an internal square from the campus.

Initially, an experiment has been carried out at 2.4 GHz to systemically evaluate the antenna performance. Figure 9 reports RSSI (received signal strength indicator) and PER (packet error rate) measurements as a function of the laser current by means of combining a 1 km fiber with a 2 m wireless link. The higher the laser current is, the higher the RSSI is. By increasing the current from 0 A (“OFF” state) to 2.5 A (“ON” state), equivalent to approximately 2 W of optical power, RSSI is significantly enhanced from −66 to −57 dBm. Moreover, PER is improved from 32 to 18%.

The maximum fiber-optic length that could be used in the optical network has been evaluated considering the maximum allowed delay established by the IEEE 802.11n MAC layer standard for each particular frequency band (2.4 and 5 GHz). It requires a shorter delay for the 5 GHz band when compared to the 2.4 GHz band [36–38]. Figures 10 and 11 present the obtained RSSI and throughput as a function of the fiber length for the two frequency bands, respectively. In both cases, a back-to-back measurement had been first conducted for comparison purposes. The fiber links have been varied from 370 m to 1.37 km. These results demonstrate that the ACROF concept has been successfully implemented, since they are in accordance with the nominal value for the 802.11n standard, in which the minimum value to establish a connection is around −90 dBm. The throughput numbers are also in agreement with the back-to-back case with 370 m and 1,020 m fiber lengths. On the other side, there was no data transmission at 5 GHz for the 1.37 km link because of the time delay. It is important to highlight the proposed architecture implied in a significant reach enhancement: from 45 to 1,045 m at 2.4 GHz (23 times longer) and from 25 to 1,035 m (41 times longer) at 5 GHz, in both cases using 1,020 m of fiber. Table 2 reports the system reach comparison between a pure wireless network and the ACROF architecture.

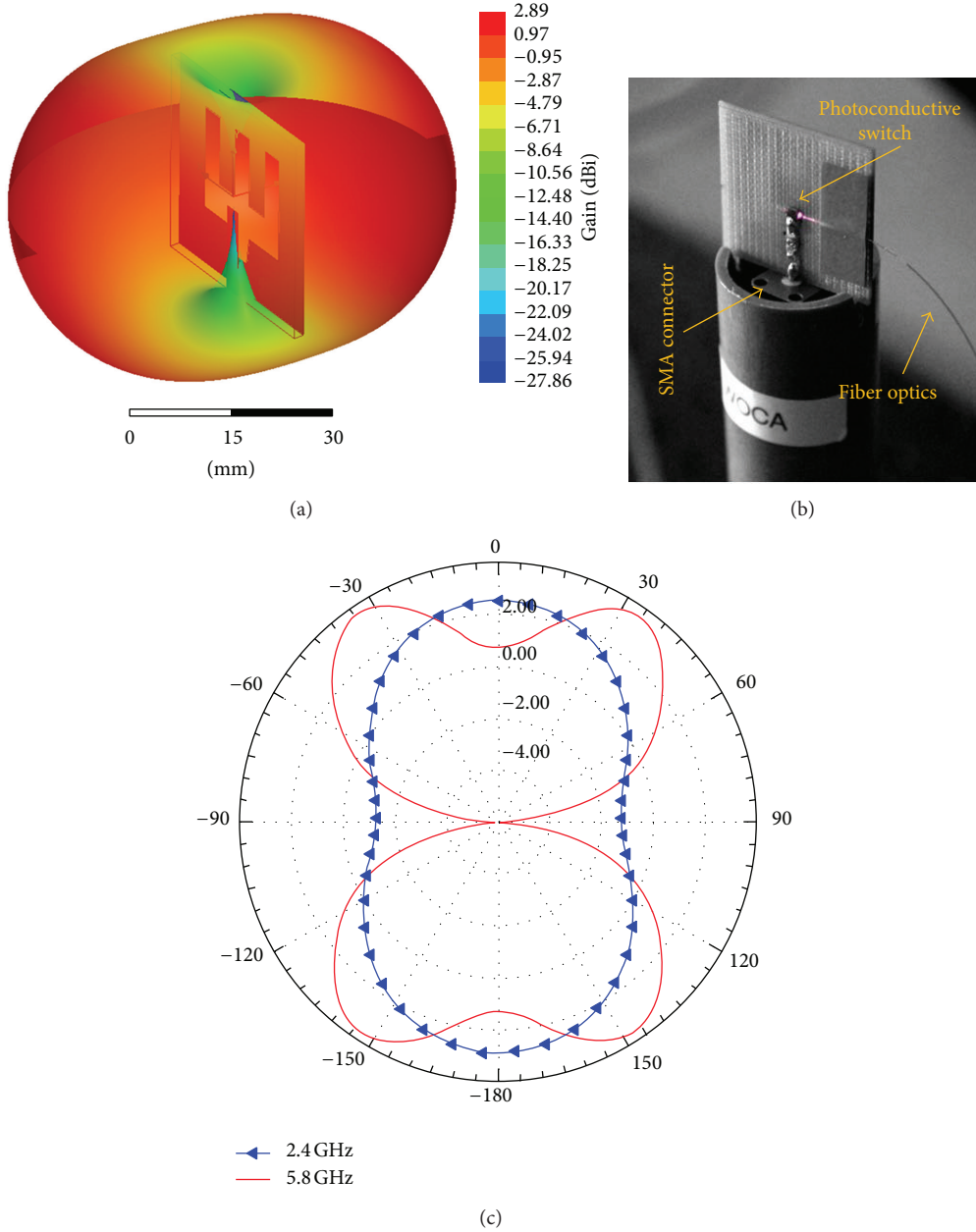


FIGURE 7: "E"-shaped optically controlled reconfigurable antenna.

The proposed dynamic spectrum allocation algorithm consists of selecting the best channel for data transmission according to the following steps: (i) the spectrum samples are processed at CO and the average power of each channel is estimated; (ii) the algorithm defines the channel with the lowest energy level at each band; (iii) the signal to noise ratio (SNR) is estimated considering the average noise level of each channel, which had been previously experimentally obtained for our portable spectrum analyzer; (iv) the ED algorithm chooses the channel that has the lowest estimated SNR between the best ones from each ISM band; (v) the notebook from CO sets the chosen channel in the AP and the

antenna optical signal control to ensure data transmission at the most appropriate channel.

The SS algorithm performed data collection considering the following system parameters: number of samples over time ($N = 50$) and samples frequency spacing $d_s = 1$ MHz. Therefore, the total number of samples over frequency was $L = 101$. All experiments have been carried out considering a 22 MHz channel. Therefore, the total number of samples for each channel status estimation was $N \cdot L = 1,100$. Figure 12 displays an example of the measurement spectrum in the 2.4 GHz band, from 2400 to 2500 MHz, which is extremely crowded as expected. Figure 13 reports an example of the

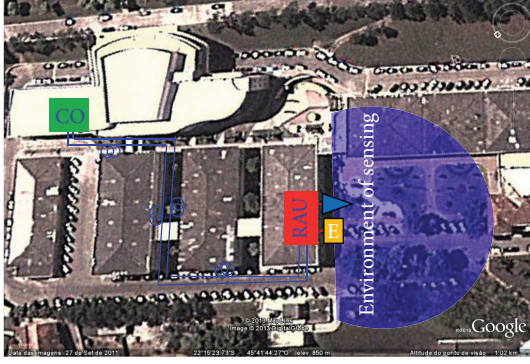


FIGURE 8: Google Earth image of the implemented real optical-wireless network.

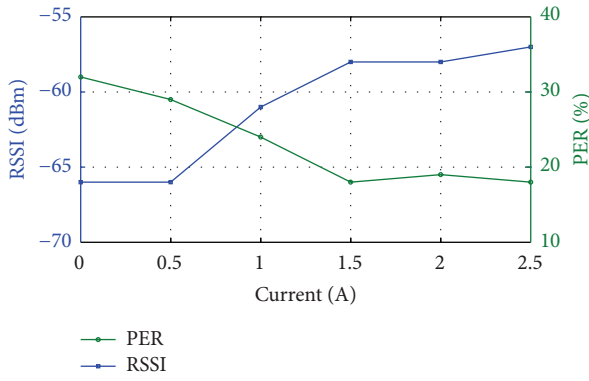


FIGURE 9: Measurements of RSSI and PER parameters as a function of the laser current.

measured SS in the 5 GHz band, from 5100 up to 5900 MHz for $L = 801$. It is clear that there were much more white spaces over this frequency band.

According to the IEEE 802.11 standard, different modulation and coding schemes (MCS) can be adopted by network devices depending on the communication channel conditions [39]. Therefore, the network throughput can be significantly increased if the interference caused by other networks is reduced. In order to evaluate the impacts caused by cochannel interference in Wi-Fi networks based on ACroF architecture, a wireless scenario has been created with other Wi-Fi networks. Three other Wi-Fi access points have been used to carry out performance measurements. The network performance has been evaluated using the following parameters: carrier to interference plus noise ratio (CINR), throughput, and PER. Moreover, four different conditions have been considered: (i) cochannel interferences originating from three other radio transmitters, (ii) cochannel interferences originating from two other radio transmitters, (iii) cochannel interferences originating from only one radio transmitter, and (iv) no cochannel interference. Tables 3 and 4 present the experiment results for 2.4 GHz and 5 GHz bands, respectively. As shown in Table 3, the CINR, throughput, and PER could be improved up to 39 dB, 29.6 Mbps, and 11%, respectively, by proper selecting of a channel over the 2.4 GHz band. They could also be enhanced to 30 dB, 22.7 Mbps, and

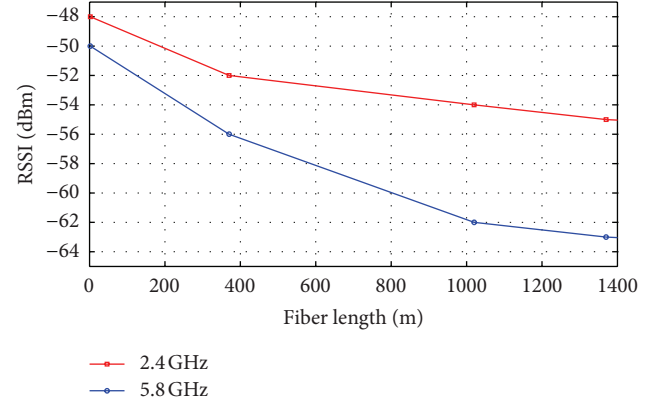


FIGURE 10: RSSI measurement as a function of the fiber length for the two frequency bands.

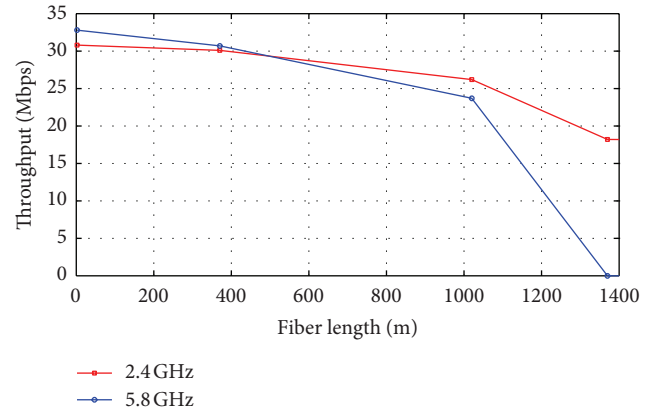


FIGURE 11: Throughput measurement as a function of the fiber length for the two frequency bands.

TABLE 3: Performance evaluation considering different levels of cochannel interference in the 2.4 GHz band.

| Test conditions | CINR (dB) | Throughput (Mbps) | PER (%) |
|---------------------------|-----------|-------------------|---------|
| 3 cochannel interferences | 0.5 | 20.5 | 25 |
| 2 cochannel interferences | 10 | 23.3 | 23 |
| 1 cochannel interference | 20 | 25.5 | 18 |
| The best channel | 39.6 | 29.6 | 11 |

TABLE 4: Performance evaluation considering different levels of cochannel interference in the 5 GHz band.

| Test conditions | CINR (dB) | Throughput (Mbps) | PER (%) |
|---------------------------|-----------|-------------------|---------|
| 3 cochannel interferences | -3 | 0.252 | 23 |
| 2 cochannel interferences | 7 | 1.087 | 22 |
| 1 cochannel interference | 17 | 2.28 | 18 |
| The best channel | 30 | 22.7 | 7 |

7%, respectively, using the same strategy in the 5 GHz band, as shown in Table 4.

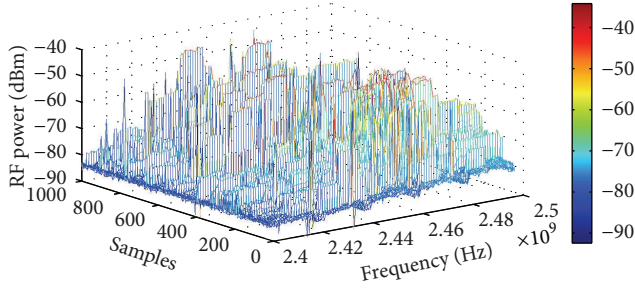


FIGURE 12: Sensed spectrum in the 2.4 GHz band.

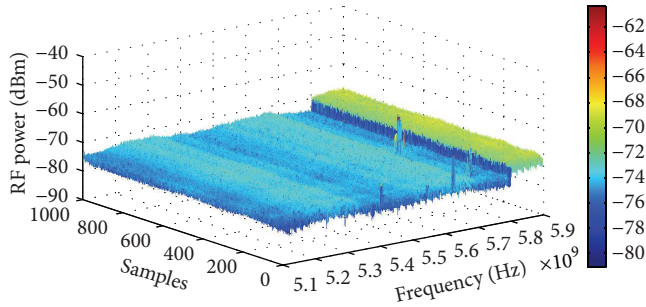


FIGURE 13: Sensed spectrum in the 5 GHz band.

Finally, the entire ACRoF architecture has been experimentally analyzed and its performance has been optimized under two different contexts: using the most appropriate channel from the 2.4 GHz band and using the most appropriate channel from 2.4 and 5 GHz bands. Initially, the data communication had been conducted by using the Wi-Fi channel 6 (2,437 MHz), which is the default channel for the most commercial APs, and then new channels have been used in accordance with the methodology previously described in the previous sections. Figure 14 reports a significant enhancement on the network performance parameters obtained by using ACRoF. CINR can be further improved to 40 dB by using the best channel from 2.4 and 5 GHz bands. It is important to remark that the maximum MCS index for this particular system is MCS 7, which has the following configurations: (i) SISO (single input single output), (ii) 1 spatial stream, (iii) 20 MHz channel bandwidth, and (iv) 800 ns of guard interval. Theoretically, for this scenario, the maximum throughput that can be achieved is 65 Mbps [40]. However, the previous experiments have shown that the maximum downlink throughput for this system is 32 Mbps.

7. Conclusions

This work has proposed the concept and reported a successful implementation of an adaptive and cognitive radio over fiber architecture in a geographically distributed optical-wireless network. It consists of a central office that centralizes all network functionalities and simple remote antenna units based on optically controlled reconfigurable antennas for data transmission and broadband antennas for performing spectrum sensing. Experimental results have demonstrated

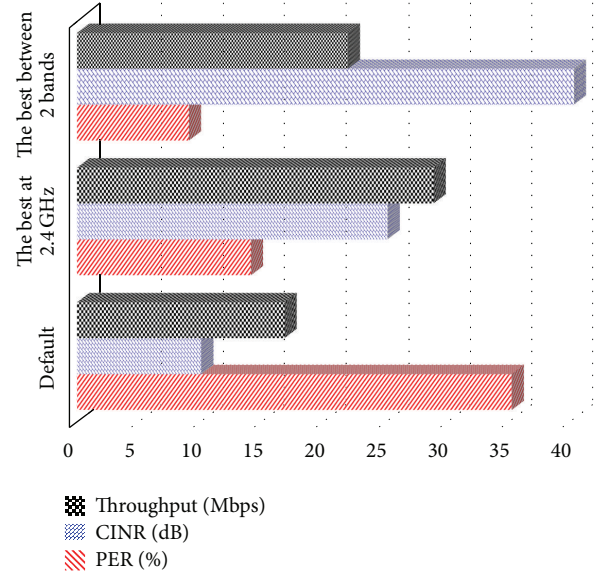


FIGURE 14: Significant enhancement on the network performance parameters using ACRoF.

that the network performance can be significantly improved in terms of CINR, throughput, and PER by using multiband spectrum sensing and dynamic resource allocation. Particularly, it has reported a reach extension of more than 40 times and an enhancement of more than 30 dB in the CINR parameter. Future works will regard the integration of ACRoF with the NovaGenesis “Future Internet” architecture [41].

Conflict of Interests

The authors declare that there is no conflict of interests regarding the publication of this paper.

Acknowledgments

The authors are grateful for the financial support from CNPq, MCTI, CAPES, FAPEMIG, FINATEL, ESSS-ANSYS, Prysmian-Draka, and Huber-Suhner and the technical support from TIM.

References

- [1] D. Wake, A. Nkansah, and N. J. Gomes, “Radio over fiber link design for next generation wireless systems,” *Journal of Lightwave Technology*, vol. 28, no. 16, pp. 2456–2464, 2010.
- [2] P. Pawelczak, K. Nolan, L. Doyle, S. Oh, and D. Cabric, “Cognitive radio: ten years of experimentation and development,” *IEEE Communications Magazine*, vol. 49, no. 3, pp. 90–100, 2011.
- [3] A. J. Seeds and K. J. Williams, “Microwave photonics,” *Journal of Lightwave Technology*, vol. 24, no. 12, pp. 4628–4641, 2006.
- [4] T. P. Villena, S. Arismar Cerqueira Jr., M. L. F. Abbade, H. E. Hernandez Figueroa, and H. L. Fragnito, “Generation of quaternary-amplitude microwave signals by using a new optical heterodyne technique,” *Microwave and Optical Technology Letters*, vol. 54, pp. 2738–2743, 2012.

- [5] S. Deronne, V. Moeyaert, and S. Bette, "WiFi transmission in radio-over-fiber systems: performance of the IEEE 802.11n aggregation mechanism," in *Proceedings of the International Conference on Optical Network Design and Modeling (ONDM '13)*, pp. 167–172, Brest, France, 2013.
- [6] C.-H. Yeh, C.-W. Chow, Y.-L. Liu et al., "Theory and technology for standard WiMAX over fiber in high speed train systems," *Journal of Lightwave Technology*, vol. 28, no. 16, pp. 2327–2336, 2010.
- [7] D. G. Lona, H. E. Hernández-Figueroa, S. A. Cerqueira Jr., R. M. Assumpção, O. C. Branquinho, and M. L. F. Abbade, "Investigation of noise sources in radio-over-fiber systems for Wi-Fi applications," in *Proceedings of the SBMO/IEEE MTT-S International Microwave and Optoelectronics Conference (IMOC '11)*, pp. 97–101, Natal, Brazil, November 2011.
- [8] T. Shao, F. Paresys, Y. le Guennec, G. Maury, N. Corrao, and B. Cabon, "Convergence of 60 GHz radio over fiber and WDM-PON using parallel phase modulation with a single Mach-Zehnder modulator," *Journal of Lightwave Technology*, vol. 30, pp. 2824–22831, 2012.
- [9] D. G. Lona, R. M. Assumpção, O. C. Branquinho, M. L. F. Abbade, H. E. Hernandez Figueroa, and S. Arismar Cerqueira Jr., "Implementation and performance investigation of radio over fiber systems in wireless sensor networks," *Microwave and Optical Technology Letters*, vol. 54, pp. 2669–2675, 2012.
- [10] S. Haykin, "Cognitive radio: brain-empowered wireless communications," *IEEE Journal on Selected Areas in Communications*, vol. 23, no. 2, pp. 201–220, 2005.
- [11] E. Axell, G. Leus, E. G. Larsson, and H. V. Poor, "Spectrum sensing for cognitive radio : state-of-the-art and recent advances," *IEEE Signal Processing Magazine*, vol. 29, no. 3, pp. 101–116, 2012.
- [12] J. Unnikrishnan and V. V. Veeravalli, "Algorithms for dynamic spectrum access with learning for cognitive radio," *IEEE Transactions on Signal Processing*, vol. 58, no. 2, pp. 750–760, 2010.
- [13] A. Al-Dulaimi, H. Al-Raweshidy, J. Cosmas, and J. Loo, "Cognitive mesh networks: cognitive radio over fiber for microcells applications," *IEEE Vehicular Technology Magazine*, vol. 5, no. 3, pp. 54–60, 2010.
- [14] A. Attar, H. Li, V. C. M. Leung, and Q. Pang, "Cognitive wireless local area network over fibers: architecture, research issues and testbed implementation," *IEEE Communications Magazine*, vol. 50, no. 6, pp. 107–113, 2012.
- [15] Y. Tawk, J. Costantine, S. Hemmady, G. Balakrishnan, K. Avery, and C. G. Christodoulou, "Demonstration of a cognitive radio front end using an optically pumped reconfigurable antenna system (OPRAS)," *IEEE Transactions on Antennas and Propagation*, vol. 60, no. 2, pp. 1075–1083, 2012.
- [16] R. Llorente, M. Morant, T. Tökle, T. Quinlan, M. Thakur, and S. Walker, "UWB radio-over-fiber and photonic sensing for cognitive optical access networks," in *Proceedings of the IEEE LEOS Annual Meeting Conference (LEOS '09)*, pp. 733–734, October 2009.
- [17] R. Llorente, M. Morant, J. Puche, J. Romme, and T. Alves, "Sensing ultra-low-power radio signals by photonic analog-to-digital conversion," in *Proceedings of the 35th European Conference on Optical Communication (ECOC '09)*, September 2009.
- [18] J. Mitola III, "Software radios: survey, critical evaluation and future directions," *IEEE Aerospace and Electronic Systems Magazine*, vol. 8, no. 4, pp. 25–36, 1993.
- [19] J. Mitola III and G. Q. Maguire Jr., "Cognitive radio: making software radios more personal," *IEEE Personal Communications*, vol. 6, no. 4, pp. 13–18, 1999.
- [20] P. Demestichas, G. Dimitrakopoulos, J. Strassner, and D. Bourse, "Introducing reconfigurability and cognitive networks concepts in the wireless world," *IEEE Vehicular Technology Magazine*, vol. 1, no. 2, pp. 32–39, 2006.
- [21] D. Jiang, S. Li, Y. Wang, and J. Chen, "A channel allocation strategy for multi-hop cognitive radio networks," in *Proceedings of the Wireless Telecommunications Symposium (WTS '13)*, pp. 1–6, Phoenix, Ariz, USA, April 2013.
- [22] P. Jun, J. Mingyang, J. Fu, and L. Weirong, "Active cooperation-aware spectrum resource allocation in cognitive radio network," in *Proceedings of the 32nd Chinese Control Conference (CCC '13)*, pp. 6409–6414, Xi'an, China, July 2013.
- [23] M. McHenry, "NSF spectrum occupancy measurements project summary," Shared Spectrum Co., August 2005.
- [24] Federal Communications Commission, Technical Spectrum Policy Task Force Report, November 2012.
- [25] Y. Zeng, Y.-C. Liang, A. T. Hoang, and R. Zhang, "A review on spectrum sensing for cognitive radio: challenges and solutions," *EURASIP Journal on Advances in Signal Processing*, vol. 2010, Article ID 381465, pp. 1–15, 2010.
- [26] S. Atapattu, C. Tellambura, and H. Jiang, "Analysis of area under the ROC curve of energy detection," *IEEE Transactions on Wireless Communications*, vol. 9, no. 3, pp. 1216–1225, 2010.
- [27] H. V. Poor, *An Introduction to Signal Detection and Estimation*, Springer, New York, NY, USA, 1994.
- [28] H. Urkowitz, "Energy detection of unknown deterministic signals," *Proceedings of the IEEE*, vol. 55, pp. 523–531, 1967.
- [29] J. Lundén, V. Koivunen, A. Huttunen, and H. V. Poor, "Collaborative cyclostationary spectrum sensing for cognitive radio systems," *IEEE Transactions on Signal Processing*, vol. 57, no. 11, pp. 4182–4195, 2009.
- [30] P. Bianchi, M. Debbah, M. Maida, and J. Najim, "Performance of statistical tests for single-source detection using random matrix theory," *IEEE Transactions on Information Theory*, vol. 57, no. 4, pp. 2400–2419, 2011.
- [31] E. Axell and E. G. Larsson, "A unified framework for GLRT-based spectrum sensing of signals with covariance matrices with known eigenvalue multiplicities," in *Proceedings of the 36th IEEE International Conference on Acoustics, Speech, and Signal Processing (ICASSP '11)*, pp. 2956–2959, Prague, Czech Republic, May 2011.
- [32] R. Wang and M. Tao, "Blind spectrum sensing by information theoretic criteria for cognitive radios," *IEEE Transactions on Vehicular Technology*, vol. 59, no. 8, pp. 3806–3817, 2010.
- [33] J. Guillory, S. Meyer, I. Sianud et al., "Radio-over-fiber architectures: future multigigabit wireless systems in the home-area network," *IEEE Vehicular Technology Magazine*, vol. 5, no. 3, pp. 30–38, 2010.
- [34] S. Arismar Cerqueira Jr., I. F. da Costa, L. T. Manera, and J. A. Diniz, "Optically controlled E-antenna for cognitive and adaptive radio over fiber systems," in *Proceedings of the IEEE Wireless Day*, Valencia, Spain, November 2013.
- [35] A. Khidre, K.-F. Lee, F. Yang, and A. Z. Elsherbeni, "Circular polarization reconfigurable wideband E-shaped patch antenna for wireless applications," *IEEE Transactions on Antennas and Propagation*, vol. 61, no. 2, pp. 960–964, 2013.
- [36] B. L. Dang and I. Niemegeers, "Analysis of IEEE 802.11 in radio over fiber home networks," in *Proceedings of the 30th IEEE*

- Conference on Local Computer Networks (LCN '05)*, pp. 744–747, Sydney, Australia, November 2005.
- [37] H. Kim, J. H. Cho, S. Kim et al., “Radio-over-fiber system for TDD-based OFDMA wireless communication systems,” *Journal of Lightwave Technology*, vol. 25, no. 11, pp. 3419–3427, 2007.
- [38] A. Das, M. Mjeku, A. Nkansah, and N. J. Gomes, “Effects on IEEE 802.11 MAC throughput in wireless LAN over fiber systems,” *Journal of Lightwave Technology*, vol. 25, no. 11, pp. 3321–3328, 2007.
- [39] M. S. Gast, *802.11n: A Survival Guide*, O'Reilly Media, Inc., Sebastopol, Calif, USA, 1st edition, 2012.
- [40] E. Parahia and R. Stacey, *Next Generation Wireless Lans, Throughput, Robustness, and Reliability in 802.11n*, Cambridge University Press, New York, NY, USA, 1st edition, 2008.
- [41] NovaGenesis, <http://www.inatel.br/novagenesis/>.

Research Article

Optically Controlled Reconfigurable Antenna Array Based on E-Shaped Elements

**Arismar Cerqueira Sodré Junior,¹ Igor Feliciano da Costa,^{1,2}
Leandro Tiago Manera,³ and José Alexandre Diniz³**

¹ *Laboratory WOCA (Wireless and Optical Convergent Access), National Institute of Telecommunications (INATEL),
João de Camargo Avenue 510, P.O. Box 05-37540-000, Santa Rita do Sapucaí, MG, Brazil*

² *Federal University of Itajubá (UNIFEI), Benedito Pereira dos Santos Avenue 1303, P.O. Box 50-37500-903, Itajubá, MG, Brazil*

³ *State University of Campinas (Unicamp), 13083-870 Campinas, SP, Brazil*

Correspondence should be addressed to Igor Feliciano da Costa; igorfelicianocosta@gmail.com

Received 14 December 2013; Revised 12 March 2014; Accepted 27 March 2014; Published 27 April 2014

Academic Editor: Mohammed Al-Husseini

Copyright © 2014 Arismar Cerqueira Sodré Junior et al. This is an open access article distributed under the Creative Commons Attribution License, which permits unrestricted use, distribution, and reproduction in any medium, provided the original work is properly cited.

This work presents the development of optically controlled reconfigurable antenna arrays. They are based on two patch elements with E-shaped slots, a printed probe, and a photoconductive switch made from an intrinsic silicon die. Numerical simulations and experiments have been shown to be in agreement, and both demonstrate that the frequency response of the antenna arrays can be efficiently reconfigured over two different frequency ISM bands, namely, 2.4 and 5 GHz. A measured gain of 12.5 dBi has been obtained through the use of two radiating elements printed in a low-cost substrate and a dihedral corner reflector.

1. Introduction

Current telecommunications networks require an efficient use of the available spectrum to meet the increasing capacity demand in the optical and wireless sectors as well as the need for energy consumption reduction. Cognitive radio (CR), radio over fiber (RoF), and reconfigurable antenna technologies have independently been utilized to fulfill the changing requirements of modern telecommunications networks. CR is able to automatically detect available frequency channels in a wireless spectrum and adapt transmission parameters, enabling different systems to operate concurrently [1]. CR uses a number of technologies, including adaptive radio, in which the communication system monitors and modifies its own performance, and software defined radio (SDR), in which traditional hardware components, including mixers, modulators, and amplifiers, are configured using advanced pieces of software [2].

RoF technology plays an important role in the integration of wireless and fiber-optic networks [3, 4]. Taking advantage of the benefits of optical fibers in conjunction with

the mobility and ubiquity of wireless networks, RoF systems connect a central office (CO) to a base station (BS) by using optical links to transmit one or multiple analogous RF signals without using optical-electronic (O/E) and electronic-optical (E/O) converters. On the BS side, the signals are recovered by photodetectors and then routed to the remote antenna unit (RAU), which is simple and cost effective because most of the processing components are centralized in the CO. RoF is an essential technology for the provision of untethered access to broadband wireless communications in a range of applications including last mile solutions, extension of existing radio coverage and capacity, backhaul, in-building coverage, outdoor cellular systems, and fixed or mobile broadband wireless access.

Reconfigurable antennas have exhibited great promise for the next generation of wireless systems [5]. This new class of antennas enables reconfigurability for not only the bandwidth but also the radiation pattern and polarization; this reconfiguration is accomplished by using frequency-agile, software-defined, and cognitive radios to cope with extendable and reconfigurable multiservice, multistandard,

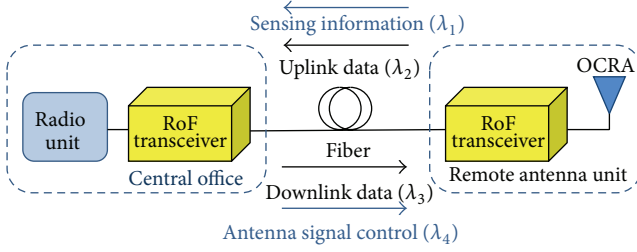


FIGURE 1: Schematic of OCRA implementation.

and multiband operation, and with efficient spectrum and power utilization. These new functionalities can efficiently reduce the number of components, hardware complexity, and cost compared with current radio technology, which relies on incompatible communications systems with inflexible hardware. There are many methods and mechanisms for reconfiguring the antenna structure and/or function [5]. The methods can be based on the integration of radiofrequency microelectromechanical systems (RF-MEMS), PIN diodes, varactors, and photoconductive elements, the physical alteration of the antenna radiating structure, or the use of smart materials such as ferrites and liquid crystal. Particularly, optically controlled reconfigurable antennas (OCRAs) have been proposed and exploited in recent years due to their unique advantages, such as [6–8] easy integration into optical systems; absence of bias lines; elimination of unwanted interference; losses and radiation pattern distortion; reliable reconfiguration mechanisms, especially compared with RF-MEMS; linear behavior and activation without producing harmonics; and intermodulation.

This work presents the development of OCRA arrays based on E-shaped elements and an example application that utilizes them, as described in Figure 1. Different wavelengths (λ) are used for simultaneously enabling data transmission, monitoring frequency spectrum, and antenna control. Initially, broadband and/or multiband antennas perform spectrum sensing (SS) to discover possible spectrum opportunities. This information is transmitted using RoF links and processed in the CO, which remotely decides how to proceed and optically controls the antenna characteristics. This technique aims to jointly apply CR, RoF, and reconfigurable antenna technologies to harmonically integrate high capacity optical backhaul with energy- and spectrum-efficient wireless access networks by exploiting new spectral resources.

In this way, the proposed OCRA array can be easily integrated into optical networks by using RoF technology to provide multiband and/or multitechnology broadband operation for last mile applications. We have very recently reported a successful implementation of an innovative and cognitive optical wireless network using an OCRA [9]. The proposed architecture allowed performing spectrum sensing and dynamic resource allocation to dynamically adapt the frequency band and/or antenna radiation pattern as a function of the wireless environment. Experimental results have demonstrated the use of the OCRA, and implementing

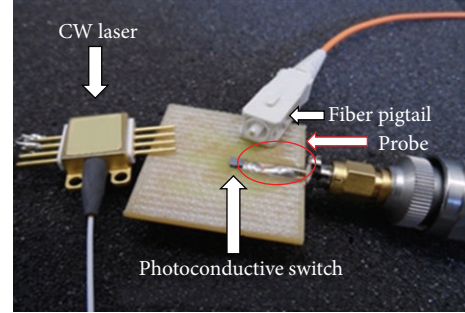
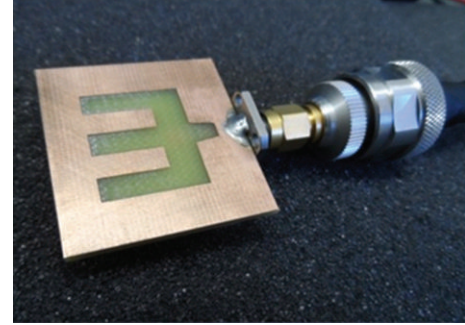


FIGURE 2: Fabricated E-antenna.

the proposed architecture can significantly improve the network performance.

The paper is organized as follows. The E-antenna design is described in Section 2, and its main numerical and experimental results are presented in Section 3. Section 4 reports the fabrication of antenna arrays based on E-shaped elements. Finally, the conclusions and final remarks are presented in Section 5.

2. E-Antenna Design

Patch antennas have been significantly exploited in the past due to their low-profile structure and compatibility with being embedded in handheld wireless devices. They also provide other advantages, such as good radiation efficiency, simple manufacturing, low cost, ease of integration with microwave integrated circuits, light weight, low volume, and the possibility of being conformed to the host surface. Particularly, Khidre et al. recently reported results on a circular polarization reconfigurable E-shaped patch antenna using two PIN diodes [10]. Our proposed patch antenna is based on an E-shaped printed slot fabricated in a low-cost fiberglass dielectric substrate, as presented in Figure 2. It is based on electromagnetic coupling ensured by a printed probe located in the bottom plane of the antenna structure, as shown in the bottom part of Figure 2. This figure also displays the other components used in the experiments, namely, a photoconductive switch made from a 2×1 mm intrinsic silicon die, a 2 W CW laser at 808 nm, and a fiber pigtail for coupling light from the CW laser to the photoconductive switch.

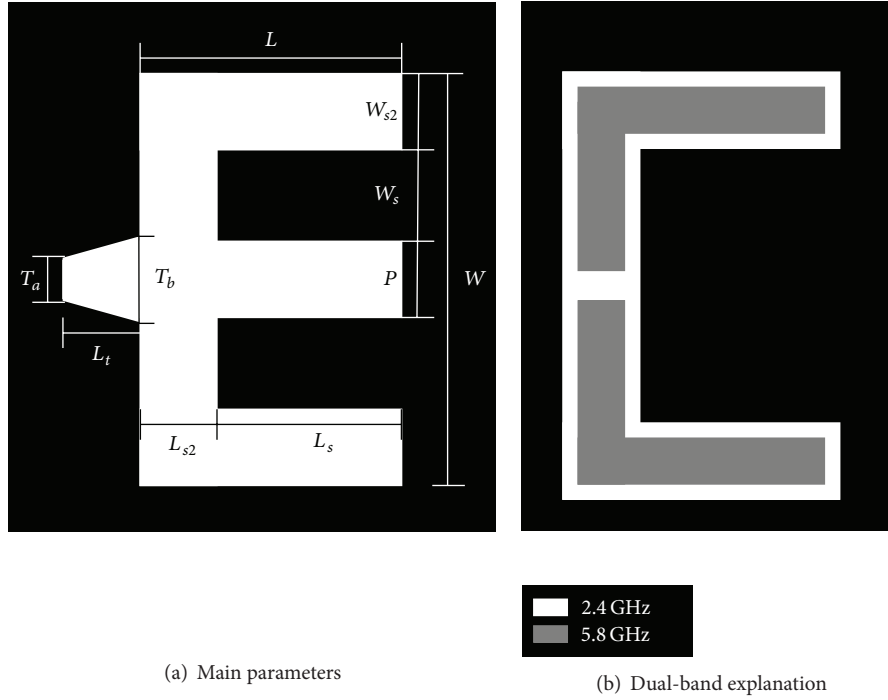


FIGURE 3: E-antenna model.

The E-antenna has been designed to provide two frequency bands (2.4 GHz and 5 GHz). Its entire structure, as detailed in Figure 3, has been optimized by manipulating the trapezoidal dimensions, W and L , and varying the E-shaped parameters, W_s , W_{s2} , and P . The highest frequency band is determined by the “C-structure,” the white region in Figure 3(b), which is approximately equal to its guided wavelength. The two gray arms from Figure 3(b), the “L-structures,” individually correspond to the guided wavelength of the central frequency from the lower band.

The prototype parameters are as follows: $W = 20.48$ mm, $L = 17.65$ mm, $W_s = W_{s2} = 4.1$ mm, $L_s = 12$ mm, $L_{s2} = 5.65$ mm, $L_t = 9.5$ mm, $T_a = 3$ mm, and $T_b = 4.31$ mm. An intrinsic silicon photoconductive switch has been fixed to the printed probe, which enables reconfiguring of the antenna electromagnetic properties as a function of optical power. A fiber pigtail has been used to illuminate the silicon die with light from the CW laser.

The antenna optical control can be explained as follows. The probe is extremely important for antenna impedance matching, and the photoconductive switch, which has been fixed to the antenna, can manage its length. For the off-state, the die assumes the highest resistance, which is approximately 6000Ω [11]; therefore, the probe length is limited to the printed metallic line. As soon as the photoconductive switch is illuminated, the silicon changes from an insulator state to a near conducting state by creating electron-hole pairs. In this way, the current starts to increase because the switch resistance is reduced and, consequently, the silicon wafer

becomes able to conduct. Its minimum value for the on-state is approximately 118Ω [6]. The incident photons must have enough energy to move electrons from the valence to the conduction band. Light in the near-infrared region is adequate for this process as it strikes a balance between the absorption coefficient and the light penetration depths [12], which are inversely proportional to each other and related to the light wavelength. Therefore, the switch conductivity can be managed by controlling the optical incident power. In this way, the probe length can be modified, and, consequently, the antenna frequency response can be reconfigured as a function of the laser current. In the proposed antenna, the CW laser is used to transpose the 1.12 eV bandgap between the valence and conduction bands from the intrinsic silicon die.

3. E-Antenna Results

ANSYS HFSS numerical simulations and experimental characterization are used to analyze the antenna. Initially, the reflection coefficient (S_{11}) was evaluated for the two main states of the photoconductive switch: the off-state (when there is an absence of light on it) and the on-state (when it is illuminated by the 808 nm laser). Figure 4 reports comparisons between the numerical and experimental results for the off- and on-states, which present good agreement. When the switch is in the off-state, the antenna frequency response is much better for the 5 GHz band, with the reflection coefficient reaching a minimum of -22 and -40 dB in the

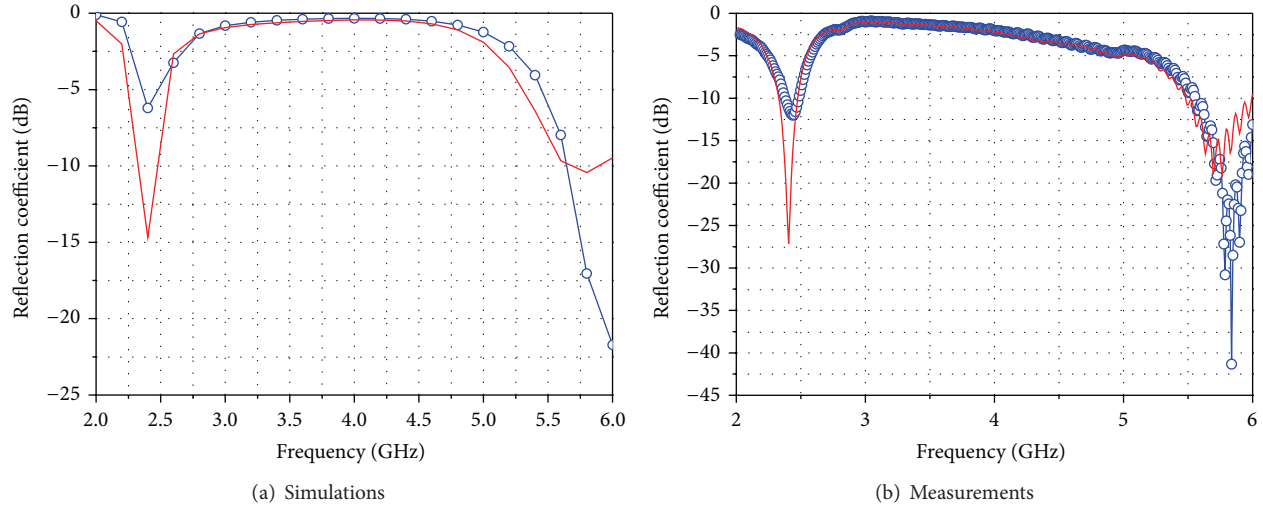


FIGURE 4: Reflection coefficient comparison as a function of the switch state: on-state (continuous red line); off-state (blue dashed line with circles).

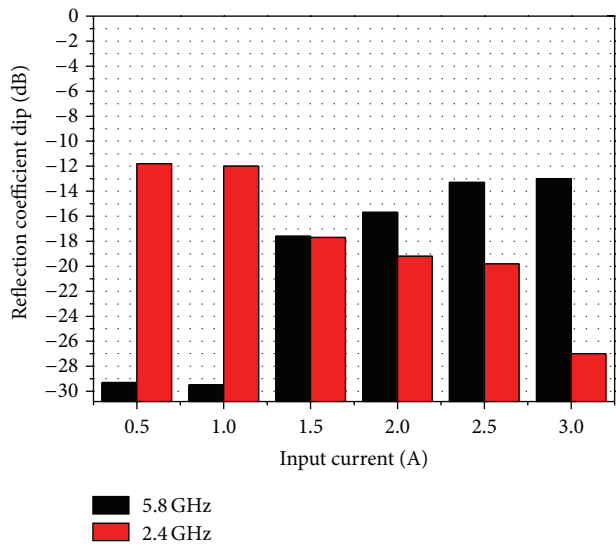


FIGURE 5: Measurement of reflection coefficient dips as a function of laser current.

simulation and experiment, respectively. For the 2.4 GHz band, it is -6 and -10 dB, respectively. As soon as the photoconductive switch is illuminated by the 808 nm CW laser, an incident power into the switch of approximately 300 mW, the antenna reconfigures its frequency response to significantly improve the reflection coefficient in the 2.4 GHz band. In this state, the 2.4 GHz band has a measured bandwidth of 8.3% and dip of -27 dB; the 5 GHz band also has good performance, with a measured bandwidth of 8.7% and dip of -19 dB. It is clear that the antenna frequency response can be efficiently reconfigured through the two ISM bands in accordance with the system requirements.

The antenna frequency response of the OCRA can also be evaluated by impedance matching. An enhancement of the antenna input impedance (Z_{in}) at 2.4 GHz, $[41.31 - 26.37j] \Omega$ and $[49.57 - 3.47j] \Omega$ for the off- and on-states, respectively, was obtained. Its imaginary part is significantly reduced, and the real part becomes very close to the ideal value (50Ω). For these two reasons, the impedance matching improves significantly for this frequency. For 5.8 GHz, the S_{11} measurements for both switch states are very close to the central point of the Smith chart because their input impedances are $[56.87 - 0.41j] \Omega$ and $[68.25 + 8.24j] \Omega$ for the off- and on-states, respectively. These results reaffirm the successful implementation of the OCRA.

The switch conductivity strongly depends on the number of generated electron-hole pairs and, consequently, the level of incident optical power. In accordance with [6], its conductivity is only 52 S/m for the off-state and can be increased to 622 S/m by illuminating it at 212 mW. An experimental analysis of the S_{11} dips (minimum points) has been performed to illustrate this effect; the obtained results for the two main ISM bands are presented in Figure 5. The higher the laser current, the better the dip at 2.4 GHz, which improves from -12 to -27 dB. The physical mechanism behind this phenomenon is the increase in the probe length. Alternatively, the dip at 5.8 GHz becomes worse as the optical power is increased due to the same reason. Additionally, it is important to highlight that there is a trade-off point approximately 1.5 A.

The software ANSYS HFSS has also been used to numerically analyze the E-shaped antenna radiation pattern. The simulated tridimensional patterns at 2.4 and 5.8 GHz for the off-state are shown in Figure 6. As expected, the gain for the 5.8 GHz band ($G = 5.30$ dBi) is higher than that for the 2.4 GHz band ($G = 3.29$ dBi) because the E-antenna operates differently for the two frequency bands. The lower band is determined by the trapezoidal dimensions, which approximately correspond to the guided wavelength for this band. For the higher band, the E-shaped antenna operates

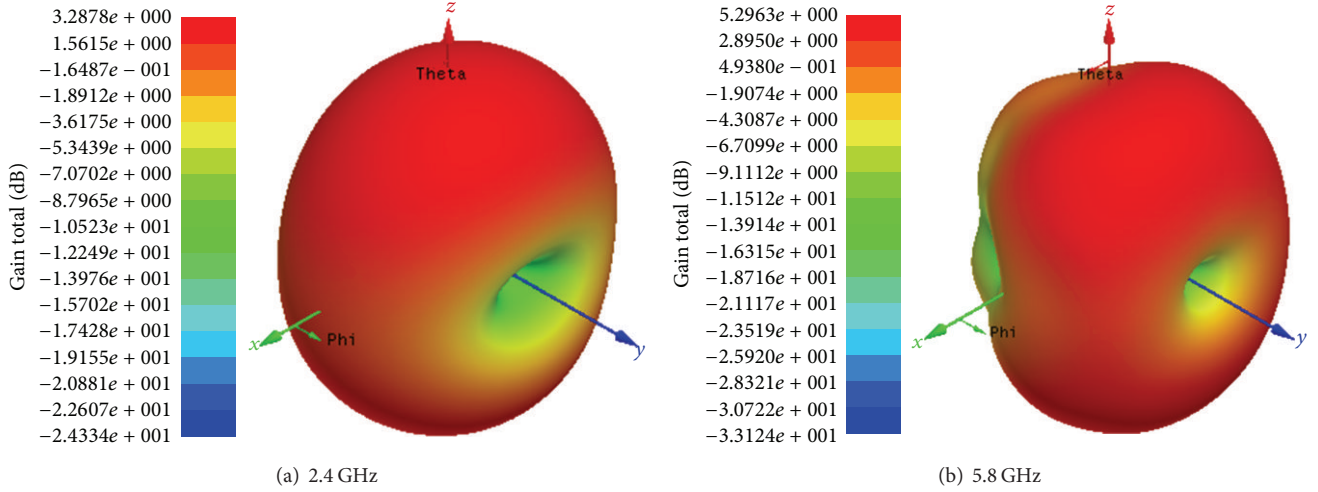


FIGURE 6: Simulation of the E-shaped antenna radiation patterns for the off-state.

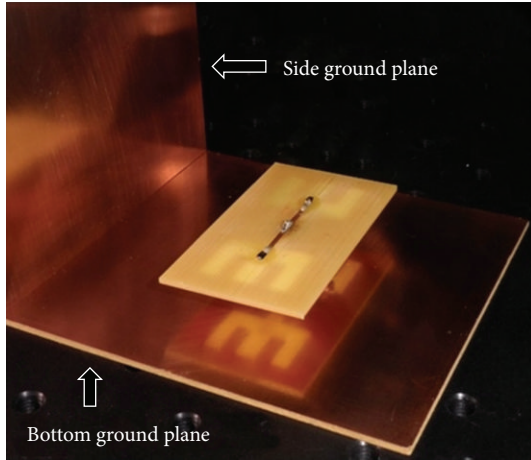


FIGURE 7: Photograph of antenna array with a corner reflector.

based on two arms that are as long as its guided wavelength. For this reason, its gain is higher than the previous one.

4. Antenna Arrays

Three different configurations of antenna arrays based on E-shaped elements have been constructed to increase the directivity. The following configurations have been numerically and experimentally evaluated:

- configuration I: one E-shaped antenna;
- configuration II: array with two E-shaped elements;
- configuration III: array with two E-shaped elements and a bottom ground plane;
- configuration IV: array with two E-shaped elements and a dihedral corner reflector based on the bottom and side ground planes.

A photograph of configuration IV is displayed in Figure 7. For this case, two photoconductive switches were used, one for each E-shaped element. The angle between the 10×10 cm metallic reflector plates is 90 degrees. The radiation pattern of all configurations has been measured in the semianechoic chamber of our institute and compared with the results of the numerical simulations.

Figure 8 presents a comparison of the simulated and measured radiation patterns from configuration III at 5.8 GHz for the off-state. There is an excellent agreement between simulations and measurements. The azimuth pattern is omnidirectional, whereas the elevation pattern presents two lobes, as in the pattern of one E-shaped element (configuration I) presented in the previous section. The main difference between configurations I and III is the gain magnitude, which increased from 5.30 to 10 dBi, respectively. As expected, the radiation pattern and gain from configuration III at 5.8 GHz for the off- and on-states are very similar. On the other hand, the gain from configuration III at 2.4 GHz can be improved when the photoconductive switch is illuminated by the 808 nm laser, as reported in Figure 9. The simulated and measured gain for the on-state is approximately 5.3 dBi in this case. Furthermore, the elevation pattern from configuration IV for both switch states was also measured and is displayed in Figure 10. The effect of the antenna optical control is similar to that from configuration III, that is, a gain improvement for 2.4 GHz and no changes for 5.8 GHz.

Finally, an analysis of the gain improvement was performed for all configurations at 2.4 and 5.8 GHz, as shown in Figure 11. It is clear that the directivity can be significantly improved by using the proposed configurations. The spacing between the array elements has been numerically optimized for 5.8 GHz. For this reason, the gain increase is higher for this frequency than that for 2.4 GHz. The gain at 2.4 GHz increased from 2.7 dBi from configuration I to 6.8 dBi by using configuration IV. The measured gains at 5.8 GHz were 5.1, 7.5, 10, and 12.5 dBi for configurations I, II, III, and IV, respectively. As in the previous sections, there is excellent

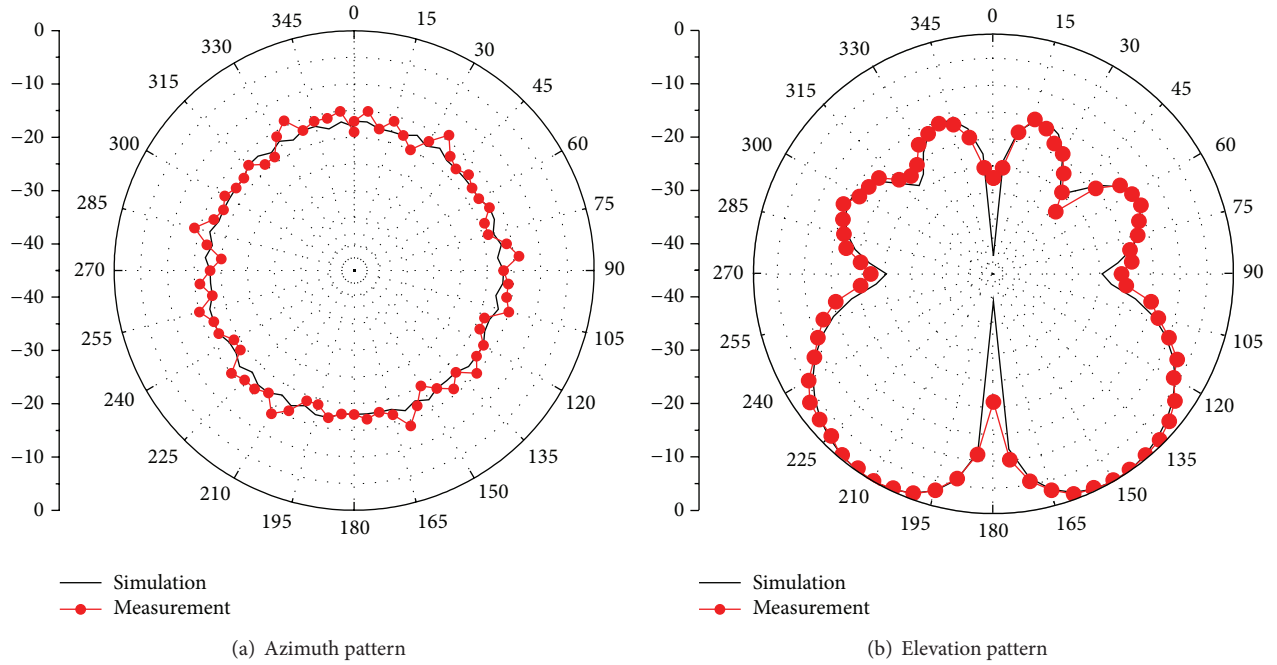


FIGURE 8: Simulated and measured radiation patterns from configuration III at 5.8 GHz.

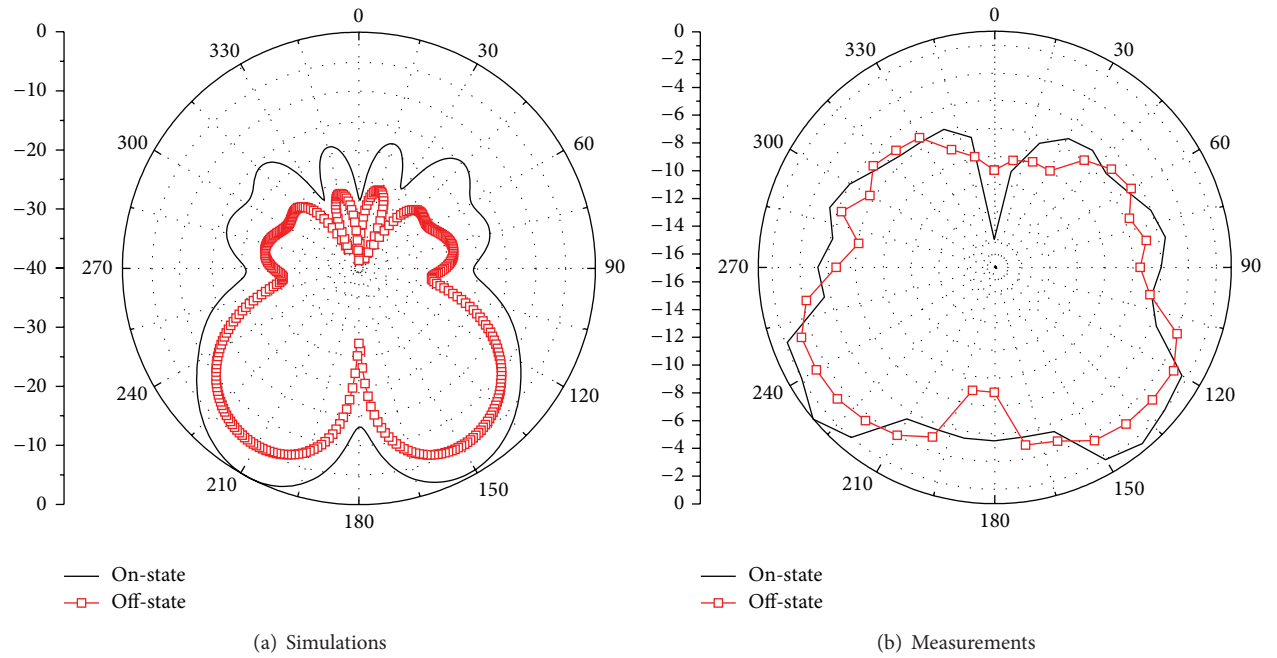


FIGURE 9: Elevation patterns from configuration III at 2.4 GHz.

agreement between HFSS simulations and experimental results.

5. Conclusions

Low-cost, frequency-agile, and high-gain optically controlled reconfigurable arrays based on E-shaped elements have been

successfully proposed and fabricated. Reconfigurable bandwidths over two ISM bands have been reported. Comparisons between the simulations and measurements of the reflection coefficient and radiation patterns have been shown to be in excellent agreement. The array composed of two E-shaped elements and a dihedral corner reflector provides measured gains of 6.8 and 12.5 dBi at 2.4 and 5.8 GHz, respectively.

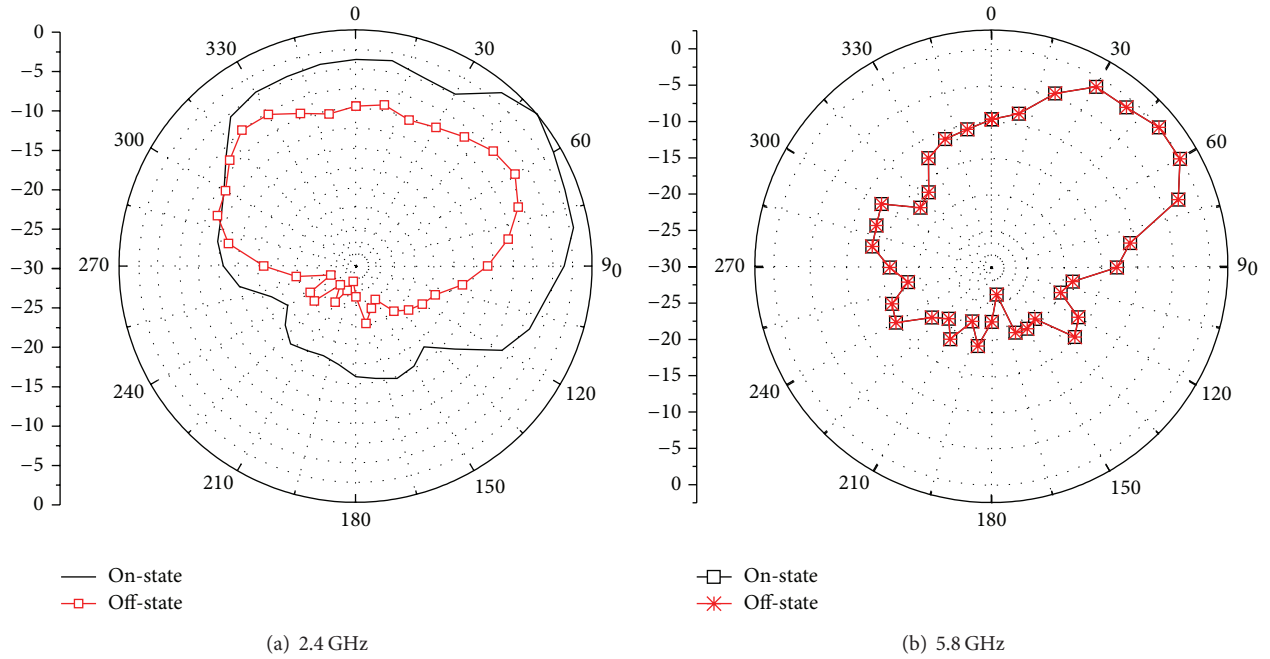


FIGURE 10: Measured elevation patterns from configuration IV.

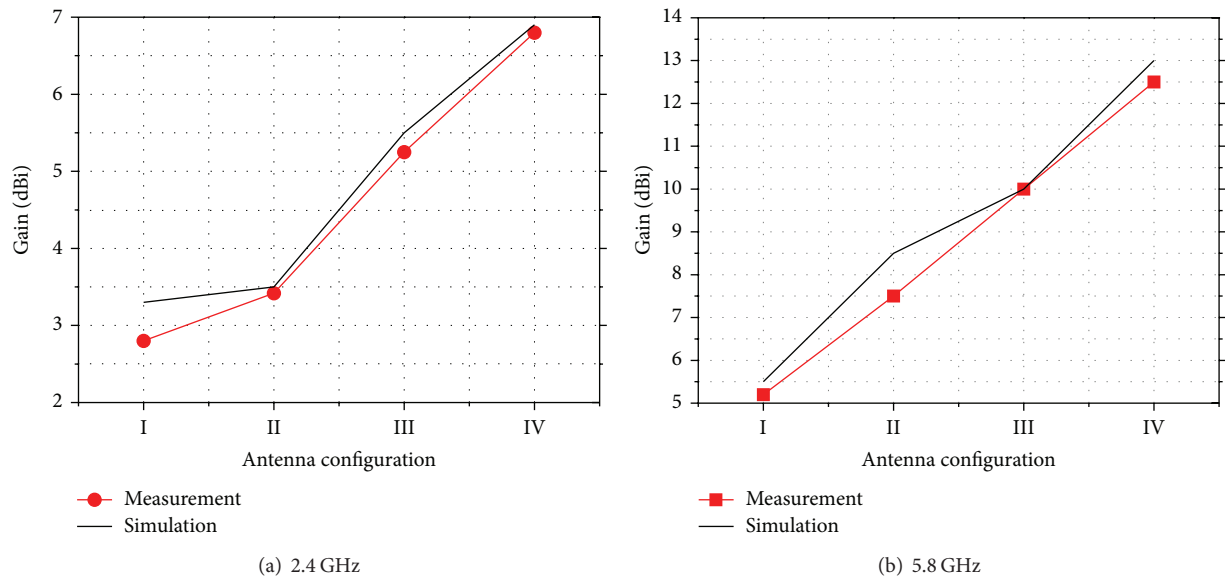


FIGURE 11: Gain analyses for all configurations.

Experimental results have demonstrated that a laser at the mid-infrared region can remotely control the antenna frequency response. This outstanding feature allows for the creation of smart, cognitive, and agile RF devices that can both sense the surrounding RF environment and communicate at the same time using different frequency bands.

Conflict of Interests

The authors declare that there is no conflict of interests regarding the publication of this paper.

Acknowledgments

The authors thank the financial support of CNPq, CAPES, MCTI, FAPEMIG, FINATEL, ESSS-ANSYS, Bradar, Prysmian-Draka, and Huber-Suhner and the technical support of TIM.

References

- [1] J. Mitola III and G. Q. Maguire Jr., "Cognitive radio: making software radios more personal," *IEEE Personal Communications*, vol. 6, no. 4, pp. 13–18, 1999.

- [2] E. Larsson and M. Skoglund, "Cognitive radio in a frequency-planned environment: some basic limits," *IEEE Transactions on Wireless Communications*, vol. 7, no. 12, pp. 4800–4806, 2008.
- [3] A. J. Seeds and K. J. Williams, "Microwave photonics," *Journal of Lightwave Technology*, vol. 24, no. 12, pp. 4628–4641, 2006.
- [4] D. G. Lona, R. M. Assumpção, O. C. Branquinho, M. L. F. Abbade, H. E. Hernandez Figueroa, and S. Arismar Cerqueira Jr., "Implementation and performance investigation of radio-over-fiber systems in wireless sensor networks," *Microwave and Optical Technology Letters*, vol. 54, pp. 2669–2675, 2012.
- [5] C. G. Christodoulou, Y. Tawk, S. A. Lane, and S. R. Erwin, "Reconfigurable antennas for wireless and space applications," *Proceedings of the IEEE*, vol. 100, no. 7, pp. 2250–2261, 2012.
- [6] Y. Tawk, A. R. Albrecht, S. Hemmady, G. Balakrishnan, and C. G. Christodoulou, "Optically pumped frequency reconfigurable antenna design," *IEEE Antennas and Wireless Propagation Letters*, vol. 9, pp. 280–283, 2010.
- [7] Y. Tawk, J. Costantine, S. Hemmady, G. Balakrishnan, K. Avery, and C. G. Christodoulou, "Demonstration of a cognitive radio front end using an optically pumped reconfigurable antenna system (OPRAS)," *IEEE Transactions on Antennas and Propagation*, vol. 60, no. 2, pp. 1075–1083, 2012.
- [8] C. J. Panagamuwa, A. Chauraya, and J. C. Vardaxoglou, "Frequency and beam reconfigurable antenna using photoconducting switches," *IEEE Transactions on Antennas and Propagation*, vol. 54, no. 2, pp. 449–454, 2006.
- [9] E. R. Neto, M. A. F. Casaroli, J. R. G. da Rosa et al., "Dynamic spectral sensing and resource allocation in optical-wireless network," in *SDR-WInnComm*, Schaumburg, Ill, USA, 2014.
- [10] A. Khidre, Kai-Fong Lee, F. Yang, and A. Z. Elsherbeni, "Circular polarization reconfigurable wideband E-shaped patch antenna for wireless applications," *IEEE Transactions on Antennas and Propagation*, vol. 61, no. 2, pp. 960–964, 2013.
- [11] E. K. Kowalczyk, C. J. Panagamuwa, R. D. Seager, and J. C. Vardaxoglou, "Characterising the linearity of an optically controlled photoconductive microwave switch," in *Proceedings of the 6th Loughborough Antennas and Propagation Conference (LAPC '10)*, pp. 597–600, Loughborough, UK, November 2010.
- [12] B. E. A. Saleh and M. C. Teich, *Fundamentals of Photonics*, Wiley, Hoboken, NJ, USA, 2007.

Research Article

Application of a Channel Estimation Algorithm to Spectrum Sensing in a Cognitive Radio Context

Vincent Savaux,¹ Moïse Djoko-Kouam,² Yves Louët,¹ and Alexandre Skrzypczak³

¹ IETR-Supélec, 35000 Rennes, France

² ECAM Rennes-Louis de Broglie, 35170 Rennes, France

³ Zodiac Data Systems, 14000 Caen, France

Correspondence should be addressed to Vincent Savaux; vincent.savaux@supelec.fr

Received 7 November 2013; Accepted 27 January 2014; Published 26 March 2014

Academic Editor: Ali El-Hajj

Copyright © 2014 Vincent Savaux et al. This is an open access article distributed under the Creative Commons Attribution License, which permits unrestricted use, distribution, and reproduction in any medium, provided the original work is properly cited.

This paper deals with spectrum sensing in an orthogonal frequency division multiplexing (OFDM) context, allowing an opportunistic user to detect a vacant spectrum resource in a licensed band. The proposed method is based on an iterative algorithm used for the joint estimation of noise variance and frequency selective channel. It can be seen as a second-order detector, since it is performed by means of the minimum mean square error criterion. The main advantage of the proposed algorithm is its capability to perform spectrum sensing, noise variance estimation, and channel estimation in the presence of a signal. Furthermore, the sensing duration is limited to only one OFDM symbol. We theoretically show the convergence of the algorithm, and we derive its analytical detection and false alarm probabilities. Furthermore, we show that the detector is very efficient, even for low SNR values, and is robust against a channel uncertainty.

1. Introduction

Wireless communications are facing a constant increase of data-rate-consuming transmissions, due to the multiplications of the applications and services, while the available spectrum resource is naturally limited. Furthermore, most of the frequency bands are already allocated to specific licenses. However, some of these licensed bands are not used at their full capacity, which results in spectrum holes along the time and frequency axes [1], whereas they could be exploited in order to achieve the requirements of data rate. Away from the usual paradigm in which the channels are allocated only for licensed users, Mitola and Maguire Jr. defined the cognitive radio [2], allowing an opportunistic access by unlicensed users to the unused frequency bands. In such network, the opportunistic users, called secondary users (SUs), can use licensed bands when primary users (PUs) are not active. The main condition for the SUs to use the licensed bands is to minimize the interferences with PUs. Thus, they must be able to sense the presence of the PUs, even if the PU's signal is attenuated compared to the noise level. Figure 1 depicts

the concept of spectrum sensing: a PU transmitter (PU-Tx) is transmitting to a PU receiver (PU-Rx) while a SU transmitter intends to transmit in the same band. In order to avoid the interferences with the PU, the SU has to perform spectrum sensing. In order to lighten the drawing, only one PU-Rx and two SU-Rxs are depicted, but the network can obviously be more complex. The process set up by the SUs to sense the presence of the PUs is called spectrum sensing. The authors of [3–5] propose detailed reviews of the different techniques of spectrum sensing. The different methods are usually classified into two main categories: the cooperative detection and the noncooperative detection. In this paper, we take an interest in the latter.

The noncooperative detection concerns a sole SU who tries to detect the presence of the PU alone. Among the wide range of methods [3–6], one can describe the main ones: the energy detector measures the energy of the received signal and compares it to a threshold. It has a low complexity of implementation and does not require any knowledge on the PU's signal features. However, the choice of the threshold value depends on the noise variance, and the uncertainties

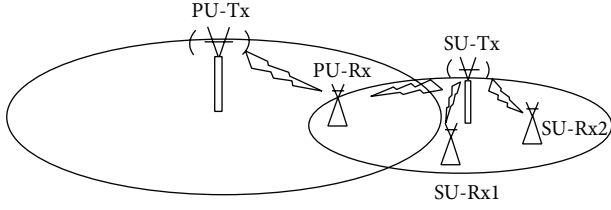


FIGURE 1: Illustration of the principle of the spectrum sensing.

on the noise level may cause important degradations of the detector performance [7, 8]. The matched-filter correlates the received signal with the one transmitted by the PU, which is supposed to be known at the receiver [9, 10]. This is the optimal detector when the signal is transmitted with AWGN only and supposed to be known at the receiver. Due to these hypotheses, this method is generally not applicable in practice, and its performance is degraded when the knowledge of the signal is erroneous [11]. Less binding than the matched-filter, the feature detectors only use several characteristics of the signal to detect the PU. Thus, the waveform-based sensing uses the preamble of the PU's signal (used for the synchronization, the estimation, etc.) to perform a correlation with the received signal [12]. However, the performance of the waveform-based sensing is degraded in the presence of selective channels. In the same way, when a CP is used in an OFDM signal, its autocorrelation function becomes time-varying, so a second-order-based method consists of detecting the peaks in the autocorrelation function at time-lag T_s . More generally, the cyclostationarity detector exploits the periodic redundancy of all telecommunications signals to differentiate it from a pure Gaussian noise [13, 14]. As indicated in [5], the redundancy can occur due to periodic patterns such as the CP, the symbol rate, or the channel code. However, these second-order detectors require large sensing time, that is, a large number of symbols to be performed. In [15], a hybrid architecture composed of both energy and cyclostationarity is proposed. It allows the energy detector to compensate its limitation due to the noise uncertainty thanks to a cyclostationarity detection stage whose computation time is reduced. Another attractive technique called eigenvalue-based detection uses the characteristics of the covariance matrix of large-sized random matrices (e.g., containing noise samples only) [16–18]. Indeed, the random matrix theory proved that the distribution of the eigenvalues of such matrix tends to a deterministic function. In [16], if the noise variance is known, the signal is detected if a peak appears outside of the domain of the function. Using the same theory, the authors of [17] propose the maximum-minimum eigenvalue (MME) detection, whose principle consists of comparing the ratio between the maximum and minimum eigenvalues with a threshold to take the decision. Based on the same theory, both techniques have the same asymptotic performance, but the latter does not require the noise level to be performed. However, these two methods require matrices with very large sizes, hence, a large number of sensors and a long sensing time. In order to use MME detection with a single sensor, the authors of [19] propose to artificially create

a large matrix by stacking the shifted vectors of the received sampled signal. However, this method is limited since the rows of the created matrix are correlated.

In this paper, we propose to perform spectrum sensing by means of a minimum mean square error (MMSE-)based iterative algorithm developed in [20] for the joint estimation of noise variance and frequency selective channel. Since we consider a sole receiver, the context of the next sections will be the noncooperative detection of a PU transmitting an OFDM signal by a single SU in a given narrow band. In the presence or absence of signal, the algorithm converges after a few iterations and performs the estimation of the noise variance. We then add a metric to the method presented in [20] in order to turn it into a spectrum sensing algorithm. The metric is defined by the difference between the second-order moment M_2 of the received signal and the estimated noise variance. If the PU is present (resp. absent), the metric is equal to the power of the transmitted signal (resp. equal to zero). As the algorithm is based on MMSE criterion, it requires the estimation of the channel covariance matrix, so the detector can be classified as a second-order statistics detector. Compared to usual second-order statistics detectors such as MME, the proposed one only needs the time duration of one OFDM symbol to be performed. It is also robust in frequency selective channels context. Furthermore, when the PU's signal is present, it achieves a joint estimation of noise variance and channel. When the PU is absent, it also performs the noise variance estimation, and it is proved that it reaches the exact noise power value. In this paper, a theoretical expression of the detection and the false alarm probabilities are derived, and we show that they are very close to the simulations.

In this paper, the normal font x is used for scalar variables, the boldface \mathbf{x} is used for vectors, and the underlined boldface $\underline{\mathbf{x}}$ is used for matrices. Furthermore, small letters x point out the variables in the time domain and capital letters X in the frequency domain.

This paper is organized as follows: Section 2 presents the system model and the algorithm developed in [20]. In Section 3, we prove the convergence of the algorithm in the absence of the signal, and we characterize the detector in Section 4. In Section 5, we give the theoretical expressions of the false alarm and detection probabilities. Simulations results are depicted in Section 6, and finally we draw our conclusions in Section 7.

2. Background

2.1. System Model. We consider the problem of the detection of an OFDM pilot preamble over a Rayleigh fading channel with additive white Gaussian noise (AWGN) in a given band. After the M -points discrete Fourier transform (DFT), the received signal is noted \mathbf{U} . According to the presence or the absence of the primary user (PU) in the band, the usual hypothesis test is given by

$$\mathbb{H}_0 : \mathbf{U} = \mathbf{W},$$

$$\mathbb{H}_1 : \mathbf{U} = \underline{\mathbf{C}}\mathbf{H} + \mathbf{W},$$

(1)

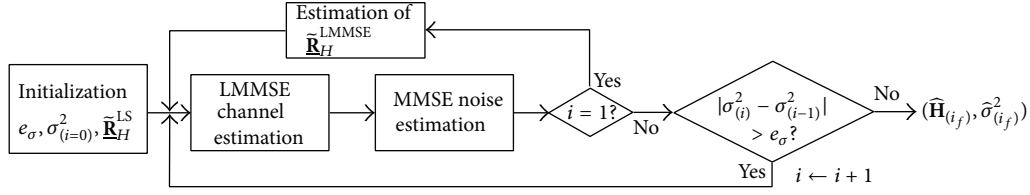


FIGURE 2: Block diagram of the iterative algorithm in the realistic scenario.

where \mathbb{H}_0 and \mathbb{H}_1 denote the absence and the presence of the PU hypotheses, respectively. According to the model given in [20], the variable \mathbf{H} is the $M \times 1$ complex vector of the frequency response of the channel, composed of the frequency response samples H_m , $m = 0, 1, \dots, M-1$:

$$H_m = \sum_{l=0}^{L-1} h_l \exp\left(-2j\pi \frac{m\tau_l}{M}\right), \quad (2)$$

where L is the number of paths of the channel and h_l and τ_l are the zero-mean Gaussian path coefficients and the sampled path delays, respectively. We assume that the channel \mathbf{H} follows a wide sense stationary uncorrelated scattering (WSSUS) model [21]. Consequently, $|H_m|$ follows a Rayleigh distribution. The variable $\underline{\mathbf{C}}$ is the $M \times M$ diagonal matrix composed of the pilots C_m such that $|C_m| = 1$, without loss of generality, and \mathbf{W} is the $M \times 1$ vector of AWGN with variance σ^2 . Let us assume that, under hypothesis \mathbb{H}_1 , the receiver is synchronized on the position of the preamble $\underline{\mathbf{C}}$.

2.2. Iterative Algorithm for the Channel and Noise Variance Estimation. We now briefly recall the steps of the algorithm for the joint and iterative estimation of the channel and the noise variance as given in [20], that is, under the hypothesis \mathbb{H}_1 . Basically, it is an MMSE-based iterative algorithm in which, at each step, the noise variance estimation feeds the channel estimation and vice versa. In addition to the noise variance, the linear-MMSE (LMMSE) channel estimation [22] requires the channel covariance matrix that has to be estimated at the receiver. This estimated channel covariance matrix is noted $\tilde{\mathbf{R}}_H$. The algorithm from [20] is described by Figure 2 and its steps are detailed in the following.

(1) At the beginning, only the LS channel estimation $\hat{\mathbf{H}}^{LS}$ performed on a pilot preamble is available at the receiver, so the only way to estimate the covariance matrix denoted by $\tilde{\mathbf{R}}_H^{LS}$ is

$$\tilde{\mathbf{R}}_H^{LS} = \hat{\mathbf{H}}^{LS} (\hat{\mathbf{H}}^{LS})^H, \quad (3)$$

where $(\cdot)^H$ is the Hermitian transposition. Furthermore, a stopping criterion e_σ is fixed. Let us denote i to be the index of the iteration.

(2) At the first step ($i = 1$) of the algorithm, the LMMSE channel estimation [22, 23] is performed with $\tilde{\mathbf{R}}_H^{LS}$:

$$\hat{\mathbf{H}}_{(i=1)}^{LMMSE} = \tilde{\mathbf{R}}_H^{LS} (\tilde{\mathbf{R}}_H^{LS} + \hat{\sigma}_{(i=0)}^2 \underline{\mathbf{C}} \underline{\mathbf{C}}^H)^{-1} \hat{\mathbf{H}}^{LS}, \quad (4)$$

where $\hat{\sigma}_{(i=0)}^2$ points out the initialization value of the noise variance and $\underline{\mathbf{C}} \underline{\mathbf{C}}^H$ is equal to the identity matrix \mathbf{I} .

(3) The noise variance is estimated by means of the MMSE criterion [24] $\hat{\sigma}_{(i=1)}^2 = (1/M) E\{\|\hat{\mathbf{H}}^{LS} - \hat{\mathbf{H}}\|^2\}$, with $\hat{\mathbf{H}} = \hat{\mathbf{H}}_{(i=1)}^{LMMSE}$:

$$\hat{\sigma}_{(i=1)}^2 = \frac{1}{M} E\{\|\hat{\mathbf{H}}^{LS} - \hat{\mathbf{H}}_{(i=1)}^{LMMSE}\|^2\}, \quad (5)$$

with $\|\cdot\|$ being the Frobenius matrix norm, defined by $\|\mathbf{A}\| = \sqrt{\text{tr}(\mathbf{A} \mathbf{A}^H)}$. If the algorithm keeps on computing with $\tilde{\mathbf{R}}_H^{LS}$, it is proved in [20] that $(\hat{\sigma}_{(i)}^2)$ converges to zero. Under this condition, the algorithm enters into an endless loop. This is due to the fact that $\tilde{\mathbf{R}}_H^{LS}$ is sensitive to the noise and then it is a rough approximation of the exact covariance matrix. In order to obtain a more accurate channel covariance matrix, it is now possible to use $\hat{\mathbf{H}}_{(i=1)}^{LMMSE}$, such that

$$\tilde{\mathbf{R}}_H^{LMMSE} = \hat{\mathbf{H}}_{(i=1)}^{LMMSE} (\hat{\mathbf{H}}_{(i=1)}^{LMMSE})^H. \quad (6)$$

(4) For $i \geq 2$, the iterative estimation steps (4) and (6) are performed by using (6):

$$\hat{\mathbf{H}}_{(i)}^{LMMSE} = \tilde{\mathbf{R}}_H^{LMMSE} (\tilde{\mathbf{R}}_H^{LMMSE} + \hat{\sigma}_{(i-1)}^2 \mathbf{I})^{-1} \hat{\mathbf{H}}^{LS}, \quad (7)$$

$$\hat{\sigma}_{(i)}^2 = \frac{1}{M} E\{\|\hat{\mathbf{H}}^{LS} - \hat{\mathbf{H}}_{(i)}^{LMMSE}\|^2\}. \quad (8)$$

It will be shown afterwards that the characterization of the initialization $\hat{\sigma}_{(i=0)}^2$ remains the same in the presence or absence of the PU. However, it is already obvious that $\hat{\sigma}_{(i=0)}^2$ must be strictly positive; otherwise, $\hat{\mathbf{H}}_{(i)}^{LMMSE} = \hat{\mathbf{H}}^{LS}$ in (7). In that case, $\hat{\sigma}_{(i)}^2 = 0$, and the algorithm enters into an endless loop.

(5) While $|\hat{\sigma}_{(i)}^2 - \hat{\sigma}_{(i-1)}^2| > e_\sigma$, go back to Step 4 with $i \leftarrow i+1$; otherwise, go to Step 6.

(6) End of the algorithm. We note i_f to be the index of the last iteration.

It is proved in [20] that this algorithm converges if the initialization value of the noise variance is chosen such that $\hat{\sigma}_{(i=0)}^2 \gg M_2$, where M_2 is the second-order moment of the received signal \mathbf{U} . Moreover, the algorithm converges to limits $(\hat{\mathbf{H}}_{(i_f)}, \hat{\sigma}_{(i_f)}^2)$ that are close to the exact values (\mathbf{H}, σ^2) . From (4) and (7) we can deduce the complexity of the algorithm. The LMMSE channel estimation requires M^3 scalar multiplications for the matrix inversion

and multiplication and the noise variance M^2 . The covariance matrices estimation also requires M^2 operations. Finally, we then evaluate the complexity of the proposed algorithm by $\mathcal{O}(i_f M^3)$.

Unlike the presented model, the next section investigates the behavior of the algorithm when the PU is absent, that is, under hypothesis \mathbb{H}_0 .

3. Convergence of the Iterative Algorithm under Hypothesis \mathbb{H}_0

The signal \mathbf{C} is now supposed to be absent, so the received signal is $\mathbf{U} = \mathbf{W}$. The convergence of the proposed algorithm in the case of absence of signal is going to be proved. Furthermore, it will be proved afterwards that the nonnull solution allows to turn the MMSE-based algorithm into a free band detector. To this end, the first four steps of the iterative algorithm presented in Section 2.2 are expressed under hypothesis \mathbb{H}_0 .

3.1. Expression of the Algorithm under \mathbb{H}_0 . Let us consider that the receiver does not know if the signal is present or absent, so the same formalism as in Section 2.2 is used, and the steps of the algorithm are recalled by considering noise only. At the beginning of the process, the LS channel estimation has been performed, $\hat{\mathbf{H}}^{\text{LS}} = \mathbf{C}^{-1}\mathbf{U} = \mathbf{C}^{-1}\mathbf{W}$. The following steps are as follows.

(1) From $\hat{\mathbf{H}}^{\text{LS}}$, the channel covariance matrix is estimated by

$$\tilde{\mathbf{R}}_H^{\text{LS}} = \hat{\mathbf{H}}^{\text{LS}}(\hat{\mathbf{H}}^{\text{LS}})^H = \mathbf{W}\mathbf{W}^H. \quad (9)$$

Additionally, a stopping criterion e_σ and an initialization $\hat{\sigma}_{(i=0)}^2$ are set.

(2) At iteration $i = 1$ of the algorithm, the LMMSE channel estimation $\hat{\mathbf{H}}_{(i=1)}^{\text{LMMSE}}$ is performed by using $\tilde{\mathbf{R}}_H^{\text{LS}}$:

$$\hat{\mathbf{H}}_{(i=1)}^{\text{LMMSE}} = \tilde{\mathbf{R}}_H^{\text{LS}}(\tilde{\mathbf{R}}_H^{\text{LS}} + \hat{\sigma}_{(i=0)}^2 \mathbf{I})^{-1} \hat{\mathbf{H}}^{\text{LS}}. \quad (10)$$

(3) The MMSE noise variance estimation $\hat{\sigma}_{(i=1)}^2$ is performed with $\hat{\mathbf{H}} = \hat{\mathbf{H}}_{(i=1)}^{\text{LMMSE}}$:

$$\hat{\sigma}_{(i=1)}^2 = \frac{1}{M} E \left\{ \left\| \hat{\mathbf{H}}^{\text{LS}} - \hat{\mathbf{H}}_{(i=1)}^{\text{LMMSE}} \right\|^2 \right\}, \quad (11)$$

and a new covariance matrix is computed by

$$\tilde{\mathbf{R}}_H^{\text{LMMSE}} = \hat{\mathbf{H}}_{(i=1)}^{\text{LMMSE}}(\hat{\mathbf{H}}_{(i=1)}^{\text{LMMSE}})^H. \quad (12)$$

Indeed, it is proved in the Appendix that if the algorithm keeps on computing with $\tilde{\mathbf{R}}_H^{\text{LS}} = \mathbf{W}\mathbf{W}^H$, then the sequence $\hat{\sigma}_{(i)}^2$ necessarily converges to zero. When $\tilde{\mathbf{R}}_H^{\text{LS}}$ is used, and in

spite of its inputs being different, the algorithm has exactly the same response whatever the hypothesis, \mathbb{H}_0 or \mathbb{H}_1 .

(4) Then, for $i \geq 2$, iteratively perform the channel and the noise variance estimation:

$$\hat{\mathbf{H}}_{(i)}^{\text{LMMSE}} = \tilde{\mathbf{R}}_H^{\text{LMMSE}} \left(\tilde{\mathbf{R}}_H^{\text{LMMSE}} + \hat{\sigma}_{(i-1)}^2 \mathbf{I} \right)^{-1} \hat{\mathbf{H}}^{\text{LS}}, \quad (13)$$

$$\hat{\sigma}_{(i)}^2 = \frac{1}{M} E \left\{ \left\| \hat{\mathbf{H}}^{\text{LS}} - \hat{\mathbf{H}}_{(i)}^{\text{LMMSE}} \right\|^2 \right\}. \quad (14)$$

From these first four steps of the algorithm, it is now possible to prove that the algorithm converges to a nonnull solution under \mathbb{H}_0 .

3.2. Scalar Expression of the Sequence $(\hat{\sigma}_{(i)}^2)$ under \mathbb{H}_0 . The convergence of the algorithm is now going to be proved, and its limit characterized. To this end, we will first obtain a scalar expression of the sequence $(\hat{\sigma}_{(i)}^2)$. We use the Hermitian property of $\tilde{\mathbf{R}}_H^{\text{LS}} = (\tilde{\mathbf{R}}_H^{\text{LS}})^H$, and we develop (12) with (10) to get

$$\begin{aligned} \tilde{\mathbf{R}}_H^{\text{LMMSE}} &= \hat{\mathbf{H}}_{(i=1)}^{\text{LMMSE}}(\hat{\mathbf{H}}_{(i=1)}^{\text{LMMSE}})^H \\ &= \tilde{\mathbf{R}}_H^{\text{LS}} \left(\tilde{\mathbf{R}}_H^{\text{LS}} + \hat{\sigma}_{(i=0)}^2 \mathbf{I} \right)^{-1} \hat{\mathbf{H}}^{\text{LS}} \\ &\quad \times \left(\tilde{\mathbf{R}}_H^{\text{LS}} \left(\tilde{\mathbf{R}}_H^{\text{LS}} + \hat{\sigma}_{(i=0)}^2 \mathbf{I} \right)^{-1} \hat{\mathbf{H}}^{\text{LS}} \right)^H \\ &= \tilde{\mathbf{R}}_H^{\text{LS}} \left(\tilde{\mathbf{R}}_H^{\text{LS}} + \hat{\sigma}_{(i=0)}^2 \mathbf{I} \right)^{-1} \hat{\mathbf{H}}^{\text{LS}} (\hat{\mathbf{H}}^{\text{LS}})^H \\ &\quad \times \left(\tilde{\mathbf{R}}_H^{\text{LS}} \left(\tilde{\mathbf{R}}_H^{\text{LS}} + \hat{\sigma}_{(i=0)}^2 \mathbf{I} \right)^{-1} \right). \end{aligned} \quad (15)$$

Let us assume that M is large enough to justify the approximation $\text{tr}(\mathbf{W}\mathbf{W}^H) = \text{tr}(\sigma^2 \mathbf{I})$. Since the estimation of the noise variance is calculated by means of the trace in (14), we make the assumption that as a first approximation $\tilde{\mathbf{R}}_H^{\text{LS}} \approx \sigma^2 \mathbf{I}$, and then it is possible to replace $\tilde{\mathbf{R}}_H^{\text{LMMSE}}$ by

$$\begin{aligned} \tilde{\mathbf{R}}_H^{\text{LMMSE}} &= \sigma^2 \mathbf{I} (\sigma^2 \mathbf{I} + \hat{\sigma}_{(i=0)}^2 \mathbf{I})^{-1} \tilde{\mathbf{R}}_H^{\text{LS}} (\sigma^2 \mathbf{I} (\sigma^2 \mathbf{I} + \hat{\sigma}_{(i=0)}^2 \mathbf{I})^{-1}) \\ &= \frac{\sigma^6}{(\sigma^2 + \hat{\sigma}_{(i=0)}^2)^2} \mathbf{I} \end{aligned} \quad (16)$$

in (14). Thus, by reinjecting (16) in (13) and (14), it yields

$$\begin{aligned}
\hat{\sigma}_{(i+1)}^2 &= \frac{1}{M} E \left\{ \left\| \hat{\mathbf{H}}^{\text{LS}} - \hat{\mathbf{H}}_{(i+1)}^{\text{LMMSE}} \right\|^2 \right\} \\
&= \frac{1}{M} E \left\{ \left\| \hat{\mathbf{H}}^{\text{LS}} - \hat{\mathbf{R}}_H^{\text{LMMSE}} \right. \right. \\
&\quad \times \left(\hat{\mathbf{R}}_H^{\text{LMMSE}} + \hat{\sigma}_{(i)}^2 \mathbf{I} \right)^{-1} \hat{\mathbf{H}}^{\text{LS}} \left. \left. \right\|^2 \right\} \\
&= \frac{1}{M} E \left\{ \left\| \mathbf{W} - \frac{\sigma^6}{(\sigma^2 + \hat{\sigma}_{(i=0)}^2)^2} \mathbf{I} \right. \right. \\
&\quad \times \left(\frac{\sigma^6}{(\sigma^2 + \hat{\sigma}_{(i=0)}^2)^2} \mathbf{I} + \hat{\sigma}_{(i)}^2 \mathbf{I} \right)^{-1} \mathbf{W} \left. \left. \right\|^2 \right\} \quad (17) \\
&= \frac{1}{M} E \left\{ \left\| \left(\hat{\sigma}_{(i)}^2 \mathbf{I} \left(\left(\frac{\sigma^6}{(\sigma^2 + \hat{\sigma}_{(i=0)}^2)^2} \right. \right. \right. \right. \right. \\
&\quad \left. \left. \left. + \hat{\sigma}_{(i)}^2 \right) \mathbf{I} \right)^{-1} \right) \mathbf{W} \right\|^2 \right\} \\
&= \frac{\sigma^2 \hat{\sigma}_{(i)}^4 (\sigma^2 + \hat{\sigma}_{(i=0)}^2)^4}{(\sigma^6 + \hat{\sigma}_{(i)}^2 (\sigma^2 + \hat{\sigma}_{(i=0)}^2)^2)^2}.
\end{aligned}$$

For a better readability, we note the following mathematical developments:

$$A = \sigma^2 + \hat{\sigma}_{(i=0)}^2. \quad (18)$$

3.3. Convergence of the Sequence $(\hat{\sigma}_{(i)}^2)$ to a Nonnull Solution. One can observe that the sequence $(\hat{\sigma}_{(i+1)}^2)$ is built from a function f_{s1} such that if we note $x = \hat{\sigma}_{(i)}^2$, we have

$$f_{s1}(x) = \frac{\sigma^2 A^4 x^2}{(\sigma^6 + A^2 x)^2}. \quad (19)$$

The sequence converges if f_{s1} has at least one fixed point. Zero is an obvious fixed point, but it has been proved in the Appendix that the algorithm enters into an endless loop if $(\hat{\sigma}_{(i)}^2)$ converges to zero. We then solve the equation $f_{s1}(x) = x$ to find the other fixed points:

$$\begin{aligned}
f_{s1}(x) &= x \\
\iff \frac{\sigma^2 A^4 x^2}{(\sigma^6 + A^2 x)^2} &= x \quad (20) \\
\iff \sigma^2 A^4 x^2 &= x(\sigma^6 + A^2 x)^2.
\end{aligned}$$

Since we exclude zero as a solution, the previous expressions can be simplified by x , and the problem amounts to look

for real roots of the polynomial $A^4 x^2 + x(2A^2 \sigma^6 - \sigma^2 A^4) + \sigma^{12}$. Since it is a second order polynomial, in order to find real solutions, the first condition on the initialization $\hat{\sigma}_{(i=0)}^2$ is to obtain the discriminant $\Delta = (2A^2 \sigma^6 - \sigma^2 A^4)^2 - 4A^4 \sigma^{12}$ positive; that is,

$$\begin{aligned}
\Delta \geq 0 &\iff (2A^2 \sigma^6 - \sigma^2 A^4)^2 \geq 4A^4 \sigma^{12} \\
&\iff A^2 \geq 4\sigma^4 \\
&\iff (\sigma^2 + \hat{\sigma}_{(i=0)}^2)^2 \geq 4\sigma^4 \\
&\iff \hat{\sigma}_{(i=0)}^2 \geq 3\sigma^2.
\end{aligned} \quad (21)$$

As σ^2 is absolutely unknown, one can find a stronger condition on $\hat{\sigma}_{(i=0)}^2$, conditionally to $\Delta > 0$. We then find the roots r_s^+ and r_{s-} of the polynomial under the condition $\Delta > 0$:

$$\begin{aligned}
r_{s-}^+ &= \frac{(\sigma^2 A^4 - 2A^2 \sigma^6) \pm \sqrt{(2A^2 \sigma^6 - \sigma^2 A^4)^2 - 4A^4 \sigma^{12}}}{2A^4} \\
&\iff r_{s-}^+ = \frac{(\sigma^2 A^2 - 2\sigma^6) \pm \sqrt{\sigma^4 A^4 - 4\sigma^8 A^2}}{2A^2}.
\end{aligned} \quad (22)$$

If we notice that when $\hat{\sigma}_{(i=0)}^2$ tends to $+\infty$, then $A = \sigma^2 + \hat{\sigma}_{(i=0)}^2$ also tends to $+\infty$, we get

$$\begin{aligned}
\lim_{A \rightarrow \infty} r_s^+ &= \frac{\sigma^2 A^2 + \sigma^2 A^2}{2A^2} = \sigma^2, \\
\lim_{A \rightarrow \infty} r_{s-} &= \frac{\sigma^2 A^2 - \sigma^2 A^2}{2A^2} = 0.
\end{aligned} \quad (23)$$

It can be seen that by choosing a sufficiently large initialization value $\hat{\sigma}_{(i=0)}^2$, the sequence $(\hat{\sigma}_{(i)}^2)$ converges to a value as close as possible to the exact value of the noise variance σ^2 . This characterization of the initialization value $\hat{\sigma}_{(i=0)}^2$ perfectly tallies with the one made for the sufficient condition in [20]; that is, $\hat{\sigma}_{(i=0)}^2 \gg M_2$. Moreover, it will be further shown that this condition allows to differentiate \mathbb{H}_0 from \mathbb{H}_1 . Thus, choosing $\hat{\sigma}_{(i=0)}^2$ with a large value is the condition for the algorithm to converge to a nonnull solution for both hypotheses \mathbb{H}_0 and \mathbb{H}_1 . Besides that, since it converges, the stopping criterion $|\hat{\sigma}_{(i)}^2 - \hat{\sigma}_{(i-1)}^2| < e_\sigma$ can also be the same under \mathbb{H}_0 . Finally, the MMSE-based algorithm can be used as a free band detector.

Figure 3 displays the function f_{s1} for different values of $(\hat{\sigma}_{(i=0)}^2)$, compared with $y = x$ and for a fixed value $\sigma^2 = 1$. By comparing the curves of f_{s1} for different initializations values, we verify that the larger the value of $\hat{\sigma}_{(i=0)}^2$, the closer $\hat{\sigma}_{(i_f)}^2$ to the real value of σ^2 .

4. Proposed Detector

4.1. Decision Rule for the Proposed Detector. In this section, a decision rule for the detector is proposed. To this end, whatever \mathbb{H}_0 or \mathbb{H}_1 , it is supposed that the algorithm has

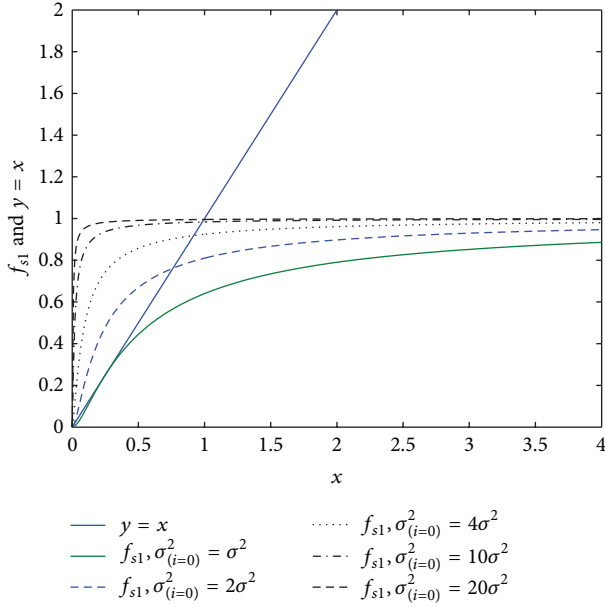


FIGURE 3: Aspect of f_{s1} for different values of $\sigma_{(0)}^2$, $\sigma^2 = 1$ compared with $y = x$.

converged; that is, the condition $|\hat{\sigma}_{(i)}^2 - \hat{\sigma}_{(i-1)}^2| < e_\sigma$ is reached and then $i = i_f$. The second-order moment $M_2 = (1/M) \sum_{m=0}^{M-1} |U_m|^2$ of the received signal is expressed under the hypotheses \mathbb{H}_0 and \mathbb{H}_1 :

$$M_2 = \begin{cases} \frac{1}{M} \sum_{m=0}^{M-1} |W_m|^2, & \text{if } \mathbb{H}_0 \\ \frac{1}{M} \sum_{m=0}^{M-1} |C_m H_m + W_m|^2, & \text{if } \mathbb{H}_1. \end{cases} \quad (24)$$

The second-order moment M_2 is the decision metric used for the energy detector. Here, a different metric noted \mathcal{M} is proposed and defined by

$$\mathcal{M} = |M_2 - \hat{\sigma}^2|, \quad (25)$$

where $\hat{\sigma}^2 = \hat{\sigma}_{(i_f)}^2$ is the noise variance estimation performed by the proposed iterative algorithm. From (24), the metric (25) is rewritten according to the hypotheses \mathbb{H}_0 and \mathbb{H}_1 :

$$\mathcal{M} = \begin{cases} \left| \frac{1}{M} \sum_{m=0}^{M-1} |W_m|^2 - \hat{\sigma}^2 \right|, & \text{under } \mathbb{H}_0 \\ \left| \frac{1}{M} \sum_{m=0}^{M-1} |C_m H_m + W_m|^2 - \hat{\sigma}^2 \right|, & \text{under } \mathbb{H}_1. \end{cases} \quad (26)$$

By fixing a threshold ς , the decision criterion is now

$$\begin{aligned} &\mathbb{H}_0, && \text{if } \mathcal{M} < \varsigma, \\ &\mathbb{H}_1, && \text{else.} \end{aligned} \quad (27)$$

The detection and false alarm probabilities are defined by

$$\begin{aligned} P_d &= P(\mathcal{M} > \varsigma \mid \mathbb{H}_1), \\ P_{fa} &= P(\mathcal{M} > \varsigma \mid \mathbb{H}_0). \end{aligned} \quad (28)$$

The detection probability P_d is the probability to decide \mathbb{H}_1 while the PU is present, and the false alarm probability P_{fa} is the probability to decide \mathbb{H}_1 while the PU is absent. As mentioned in [6, 25], the sensibility of the detector (the expected value of P_{fa} and P_d) depends on the application. In a cognitive radio context, the SU has to minimize the interference with the PU, so the probability of detection has to be maximized, whereas if the false alarm probability is not optimized, it only implies that the SU misses white spaces. On the contrary, in a radar application, a false alarm could have serious consequences, especially in a military context.

4.2. Expression of the Proposed Detector. By taking into account the previous decision rule, it is possible to extend the practical algorithm proposed in the scenario of the joint estimation of the SNR and the channel for free band detections, as it is summed up in Algorithm 1.

It can be seen that the structure of Algorithm 1 is similar to the one of [20] and summarized in Section 2.2, but with a detection part. Thus, compared to the methods of the literature, the proposed one not only returns the decision \mathbb{H}_0 and \mathbb{H}_1 but also provides

- (i) the noise variance estimation, if \mathbb{H}_0 ;
- (ii) the channel and SNR estimations, if \mathbb{H}_1 .

An a priori qualitative analysis of the detector can be done. Indeed, from (26), one can deduce that by supposing a good estimation of $\hat{\sigma}^2$, \mathcal{M} tends to a value close to zero under \mathbb{H}_0 and to a value close to P_s under \mathbb{H}_1 . By supposing a normalized signal power, one can suppose that choosing a value ς between zero and one allows getting a viable detector. Concerning the value of the threshold e_σ , since it ensures the convergence of the algorithm, it has no effect on the detector performance. This property will be shown by simulations afterward.

In the context of cognitive radio, the SUs have to target a given detection probability, noted P_d^t . Thus, according to the Neyman-Pearson criterion [26], the best value of the threshold ς can be analytically derived (when it is possible) by solving $P(\mathcal{M} > \varsigma \mid \mathbb{H}_1) \geq P_d^t$ and by maximizing the likelihood ratio test (LRT)

$$\Lambda(x) = \frac{p(x \mid \mathbb{H}_1)}{p(x \mid \mathbb{H}_0)} \underset{\mathbb{H}_0}{\overset{\mathbb{H}_1}{\geq}} \varsigma. \quad (29)$$

To this end, the probability density functions (pdfs) of \mathcal{M} have to be expressed, which is proposed in the next section.

```

begin
  Initialization:  $\tilde{\mathbf{R}}_H^{\text{LS}}, e_\sigma > 0, \hat{\sigma}_{(i=0)}^2$  and  $\varsigma$ ;
   $i \leftarrow 1$ ;
  while  $|\hat{\sigma}_{(i)}^2 - \hat{\sigma}_{(i-1)}^2| > e_\sigma$  do
    if  $i = 1$  then
      Perform LMMSE channel estimation;
      Perform the noise variance estimation;
      Calculate the matrix  $\tilde{\mathbf{R}}_H^{\text{LMMSE}}$ ;
    else
      Perform an LMMSE channel estimation with  $\tilde{\mathbf{R}}_H^{\text{LMMSE}}$ ;
      Perform the noise variance estimation;
    end
     $i \leftarrow i + 1$ ;
  end
  Calculate the metric  $\mathcal{M}$ ;
  if  $\mathcal{M} < \varsigma$  then
    return  $\mathbb{H}_0$ ;
  else
    return  $\mathbb{H}_1$ ;
  end
end

```

ALGORITHM 1: Application of the MMSE-based algorithm to free band detection.

5. Detection and False Alarm Probabilities

5.1. Probability Density Function of \mathcal{M} under \mathbb{H}_1 . Under the hypothesis \mathbb{H}_1 , since it is proved in [20] that the noise variance estimation is very accurate, it is reasonable to suppose that the noise variance estimation is good enough to consider that $\hat{\sigma}^2 \approx (1/M) \sum_{m=0}^{M-1} |W_m|^2$, so the contribution of $C_m H_m$ is prevailing in \mathcal{M} (26) so that

$$\begin{aligned} \mathcal{M} &= \left| \frac{1}{M} \sum_{m=0}^{M-1} (|C_m H_m + W_m|^2) - \hat{\sigma}^2 \right| \\ &= \left| \frac{1}{M} \sum_{m=0}^{M-1} (|C_m H_m|^2 + |W_m|^2 + \text{CF}_m) - \hat{\sigma}^2 \right|, \end{aligned} \quad (30)$$

where $\forall m = 0, \dots, M-1$, CF_m are the cross-factors $(C_m H_m W_m^*) + (C_m H_m W_m^*)^*$, whose means (for a sufficiently large value of M) are equal to zero, since H_m and W_m are zero-mean uncorrelated Gaussian processes. The development of (30) then simply yields

$$\begin{aligned} \mathcal{M} &= \left| \frac{1}{M} \sum_{m=0}^{M-1} |C_m H_m|^2 + |W_m|^2 - \hat{\sigma}^2 \right| \\ &= \frac{1}{M} \sum_{m=0}^{M-1} |H_m C_m|^2. \end{aligned} \quad (31)$$

The result in (31) obtained with the approximation $\hat{\sigma}^2 \approx (1/M) \sum_{m=0}^{M-1} |W_m|^2$ may be debated, since it has been proved in [20] that the noise estimation under hypothesis \mathbb{H}_1 is slightly biased. However, it will be shown in Section 6 that this approximation is accurate for low values of σ^2 . From

the channel frequency response expression (2) and remembering that $C_m C_m^* = 1$, the metric (31) can be rewritten by

$$\begin{aligned} \mathcal{M} &= \frac{1}{M} \sum_{m=0}^{M-1} \left| \sum_{l=0}^{L-1} h_l \exp \left(-2j\pi \frac{m\beta_l}{M} \right) C_m \right|^2 \\ &= \frac{1}{M} \sum_{m=0}^{M-1} \left(\sum_{l_1=0}^{L-1} h_{l_1} \exp \left(-2j\pi \frac{m\beta_{l_1}}{M} \right) C_m \right) \\ &\quad \times \left(\sum_{l_2=0}^{L-1} h_{l_2} \exp \left(-2j\pi \frac{m\beta_{l_2}}{M} \right) C_m \right)^* \\ &= \sum_{l=0}^{L-1} |h_l|^2 \\ &\quad + \frac{1}{M} \sum_{m=0}^{M-1} \sum_{l_1=0}^{L-1} \sum_{\substack{l_2=0 \\ l_2 \neq l_1}}^{L-1} h_{l_1} h_{l_2}^* \exp \left(-2j\pi \frac{m(\beta_{l_1} - \beta_{l_2})}{M} \right). \end{aligned} \quad (32)$$

According to the Rayleigh distributed WSSUS channel model, whatever $l = 0, \dots, L-1$, the gains h_l are uncorrelated zero-mean Gaussian processes. For a large enough value M , let us assume that the mean of the cross-factors of the right side in (32) are equal to zero. Finally, the metric \mathcal{M} is simply written as follows:

$$\mathcal{M} = \sum_{l=0}^{L-1} |h_l|^2, \quad \text{under } \mathbb{H}_1. \quad (33)$$

\mathcal{M} then follows a chi-square distribution with $2L$ degrees of freedom. The probability density function (pdf) noted $p_{\mathcal{M}}(x)$ of the decision statistic under \mathbb{H}_1 is then expressed by

$$p_{\mathcal{M}}(x) = \frac{1}{2^L P_s^L \Gamma(L)} x^{L-1} \exp\left(-\frac{x}{2P_s}\right), \quad \text{under } \mathbb{H}_1, \quad (34)$$

where $\Gamma(\cdot)$ is the gamma function [27].

5.2. Probability Density Function of \mathcal{M} under \mathbb{H}_0 . The theoretical probability density function (pdf) expression of the metric under the hypothesis \mathbb{H}_0

$$\mathcal{M} = \left| \frac{1}{M} \sum_{m=0}^{M-1} |W_m|^2 - \hat{\sigma}_{(i)}^2 \right| \quad (35)$$

is now developed. To this end, let us assume that the initialization value of the algorithm is chosen large enough to state $\hat{\sigma}^2 \approx \sigma^2$, in accordance with the previously formulated hypotheses in Section 3.3. Whatever $m = 0, \dots, M-1$, each sample W_m follows a zero-mean Gaussian process with variance σ^2 ; $|W_m|^2$ has a chi-square distribution χ_2^2 with a degree of liberty equal to 2:

$$\chi_2^2(x) = \frac{1}{\sigma^2} e^{-x/\sigma^2}. \quad (36)$$

The mean and the variance of this distribution are equal to σ^2 and σ^4 , respectively. In an OFDM context, we reasonably suppose that M is large enough (e.g., $M > 100$) to consider that from the central limit theorem $(1/M) \sum_{m=0}^{M-1} |W_m|^2$ follows a normal distribution $\mathcal{N} \sim (\sigma^2, \sigma^4/M)$, and then $(1/M) \sum_{m=0}^{M-1} |W_m|^2 - \hat{\sigma}^2$ follows a centered normal distribution $\mathcal{N} \sim (0, \sigma^4/M)$. Consequently, the metric $\mathcal{M} = |(1/M) \sum_{m=0}^{M-1} |W_m|^2 - \hat{\sigma}_{(i)}^2|$ has a chi distribution χ_1 with one degree of liberty:

$$p_{\mathcal{M}}(x) = \frac{\sqrt{2}}{\Gamma(1/2) \sqrt{\sigma^4/M}} \exp\left(-\frac{1}{2} \left(\frac{x}{\sqrt{\sigma^4/M}}\right)^2\right), \quad (37)$$

under \mathbb{H}_0 .

As a conclusion, the probability density functions of the metric \mathcal{M} , according to \mathbb{H}_0 and \mathbb{H}_1 , are given by

$$p_{\mathcal{M}}(x) = \begin{cases} \frac{\sqrt{2}}{\Gamma(1/2) \sqrt{\sigma^4/M}} \exp\left(-\frac{1}{2} \left(\frac{x}{\sqrt{\sigma^4/M}}\right)^2\right), & \text{under } \mathbb{H}_0 \\ \frac{1}{2^L P_s^L \Gamma(L)} x^{L-1} \exp\left(-\frac{x}{2P_s}\right), & \text{under } \mathbb{H}_1. \end{cases} \quad (38)$$

5.3. Analytical Expressions of P_d and P_{fa} . The detection and false alarm probabilities P_d and P_{fa} are obtained by

TABLE 1: Table of parameters of the channel model.

| | Channel model | | | |
|-------|---------------|--------|--------|--------|
| | Path 1 | Path 2 | Path 3 | Path 4 |
| Delay | 0 ms | 0.7 ms | 1.5 ms | 2.2 ms |
| Gain | 0.7448 | 0.5214 | 0.3724 | 0.1862 |

integrating (38) between the fixed threshold ς and $+\infty$. For the calculation of P_d , the solution is derived in [28, 29]:

$$\begin{aligned} P_d &= P(\mathcal{M} > \varsigma \mid \mathbb{H}_1) \\ &= \int_{\varsigma}^{+\infty} \frac{x^{L-1}}{2^L P_s^L \Gamma(L)} \exp\left(-\frac{x}{2P_s}\right) dx \\ &= \frac{\Gamma(L, \varsigma/2P_s)}{\Gamma(L)}, \end{aligned} \quad (39)$$

where $\Gamma(\cdot, \cdot)$ is the incomplete gamma function [27]. In the case \mathbb{H}_0 , we have

$$\begin{aligned} P_{fa} &= \int_{\varsigma}^{+\infty} p_{\mathcal{M}}(x) dx \\ &= \int_{\varsigma/\sqrt{2\sigma^4/M}}^{+\infty} \frac{\sqrt{2}}{\Gamma(1/2) \sqrt{\sigma^4/M}} e^{-(1/2)(x/\sqrt{\sigma^4/M})^2} dX. \end{aligned} \quad (40)$$

By using the variable change $X = x/\sqrt{2\sigma^4/M}$ and knowing that $\Gamma(1/2) = \sqrt{\pi}$, one can recognize the complementary error function $\text{erfc}(x) = 1 - \text{erf}(x)$:

$$P_{fa} = \int_{\varsigma/\sqrt{2\sigma^4/M}}^{+\infty} \frac{2}{\sqrt{\pi}} e^{-X^2} dX = \text{erfc}\left(\frac{\varsigma\sqrt{M}}{\sqrt{2}\sigma^2}\right). \quad (41)$$

Since the incomplete gamma function is not directly invertible in (39), it is not possible to derive an analytical expression of the threshold ς in function of the targeted detection probability P_d^t . However, an approximation by means of a computer calculation or a series expansion of the invert of (39) or a simple characterization of ς by simulations can be done. We will consider this third solution thereafter. Furthermore, the next section aims to characterize the performance of the proposed detection algorithm and the validity of the proposed analytical developments.

6. Simulations Results

6.1. Simulations Parameters. The signal parameters used for the simulations are based on those of the digital radio mondiale (DRM/DRM+) standard [30]. This standard designs the digital radio broadcasting over the current AM/FM bands. When it is transmitted, the signal is composed of 148 independent carriers. The symbol and the cyclic prefix durations are 14.66 ms and 5.33 ms, respectively. Although the DRM standard recommends a pilot distribution in staggered rows, we consider a block-type pilot arrangement, according to the model used in [20]. The channel used in the presence of a PU is based on the *US Consortium* model of the DRM/DRM+ standard, whose path gains are normalized. The channel parameters are summed up in Table 1.

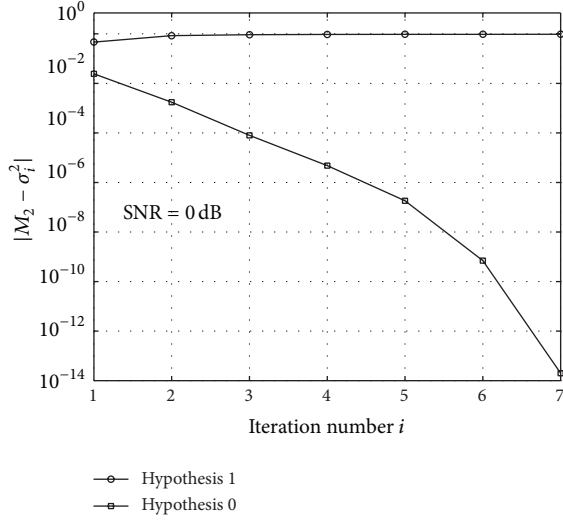


FIGURE 4: $|M_2 - \hat{\sigma}^2|$ versus the iteration number under \mathbb{H}_0 and \mathbb{H}_1 , for SNR = 0 dB.

6.2. Choice of the Threshold ς . Figure 4 depicts the metric $\mathcal{M} = |M_2 - \hat{\sigma}^2|$ versus the number of iterations, under the hypotheses \mathbb{H}_0 and \mathbb{H}_1 . The SNR is fixed equal to 0 dB. In presence of signal, the average signal power P_s is equal to 1. The simulation is performed by means of 4000 simulation runs.

It can be seen that the a priori qualitative analysis is verified. Indeed, for a sufficient number of iterations (according to the value e_σ , as shown thereafter), \mathcal{M} converges to P_s under \mathbb{H}_1 and converges toward zero under \mathbb{H}_0 . It has been noticed that it is not possible to find an exact value of ς according to $P(\mathcal{M} > \varsigma \mid \mathbb{H}_1) = P_d^t$. However, it is observable on Figure 4 that the choice of the threshold is not restrictive. Indeed, choosing ς as small as expected ensures a probability P_d close to one, and, for a sufficient number of iterations, it also ensures a low value for P_{fa} . Nevertheless, reducing the value of e_σ increases the number of required iterations, as shown in the following. Hence, for an expected detection probability, a tradeoff between the complexity and the acceptable level of false alarm probability has to be taken into account, since each iteration requires $\mathcal{O}(i_f M^3)$ operations.

6.3. Effect of the Choice of e_σ on the Detector Performance. It is shown in this section that the choice of the threshold e_σ value does not have any effect on the detection performance of the proposed method but only impacts the convergence speed of the algorithm. Figure 5 depicts the curves of detection and false alarm probabilities P_d and P_{fa} versus the SNR from -15 dB to 10 dB. In order to ensure the convergence of the algorithm, e_σ must have a low value. The subfigures (a) and (b) then depict the curves P_d and P_{fa} for $e_\sigma = 0.01$ and $e_\sigma = 0.0001$, respectively. According to the previous recommendations, the initialization $\sigma_{(i=0)}^2$ is equal to $40 \times M_2$. We also arbitrarily fix the threshold $\varsigma = 0.01$, its effect on the detection performance being further studied. The figure is obtained thanks to 2000 simulation runs.

We observe that the curves of P_d and P_{fa} match from Figures 5(a) to 5(b). P_{fa} is equal to zero or nearly for all SNR values and P_d reaches one from SNR = -5 dB. The detector can then reach the perfect one from SNR ≥ -5 dB, that is, in low SNR environment. We conclude that, assuming a value of e_σ low enough to ensure the convergence of the algorithm, this threshold does not have any effect on the detection performance of the proposed method.

Figure 6 displays the iterations number the algorithm needs before it stops versus the SNR from -10 to 10 dB. We consider three different values for the threshold: $e_\sigma = 0.01$, 0.001, and 0.0001. The simulations conditions remain the same.

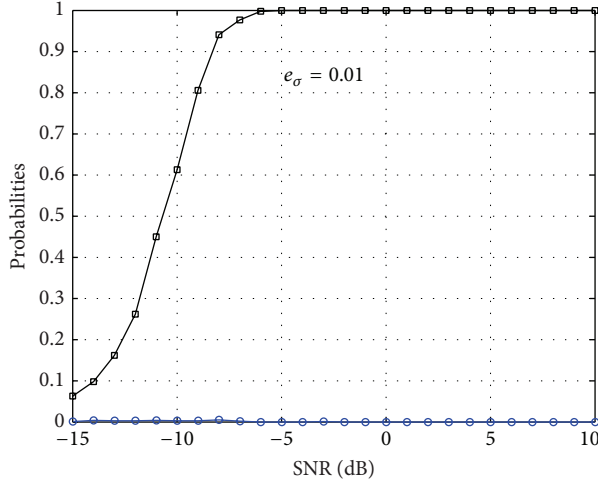
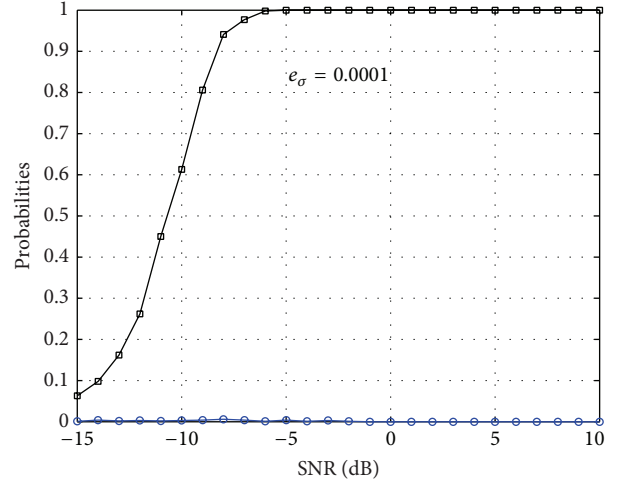
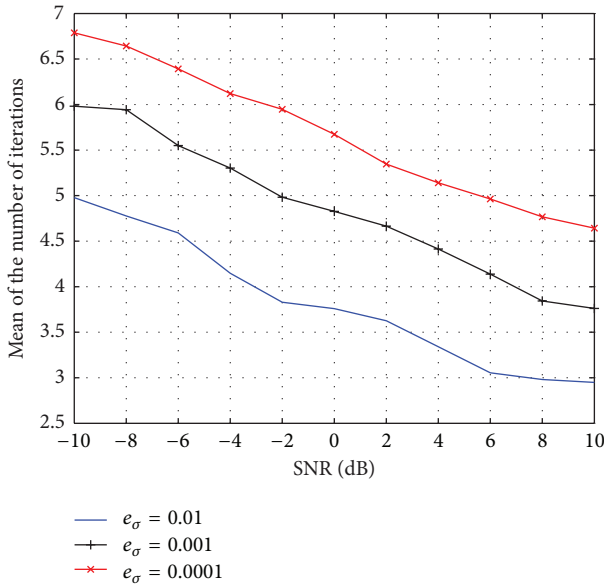
Although Figures 5(a) and 5(b) display almost the same probabilities whatever the threshold e_σ , they differ from each other according to the number of iterations the algorithm requires before stopping. Indeed, remembering that we compare $|\hat{\sigma}_{(i)}^2 - \hat{\sigma}_{(i-1)}^2|$ with e_σ , the lower e_σ , the larger the number i of iterations needed to reach e_σ . However, Figure 6 shows that the maximum mean of iterations is less than 7 for SNR = -10 dB and shows the maximum mean of iterations is less than 5 for SNR = -10 dB and $e_\sigma = 0.0001$, which is a reasonable number of iterations. We conclude that the choice of e_σ has no effect on the detector efficiency, while it allows the convergence of the algorithm. Besides this result, the number of required iterations reasonably increases when e_σ and the SNR have low values. The detector then remains usable in practice under these conditions.

6.4. Detector Performance with Channel Uncertainty. In this part, we study the behavior of the proposed detector when a non-WSS channel is considered. To this end, we artificially correlate the different paths by inserting the gain h_0 into the other path gains. Thus, from the originally created channel impulse response $[h_0, \dots, h_{L-1}]$ with independent paths, we build a new correlated vector $[h_0, \dots, \tilde{h}_1, \dots, \tilde{h}_{L-1}]$ such that, for $l = 1, \dots, L-1$, we define a correlation coefficient ρ_h by

$$\rho_h = \frac{E \{h_0 \tilde{h}_l^*\}}{\sigma_0 \tilde{\sigma}_l}, \quad (42)$$

where $\tilde{h}_l = h_l + \alpha_l h_0$, α_l being a coefficient that is calculated in function of the expected ρ_h , and σ_0^2 and $\tilde{\sigma}_l^2$ are the variances of h_0 and \tilde{h}_l , respectively. Figure 7 displays the detection probability P_d versus the SNR for the proposed detection under a channel correlation condition. Three curves are considered: the reference ($\rho_h = 0$) and two correlated channels with $\rho_h = 0.1$ and $\rho_h = 0.5$. We observe a limited gap of 1 dB between the reference curve and the two others. We conclude that the proposed detector is robust against the channel uncertainty.

6.5. Receiver Operating Characteristic of the Detector. The performance of a detector is usually evaluated by means of the receiver operating characteristic (ROC) curves, depicting the detection probability P_d in function of the false alarm probability P_{fa} . The optimal detector is logically reached at the point ($P_{fa} = 0, P_d = 1$). The curve $P_{fa} = P_d$ is called line

(a) P_d and P_{fa} versus SNR, for $e_\sigma = 0.01$ (b) P_d and P_{fa} versus SNR, for $e_\sigma = 0.0001$ FIGURE 5: Detection and false alarm probabilities versus SNR, for two values e_σ and for a fixed value $\zeta = 0.01$.FIGURE 6: Means of the number of iterations needed by the algorithm to stop versus SNR (in dB), for three values of threshold e_σ .

of chance and corresponds to a detector that makes as much good decisions as false alarms. If the ROC curve is above the first bisector, the detector is efficient, since $P_d > P_{fa}$.

Figure 8 shows the ROC curves of the proposed detector for low SNR values (-10 dB and $\text{SNR} = 0$ dB). It is compared to the energy detector and the second-order moment-based MME [31]. The simulations conditions remain the same, and we fix the threshold $e_\sigma = 0.01$. In Figure 8(a), the proposed detector is compared to the usual energy detector, whose metric \mathcal{M} is equal to the second order-moment of

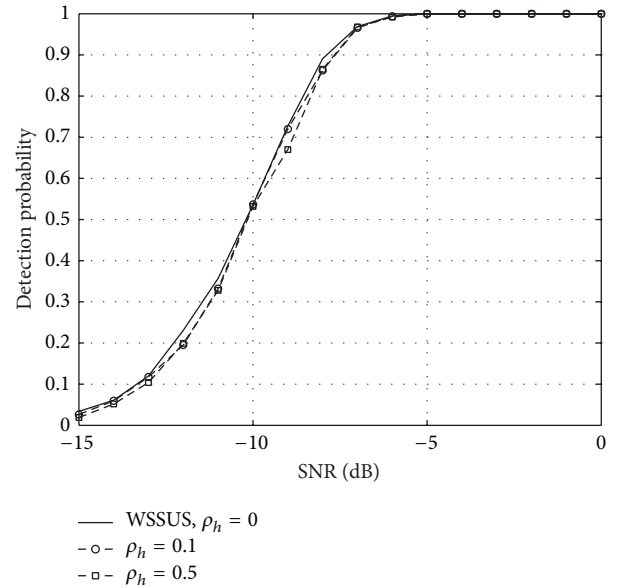


FIGURE 7: Detection probability versus SNR for a non-WSSUS channel.

the received signal M_2 . This metric is compared to a threshold ζ_e to obtain the following decision rule:

$$\begin{aligned} \mathbb{H}_0, & \quad \text{if } \mathcal{M} < \zeta_e \\ \mathbb{H}_1, & \quad \text{else.} \end{aligned} \quad (43)$$

In Figure 8(b), the proposed detector is also compared to the usual MME detector, whose metric \mathcal{M} is equal to the ratio of the maximum and the nonzero minimum eigenvalues of the received signal covariance matrix \mathbf{R} ; that is, $\mathcal{M} = \lambda_{\max}/\lambda_{\min}$. The same aforementioned decision rule

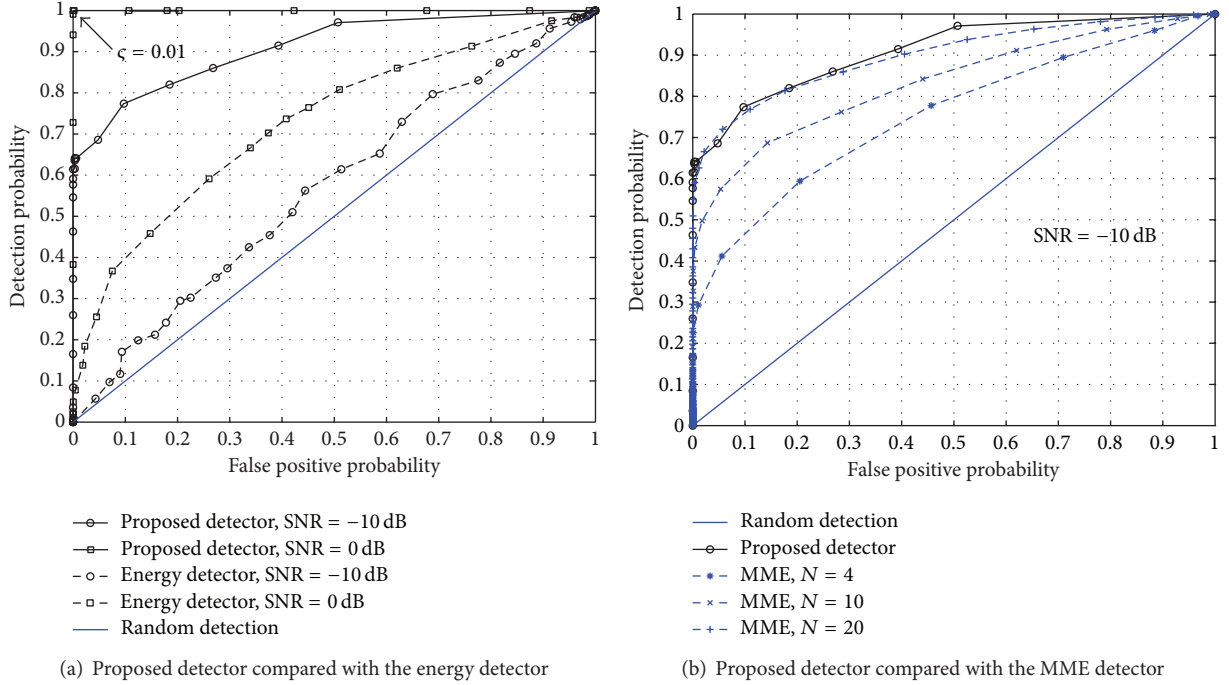


FIGURE 8: Receiver operating characteristic (ROC) curves of the proposed method compared to the energy and MME detectors.

is used. Since a SISO system is assumed, $\tilde{\mathbf{R}}$ is obtained by concatenating N consecutive OFDM symbols so that $\mathbf{U}_N = [\mathbf{U}_1, \dots, \mathbf{U}_N]$ and then $\tilde{\mathbf{R}} = \mathbf{U}_N \mathbf{U}_N^T$. In that way, $\tilde{\mathbf{R}}$ is equivalent to a system with N sensors. However, due to the nature of the channel, the different received OFDM symbols are correlated. In Figure 8(b), the ROC curves of MME are obtained for $N = 4, 10$, and 20 symbols, and the SNR is equal to -10 dB. Each point of the curves is obtained by means of 2000 simulation runs.

We observe in Figure 8(a) that the proposed detector outperforms the energy detector, whatever the SNR. Indeed, as we consider the detection of a preamble transmitted over a Rayleigh channel, the power of the received signal P_s in (30) is not constant and follows a chi-square distribution. Consequently, for simulations made at a fixed SNR, the noise variance is also a varying process, which deteriorates the detector performance. For additional details about the theoretical development of the energy detection of signals with random amplitude, please refer to [28, 29]. We also may explain the performance of our detector by the fact that we use the same sensing time to compare the energy detector and the proposed algorithm, that is, only one OFDM symbol length. The 148 samples of one OFDM symbol are not enough to obtain an accurate energy detector. Figure 8(a) also confirms that the proposed detector is very efficient, since it is able to reach the perfect detector for $\zeta = 0.01$. Indeed, for SNR = 0 dB, we observe that the ROC curve reaches the point $(P_{fa} = 0, P_d = 1)$, as we remarked in Figures 5(a) and 5(b) for SNR ≥ -5 dB. In Figure 8(b), we observe that MME requires $N = 20$ symbols to reach the performance of the proposed method, because MME is efficient for a very large size of \mathbf{U}_N , and the vectors of the latter matrix are correlated. Thus, for

a given performance, the complexity of MME is $\mathcal{O}(NM^2)$ (for the computation and the diagonalization of $\tilde{\mathbf{R}}$) and the one of the proposed algorithm is $\mathcal{O}(i_f M^3)$. Since we reasonably have $N < i_f M$, we conclude that the iterative method is more complex than usual second-order moment-based techniques. However, the proposed algorithm also performs the noise variance estimation if \mathbb{H}_0 and the SNR and channel estimation if \mathbb{H}_1 , which is an advantage by comparison with the techniques of the literature.

Figure 9 compares the ROC curves of the proposed detector given by simulation with the theoretical ones P_d and P_{fa} given by (39) and (41), respectively. We notice that the theoretical curve for SNR = 0 dB is very close to the one obtained by simulation, whereas for SNR = -10 dB, the difference is more noticeable. This observation tallies with the discussion on the approximation $\hat{\sigma}^2 \approx (1/M) \sum_{m=0}^{M-1} |W_m|^2$ in the calculation of the metric \mathcal{M} under the hypothesis \mathbb{H}_1 . Indeed, this approximation is justified for high values of SNR but becomes wrong for the very low SNR values. However, the theoretical curves give an idea of the detector performance for a given SNR, even for low SNR values.

7. Conclusion

In this paper, an iterative algorithm for spectrum sensing in a cognitive radio context has been presented. Originally proposed in [20] for the joint estimation of the noise and the channel, this method is based on the second-order moment of the received signal. In the presence of a primary user (PU), the algorithm estimates the channel and the noise variance. If the PU is not active, the algorithm returns a very accurate estimation of the noise level. By comparing

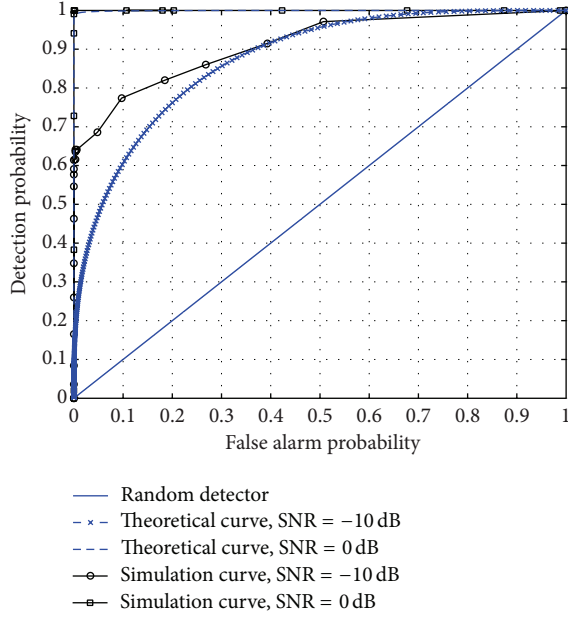


FIGURE 9: Comparison of the receiver operating characteristic (ROC) curves obtained by simulation and in theory.

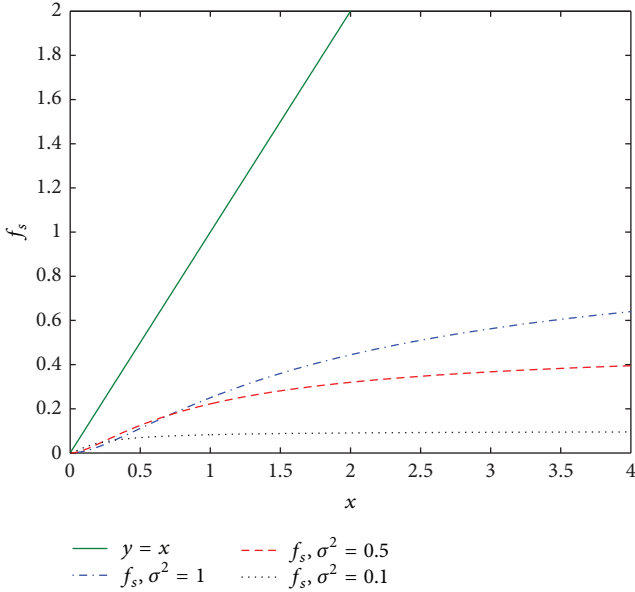


FIGURE 10: Aspect of f for different values of σ^2 compared with $y = x$.

the noise variance to the second moment of the received signal estimation (useful signal with noise or only noise), it is then possible to determine if the PU is present or absent. From that an analytical expression of the detection and false alarm probabilities have been proposed, and it is shown that they are very close to the simulations. It is also shown that the detector reaches the perfect one from very low SNR values. The algorithm offers numerous advantages as it performs a PU detection, the noise variance, and the channel estimation if the PU is active and it returns the noise level in

the frequency band when the PU is absent, without changing the structure proposed in [20]. The future work concerning the detector will focus on the synchronization of the SU on the PU's signal.

Appendix

If the algorithm keeps on computing at each iteration i with the covariance matrix $\tilde{\mathbf{R}}_H^{\text{LS}}$ under hypothesis \mathbb{H}_0 , then we deduce the following for Step 4.

Perform the LMMSE channel estimation

$$\hat{\mathbf{H}}_{(i+1)}^{\text{LMMSE}} = \tilde{\mathbf{R}}_H^{\text{LS}} (\tilde{\mathbf{R}}_H^{\text{LS}} + \hat{\sigma}_{(i)}^2 \mathbf{I})^{-1} \hat{\mathbf{H}}^{\text{LS}}. \quad (\text{A.1})$$

Perform the MMSE noise variance estimation

$$\hat{\sigma}_{(i+1)}^2 = \frac{1}{M} E \left\{ \left\| \hat{\mathbf{H}}^{\text{LS}} - \hat{\mathbf{H}}_{(i+1)}^{\text{LMMSE}} \right\|_F^2 \right\}. \quad (\text{A.2})$$

It is assumed that M is large enough to get $\text{tr}(\mathbf{W}\mathbf{W}^H) = \text{tr}(\sigma^2 \mathbf{I})$. We make in first approximation $\tilde{\mathbf{R}}_H^{\text{LS}} \approx \sigma^2 \mathbf{I}$, so the development of (A.2) yields

$$\begin{aligned} \hat{\sigma}_{(i+1)}^2 &= \frac{1}{M} E \left\{ \left\| \hat{\mathbf{H}}^{\text{LS}} - \hat{\mathbf{H}}_{(i+1)}^{\text{LMMSE}} \right\|_F^2 \right\} \\ &= \frac{1}{M} E \left\{ \left\| \hat{\mathbf{H}}^{\text{LS}} - \tilde{\mathbf{R}}_H^{\text{LS}} (\tilde{\mathbf{R}}_H^{\text{LS}} + \hat{\sigma}_{(i)}^2 \mathbf{I})^{-1} \hat{\mathbf{H}}^{\text{LS}} \right\|_F^2 \right\}, \end{aligned} \quad (\text{A.3})$$

and by factorizing by \mathbf{C}^{-1} :

$$\begin{aligned} &= \frac{1}{M} E \left\{ \left\| \mathbf{W} - \sigma^2 \mathbf{I} (\sigma^2 \mathbf{I} + \hat{\sigma}_{(i)}^2 \mathbf{I})^{-1} \mathbf{W} \right\|_F^2 \right\} \\ &= \frac{1}{M} E \left\{ \left\| (\mathbf{I} - (\sigma^2 + \hat{\sigma}_{(i)}^2 - \hat{\sigma}_{(i)}^2) \mathbf{I}) (\sigma^2 + \hat{\sigma}_{(i)}^2)^{-1} \mathbf{W} \right\|_F^2 \right\} \\ &= \frac{1}{M} E \left\{ \left\| (\hat{\sigma}_{(i)}^2 \mathbf{I}) (\sigma^2 + \hat{\sigma}_{(i)}^2)^{-1} \mathbf{W} \right\|_F^2 \right\} \\ &= \frac{\hat{\sigma}_{(i)}^4}{(\sigma^2 + \hat{\sigma}_{(i)}^2)^2} \frac{1}{M} E \left\{ \left\| \mathbf{W} \right\|_F^2 \right\} \\ &= \frac{\hat{\sigma}_{(i)}^4 \sigma^2}{(\sigma^2 + \hat{\sigma}_{(i)}^2)^2}. \end{aligned} \quad (\text{A.4})$$

The sequence $(\hat{\sigma}_{(i)}^2)$ is built from a function f_s such that if we note $x = \hat{\sigma}_{(i)}^2$, we obtain

$$f_s(x) = \frac{x^2 \sigma^2}{(\sigma^2 + x)^2}, \quad (\text{A.5})$$

with $x \in \mathbb{R}^+$. Figure 10 displays the curve of f_s for different values of σ^2 and compares them with $y = x$.

It is trivial that from the expression of f_s in (A.5) that the only solution of $f_s(x) = x$ is zero. We find the same results as in the case of a received pilot preamble under hypothesis

\mathbb{H}_1 ; that is, if the algorithm is exclusively performed with $\tilde{\mathbf{R}}_H^{LS}$, then the sole limit of $\hat{\sigma}_{(i+1)}^2$ is zero and the algorithm enters into an endless loop. It justifies the change of channel covariance matrix from $\tilde{\mathbf{R}}_H^{LS}$ to $\tilde{\mathbf{R}}_H^{LMMSE}$ under hypothesis \mathbb{H}_1 as well as under hypothesis \mathbb{H}_0 .

Conflict of Interests

The authors declare that there is no conflict of interests regarding the publication of this paper.

References

- [1] Spectrum Efficiency Working Group, "Report of the spectrum efficiency working group," Tech. Rep., Federal Communications Commission, 2002.
- [2] J. Mitola III and G. Q. Maguire Jr., "Cognitive radio: making software radios more personal," *IEEE Personal Communications*, vol. 6, no. 4, pp. 13–18, 1999.
- [3] T. Yücek and H. Arslan, "A survey of spectrum sensing algorithms for cognitive radio applications," *IEEE Communications Surveys and Tutorials*, vol. 11, no. 1, pp. 116–130, 2009.
- [4] L. Lu, X. Zhou, U. Onunkwo, and G. Y. Li, "Ten years of research in spectrum sensing and sharing in cognitive radio," *EURASIP Journal on Wireless Communications and Networking*, vol. 2012, article 28, 2012.
- [5] E. Axell, G. Leus, E. G. Larsson, and H. V. Poor, "Spectrum sensing for cognitive radio: state-of-the-art and recent advances," *IEEE Signal Processing Magazine*, vol. 29, no. 3, pp. 101–116, 2012.
- [6] Z. Khalaf, *Contributions à l'étude de détection des bandes libres dans le contexte de la radio intelligente [Ph.D. thesis]*, Supélec, Rennes, France, 2013.
- [7] R. Tandra and A. Sahai, "SNR walls for signal detection," *IEEE Journal on Selected Topics in Signal Processing*, vol. 2, no. 1, pp. 4–17, 2008.
- [8] W. Jouini, "Energy detection limits under log-normal approximated noise uncertainty," *IEEE Signal Processing Letters*, vol. 18, no. 7, pp. 423–426, 2011.
- [9] J. Proakis and M. Salehi, *Digital Communications*, McGraw-Hill, 2008.
- [10] R. Price and N. Abramson, "Detection theory," *IEEE Transactions on Information Theory*, vol. 7, no. 3, pp. 135–139, 1961.
- [11] A. Sahai, N. Hoven, and R. Tandra, "Some fundamental limits on cognitive radio," *Proceedings of the Forty-Second Allerton Conference on Communication, Control and Computing*, 2004.
- [12] H. Tang, "Some physical layer issues of wide-band cognitive radio systems," in *2005 1st IEEE International Symposium on New Frontiers in Dynamic Spectrum Access Networks, DySPAN 2005*, pp. 151–159, USA, November 2005.
- [13] W. A. Gardner, "Exploitation of spectral redundancy in cyclostationary signals," *IEEE Signal Processing Magazine*, vol. 8, no. 2, pp. 14–36, 1991.
- [14] J. Lundén, V. Koivunen, A. Huttunen, and H. V. Poor, "Spectrum sensing in cognitive radios based on multiple cyclic frequencies," in *Proceedings of the 2nd International Conference on Cognitive Radio Oriented Wireless Networks and Communications (CrownCom '07)*, pp. 37–43, Orlando, Fla, USA, August 2007.
- [15] Z. Khalaf, A. Nafkha, J. Palicot, and M. Ghoszi, "Hybrid spectrum sensing architecture for cognitive radio equipment," in *Proceedings of the 6th Advanced International Conference on Telecommunications (AICT '10)*, pp. 46–51, May 2010.
- [16] L. S. Cardoso, M. Debbah, P. Bianchi, and J. Najim, "Cooperative spectrum sensing using random matrix theory," in *Proceedings of the 3rd International Symposium on Wireless Pervasive Computing (ISWPC '08)*, pp. 334–338, Santorini, Greece, May 2008.
- [17] Y. Zeng and Y.-C. Liang, "Eigenvalue-based spectrum sensing algorithms for cognitive radio," *IEEE Transactions on Communications*, vol. 57, no. 6, pp. 1784–1793, 2009.
- [18] F. Penna and R. Garello, "Theoretical performance analysis of eigenvalue-based detection," <http://arxiv.org/abs/0907.1523>.
- [19] F. Liu, S. Guo, and Y. Sun, "Primary user signal detection based on virtual multiple antennas for cognitive radio networks," *Progress in Electromagnetics Research C*, vol. 42, pp. 213–227, 2013.
- [20] V. Savaux, Y. Louët, M. Djoko-Kouam, and A. Skrzypczak, "Application of a joint and iterative MMSE-based estimation of SNR and frequency selective channel for OFDM systems," *EURASIP Journal on Advances in Signal Processing*, vol. 2013, article 128, 2013.
- [21] P. Bello, "Characterization of randomly time-variant linear channels," *IEEE Transactions on Communications Systems*, vol. 11, no. 4, pp. 360–393, 1963.
- [22] O. Edfors, M. Sandell, J.-J. D. van de Beek, S. K. Wilson, and P. O. Börjesson, "OFDM channel estimation by singular value decomposition," *IEEE Transactions on Communications*, vol. 46, no. 7, pp. 931–939, 1998.
- [23] M. Biguesh and A. B. Gershman, "Downlink channel estimation in cellular systems with antenna arrays at base stations using channel probing with feedback," *Eurasip Journal on Applied Signal Processing*, vol. 2004, no. 9, pp. 1330–1339, 2004.
- [24] S. Kay, *Fundamentals of Statistical Signal Processing: Estimation Theory*, Prentice-Hall, 2003.
- [25] F. Iutzler and P. Ciblat, "Fully distributed signal detection: application to cognitive radio," in *Proceedings of the European Signal Processing Conference (EUSIPCO '13)*, 2013.
- [26] S. M. Kay, *Fundamentals of Statistical Signal Processing: Detection Theory*, vol. 2, Prentice Hall, 1998.
- [27] M. Abramowitz and I. Stegun, *Handbook of Mathematical Functions with Formulas, Graphs, and Mathematical Tables*, Dover, New York, NY, USA, 1970.
- [28] V. I. Kostylev, "Energy detection of a signal with random amplitude," in *Proceedings of the International Conference on Communications (ICC '02)*, vol. 3, pp. 1606–1610, May 2002.
- [29] F. F. Digham, M.-S. Alouini, and M. K. Simon, "On the energy detection of unknown signals over fading channels," *IEEE Transactions on Communications*, vol. 55, no. 1, pp. 21–24, 2007.
- [30] ETSI, "Digital Radio Mondiale (DRM), system specification," Tech. Rep. ES 201 980 V 3.1.1, ETSI, 2009.
- [31] Y. Zeng and Y.-C. Liang, "Spectrum-sensing algorithms for cognitive radio based on statistical covariances," *IEEE Transactions on Vehicular Technology*, vol. 58, no. 4, pp. 1804–1815, 2009.

Review Article

Cognitive Radio Transceivers: RF, Spectrum Sensing, and Learning Algorithms Review

Lise Safatly,¹ Mario Bkassiny,² Mohammed Al-Husseini,³ and Ali El-Hajj¹

¹ ECE Department, American University of Beirut, Beirut 1107 2020, Lebanon

² ECE Department, State University of New York, Oswego, NY 13126, USA

³ Beirut Research & Innovation Center, Lebanese Center for Studies & Research, Beirut 2030 8303, Lebanon

Correspondence should be addressed to Lise Safatly; les12@aub.edu.lb

Received 13 November 2013; Revised 14 January 2014; Accepted 17 January 2014; Published 24 March 2014

Academic Editor: Said E. El-Khamy

Copyright © 2014 Lise Safatly et al. This is an open access article distributed under the Creative Commons Attribution License, which permits unrestricted use, distribution, and reproduction in any medium, provided the original work is properly cited.

A cognitive transceiver is required to opportunistically use vacant spectrum resources licensed to primary users. Thus, it relies on a complete adaptive behavior composed of: reconfigurable radio frequency (RF) parts, enhanced spectrum sensing algorithms, and sophisticated machine learning techniques. In this paper, we present a review of the recent advances in CR transceivers hardware design and algorithms. For the RF part, three types of antennas are presented: UWB antennas, frequency-reconfigurable/tunable antennas, and UWB antennas with reconfigurable band notches. The main challenges faced by the design of the other RF blocks are also discussed. Sophisticated spectrum sensing algorithms that overcome main sensing challenges such as model uncertainty, hardware impairments, and wideband sensing are highlighted. The cognitive engine features are discussed. Moreover, we study unsupervised classification algorithms and a reinforcement learning (RL) algorithm that has been proposed to perform decision-making in CR networks.

1. Introduction

Cognitive radio (CR) provides a solution to the inefficient use of the frequency spectrum [1–3]. This inefficiency is due to the current radio spectrum regulations which assign specific bands to particular services and grant licensed bands access to only licensed users. CR implements dynamic spectrum allocation policies by allowing unlicensed users (secondary users) to access spectrum bands licensed to primary users while avoiding interference with them [2, 3]. This necessitates at the RF front end more constraints on the antenna design, the development of algorithms for sensing the surrounding environment, and autonomously adapting to particular situations through a cognitive engine [1, 4–9]. These three design elements are introduced in this section and presented in more detail in the rest of this paper.

Spectrum underlay and spectrum overlay represent the two main approaches of sharing spectrum between primary users (PUs) and secondary users (SUs). The underlay approach imposes constraints on the transmission power, which can be satisfied using ultrawideband antennas (UWB).

UWB antennas are also used for channel sensing in overlay CR but must be frequency reconfigurable or tunable. In this case, a single-port antenna can have UWB response for sensing and can be reconfigured for tunable narrowband operation when needed to communicate over a white space. It is also possible to use dual-port antennas for overlay CR, in which one port has UWB frequency response and is used for channel sensing, and the second port is frequency-reconfigurable/tunable and used for communicating. In a third possible spectrum sharing approach, the antennas could be UWB antennas but should have the ability to selectively induce frequency notches in the bands used by PUs, thus avoiding any interference to them and giving the UWB transmitters of the SUs the chance to achieve long-distance communication.

Aside from the antenna, the design of the other RF blocks faces main challenges related to the ADC/DAC, the dynamic range or range of signal strengths to deal with, to the linearity of low-noise amplifiers (LNAs), and to the frequency agility of the duplexer and filters.

In CR, smart transceivers scan the spectrum in order to find white spaces and transmit adaptive signals. This functionality requires sophisticated algorithms to overcome practical imperfections such as model uncertainty and hardware nonideality. Some of the well-known spectrum sensing algorithms are energy detection [10–12], matched filter-based detection [11, 13], cyclostationarity-based detection [14–18], covariance-based sensing [19, 20], and eigenvalue-based sensing [21–23]. Blind detectors were also introduced to elude the model uncertainty problem. Spectrum sensing algorithms could be affected by RF impairments by inducing unwanted frequency components in the collected signal spectrum. The effects of such impairments are reduced through a postprocessing of the signal [24–26]. In addition, a robust detector based on smart digital signal processing lowers the effects of RF impairments and guarantees a high sensing accuracy.

The concept of cognitive radios (CRs) goes beyond dynamic spectrum access (DSA) applications and aims to improve the quality of information (QoI) of users [5]. This requires an intelligent radio that uses spectrum sensing techniques to observe the RF activities and is able to autonomously adapt to particular situations [9]. This is achieved through a reasoning engine which executes actions based on certain hard-coded rules and strategies [27]. Hard-coded policies are completely specified by the system designer and may result in the desired performance as long as the operating conditions do not deviate from the original assumed model. However, due to unexpected changes in the RF environment, the hard-coded rules may not lead to optimal performance, making them inefficient in this case. Cognitive radios, however, can overcome this problem by updating or augmenting their own sets of policies and rules based on past experience [27], which may lead to a more reliable communication performance [9, 27]. This makes the learning ability a fundamental building block of any CR to achieve autonomous intelligent behavior [9, 27–29].

In this paper, Section 2 presents the antenna designs for CR: ultrawideband (UWB) antennas, antennas with reconfigurable band rejection, and frequency-reconfigurable or tunable antennas. It also briefly discusses the challenges faced by the design of RF blocks for CR devices. Section 3 discusses spectrum sensing by presenting challenges, novel solutions, and spectrum sensing algorithms. RF imperfections and wideband sensing are also studied and recent blind detectors, robust algorithms, and wideband techniques are presented. Section 4 presents a cognitive engine and several unsupervised classification algorithms for autonomous signal classification in CRs, and a reinforcement learning (RL) algorithm that performs decision-making in CR networks. Conclusive remarks are given in Section 6.

2. RF Frontends for Cognitive Radio

CR transceivers are required to look for and operate in white spaces, which could exist anywhere inside a wide frequency range. This comes different from conventional wireless transceivers which are bound to certain preallocated

frequency bands. As a result, significant challenges have to be dealt with when designing the RF components of a CR transceiver, such as the antennas, the power amplifiers (PAs), the filters/duplexers, and the analog-to-digital and digital-to-analog converters (ADCs/DACs).

2.1. Antennas for Cognitive Radio. Two main approaches of sharing spectrum between primary users (PUs) and secondary users (SUs) exist: spectrum underlay and spectrum overlay. In the underlay approach, SUs should operate below the noise floor of PUs, and thus contingent constraints are imposed on their transmission power. Ultrawideband (UWB) technology is very suitable as the enabling technology for this approach. In spectrum overlay CR, SUs search for unused frequency bands, called white spaces, and use them for communication.

UWB antennas are used for underlay CR and also for channel sensing in overlay CR. For communication in overlay CR, the antenna must be frequency reconfigurable or tunable. Single- and dual-port antennas for overlay CR can be designed. In the dual-port case, one port has UWB frequency response and is used for channel sensing, and the second port, which is frequency reconfigurable/tunable, is used for communicating. In the more challenging single-port design, the same port can have UWB response for sensing and can be reconfigured for tunable narrowband operation when required to communicate over a white space.

A third possible spectrum sharing approach results from the use of the UWB technology in an overlay scheme. Here, the antennas could basically be UWB antennas but should have the ability to selectively induce frequency notches in the bands used by PUs, thus avoiding any interference to them and giving the UWB transmitters of the SUs the chance to increase their output power and hence to achieve long-distance communication.

A concise review of antenna designs for cognitive radio, covering the above three antenna types, is given in [30].

2.1.1. UWB Antennas. UWB antennas were originally meant to radiate very short pulses over short distances. They have been used in medical applications, GPRs, and other short-range communications requiring high throughputs. The literature is rich with articles pertaining to the design of UWB antennas [31–41]. For example, the authors in [31] present a unidirectional UWB antenna based on a full-ground plane. To keep this full-ground plane, they sequentially employ a list of broadbanding techniques: (1) resonance overlapping, (2) slot, (3) parasitic patch, (4) Vivaldi blending, (5) stepped notch, and (6) rectangular and T-shape slits. The resulting antenna has an impedance bandwidth from 3.6 GHz to 10.3 GHz while keeping the unidirectionality of the radiation pattern.

In general, the guidelines to design UWB antennas include the following.

- (i) The proper selection of the patch shape. Round shapes and round edges lead to smoother current flow and, as a result, to better wideband characteristics.

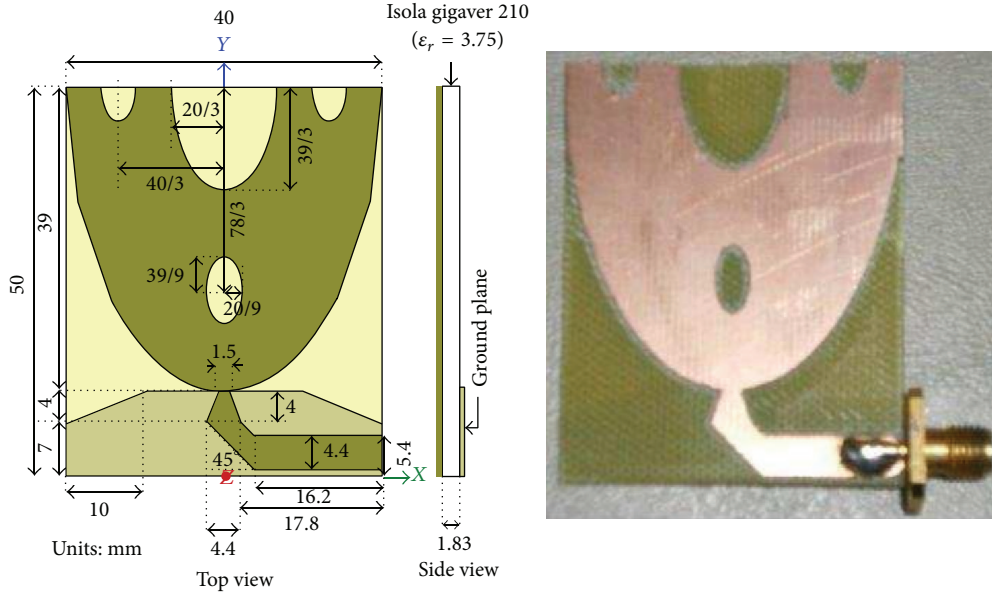


FIGURE 1: Configuration and photo of the UWB antenna in [42]. The antenna combines several bandwidth enhancement techniques.

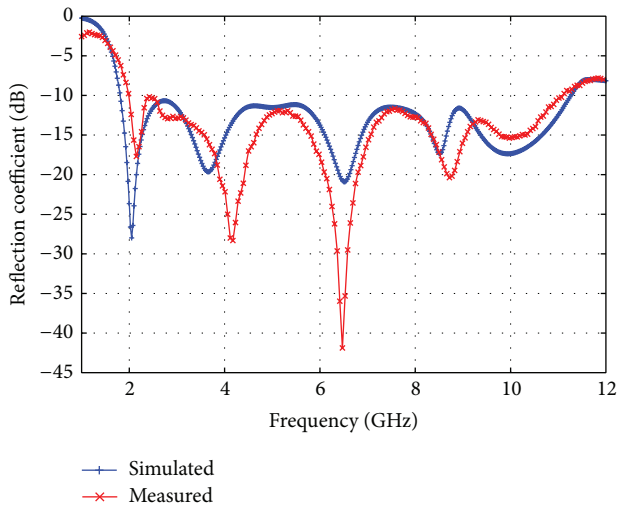


FIGURE 2: Reflection coefficient of the UWB antenna in Figure 1.

- (ii) The good design of the ground plane. Partial ground planes, and ground planes with specially designed slots, play a major role in obtaining UWB response. Keeping a full-ground plane is possible, but in that case an elaborate work has to be done on the patch design.
- (iii) The matching between the feed line and the patch. This is achieved using either tapered connections, inset feed, or slits under the feed in the ground plane.
- (iv) The use of fractal shapes, which are known for their self-repetitive characteristic, used to obtain multi- and wideband operation, and their space-filling property, which leads to increasing the electrical length of the antenna without tampering with its overall physical size.

Combinations of these guidelines were used in the following two examples. The UWB design presented in [42] features a microstrip feed line with two 45° bends and a tapered section for size reduction and matching, respectively. The ground plane is partial and comprises a rectangular part and a trapezoidal part. The patch is a half ellipse with the cut made along the minor axis. Four slots whose location and size relate to a modified Sierpinski carpet, with the ellipse as the basic shape, are incorporated into the patch. The geometry of this antenna is shown in Figure 1. Four techniques are applied for good impedance matching over the UWB range: (1) the specially selected patch shape, (2) the tapered connection between the patch and the feed line, (3) the optimized partial ground plane, and (4) the slots whose design is based on the knowledge of fractal shapes. As a result, this antenna has an impedance bandwidth over the 2–11 GHz range, as shown in Figure 2, and thus can operate in the bands used for UMTS, WLAN, WiMAX, and UWB applications. It has omnidirectional radiation patterns due to the partial ground plane.

The effect of the ground plane on the performance of UWB antennas is studied in [43]. Herein, it is proven that it is possible to obtain an ultrawide impedance bandwidth using either a partial ground plane or a ground plane with an optimized large slot, where in both cases the same exact patch is used. This design has a coplanar-waveguide feed that connects to an egg-shaped radiator. A photo of both versions is given in Figure 3.

2.1.2. Antennas with Reconfigurable Band Rejection. As previously stated, UWB technology is usually associated with the CR underlay mode. It can, however, be implemented in the overlay mode. The difference between the two modes is the amount of transmitted power. In the underlay mode, UWB has a considerably restricted power, which is spread over a wide frequency band. In the overlay mode, however,

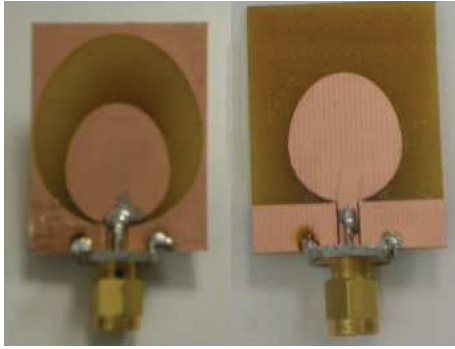


FIGURE 3: Two UWB antennas with optimized ground planes [43]. One has a partial ground plane and the other has a ground plane with a large slot.

the transmitted power can be much higher. It actually can be increased to a level that is comparable to the power of licensed systems, which allows for communication over medium to long distances. But this mode is only applicable if two conditions are met: (1) if the UWB transmitter ensures that the targeted spectrum is completely free of signals of other systems, or if it shapes its pulse to have nulls in the bands used by these systems, and (2) if the regulations are revised to allow for this mode of operation [44]. Pulse adaptation for overlay UWB CR has been discussed in [45]. UWB can also operate in both underlay and overlay modes simultaneously. This can happen by shaping the transmitted signal so as to make part of the spectrum occupied in an underlay mode and some other parts occupied in an overlay mode. In the overlay UWB scenario, the antenna at the front end of the CR device should be capable of operating over the whole UWB range, for sensing and determining the bands that are being used by primary users, and should also be able to induce band notches in its frequency response to prevent interference to these users. Even if the UWB power is not increased having these band notches prevent raising the noise floor of primary users.

Antennas that allow the use of UWB in overlay CR should have reconfigurable band notches. Several band-notching techniques are used in such antennas, the most famous of which is the use of split-ring resonators (SRRs) [46] and the complementary split-ring resonators (CSRRs) [47]. SRRs have attracted great interest among electromagneticians and microwave engineers due to their applications to the synthesis of artificial materials (metamaterials) with negative effective permeability. From duality arguments, CSRRs, which are the negative image of SRRs and roughly behave as their dual counterparts, can generate a negative permittivity media.

Some recent UWB antenna designs with fixed band notches are reported in [48–55]. The works in [56–59] are for UWB antennas with reconfigurable band notches.

A UWB design with a single reconfigurable band notch is proposed in [60]. The configuration of this design and a photo of its fabricated prototype are shown in Figure 4. Originally, the antenna is a UWB monopole based on a microstrip line feed and a partial ground plane. The patch is rectangular with rounded corners. A slit is etched in the ground below the

feed, for better matching. As a result, this antenna has an impedance bandwidth that covers the whole UWB frequency range. Four nested CSRRs are incorporated in the patch. Three electronic switches are mounted across the slots. The sequential activation (deactivation) of the switches leads to the functioning of a larger (smaller) CSRR and thus results in a notch at a lower (higher) frequency. The following switching cases are considered: Case 1 when all three switches are ON, Case 2 when only S3 is deactivated, Case 3 when only S1 is ON, and finally Case 4 when all switches are OFF. The resulting reflection coefficient plots, corresponding to the different switching states, are shown in Figure 5. The plots show one notch, which can occur in one of 3 bands or can completely disappear. In the latter case, the antenna retrieves its UWB response, which enables it to sense the whole UWB range.

The antenna reported in [61] is capable of concurrently inducing three band notches, which are independently controllable, using only three RF switches. This is done using three CSRRs etched on the patch. There are eight switching cases for this design, with one of them being the original UWB no-notch case. A UWB antenna with reconfigurable band notches can also be designed by incorporating a bandstop filter in the feed line of a UWB antenna. With this structure, the switching elements will be mounted on the feed line, away from the radiating patch, which makes the bias circuit of the switches simpler to design. Such a filter antenna (filtenna) with two reconfigurable rejection bands is presented in [62]. Its structure is shown in Figure 6. The UWB antenna is based on a rounded patch and a partial rectangular ground plane. A reconfigurable filter with two stop bands is incorporated along its microstrip feed line. The filter is based on one rectangular single-ring CSRR etched on the line and two identical rectangular single-ring SRRs placed in close proximity to it. The resonance of the CSRR is controlled via a switch and that of the two SRRs via two switches that are operated in parallel. As a result, there are four switching scenarios. The resulting reflection coefficient plots are shown in Figure 7. Case 1, where no band notches exist, allows the antenna to sense the UWB range to determine the narrowband primary services that are transmitting inside the range. In the other three cases, the notches block the UWB pulse components in the 3.5 GHz band, the 5.5 GHz band, or both. It should be noted that notches due to the SRRs and the CSRR around the feed are stronger than those due to CSRRs or any notching structures implemented in the patch. This is because energy is concentrated in a smaller area in the feed and coupling with the SRRs/CSRR is higher. Due to the location of the switches, connecting the DC bias lines, especially to the SRRs, which are DC-separated from anything else, is an easy task. A wire can be used to drive the switch on the CSRR. A note is that extra band notches can be obtained by placing more SRRs around the feed line. Tunable versions of these notches can be obtained by replacing the RF switches with varactors.

2.1.3. Frequency-Reconfigurable/Tunable Antennas. Antennas designed for overlay CR should have the capability to sense the channel and communicate over a small portion

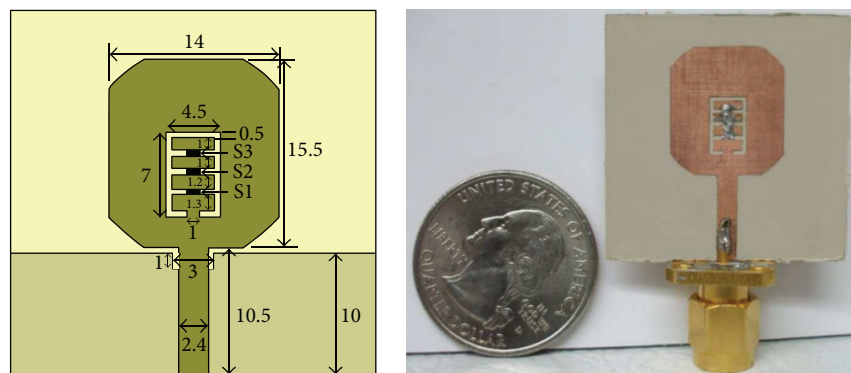


FIGURE 4: Geometry and photo of an antenna with one reconfigurable rejection band [60].

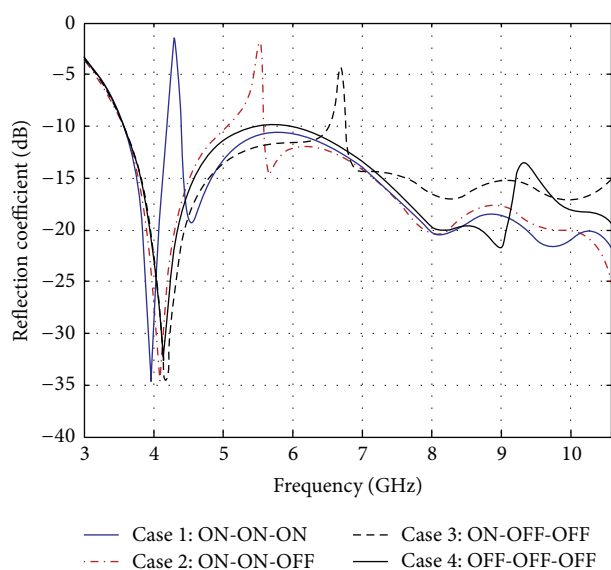


FIGURE 5: Reflection coefficient for the different switching cases of the antenna in Figure 4.

of it. These antennas can be implemented as dual port, where one port is UWB and the other is narrowband and frequency reconfigurable. They can also be designed as single port, where the same port is used for both sensing and communicating, and thus should switch between wideband and narrowband operations. For the dual-port designs, the isolation between the two ports is an issue. More elaborate work is required for single-port designs.

A dual-port antenna for overlay was proposed in [63]. Its structure consists of two printed antennas, namely, wide- and narrowband antennas. The design in [64] also combines wide and narrow band antennas, where the wideband one covers the 2.6–11 GHz range and the narrowband one is tunable, using a varactor, between 6.85 GHz and 7.20 GHz. A simple dual-port design is presented in [65]. The configuration of this design, which comprises two microstrip-line-fed monopoles sharing a common partial ground, is shown in Figure 8. The sensing UWB antenna is based on an egg-shaped patch. The UWB response of the sensing antenna is guaranteed by the design of the patch, the partial ground

plane, and a feed matching section. The communicating antenna is a simple microstrip line matched to the $50 - \Omega$ feed line. Two electronic switches are incorporated along this line. Controlling these switches leads to various resonance frequencies within the UWB range, as shown in Figure 9 for three considered switching cases.

Dual-port antennas enable simultaneous sensing and communicating over the channel, but have limitations in terms of their relatively large size, the coupling between the two ports, and the degraded radiation patterns. These limitations are solved by the use of single-port antennas, but these are only suitable when the channel does not change very fast, and thus sensing and communication are possible, sequentially.

Single-port reconfigurable wideband/narrowband antennas are reported in [66–68]. The design in [66] has a wide bandwidth mode covering the 1.0–3.2 GHz range and three narrowband modes within this range. In [67], fifteen PIN diode switches are used on a single-port Vivaldi antenna, leading to a wideband operation over the 1–3 GHz band and six narrowband states inside this range. GaAs field-effect transistor (FET) switches are used in [68] to connect multiple stubs of different lengths to the main feed line of a UWB circular-disc monopole. The result is an antenna that can be operated in a UWB mode or in a reconfigurable narrowband mode over one of three frequency subbands: the first covers 2.1–2.6 GHz, the second covers 3.6–4.6 GHz, and finally the third covers a dual band of 2.8–3.4 GHz and 4.9–5.8 GHz. The design in [69] is a filtenna based on a reconfigurable bandpass filter embedded in the feed line of a UWB monopole. A UWB and five narrowband operation modes characterize this design.

A printed Yagi-Uda antenna tunable over the 478–741 MHz UHF TV band is presented in [70], where the narrowband frequency tunability is obtained by loading the driver dipole arms and four directors with varactor diodes. A miniaturized tunable antenna for TV white spaces is reported in [71]. In [72], two PIN diodes and two varactors are employed for narrow band tuning between 1.39 and 2.36 GHz. A Vivaldi-based filtenna with frequency tunability over the 6.1–6.5 GHz range is presented in [73]. The single-port designs in [70, 72, 73] are only capable of narrowband operation, which means that wideband spectrum sensing has

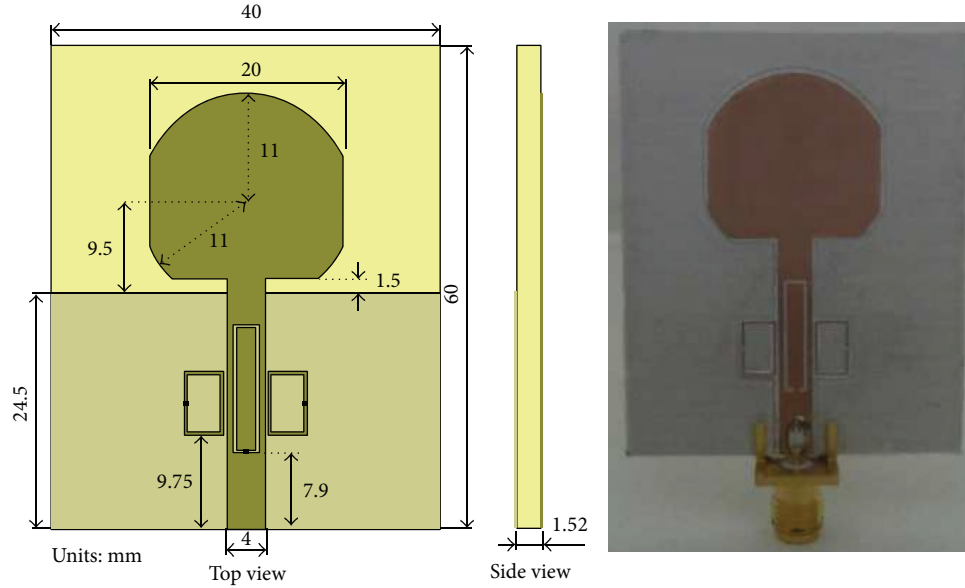


FIGURE 6: Geometry and photo of a filter antenna with two reconfigurable band notches [62].

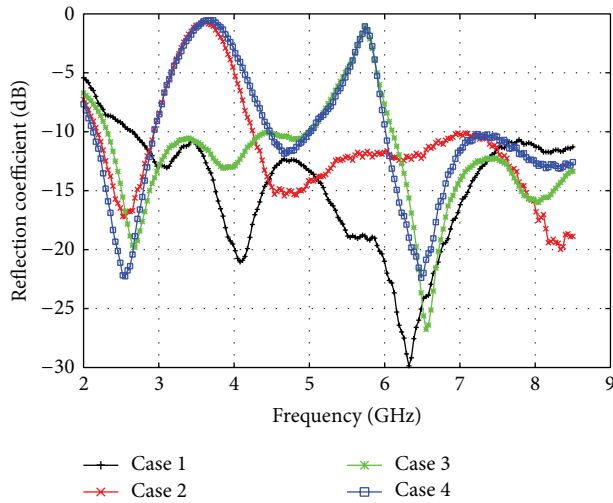


FIGURE 7: Reflection coefficient for the different switching cases of the antenna in Figure 6.

to be done progressively, a narrow chunk of frequencies at a time. This is also the case with the filter antenna design shown in Figure 10. Here, a tunable bandpass filter is embedded along the microstrip feed line of a UWB monopole antenna, where the filter is based on a T-shaped slot incorporated in the microstrip line between a pair of gaps. For the purpose of achieving frequency tunability, a varactor is included in the design, as indicated. Changing the capacitance of the varactor changes the notch band, caused by the T-shaped slot, and as a result the narrow passband of the overall filter. The DC lines of the varactors are connected with ease. Due to the presence of the two gaps, DC is separated from both the antenna port and the patch. Two surface-mount inductors are used over the DC lines as RF chokes. The computed reflection coefficient plots are given in Figure 11. They show narrowband tunability

over the 4.5–7 GHz frequency range, for capacitance values between 0.3 and 7 pF.

2.2. RF Design Challenges. The design challenges for the RF section of a CR transceiver are well reviewed in [74–76]. Diagrams of a CR transceiver architecture appear in [74]. For wideband operation, such as that required for sensing, the main challenges relate to the ADC/DAC, the dynamic range, or range of signal strengths to deal with, which could be as wide as 100 dB, to the linearity of low-noise amplifiers (LNAs), which has to be high, and to achieve impedance matching over a wide frequency range. For tunable narrow-band operation, the key issues are the frequency agility of the duplexer and filters.

2.2.1. ADCs and DACs. In many situations, the desired signal received by wireless device could sometimes be 100 dB weaker than other in-band signals generated by nearby transmitters of the same communication standard or some out-of-band blockers caused by any transmitter. This would demand a dynamic range of about 100 dB on the ADC. Ideally, the RF signals received by a CR system should be digitized as close to the antenna as possible, so that all the processing is done at the level of the digital signal processor (DSP). In this case, the ADC and DAC should have the 100 dB dynamic range, explained earlier, be operable over a UWB frequency range and handle significant levels of power. These requirements are still far beyond the limits of available technology, that is why the more realistic CR receivers reduce both the required dynamic range and the conversion bandwidth by having downconversion and filtering functions implemented before ADC.

On the path towards ideal CR receivers, several ADCs can be used in parallel to widen the conversion bandwidth. In [77], a parallel continuous time $\Delta\Sigma$ ADC is presented, which

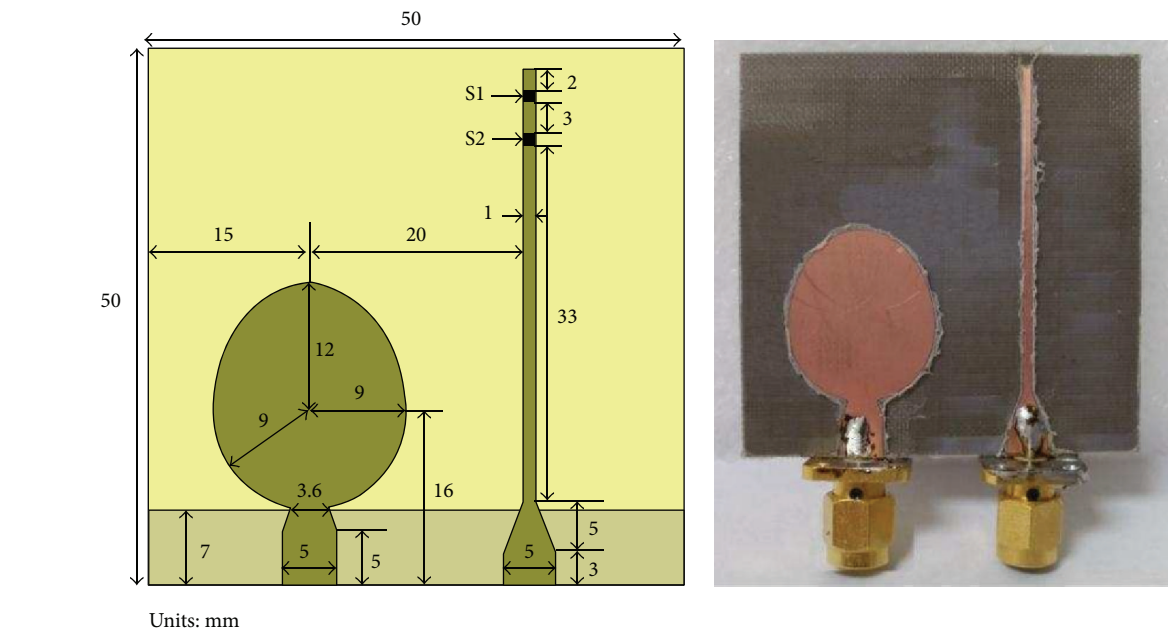


FIGURE 8: Geometry and photo of the dual-port ultrawideband-narrowband antennas in [65].

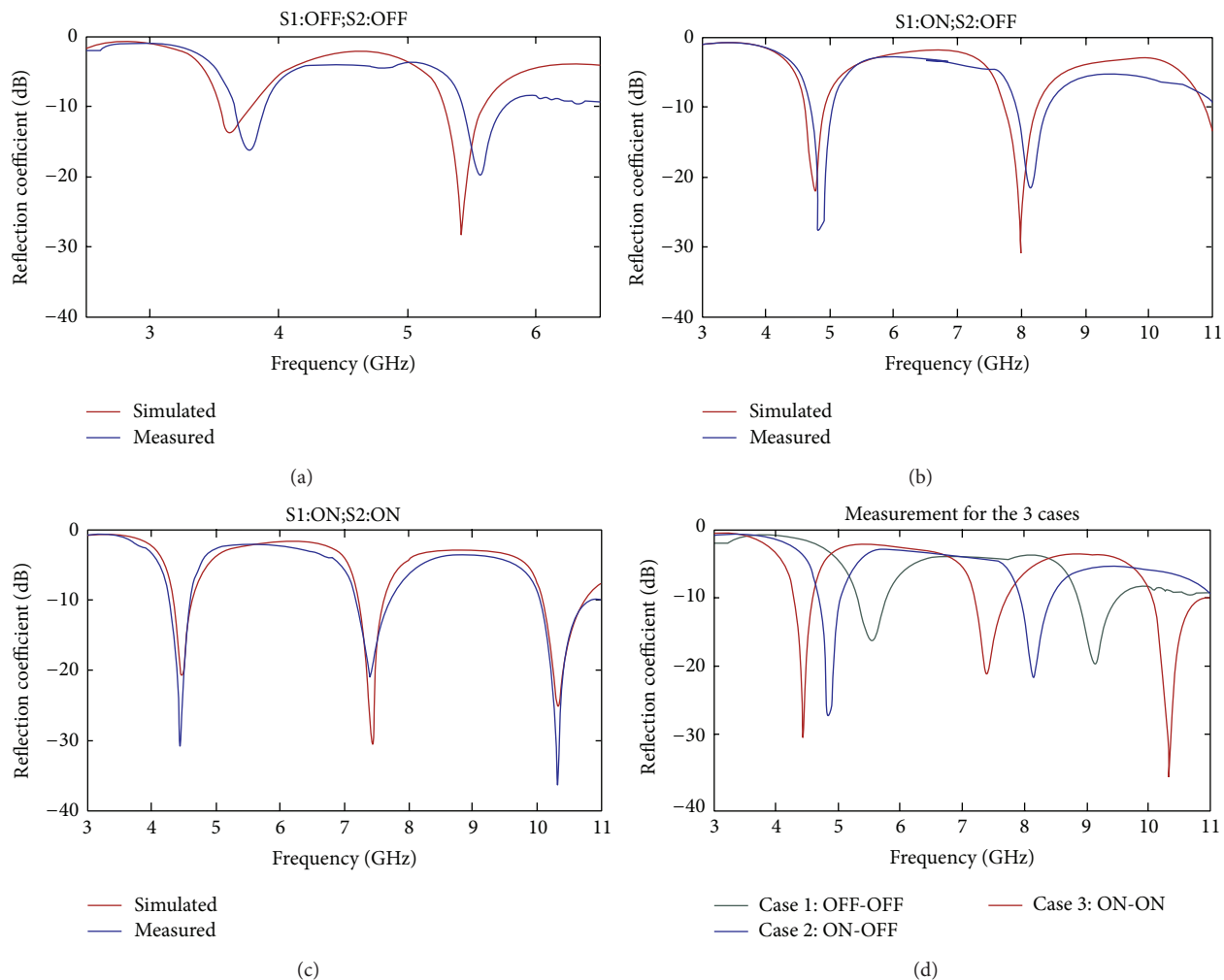


FIGURE 9: Reflection coefficient for 3 selected switching cases of the antenna in Figure 8.

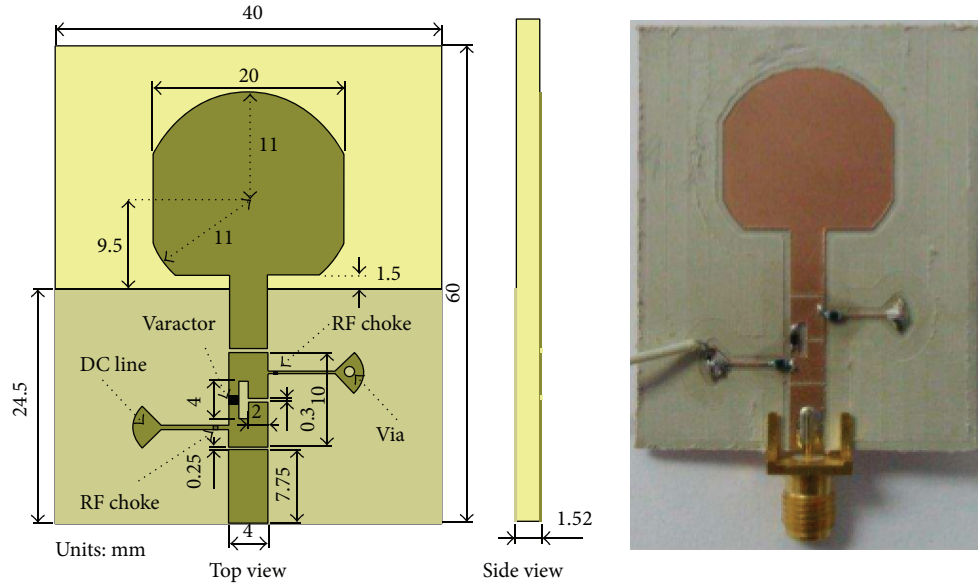


FIGURE 10: Geometry and photo of a tunable narrowband filtenna.

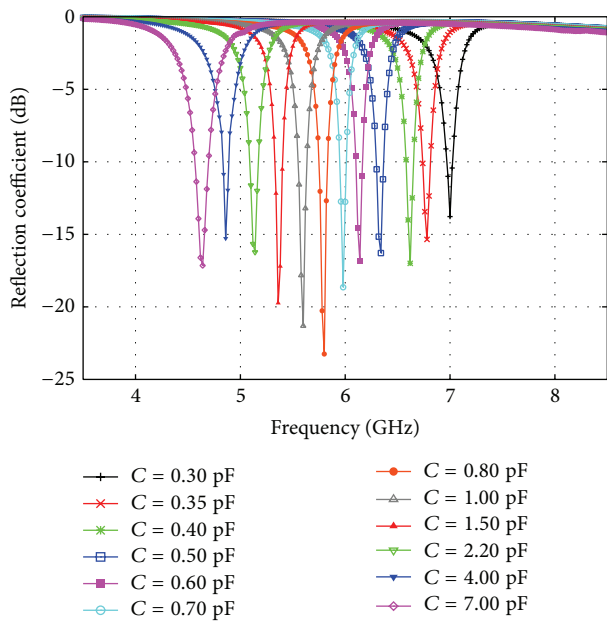


FIGURE 11: Reflection coefficient of the filtenna in Figure 10 for the indicated varactor capacitance values.

requires very complex digital synthesis filters. The hybrid filter bank-based ADC presented in [78] could be a promising solution for CR applications, but its use necessitates high resource calibration since it is sensitive to analog filter errors and imperfections. A solution that provides good performance in terms of speed employs time interleaving [79], but it lacks the resolution and dynamic range. To suppress low order nonlinearities of parallel ADCs and nonlinearities caused by pre-ADC analog components, digital postlinearization is desired. The technique in [80, 81] combines time multiplexing and frequency multiplexing by using bandpass charge sampling filters as analysis filters in hybrid filter banks

architecture. This leads to reduced complexity of analog analysis filters and simultaneously of the sensitivity to analog errors and imperfections. Yet, the practical implementation with the aim of widening the bandwidth and sensitivity still requires a deeper investigation.

RF DACs are utilized in the fully digital RF transmitters presented in [82, 83]. The design of these DACs is less challenging than that of ADCs, although more improvements are still necessary.

2.2.2. Low-Noise Amplifier. A receiver's performance is primarily determined by the linearity and adequate matching over a wide frequency range of the broadband or tunable LNA. A broadband LNA topology achieving a frequency range of 50 MHz to 10 GHz was proposed in [76]. The input capacitance is canceled by the LNA using inductive behavior provided by negative feedback. Advanced CMOS technologies make it easier to design such high-frequency LNAs without any large inductors. On the other hand, the linearity issue becomes crucial because the supply voltage for core transistors decreases to around 1V in 90 nm or more advanced processes, which results in a limited voltage swing. LNAs using thick-oxide transistors may prevent this problem [84]. The mixer-first RF front ends [85, 86] are another approach for improving linearity performance. An impedance translation technique, which uses passive mixers followed by capacitive loads, can provide low impedance for out-of-band blockers [87, 88], which makes it attractive.

The even-order nonlinearity of the LNA also should be considered in wideband CR systems. This is because second-order intermodulation (IM2) products generated by an LNA can fall within the CR band, thus corrupting the desired signal even before downconversion. A differential LNA topology seems attractive here, but a balun is necessary if the antenna is single ended. Design of low-loss baluns operating across two or three decades of bandwidth is challenging. A useful balun-LNA topology is proposed in [89].

2.2.3. Downconversion Mixer. Another issue in the wideband operation of a CR device is harmonic mixing. The RF signal is often downconverted using square-wave local-oscillator (LO) signals that contain large odd-order harmonic components. This is done to obtain flat performances of noise and gain across a wide frequency range. The use of a harmonic-rejection mixer (HRM) is one way to remove odd-order LO harmonics. The authors in [90, 91] propose techniques to improve harmonic rejection ratios (HRRs). However, if seventh- and higher-order LO harmonics are to be rejected, the HRMs become much more complex.

2.2.4. Wideband Frequency Synthesizer. Multiple oscillators could be used to cover a wide frequency range. This solves the issue of the trade-off between tuning range and phase noises. For acceptable phase noise figures, the tuning range of inductor-capacitor (LC-) type oscillators is typically limited to about $\pm 15\%$ at frequencies of tens of gigahertz. Frequency synthesizers for CR having two oscillators to support a wider frequency range are reported in [84, 92].

3. Spectrum Sensing in Cognitive Radios

In a CR scenario, secondary users are allowed to detect, exploit, and use underutilized spectral resources licensed to primary users. Such opportunistic behavior urges CR transceivers to scan the spectrum in order to find white spaces and transmit adaptive signals. Thus, spectrum sensing is the key function of smart receivers since it enables the cognitive cycle proposed by Mitola in [4, 93]. This functionality creates unique signal processing challenges and requires sophisticated algorithms to overcome practical imperfections such as model uncertainty and hardware imperfections.

To address these challenges, CR researchers proposed in the last decade various detectors that have different complexity levels, performance results, and requirements for implementation. Well-known spectrum sensing algorithms, sorted in an ascending order of complexity are energy detection (ED) [10–12], matched filter (MF-) based detection [11, 13], cyclostationarity-based detection (CSD) [14–18], covariance-based sensing [19, 20], and eigenvalue-based sensing [21–23]. Some of these methods require a priori knowledge of noise and/or signal power information; these include MF, CSD (relying on the full or partial knowledge of signal and noise levels), and ED (having a threshold dependent on the estimated noise power level). Blind detectors were recently proposed to elude the model uncertainty problem relying on advanced digital signal processing techniques.

In a cognitive receiver, RF impairments could harm the performance of the spectrum sensing algorithm by inducing unwanted frequency components in the collected signal spectrum. To mitigate the effects of such impairments, “Dirty RF” is applied on the SU receiver inducing a postprocessing of the signal, thus compensating analog imperfections [24–26]. A robust detector, based on smart digital signal processing, should be able to digitally lower the effects of RF impairments and guarantee a high sensing accuracy.

The early-designed spectrum sensing algorithms aimed to detect a white space from narrow frequency bands where many emerging wireless applications require an opportunistic usage of a wideband spectrum [94–97]. Consequently, SUs are forced to scan a wide range of potential spectra and detect available holes to be able to transmit. One of the main concerns of the CR community is to conceive wideband spectrum sensing methods to replace the complicated implementation of high sampling rate ADCs, capable of downconverting wideband signals.

The selection of signal processing algorithms and their parameters reflects the speed and sensing time of the cognitive receiver. A complex signal processing algorithm should respect an optimum sensing value depending on the capabilities of the radio and its temporal characteristics in the environment. On the other hand, the ADC is considered as the primary bottleneck of the DSP architecture since it forces the clock speed of the system. Moreover, the selection of the digital signal processing platform affects the speed of the front end. All these parameters influence the sensing frequency and speed of cognitive radio receivers. For that, researchers focus on implementing sensing algorithms with low complexity, high speed, and flexibility in order to conceive an adaptive CR terminal.

In the following sections, we will describe three main practical spectrum sensing challenges and novel solutions. Model uncertainty, RF imperfections, and wideband sensing are studied and recent blind detectors, robust algorithms, and wideband techniques are presented. Accordingly, in the rest of this paper, we provide an overview of the state of the art of spectrum sensing algorithms that were proposed to answer these three major and hot research challenges.

3.1. Blind Detectors. As per regulation specifications, secondary users are required to detect very weak licensed users in order to protect primary transmissions [98, 99]. Any missed detection will enable an unlicensed transmission on a busy channel harming the incumbent primary signal. Unfortunately, many detectors reveal performance degradation at low SNR due to inappropriate estimation of the signal or noise models. This phenomenon is known as SNR wall [10, 100]. For the ED, an estimation of the noise variance is required to select a suitable threshold. Imperfect knowledge of the noise model, especially in low SNR scenarios, will consequently deteriorate the efficiency of this algorithm. The SNR wall phenomenon also harms any detector based on the received signal’s moments. Using cooperative spectrum sensing techniques or relying on calibration and compensation algorithms are possible solutions to the model uncertainty problem [100, 101]. However, using totally blind detectors, which detect the presence of a signal without any knowledge of signal or noise parameters, is considered the ideal alternative. Two recently proposed blind detectors are described below.

3.1.1. Blind Eigenvalue-Based Detector. Zeng et al. devised a blind detector based on the computation of the minimum and maximum eigenvalues λ_{\min} and λ_{\max} of the sample covariance matrix $\mathbf{R}(N_s)$ defined in [22]. The test statistics

Initialize: Acquire L consecutive data samples and assume that there are $(M \geq 1)$ receivers (antennas), and (N_s) is the total number of collected samples.

(a) Define the received vector x_n given by:

$$\mathbf{x}(n) = [x_1(n), x_2(n), \dots, x_M(n)]^T$$

(b) The collection of L consecutive outputs $\hat{\mathbf{x}}_n$ is defined as:

$$\hat{\mathbf{x}}_n = [\mathbf{x}^T(n), \mathbf{x}^T(n-1), \dots, \mathbf{x}^T(n-L+1)]^T$$

(c) Compute the sample covariance matrix $\mathbf{R}(N_s)$:

$$\mathbf{R}(N_s) = \frac{1}{N_s} \sum_{n=L}^{L-1+N_s} \hat{\mathbf{x}}_n \hat{\mathbf{x}}_n^H$$

(d) Compute λ_{\max} and λ_{\min} the maximum and minimum eigenvalues of the matrix $\mathbf{R}(N_s)$.

(e) Compute the threshold ν for the test statistics:

$$\nu = \frac{(\sqrt{N_s} + \sqrt{ML})^2}{(\sqrt{N_s} - \sqrt{ML})^2} \left(1 + \frac{(\sqrt{N_s} + \sqrt{ML})^{-2/3}}{(N_s ML)^{1/6}} F_1^{-1}(1 - P_{FA}) \right),$$

where F_1 is the Tracy-Widom distribution of order 1 [102].

The decision test:

(f) Decide on H_0 or H_1 by computing the ratio between λ_{\max} and λ_{\min} :

$$\frac{\lambda_{\max}}{\lambda_{\min}} \underset{H_0}{\overset{H_1}{\gtrless}} \nu$$

ALGORITHM 1: Steps of the MME detector.

of this maximum-minimum eigenvalue (MME) detection is simply given by

$$\frac{\lambda_{\max}}{\lambda_{\min}} \underset{H_0}{\overset{H_1}{\gtrless}} \nu, \quad (1)$$

where ν is the threshold calculated by using the number of acquired samples, the smoothing factor used for the calculation of $\mathbf{R}(N_s)$, and a selected probability of false alarm. It is expected that noise produces small eigenvalues, whereas the correlation inherited in modulated signals increases the eigenvalues. The proposed test statistic does not depend on any knowledge of noise, signal, or channel models; thus it is not sensitive to the model uncertainty problem. The detailed computational steps of this scheme are described in Algorithm 1.

3.1.2. The CAF Symmetry-Based Detector. This blind spectrum sensing detector is based on the symmetry property of the cyclic autocorrelation function (CAF). Benefiting from the sparsity property of CAF, the compressed sensing tool is adopted in this algorithm. A test statistic is defined, without the computation of any threshold, by checking if the estimated CAF exhibits symmetry or not. As demonstrated in [103], a positive symmetry check affirms the presence of a primary signal. The estimation of the cyclic autocorrelation vector is computed using an iterative optimization technique, called the orthogonal matching pursuit (OMP) [104]. The computational complexity of this algorithm is reduced by limiting the number of acquired samples and the number of needed iterations to ensure its practical feasibility. Algorithm 2 summarizes the main steps of this detector.

3.2. Robust Sensing Algorithms. In practice, CR receivers are composed of several sources of hardware imperfections

such as low noise amplifiers (LNA), mixers, local oscillators (LO), and analog-to-digital converters (ADC). The most critical result of such impairments is the appearance of new frequency components in the received signal, classified in intermodulation distortions (IM), cross modulation (XM), and phase distortion (AM/PM). Consequently, strong primary users could harm the performance of traditional spectrum sensing techniques by adding unwanted spectrum components via front-end's nonlinearity. When these components overlap with weak secondary users, a degradation in the reliability of SU transmissions occurs. They can also virtually occupy the whole spectrum, thus decreasing the opportunity to find a vacant transmission band. In both scenarios, the accuracy of any proposed algorithm will be deteriorated. To mitigate these effects, a robust detector algorithm should be equipped with a compensation functionality to digitally reduce the effects of nonlinearities. Possible compensation algorithms could be based on feed-forward techniques with reference nonlinearity, feed-back equalization, and training symbol-based equalization. A well-known feed-forward technique to alleviate phase noise, carrier frequency offset, nonlinearities, I/Q imbalance, or ADC impairments is described below.

3.2.1. The AIC Algorithm. In [25], Valkama et al. devised the adaptive interference cancellation (AIC) algorithm, which is a feed-forward algorithm for the mitigation of second, third, and fifth order intermodulation distortion. The idea is to model the distortion caused by the interferer and then subtract them from the received signal. A mathematical formulation of the distortion model and order is studied before implementing the algorithm. Then, an imitation of the distortion products and an adaptive adjustment of their levels are performed to compensate the distorted signal.

Initialize: Acquire n data samples from the spectrum sensing interval formed by N samples and set $(l + 1)$ the number of OMP iterations, and (M) the number of delays τ s

For M different values of τ ,

(a) Calculate the autocorrelation vector \mathbf{f}_{τ_0} given by:

$$\mathbf{f}_{\tau} = [f_{\tau}(0), f_{\tau}(1), \dots, f_{\tau}(N-1)]^T,$$

where $f_{\tau}(t) = y(t)y(t + \tau)$.

(b) Calculate the elements of the matrix A performing the IDFT transform:

$$a_{(p,q)} e^{2i\pi(p-1)(q-1)/N}$$

The OMP algorithm

(c) Estimate the cyclic autocorrelation vector by solving the following system of equations: $A\mathbf{r}_{\tau} = \mathbf{f}_{\tau}$ by using an iterative optimization technique called Orthogonal Matching Pursuit (OMP) that delivers an approximated solution $\hat{\mathbf{r}}_{\tau}$.

Symmetry check

(d) Calculate the symmetry index for this value of τ , by ignoring the first amplitude that corresponds to the first iteration of OMP, and measuring the mean value of the abscissa of the remaining $(l - 1)$ non zero elements in $\hat{\mathbf{r}}_{\tau}$. The symmetry index is given by:

$$\text{IND}_{\text{sym}}^{(\tau)} = \frac{1}{l} \sum_{i=1}^l \hat{r}_{\tau_i}.$$

End For

Equivalent symmetry check:

$$\text{IND}_{\text{sym}}^{(\text{equ})} = \frac{1}{M} \sum_{i=1}^M |\text{IND}_{\text{sym}}^{(\tau_i)}| < 0.$$

ALGORITHM 2: Steps of the CAF symmetry-based detector.

The algorithm, illustrated in Figure 12, starts by splitting the band of the received signal in order to differentiate between the strong PU and other frequency components (SUs + distortions). The band splitting is accompanied by a coarse energy detector used to locate the strong interferer. Then a parallel block of reference nonlinearities is used to extract potential distortion products from the strong interferer. An adaptive filter, the least mean square (LMS), is used to adjust digitally created distortions levels. The adaptive filter utilizes the distorted signal resulted from the band splitter as an input parameter and minimizes the common error signal $e(t)$. The adjusted nonlinearities are finally subtracted from the received signal to cleanse the band from nonlinearity distortions. It is shown in [26] that the application of the AIC algorithm before the detector increases the detection reliability in CR devices.

3.3. Wideband Spectrum Sensing. Several emerging wireless applications and regulation encourage cognitive receivers to scan a wideband spectrum to find potential spectrum holes. In contrast to the narrowband techniques mentioned above, wideband spectrum sensing methods aim to sense a frequency bandwidth exceeding the coherence bandwidth of the channel. A frequent example deals with the design of an algorithm capable of sensing the whole ultra-high-frequency (UHF) TV band (between 300 MHz and 3 GHz). Practically, wideband scanning could be performed via the following two different methods.

(1) By using a filter bank formed by preset multiple narrowband pass filters BPFs [105]. This hardware-based solution requires more hardware components, thus increasing the cost and the RF impairments harmful

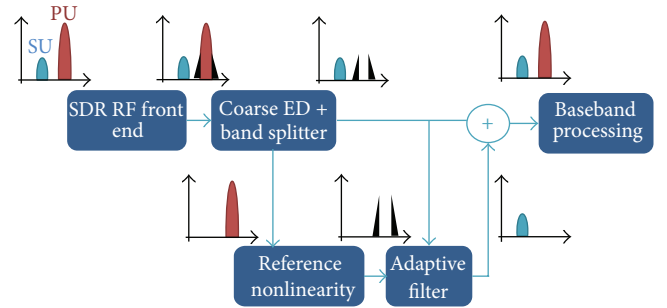


FIGURE 12: The AIC algorithm.

effect, and limiting the flexibility of the radio by fixing the number of filters. After each filter, a narrowband state-of-the-art technique is implemented.

(2) By using sophisticated signal processing techniques. In fact, narrowband sensing techniques cannot be directly applied to scan a wideband since they are based on single binary decision for the whole spectrum. Thus, they cannot simultaneously identify vacant channels that lie within the wideband spectrum. Recently proposed wideband spectrum sensing can be broadly categorized into two types:

- (i) Nyquist wideband sensing processes digital signals taken at or above the Nyquist rate, for example, the wavelet transform-based technique;
- (ii) sub-Nyquist wideband sensing acquires signals using a sampling rate lower than the Nyquist rate, for example, the compressive sensing technique.

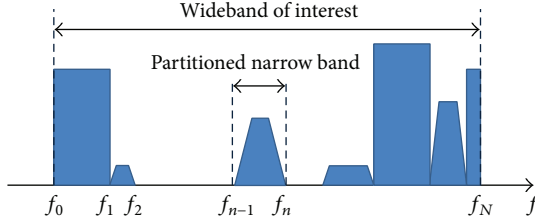


FIGURE 13: A wideband spectrum seen as a train of narrowband signals and presenting frequency irregularities.

In the following sections, two approaches to perform wideband spectrum sensing are discussed.

3.3.1. Wavelet Transform-Based Technique. In this method, the SU transceiver scans a wideband without using a bank of narrow BPFs. Alternatively, a wideband receiver will be based on high-speed digital signal processing to search over multiple frequency bands in an adaptive manner. The obtained digital signal will be modeled as a train of consecutive narrow frequency bands as illustrated in Figure 13. To identify these bands and search for potential spectrum holes, the wavelet transform will be used to locate edges between different narrow subbands [106]. The corresponding block diagram is depicted in Figure 14. Wavelet transform is used in mathematics to locate irregularities [95]. Consequently, it will be a good candidate to differentiate between the narrow subbands of wideband signal [97, 107]. A wavelet edge detector is able to identify the average power level within each identified subband which will lead to the localization of the spectrum holes.

The analysis using wavelet transform is based on a function known as the principal wavelet ψ which has a finite energy. Wavelets are used to transform a given signal into another representation that models the information related to the signal in a more utile way. Wavelets could be manipulated in two different ways: moved along the frequency axis or stretched with a variable energy. A Wavelet transform, obtained by summing the product of the signal multiplied by the wavelet, is calculated at different spots of the signal and for different combinations of the wavelet. This calculation could be monitored to detect the irregularities of the signal by observing the different values of the wavelet transform.

3.3.2. Compressive Sensing Technique. A major implementation challenge lies in the very high sampling rates required by conventional spectral estimation methods which have to operate at or above the Nyquist rate. However, to solve this issue, the compressive sampling CS technique is used for the acquisition of sparse signals at rates significantly lower than the Nyquist rate. Signal reconstruction is no more based on old reconstruction techniques but will be a solution to an optimization problem. Several schemes were suggested in the literature for the reconstruction of the signal, by using wavelet transforms [97], the autocorrelation of the signal [108], or advanced algorithms for sparse approximation methods [104, 109]. It is shown that such methods could preserve the

adaptive response of the algorithm by offering a relatively small processing time.

Sparse approximation consists of finding a signal or a vector with sparseness property; that is, it has a small number of nonzero elements that satisfies (approximately) a system of equations. For example, consider a linear system of equations $y = Ax$, where A is an n – by – M matrix with $n < M$. Since A is overcomplete ($n < M$), this problem does not have a unique solution. Among all the possible solutions, if the true one is known a priori to be sparse then it happens that the sparsest, that is, the solution x , containing as many as possible zero components and satisfying $y \cong Ax$, is close to the true solution. Reducing the problem complexity to n instead of M increases the adaptation time of the reconstruction algorithm and thus provides better processing time.

4. Machine Learning in Cognitive Radios

Cognitive radios (CRs) are considered as intelligent radio devices that use the methodology of understanding-by-building to learn and adapt to their radio frequency (RF) environment [1]. Several CR architectures have been proposed over the past years in order to achieve dynamic spectrum access (DSA) [1–3]. However, as initially proposed by [4], the concept of CRs goes beyond DSA applications and aims to improve the quality of information (QoI) of wireless users [5]. This functionality requires an intelligent radio that is aware of its RF environment and is able to autonomously adapt to the variations in the wireless medium [9].

Cognitive radios are assumed to use spectrum sensing techniques to identify the RF activities in their surrounding environment [6]. Based on their observations, CRs apply their reasoning abilities to modify their behavior and adapt to particular situations. This is achieved through a reasoning engine which executes actions based on certain rules and strategies [27]. Similar reasoning engines could be identified in conventional radios that behave according to a set of hard-coded rules [27]. For example, according to the IEEE 802.11 specifications, such hard-coded rules determine the switching of a radio device among different modulation schemes depending on the signal-to-noise ratio (SNR) [27]. Hard-coded policies are completely specified by the system designer and may result in the desired performance as long as the operating conditions do not deviate from the original assumed model. However, in situations where the RF environment changes due to unexpected agents or factors (e.g., jammers, interferers, extreme fading conditions, etc.), the hard-coded rules may not lead to optimal performance, making them inefficient in this case. Cognitive radios, however, can overcome this limitation by updating their own sets of policies and rules based on past experience [27]. For example, if a CR is subject to jamming or significant interference on a certain channel, it could come up with new actions to switch to a new frequency band, instead of simply modifying its modulation scheme, in contrast with the IEEE 802.11 case. Hence, based on its learning ability, a CR can update or augment its set of rules and policies based on its own experience, which may lead to a more reliable

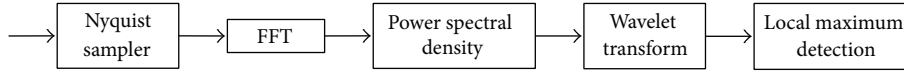


FIGURE 14: Block diagram of Wavelet transform-based technique.

communication performance [9, 27]. This makes the learning ability a fundamental building block in any CR to achieve autonomous intelligent behavior [9, 27–29].

Machine learning techniques are gaining more importance in the current and future wireless networks due to the increase in system complexity and the heterogeneous nature of the wireless medium [29, 110–117]. In particular, significant research efforts are being focused on developing link aggregation techniques using multiple radio access networks (RANs) [111]. For example, the authors in [111] have demonstrated a CR system that is able to access a heterogeneous RAN aggregation system including HSDPA, Wi-Max, and W-CDMA systems. In order to ensure efficient system operation, the system parameters need to be optimized to maximize the overall performance. However, due to the dynamic nature of the wireless network and the large number of system parameters, the operating parameters cannot be optimized manually, but require intelligent algorithms that are able to autonomously adjust the system parameters, leading to optimal performance. In [111], the support vector regressor (SVR)-based learning algorithm has been proposed for parameter optimization. This algorithm requires a set of training data to estimate the system model. Other learning approaches may be considered in the future to optimize various system parameters under different operating environments [111]. In this paper, however, we focus on unsupervised learning methods to ensure autonomous CR operation, as we will discuss next.

5. The Cognitive Engine

Cognitive radios extend software-defined radios (SDRs) by adding a cognitive engine (CE) to the radio platform [27]. According to [27], a CE can be composed of three main components: (1) a knowledge base, (2) a reasoning engine, and (3) a learning engine, as illustrated in Figure 15 [27]. The reasoning engine executes the actions and policies that are stored in the knowledge base, while the learning engine updates these policies based on past experience [9, 27]. By applying learning algorithms, the learning engine can transform the observed data into knowledge, thus allowing the CR to be aware of certain characteristics of its environment [4, 29].

The machine learning literature is rich with learning algorithms that can be used in various contexts [29, 110–117]. These learning algorithms can be categorized under either supervised or unsupervised methods. In supervised learning, a set of labeled training data is available for the learning agent to specify whether a certain action is correct or wrong [29, 118]. In unsupervised learning, however, the learning agent is supposed to identify the correct and wrong actions based on its own experience and interactions with the environment [118]. This makes unsupervised learning algorithms

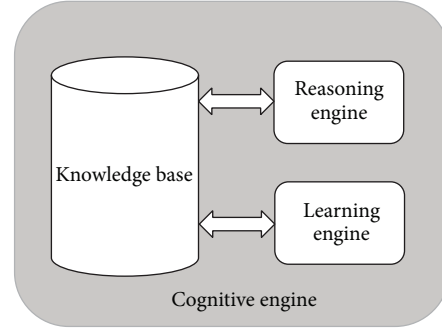


FIGURE 15: The cognitive engine (CE).

more appealing for CR applications, compared to supervised learning, since they lead to autonomous cognitive behavior in the absence of instructors [9]. Hence, unsupervised learning has been the focus of recent autonomous CRs formulations [7, 9, 119–123].

Several unsupervised learning algorithms have been proposed for CRs to perform either feature classification or decision-making [29]. Classification algorithms can be used to infer hidden information about a set of noisy data. They allow, for example, inferring both number and types of wireless systems that are active in a certain environment [120, 124]. In addition, classification algorithms were also proposed for modulation classification based on Bayesian networks, as in [125]. On the other hand, decision-making algorithms can be used to update or modify the policies and rules that are stored in the knowledge base of a CR. Thus, the learning process may result in a new set of actions, allowing the CR to adapt to completely new RF environments [27].

In the followings, we present several unsupervised classification algorithms that have been proposed for autonomous signal classification in CRs. We also present a reinforcement learning (RL) algorithm that has been proposed to perform decision-making in CR networks.

5.1. Unsupervised Classification Algorithms. Classification algorithms have been proposed for CRs to extract knowledge from noisy data [120, 121, 124]. As we have mentioned above, the classification algorithms based on machine learning techniques can be divided into two main categories: supervised and unsupervised classifiers [29, 120]. Supervised classifiers require an “instructor” that specifies whether a certain classification decision is “correct” or not. These supervised classifiers require a set of labeled training data (or expert-annotated data [120]) that specify the correct classes (or clusters). Supervised classifiers can be applied in certain conditions when prior knowledge (e.g., labeled data) is available to the learning agent. However, in situations where no such

prior information is available, unsupervised classifiers can be used instead. Unsupervised classifiers do not require labeled data and process the detected data to determine the class or cluster of each data element. Hence, unsupervised classifiers can be considered more suitable for autonomous CRs when operating in unknown RF environments [9, 124].

In the followings, we present three examples of unsupervised classifiers that have been proposed for CRs: (1) the K -means, (2) X -means, and (3) Dirichlet process mixture model (DPMM) classifiers. We give a brief description of each algorithm and show their different applications in CRs.

5.1.1. The K -Means Classifier. The K -means algorithm has been proposed for robust signal classification in CRs [120]. It is considered as an unsupervised classifier since it does not require labeled training data [29, 120]. However, the K -means algorithm requires prior knowledge about the number of clusters K , making it a unsupervised parametric classifier.

Given a set of N feature points $\{\mathbf{y}_i\}_{i=1}^N$, the K -means algorithm classifies these data points into K clusters, where K is determined a priori. The algorithm starts with a set of K arbitrary centroids $\{\mathbf{c}_1, \dots, \mathbf{c}_K\}$, defining the centers of K initial clusters. Each feature point \mathbf{y}_i is then selected sequentially and assigned to the closest centroid (in terms of Euclidean distance). Once a feature point is assigned to a particular cluster, the corresponding centroid is updated and computed as the mean of the feature points belonging to that cluster. Eventually, the means converge to the clusters centers [120].

In CR applications, the K -means algorithm was applied to classify different types of RF signals based on their spectral or modulation characteristics. For example, in [120], the K -means were allowed to classify primary and secondary signals transmitting within the TV band. The authors in [120] demonstrated the robustness of this classifier against fluctuations in the signal parameters, such as the signal-to-noise ratio (SNR). In general, such fluctuations lead to larger variance in the extracted features, which may cause

poor classification performance. Nevertheless, the K -means algorithm was shown to be robust against such variations and achieved good performance in classifying both 8-level vestigial sideband (8VSB) modulated signals (primary TV transmission) and BPSK modulated signals (cognitive secondary transmission) [120].

The K -means algorithm is characterized by its low complexity and fast convergence. However, it requires accurate knowledge about the number of signal classes, which may not be practical in many cases [9, 120, 124]. For example, in many CR applications, it may be required to classify signals belonging to an unknown number of systems, which requires nonparametric approaches, as we will describe next [9, 119, 120].

5.1.2. The X -Means Classifier. The X -means algorithm has been proposed as an extension of the K -means algorithm, allowing the classifier to estimate the number of clusters from the data itself [126]. The X -means algorithm is formulated as an iterative K -means algorithm which computes the optimal number of clusters that maximizes either the Bayesian information criterion (BIC) or Akaike information criterion (AIC) [126]. In contrast with the K -means, the X -means algorithm assumes an unknown number of clusters, making it suitable for nonparametric classification.

This algorithmic approach was successful in detecting primary user emulation (PUE) attacks in CR applications, as discussed in [120]. In this case, the signal detector can first estimate the number of clusters X and then obtain the different classification regions for each cluster, similar to the K -means algorithm. Both K -means and X -means algorithms can be implemented at low complexity. However, they are suitable only for spherical Gaussian mixture models [124]. In CRs, however, feature vectors can be extracted from complex observation models which are not necessarily Gaussian [124]. This situation can thus be addressed using the DPMM classifier which assumes an arbitrary distribution of the observation model but requires higher computational complexity, compared to both X -means and K -means algorithms, as we will discuss next [124]:

$$\theta_i \mid \{\theta_j\}_{j \neq i}, \mathbf{y}_1, \dots, \mathbf{y}_N \begin{cases} = \theta_j & \text{with prob. } q_j = \frac{f_{\theta_j}(\mathbf{y}_i)}{\alpha_0 f(\mathbf{y}_i) + \sum_{j=1, j \neq i}^N f_{\theta_j}(\mathbf{y}_i)} \\ \sim f(\theta_i \mid \mathbf{y}_i) & \text{with prob. } q_0 = \frac{\alpha_0 f(\mathbf{y}_i)}{\alpha_0 f(\mathbf{y}_i) + \sum_{j=1, j \neq i}^N f_{\theta_j}(\mathbf{y}_i)}. \end{cases} \quad (2)$$

5.1.3. The DPMM Classifier. The DPMM classifier has been proposed for unsupervised signal classification in CRs [29, 121, 124]. It is considered a Bayesian nonparametric unsupervised classifier in the sense of allowing the number of clusters (or classes) to increase with the data size [29, 121, 124]. This model allows classifying a set of feature vectors $\{\mathbf{y}_i\}_{i=1}^N$ into K clusters, where K is to be estimated from the data (in contrast with the K -means which require prior knowledge about K).

The DPMM is based on the Chinese restaurant process (CRP) which models the feature vectors as customers joining specific tables [127]. The CRP has been previously proposed for both feature classification and decision-making [124, 128]. In particular, [128] proposed a strategic game model based on the CRP, which is referred to as the Chinese restaurant game. This framework has been applied for channel access in CR networks [128]. In this paper, on the other hand,

we will present the CRP as an underlying framework for nonparametric signal classification in CRs, as in [124]. This model is formulated based on the DPMM, as discussed next.

The DPMM assumes that the feature vectors are drawn from a mixture model such that [29, 124, 127]

$$\begin{aligned} G &\sim DP(\alpha_0, G_0) \\ \theta_i | G &\sim G \\ \mathbf{y}_i | \theta_i &\sim f_{\theta_i}(\mathbf{y}_i), \end{aligned} \quad (3)$$

where G is a realization of the Dirichlet process $DP(\alpha_0, G_0)$ with parameters $\alpha_0 > 0$ and a prior distribution G_0 [29, 124, 127]. The nonparametric nature of the DPMM stems from the support distribution G which is drawn from a nonparametric set of distributions according to the Dirichlet process. The realization $G \sim DP(\alpha_0, G_0)$ is discrete and defined over an infinite set, thus allowing for infinitely many clusters. Based on this model, a feature vector \mathbf{y}_i is assumed to be drawn from a distribution $f_{\theta_i}(\mathbf{y}_i)$, where θ_i is drawn from G [29, 124]. According to this formulation, a cluster is defined as a set of feature vectors \mathbf{y}_i 's having identical parameters θ_i 's. Thus, we define the clusters parameters ϕ_k 's to denote the unique values of θ_i 's [29, 124, 127].

By assuming the above DPMM framework, the problem of feature classification can be formulated following a Bayesian approach which estimates the parameters θ_i 's for a set of feature vectors $\{\mathbf{y}_i\}_{i=1}^N$, assuming a nonparametric prior $G \sim DP(\alpha_0, G_0)$ for θ_i 's [129, 130]. The optimal parameters θ_i 's can thus be estimated based on the maximum a posteriori probability (MAP) criterion, which finds the parameters θ_i 's maximizing the posterior distribution of $f(\theta_1, \dots, \theta_N | \mathbf{y}_1, \dots, \mathbf{y}_N)$ [124, 129]. However, this posterior distribution cannot be obtained in closed form under the above DPMM construction. Thus, stochastic simulation approaches have been proposed to estimate θ_i 's by using the Gibbs sampling method [124, 129]. By following the Gibbs sampling approach, the DPMM-based classifier can be obtained by sampling θ_i 's from the posterior distribution $\theta_i | \{\theta_j\}_{j \neq i}, \mathbf{y}_1, \dots, \mathbf{y}_N$ in (2) [29, 124, 127, 129, 130].

This classification algorithm has been used for signal classification in CRs to determine the number of wireless systems in a certain RF environment [121, 124]. It was shown to accurately estimate the number of existing wireless systems without any prior information about the environment. However, this algorithm requires extensive computational efforts since it relies on an iterative Gibbs sampling process.

5.2. Reinforcement Learning Algorithms. In addition to its ability of classifying wireless signals, a CR is assumed to use machine learning techniques for decision-making [4, 9, 27, 29, 131–133]. This includes the ability to develop and adapt new strategies allowing us to maximize certain performance measures. In particular, the RL algorithms have been proposed to achieve such unsupervised decision-making in CRs [7, 29, 122, 123, 133–135]. The concept of RL is based on learning from experience by trial and error [29, 118]. After executing a certain action, the learning agent receives a certain reward showing how good it is to take a particular

action in a certain environment state [29, 118, 122]. As a result, the learning agent (the CR, in this case) will select certain actions that lead to the highest rewards in a particular state. The corresponding action selection method is based on an exploration-exploitation strategy that selects the highest reward action with a higher probability, compared to the other available actions [118]. This can be usually implemented using the ϵ -greedy approach which selects a greedy action with a probability $1 - \epsilon$ and a random action with small probability ϵ , thus allowing us to avoid local optima [7, 118].

The Q-learning algorithm is one of the RL algorithms that has been proposed for CR applications [7, 118, 122]. Under a Markov decision process (MDP) framework, the Q-learning can lead to optimal policy, yet without knowledge of the state transition probabilities [136, 137]. An MDP is characterized by the following elements [7, 29, 122, 133, 137]:

- (i) a finite set \mathcal{S} of states for the agent (i.e., secondary user);
- (ii) a finite set \mathcal{A} of actions that are available to the agent;
- (iii) a nonnegative function $p_t(s' | s, a)$ denoting the probability that the system is in state s' at time epoch $t + 1$, when the decision-maker chooses action $a \in \mathcal{A}$ in state $s \in \mathcal{S}$ at time t ;
- (iv) a real-valued function $r_t^{\text{MDP}}(s, a)$ defined for state $s \in \mathcal{S}$ and action $a \in \mathcal{A}$ to denote the value at time t of the reward received in period t [137].

At each time epoch t , the agent observes the current state s and chooses an action a . The objective is to find the optimal policy π that maximizes the expected discounted return [118]:

$$R(t) = \sum_{k=0}^{\infty} \gamma^k r_{t+k+1}(s_{t+k}, a_{t+k}), \quad (4)$$

where s_t and a_t are, respectively, the state and action at time $t \in \mathbb{Z}$.

The optimal policy of the MDP can be based on the Q-function (or action-value function) which determines how good it is to take a particular action a in a given state s . Formally, the Q-function is defined as the value of taking action a in state s under a policy π [118]:

$$Q^{\pi}(s, a) = \mathbb{E}_{\pi} \{R(t) | s_t = s, a_t = a\}. \quad (5)$$

This function can be computed using an iterative procedure as follows [7, 29, 122, 133, 136]:

$$\begin{aligned} Q(s_t, a_t) &\leftarrow (1 - \alpha) Q(s_t, a_t) \\ &+ \alpha \left[r_{t+1}(s_t, a_t) + \gamma \max_a Q(s_{t+1}, a) \right]. \end{aligned} \quad (6)$$

The RL algorithm can be represented in the block diagram of Figure 16 in which the learning agent receives the state observation o_t and the reward function r_t at each instant t [29, 118]. It then updates its Q-function at the learning stage and selects an appropriate action a_t . Under the MDP assumption, the Q-learning can guarantee convergence of the Q-function to its optimal value [136]. Thus, the optimal policy

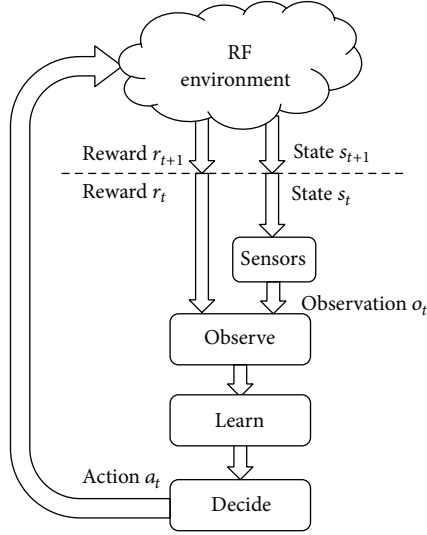


FIGURE 16: The RL cycle.

π can be obtained in function of the Q -function such that [29, 118]

$$a^*(s) = \begin{cases} \arg \max_{a \in \mathcal{A}} Q(s, a), & \text{with } \Pr = 1 - \epsilon \\ \sim U(\mathcal{A}), & \text{with } \Pr = \epsilon, \end{cases} \quad (7)$$

where $U(\mathcal{A})$ is the discrete uniform probability distribution over the set of actions \mathcal{A} and $a^*(s)$ is the optimal action selected in state s and corresponding to the optimal policy π .

The Q -learning algorithm has been proposed for two main CR applications:

- (1) aggregate interference control [8, 122];
- (2) spectrum sensing policy [7, 123].

In aggregate interference control, the Q -learning was proposed to optimize the power transmission of secondary CRs in a WRAN IEEE 802.22 CR network (CRN) [122]. The objective is to maintain the aggregated interference caused by the secondary networks to the DTV network below a certain threshold. In this scenario, the CRs constitute a distributed network and each radio tries to determine how much power it can transmit so that the aggregated interference on the primary receivers does not exceed a certain threshold level [122]. Simulation results have shown that the Q -learning algorithm can successfully control the aggregate interference in a WRAN scenario [122].

On the other hand, the Q -learning algorithm has been proposed for opportunistic spectrum access (OSA) applications to coordinate the actions of CRs in a distributed CRN [7]. Given a set of CRs, the Q -learning can determine the channel that should be sensed by each CR at each time instant in order to maximize the average utilization of idle primary channels while limiting collision among secondary cognitive users [7]. The Q -learning algorithm was shown to achieve near-optimal performance in such OSA applications [7]. However, it cannot guarantee optimal policy

for the decentralized partially observable decision-making problem, which is considered one of the most challenging problems for MDPs, in general [137, 138]. However, given the limited amount of information, the Q -learning algorithm can be considered as one of the most effective low-complexity approaches for distributed partially observable decision-making scenarios [7, 122, 133].

6. Conclusion

This paper presented a review of three major front-end CR elements: the RF part, spectrum sensing, and machine learning. For the RF part, three types of antennas were presented: UWB antennas, used for spectrum sensing, frequency-reconfigurable/tunable antennas for communicating over white spaces (also for sequential channel sensing), and UWB antennas with reconfigurable band notches for overlay UWB CR. Also for the RF part, it was shown that the main design challenges are those pertaining to the ADCs/DACs, dynamic range, LNAs, filters, mixers, and synthesizers. Sophisticated spectrum sensing algorithms that overcome the challenges resulting from the adaptive behavior of CR transceivers need to be developed to relax RF designs and provide accurate decisions. A CE executes actions based on certain rules and policies that are learnt from past experience. With the growing complexity of the current wireless networks, more sophisticated learning algorithms should be developed, taking into account the heterogeneous structure of existing and future communication networks.

Conflict of Interests

The authors declare that there is no conflict of interests regarding the publication of this paper.

References

- [1] S. Haykin, "Cognitive radio: brain-empowered wireless communications," *IEEE Journal on Selected Areas in Communications*, vol. 23, no. 2, pp. 201–220, 2005.
- [2] A. Goldsmith, S. A. Jafar, I. Maric, and S. Srinivasa, "Breaking spectrum gridlock with cognitive radios: an information theoretic perspective," *Proceedings of the IEEE*, vol. 97, no. 5, pp. 894–914, 2009.
- [3] N. Devroye, M. Vu, and V. Tarokh, "Cognitive radio networks: highlights of information theoretic limits, models, and design," *IEEE Signal Processing Magazine*, vol. 25, no. 6, pp. 12–23, 2008.
- [4] J. Mitola III and G. Q. Maguire Jr., "Cognitive radio: making software radios more personal," *IEEE Personal Communications*, vol. 6, no. 4, pp. 13–18, 1999.
- [5] J. Mitola III, "Cognitive radio architecture evolution," *Proceedings of the IEEE*, vol. 97, no. 4, pp. 626–641, 2009.
- [6] T. Yücek and H. Arslan, "A survey of spectrum sensing algorithms for cognitive radio applications," *IEEE Communications Surveys and Tutorials*, vol. 11, no. 1, pp. 116–130, 2009.
- [7] M. Bkassiny, S. K. Jayaweera, and K. A. Avery, "Distributed Reinforcement Learning based MAC protocols for autonomous cognitive secondary users," in *Proceedings of the 20th Annual Wireless and Optical Communications Conference (WOCC '11)*, pp. 1–6, Newark, NJ, USA, April 2011.

- [8] L. Giupponi, A. Galindo-Serrano, P. Blasco, and M. Dohler, "Docitive networks: an emerging paradigm for dynamic spectrum management," *IEEE Wireless Communications*, vol. 17, no. 4, pp. 47–54, 2010.
- [9] S. K. Jayaweera and C. G. Christodoulou, "Radiobots: architecture, algorithms and realtime reconfigurable antenna designs for autonomous, self-learning future cognitive radios," Tech. Rep. EECETR-11-0001, University of New Mexico, 2011, <http://repository.unm.edu/handle/1928/12306>.
- [10] A. Sonnenschein and P. M. Fishman, "Radiometric detection of spread-spectrum signals in noise of uncertain power," *IEEE Transactions on Aerospace and Electronic Systems*, vol. 28, no. 3, pp. 654–660, 1992.
- [11] S. M. Kay, *Fundamentals of Statistical Signal Processing: Detection Theory*, Prentice-Hall, Upper Saddle River, NJ, USA, 1998.
- [12] Z. Ye, G. Memik, and J. Grosspietsch, "Energy detection using estimated noise variance for spectrum sensing in cognitive radio networks," in *Proceedings of the IEEE Wireless Communications and Networking Conference (WCNC '08)*, pp. 711–716, Las Vegas, Nev, USA, March–April 2008.
- [13] H. S. Chen, W. Gao, and D. G. Daut, "Signature based spectrum sensing algorithms for IEEE 802.22 WRAN," in *Proceedings of the IEEE International Conference on Communications (ICC '07)*, pp. 6487–6492, Glasgow, UK, June 2007.
- [14] S. Xu, Z. Zhao, and J. Shang, "Spectrum sensing based on cyclostationarity," in *Proceedings of the IEEE Workshop on Power Electronics and Intelligent Transportation System (PEITS '08)*, pp. 171–174, Guangzhou, China, August 2008.
- [15] W. A. Gardner, "Exploitation of spectral redundancy in cyclostationary signals," *IEEE Signal Processing Magazine*, vol. 8, no. 2, pp. 14–36, 1991.
- [16] W. A. Gardner, A. Napolitano, and L. Paura, "Cyclostationarity: half a century of research," *Signal Processing*, vol. 86, no. 4, pp. 639–697, 2006.
- [17] W. A. Gardner, "Spectral correlation of modulated signals—part I: analog modulation," *IEEE Transactions on Communications*, vol. 35, no. 6, pp. 584–595, 1987.
- [18] W. A. Gardner, W. A. Brown III, and C. Chen, "Spectral correlation of modulated signals—part II: digital modulation," *IEEE Transactions on Communications*, vol. 35, no. 6, pp. 595–601, 1987.
- [19] Y. H. Zeng and Y. C. Liang, "Covariance based signal detections for cognitive radio," in *Proceedings of the 2nd IEEE International Symposium on New Frontiers in Dynamic Spectrum Access Networks (DySPAN '07)*, pp. 202–207, Dublin, Ireland, April 2007.
- [20] Y. H. Zeng and Y. C. Liang, "Spectrum-sensing algorithms for cognitive radio based on statistical covariances," *IEEE Transactions on Vehicular Technology*, vol. 58, no. 4, pp. 1804–1815, 2009.
- [21] Y. H. Zeng and Y. C. Liang, "Eigenvalue based sensing algorithms," *IEEE 802. 22-06/0118r0*, 2006.
- [22] Y. H. Zeng and Y. C. Liang, "Maximum-minimum eigenvalue detection for cognitive radio," in *Proceedings of the 18th Annual IEEE International Symposium on Personal, Indoor and Mobile Radio Communications (PIMRC '07)*, Athens, Greece, September 2007.
- [23] Y. H. Zeng and Y. C. Liang, "Eigenvalue-based spectrum sensing algorithms for cognitive radio," *IEEE Transactions on Communications*, vol. 57, no. 6, pp. 1784–1793, 2009.
- [24] G. Fettweis, M. Lohning, D. Petrovic, M. Windisch, P. Zillmann, and W. Rave, "Dirty RF: a new paradigm," in *Proceedings of the IEEE 16th International Symposium on Personal, Indoor and Mobile Radio Communications (PIMRC '05)*, vol. 4, pp. 2347–2355, Berlin, Germany, September 2005.
- [25] M. Valkama, A. S. H. Ghadam, L. Anttila, and M. Renfors, "Advanced digital signal processing techniques for compensation of nonlinear distortion in wideband multicarrier radio receivers," *IEEE Transactions on Microwave Theory and Techniques*, vol. 54, no. 6, pp. 2356–2366, 2006.
- [26] M. Grimm, R. K. Sharma, M. A. Hein, and R. S. Thomä, "DSP-based mitigation of RF front-end non-linearity in cognitive wideband receivers," *Frequenz*, vol. 6, no. 9–10, pp. 303–310, 2012.
- [27] C. Clancy, J. Hecker, E. Stuntebeck, and T. O'Shea, "Applications of machine learning to cognitive radio networks," *IEEE Wireless Communications*, vol. 14, no. 4, pp. 47–52, 2007.
- [28] S. K. Jayaweera, Y. Li, M. Bkassiny, C. Christodoulou, and K. A. Avery, "Radiobots: the autonomous, self-learning future cognitive radios," in *Proceedings of the International Symposium on Intelligent Signal Processing and Communication Systems (ISPACS '11)*, pp. 1–5, Chiang Mai, Thailand, December 2011.
- [29] M. Bkassiny, Y. Li, and S. K. Jayaweera, "A survey on machine-learning techniques in cognitive radios," *IEEE Communications Surveys Tutorials*, vol. 15, no. 3, pp. 1136–1159, 2013.
- [30] M. Al-Husseini, K. Y. Kabalan, A. El-Hajj, and C. G. Christodoulou, "Reconfigurable microstrip antennas for cognitive radio," in *Advancement in Microstrip Antennas with Recent Applications*, A. Kishk, Ed., chapter 14, pp. 337–362, InTech, Rijeka, Croatia, 2013.
- [31] P. Samal, P. Soh, and G. Vandenbosch, "A systematic design procedure for microstrip-based unidirectional UWB antennas," *Progress In Electromagnetics Research*, vol. 143, pp. 105–130, 2013.
- [32] B. Gong, J. Li, Q. R. Zheng, Y. Z. Yin, and X. S. Ren, "A compact inductively loaded monopole antenna for future UWB applications," *Progress In Electromagnetics Research*, vol. 139, pp. 265–275, 2013.
- [33] W. Liu, Y. Yin, W. Xu, and S. Zuo, "Compact open-slot antenna with bandwidth enhancement," *IEEE Antennas and Wireless Propagation Letters*, vol. 10, pp. 850–853, 2011.
- [34] M.-R. Ghaderi and F. Mohajeri, "A compact hexagonal wide-slot antenna with microstrip-fed monopole for UWB application," *IEEE Antennas and Wireless Propagation Letters*, vol. 10, pp. 682–685, 2011.
- [35] H. Oraizi and S. Hedayati, "Miniaturized UWB monopole microstrip antenna design by the combination of Giuseppe Peano and Sierpinski carpet fractals," *IEEE Antennas and Wireless Propagation Letters*, vol. 10, pp. 67–70, 2011.
- [36] P. C. Ooi and K. T. Selvan, "The effect of ground plane on the performance of a square loop CPW-fed printed antenna," *Progress In Electromagnetics Research Letters*, vol. 19, pp. 103–111, 2010.
- [37] M. Al-Husseini, A. Ramadan, Y. Tawk, A. El-Hajj, and K. Y. Kabalan, "Design and ground plane consideration of a CPW-Fed UWB antenna," in *Proceedings of the International Conference on Electrical and Electronics Engineering (ELECO '09)*, pp. II-151–II-153, Bursa, Turkey, November 2009.
- [38] M. Al-Husseini, A. Ramadan, A. El-Hajj, and K. Kabalan, "Design of a compact and low-cost fractal-based UWB PCB Antenna," in *Proceedings of the National Radio Science Conference (NRSC '09)*, pp. 1–8, Cairo, Egypt, March 2009.
- [39] A. Mehdipour, K. Mohammadpour-Aghdam, R. Faraji-Dana, and M.-R. Kashani-Khatib, "A novel coplanar waveguide-fed

- slot antenna for ultrawideband applications," *IEEE Transactions on Antennas and Propagation*, vol. 56, no. 12, pp. 3857–3862, 2008.
- [40] M. Al-Husseini, A. El-Hajj, and K. Y. Kabalan, "A 1.9–13.5 GHz low-cost microstrip antenna," in *Proceedings of the International Wireless Communications and Mobile Computing Conference (IWCMC '08)*, pp. 1023–1025, Crete Island, Greece, August 2008.
- [41] Z. N. Low, J. H. Cheong, and C. L. Law, "Low-cost PCB antenna for UWB applications," *IEEE Antennas and Wireless Propagation Letters*, vol. 4, no. 1, pp. 237–239, 2005.
- [42] M. Al-Husseini, Y. Tawk, A. El-Hajj, and K. Y. Kabalan, "A low-cost microstrip antenna for 3G/WLAN/WiMAX and UWB applications," in *Proceedings of the International Conference on Advances in Computational Tools for Engineering Applications (ACTEA '09)*, pp. 68–70, Zouk Mosbeh, Lebanon, July 2009.
- [43] M. Al-Husseini, A. Ramadan, Y. Tawk, A. El-Hajj, and K. Y. Kabalan, "Design and ground plane optimization of a CPW-fed ultra-wideband antenna," *Turkish Journal of Electrical Engineering and Computer Sciences*, vol. 19, no. 2, pp. 243–250, 2011.
- [44] H. Zhang, X. Zhou, and T. Chen, "Ultra-wideband cognitive radio for dynamic spectrum accessing networks," in *Cognitive Radio Networks*, Y. Xiao and F. Hu, Eds., pp. 353–382, CRC Press, Boca Raton, Fla, USA, 2009.
- [45] L. Safatly, M. Al-Husseini, A. El-Hajj, and K. Kabalan, "Advanced techniques and antenna design for pulse shaping in UWB cognitive radio," *International Journal of Antennas and Propagation*, vol. 2012, Article ID 390280, 8 pages, 2012.
- [46] J. B. Pendry, A. J. Holden, D. J. Robbins, and W. J. Stewart, "Magnetism from conductors and enhanced nonlinear phenomena," *IEEE Transactions on Microwave Theory and Techniques*, vol. 47, no. 11, pp. 2075–2084, 1999.
- [47] F. Falcone, T. Lopetegui, M. A. G. Laso et al., "Babinet principle applied to the design of metasurfaces and metamaterials," *Physical Review Letters*, vol. 93, no. 19, Article ID 197401, 4 pages, 2004.
- [48] P. Moeikham, C. Mahatthanajatuphat, and P. Akkaraekthalin, "A compact uwb antenna with a quarter-wavelength strip in a rectangular slot for 5.5 GHz band notch," *International Journal of Antennas and Propagation*, vol. 2013, Article ID 574128, 9 pages, 2013.
- [49] B. Yan, D. Jiang, R. M. Xu, and Y. H. Xu, "A UWB band-pass antenna with triple-notched band using common direction rectangular complementary split-ring resonators," *International Journal of Antennas and Propagation*, vol. 2013, Article ID 934802, 6 pages, 2013.
- [50] X. Liu, Y.-Z. Yin, P. Liu, J. Wang, and B. Xu, "A CPW-fed dual bandnotched UWB antenna with a pair of bended dual-L-shape parasitic branches," *Progress In Electromagnetics Research*, vol. 136, pp. 623–634, 2013.
- [51] R. Azim and M. Islam, "Compact planar UWB antenna with band notch characteristics for WLAN and DSRC," *Progress In Electromagnetics Research*, vol. 133, pp. 391–406, 2013.
- [52] J. R. Kelly, P. S. Hall, and P. Gardner, "Band-notched UWB antenna incorporating a microstrip open-loop resonator," *IEEE Transactions on Antennas and Propagation*, vol. 59, no. 8, pp. 3045–3048, 2011.
- [53] T.-D. Nguyen, D.-H. Lee, and H.-C. Park, "Design and analysis of compact printed triple band-notched UWB antenna," *IEEE Antennas and Wireless Propagation Letters*, vol. 10, pp. 403–406, 2011.
- [54] M. Almalkawi and V. Devabhaktuni, "Ultrawideband antenna with triple band-notched characteristics using closed-loop ring resonators," *IEEE Antennas and Wireless Propagation Letters*, vol. 10, pp. 959–962, 2011.
- [55] D.-O. Kim, N.-I. Jo, H.-A. Jang, and C.-Y. Kim, "Design of the ultrawideband antenna with a quadruple-band rejection characteristics using a combination of the complementary split ring resonators," *Progress In Electromagnetics Research*, vol. 112, pp. 93–107, 2011.
- [56] Y. Li, W. Li, and Q. Ye, "A reconfigurable triple-notch-band antenna integrated with defected microstrip structure band-stop filter for ultrawideband cognitive radio applications," *International Journal of Antennas and Propagation*, vol. 2013, Article ID 472645, 13 pages, 2013.
- [57] T. Aboufoul, A. Alomainy, and C. Parini, "Reconfigured and notched tapered slot UWB antenna for cognitive radio applications," *International Journal of Antennas and Propagation*, vol. 2012, Article ID 160219, 8 pages, 2012.
- [58] J. Perruisseau-Carrier, P. Pardo-Carrera, and P. Miskovsky, "Modeling, design and characterization of a very wideband slot antenna with reconfigurable band rejection," *IEEE Transactions on Antennas and Propagation*, vol. 58, no. 7, pp. 2218–2226, 2010.
- [59] C.-Y. Sim, W.-T. Chung, and C.-H. Lee, "Planar uwb antenna with 5ghz band rejection switching function at ground plane," *Progress In Electromagnetics Research*, vol. 106, pp. 321–333, 2010.
- [60] M. Al-Husseini, J. Costantine, C. G. Christodoulou, S. E. Barbin, A. El-Hajj, and K. Y. Kabalan, "A reconfigurable frequency-notched UWB antenna with split-ring resonators," in *Proceedings of the Asia-Pacific Microwave Conference (APMC '10)*, pp. 618–621, Yokohama, Japan, December 2010.
- [61] M. Al-Husseini, A. Ramadan, A. El-Hajj, K. Y. Kabalan, Y. Tawk, and C. G. Christodoulou, "Design based on complementary split-ring resonators of an antenna with controllable band notches for UWB cognitive radio applications," in *Proceedings of the IEEE International Symposium on Antennas and Propagation (APSURSI)*, pp. 1120–1122, Spokane, Wash, USA, July 2011.
- [62] M. Al-Husseini, L. Safatly, A. Ramadan, A. El-Hajj, K. Y. Kabalan, and C. G. Christodoulou, "Reconfigurable filter antennas for pulse adaptation in UWB cognitive radio systems," *Progress In Electromagnetics Research B*, no. 37, pp. 327–342, 2011.
- [63] E. Ebrahimi, J. R. Kelly, and P. S. Hall, "Integrated wide-narrowband antenna for multi-standard radio," *IEEE Transactions on Antennas and Propagation*, vol. 59, no. 7, pp. 2628–2635, 2011.
- [64] G. Augustin and A. Denidni, "An integrated ultra wideband/narrow band antenna in uniplanar configuration for cognitive radio systems," *IEEE Transactions on Antennas and Propagation*, vol. 60, no. 11, pp. 5479–5484, 2012.
- [65] M. Al-Husseini, Y. Tawk, C. G. Christodoulou, A. El-Hajj, and K. Y. Kabalan, "A reconfigurable cognitive radio antenna design," in *Proceedings of the IEEE Antennas and Propagation Society International Symposium (APSURSI)*, pp. 1–4, Toronto, Canada, July 2010.
- [66] M. R. Hamid, P. Gardner, P. S. Hall, and F. Ghanem, "Switched-band Vivaldi antenna," *IEEE Transactions on Antennas and Propagation*, vol. 59, no. 5, pp. 1472–1480, 2011.
- [67] M. R. Hamid, P. Gardner, P. S. Hall, and F. Ghanem, "Vivaldi antenna with integrated switchable band pass resonator," *IEEE Transactions on Antennas and Propagation*, vol. 59, no. 11, pp. 4008–4015, 2011.
- [68] T. Aboufoul, A. Alomainy, and C. Parini, "Reconfiguring UWB monopole antenna for cognitive radio applications using GaAs FET switches," *IEEE Antennas and Wireless Propagation Letters*, vol. 11, pp. 392–394, 2012.

- [69] M. Al-Husseini, A. Ramadan, M. E. Zamudio, C. G. Christodoulou, A. El-Hajj, and K. Y. Kabalan, "A UWB antenna combined with a reconfigurable bandpass filter for cognitive radio applications," in *Proceedings of the IEEE-APS Topical Conference on Antennas and Propagation in Wireless Communications (APWC '11)*, pp. 902–904, Torino, Italy, September 2011.
- [70] Y. Cai, Y. Guo, and T. Bird, "A frequency reconfigurable printed yagiuda dipole antenna for cognitive radio applications," *IEEE Transactions on Antennas and Propagation*, vol. 60, no. 6, pp. 2905–2912, 2012.
- [71] M. Y. A. Shahine, M. Al-Husseini, Y. Nasser, K. Y. Kabalan, and A. El-Hajj, "A reconfigurable miniaturized spiral monopole antenna for TV white spaces," in *Proceedings of the 34th Progress in Electromagnetics Research Symposium (PIERS '13)*, Stockholm, Sweden, August 2013.
- [72] G. Mansour, P. Hall, P. Gardner, and M.-K. A. Rahim, "Tunable slotloaded patch antenna for cognitive radio," in *Proceedings of the Loughborough Antennas and Propagation Conference (LAPC '12)*, Loughborough, UK, November 2012.
- [73] Y. Tawk, M. E. Zamudio, J. Costantine, and C. Christodoulou, "A cognitive radio reconfigurable 'filtenna'," in *Proceedings of the 6th European Conference on Antennas and Propagation (EUCAP '12)*, pp. 3565–3568, Prague, Czech Republic, March 2012.
- [74] V. Nguyen, F. Villain, and Y. Le Guillou, "Cognitive radio RF: overview and challenges," *VLSI Design*, 2012.
- [75] M. Kitsunezuka, K. Kunihiro, and M. Fukaishi, "Efficient use of the spectrum," *IEEE Microwave Magazine*, vol. 13, no. 1, pp. 55–63, 2012.
- [76] B. Razavi, "Cognitive radio design challenges and techniques," *IEEE Journal of Solid-State Circuits*, vol. 45, no. 8, pp. 1542–1553, 2010.
- [77] J. Arias, L. Quintanilla, J. Segundo, L. Enríquez, J. Vicente, and J. M. Hernández-Mangas, "Parallel continuous-time $\Delta\Sigma$ ADC for OFDM UWB receivers," *IEEE Transactions on Circuits and Systems I*, vol. 56, no. 7, pp. 1478–1487, 2009.
- [78] C. Lelandais-Perrault, T. Petrescu, D. Poulton, P. Duhamel, and J. Oksman, "Wideband, bandpass, and versatile hybrid filter bank A/D conversion for software radio," *IEEE Transactions on Circuits and Systems I*, vol. 56, no. 8, pp. 1772–1782, 2009.
- [79] C.-C. Huang, C.-Y. Wang, and J.-T. Wu, "A CMOS 6-Bit 16-GS/s time-interleaved ADC using digital background calibration techniques," *IEEE Journal of Solid-State Circuits*, vol. 46, no. 4, pp. 848–858, 2011.
- [80] A. Gruget, M. Roger, V. T. Nguyen, C. Lelandais-Perrault, P. Bénabès, and P. Loumeau, "Wide-band multipath A to D converter for cognitive radio applications," in *Proceedings of the IEEE International Microwave Workshop Series on RF Front-ends for Software Defined and Cognitive Radio Solutions (IMWS '10)*, pp. 73–76, Aveiro, Portugal, February 2010.
- [81] A. Gruget, M. Roger, V. T. Nguyen, C. Lelandais-Perrault, P. Bénabès, and P. Loumeau, "Optimization of bandpass charge sampling filters in hybrid filter banks converters for cognitive radio applications," in *Proceedings of the 20th European Conference on Circuit Theory and Design (ECCTD '11)*, pp. 785–788, Linköping, Sweden, August 2011.
- [82] Z. Boos, A. Menkhoff, F. Kuttner et al., "A fully digital multi-mode polar transmitter employing 17b RF DAC in 3G mode," in *Proceedings of the IEEE International Solid-State Circuits Conference (ISSCC '11)*, pp. 376–377, San Francisco, Calif, USA, February 2011.
- [83] A. Pozsgay, T. Zoune, R. Hossain, M. Boulemnaker, V. Knapik, and S. Grange, "A fully digital 65 nm CMOS transmitter for the 2.4-to-2.7GHz WiFi/WiMAX bands using 5.4 GHz $\delta\sigma$ RF DACs," in *Proceedings of the IEEE International Solid State Circuits Conference (ISSCC '08)*, pp. 355–619, San Francisco, Calif, USA, February 2008.
- [84] J. Borremans, G. Mandal, V. Giannini et al., "A 40 nm CMOS 0.4–6 GHz receiver resilient to out-of-band blockers," *IEEE Journal of Solid-State Circuits*, vol. 46, no. 7, pp. 1659–1671, 2011.
- [85] M. C. M. Soer, E. A. M. Klumperink, Z. Ru, F. E. van Vliet, and B. Nauta, "A 0.2-to-2.0 GHz 65 nm CMOS receiver without LNA achieving >11 dBm IIP3 and <6.5 dB NF," in *Proceedings of the IEEE International Solid-State Circuits Conference (ISSCC '09)*, pp. 222–223, San Francisco, Calif, USA, February 2009.
- [86] C. Andrews and A. C. Molnar, "A passive mixer-first receiver with digitally controlled and widely tunable RF interface," *IEEE Journal of Solid-State Circuits*, vol. 45, no. 12, pp. 2696–2708, 2010.
- [87] A. Mirzaie, A. Yazdi, Z. Zhou, E. Chang, P. Suri, and H. Darabi, "A 65 nm CMOS quad-band SAW-less receiver for GSM/GPRS/EDGE," in *Proceedings of the Symposium on VLSI Circuits (VLSIC '10)*, pp. 179–180, Honolulu, Hawaii, USA, June 2010.
- [88] A. Ghaffari, E. A. M. Klumperink, M. C. M. Soer, and B. Nauta, "Tunable high-q N-Path Band-Pass filters: modeling and verification," *IEEE Journal of Solid-State Circuits*, vol. 46, no. 5, pp. 998–1010, 2011.
- [89] S. C. Blaakmeer, E. A. M. Klumperink, B. Nauta, and D. M. W. Leenaerts, "An inductorless wideband balun-LNA in 65 nm CMOS with balanced output," in *Proceedings of the 33rd European Solid-State Circuits Conference (ESSCIRC '07)*, pp. 364–367, Munich, Germany, September 2007.
- [90] Z. Ru, N. A. Moseley, E. A. M. Klumperink, and B. Nauta, "Digitally enhanced software-defined radio receiver robust to out-of-band interference," *IEEE Journal of Solid-State Circuits*, vol. 44, no. 12, pp. 3359–3375, 2009.
- [91] A. A. Rafi, A. Piovaccari, P. Vancorenland, and T. Tuttle, "A harmonic rejection mixer robust to RF device mismatches," in *Proceedings of the IEEE International Solid-State Circuits Conference (ISSCC '11)*, pp. 66–68, San Francisco, Calif, USA, February 2011.
- [92] J. Borremans, K. Vengattaramane, V. Giannini, B. Debaillie, W. van Thillo, and J. Craninckx, "A 86 MHz–12 GHz digital-intensive PLL for software-defined radios, using a 6 fJ/step TDC in 40 nm digital CMOS," *IEEE Journal of Solid-State Circuits*, vol. 45, no. 10, pp. 2116–2129, 2010.
- [93] J. Mitola, *Cognitive radio: an integrated agent architecture for software defined radio [Ph.D. thesis]*, Royal Institute of Technology, KTH, 2000.
- [94] Z. Quan, S. Cui, A. H. Sayed, and H. V. Poor, "Optimal multi-band and joint detection for spectrum sensing in cognitive radio networks," *IEEE Transactions on Signal Processing*, vol. 57, no. 3, pp. 1128–1140, 2009.
- [95] Z. Tian and G. B. Giannakis, "A wavelet approach to wideband spectrum sensing for cognitive radios," in *Proceedings of the 1st International Conference on Cognitive Radio Oriented Wireless Networks and Communications (CROWNCOM '06)*, pp. 1–5, Mykonos Island, Greece, June 2006.
- [96] W. Liu and S. Ding, "Multiuser detections based on global optimality necessary conditions for binary quadratic programming," in *Proceedings of the 2nd International Conference on Innovative Computing, Information and Control (ICICIC '07)*, Kumamoto, Japan, September 2007.
- [97] Z. Tian and G. B. Giannakis, "Compressed sensing for wideband cognitive radios," in *Proceedings of the IEEE International*

- Conference on Acoustics, Speech and Signal Processing (ICASSP '07)*, vol. 4, pp. IV-1357–IV-1360, Honolulu, Hawaii, USA, April 2007.
- [98] E. G. Larsson and M. Skoglund, "Cognitive radio in a frequency-planned environment: some basic limits," *IEEE Transactions on Wireless Communications*, vol. 7, no. 12, pp. 4800–4806, 2008.
 - [99] A. Sahai, N. Hoven, and R. Tandra, "Some fundamental limits on cognitive radio," in *Proceedings of the 42nd Annual Allerton Conference on Communication, Control, and Computing*, pp. 1662–1671, Monticello, Ill, USA, October 2004.
 - [100] R. Tandra and A. Sahai, "SNR walls for signal detection," *IEEE Journal on Selected Topics in Signal Processing*, vol. 2, no. 1, pp. 4–17, 2008.
 - [101] E. G. Larsson and G. Regnoli, "Primary system detection for cognitive radio: does small-scale fading help?" *IEEE Communications Letters*, vol. 11, no. 10, pp. 799–801, 2007.
 - [102] I. M. Johnstone, "On the distribution of the largest eigenvalue in principal components analysis," *Annals of Statistics*, vol. 29, no. 2, pp. 295–327, 2001.
 - [103] Z. Khalaf, A. Nafkha, and J. Palicot, "Blind spectrum detector for cognitive radio using compressed sensing and symmetry property of the second order cyclic autocorrelation," in *Proceedings of the 7th International ICST Conference on Cognitive Radio Oriented Wireless Networks and Communications (CROWN-COM '12)*, pp. 291–296, Stockholm, Sweden, June 2012.
 - [104] G. Davis, S. Mallat, and M. Avellaneda, "Adaptive greedy approximations," *Constructive Approximation*, vol. 13, no. 1, pp. 57–98, 1997.
 - [105] A. Sahai and D. Cabric, "Spectrum sensing: fundamental limits and practical challenges," in *Proceedings of the IEEE International Symposium on New Frontiers in Dynamic Spectrum Access Networks (DySPAN '05)*, 2005.
 - [106] H. Sun, A. Nallanathan, C. X. Wang, and Y. Chen, "Wideband spectrum sensing for cognitive radio networks: a survey," *IEEE Wireless Communications*, vol. 20, no. 2, pp. 74–81, 2013.
 - [107] S. Chantaraskul and K. Moessner, "Implementation of wavelet analysis for spectrum opportunity detection," in *Proceedings of the IEEE 20th Personal, Indoor and Mobile Radio Communications Symposium (PIMRC '09)*, pp. 2310–2314, Tokyo, Japan, September 2009.
 - [108] Y. L. Polo, Y. Wang, A. Pandharipande, and G. Leus, "Compressive wide-band spectrum sensing," in *Proceedings of the IEEE International Conference on Acoustics, Speech, and Signal Processing (ICASSP '09)*, pp. 2337–2340, Taipei City, Taiwan, April 2009.
 - [109] S. G. Mallat and Z. Zhang, "Matching pursuits with time-frequency dictionaries," *IEEE Transactions on Signal Processing*, vol. 41, no. 12, pp. 3397–3415, 1993.
 - [110] Y. Zhao and L. Morales-Tirado, "Cognitive radio technology: principles and practice," in *Proceedings of the International Conference on Computing, Networking and Communications (ICNC '12)*, pp. 650–654, Maui, Hawaii, USA, February 2012.
 - [111] Y. Kon, M. Ito, N. Hassel, M. Hasegawa, K. Ishizu, and H. Harada, "Autonomous parameter optimization of a heterogeneous wireless network aggregation system using machine learning algorithms," in *Proceedings of the IEEE Consumer Communications and Networking Conference (CCNC '12)*, pp. 894–898, Las Vegas, Nev, USA, January 2012.
 - [112] P. Venkatraman, B. Hamdaoui, and M. Guizani, "Opportunistic bandwidth sharing through reinforcement learning," *IEEE Transactions on Vehicular Technology*, vol. 59, no. 6, pp. 3148–3153, 2010.
 - [113] J. Oksanen, J. Lundén, and V. Koivunen, "Reinforcement learning method for energy efficient cooperative multiband spectrum sensing," in *Proceedings of the IEEE International Workshop on Machine Learning for Signal Processing (MLSP '10)*, pp. 59–64, Kittila, Finland, September 2010.
 - [114] Z. Chen and R. C. Qiu, "Q-learning based bidding algorithm for spectrum auction in cognitive radio," in *Proceedings of the IEEE SoutheastCon 2011*, pp. 409–412, Nashville, Tenn, USA, March 2011.
 - [115] K.-L. A. Yau, P. Komisarczuk, and P. D. Teal, "Performance analysis of reinforcement learning for achieving context awareness and intelligence in mobile cognitive radio networks," in *Proceedings of the IEEE International Conference on Advanced Information Networking and Applications (AINA '11)*, pp. 1–8, Singapore, March 2011.
 - [116] P. Venkatraman and B. Hamdaoui, "Cooperative Q-learning for multiple secondary users in dynamic spectrum access," in *Proceedings of the 7th International Wireless Communications and Mobile Computing Conference (IWCMC '11)*, pp. 238–242, Istanbul, Turkey, July 2011.
 - [117] D. Kumar, N. Kanagaraj, and R. Srilakshmi, "Harmonized q-learning for radio resource management in lte based networks," in *Proceedings of ITU Kaleidoscope: Building Sustainable Communities*, 2013.
 - [118] R. S. Sutton and A. G. Barto, *Reinforcement Learning: An Introduction*, MIT Press, Cambridge, Mass, USA, 1998.
 - [119] M. Bkassiny, S. K. Jayaweera, Y. Li, and K. A. Avery, "Wideband spectrum sensing and non-parametric signal classification for autonomous self-learning cognitive radios," *IEEE Transactions on Wireless Communications*, vol. 11, no. 7, pp. 2596–2605, 2012.
 - [120] T. C. Clancy, A. Khawar, and T. R. Newman, "Robust signal classification using unsupervised learning," *IEEE Transactions on Wireless Communications*, vol. 10, no. 4, pp. 1289–1299, 2011.
 - [121] N. Shetty, S. Pollin, and P. Pawelczak, "Identifying spectrum usage by unknown systems using experiments in machine learning," in *Proceedings of the IEEE Wireless Communications and Networking Conference (WCNC '09)*, pp. 1–6, Budapest, Hungary, April 2009.
 - [122] A. Galindo-Serrano and L. Giupponi, "Distributed Q-learning for aggregated interference control in cognitive radio networks," *IEEE Transactions on Vehicular Technology*, vol. 59, no. 4, pp. 1823–1834, 2010.
 - [123] K.-L. A. Yau, P. Komisarczuk, and P. D. Teal, "Applications of reinforcement learning to cognitive radio networks," in *Proceedings of the IEEE International Conference on Communications Workshops, ICC 2010*, pp. 1–6, Capetown, South Africa, May 2010.
 - [124] M. Bkassiny, S. K. Jayaweera, and Y. Li, "Multidimensional Dirichlet process-based non-parametric signal classification for autonomous self-learning cognitive radios," *IEEE Transactions on Wireless Communications*, vol. 12, no. 11, pp. 5413–5423, 2013.
 - [125] C. Phelps and R. Buehrer, "Signal classification by probabilistic reasoning," in *Proceedings of the IEEE Radio and Wireless Symposium (RWS '13)*, pp. 154–156, Austin, Tex, USA, January 2013.
 - [126] D. Pelleg and A. Moore, "X-means: extending k-means with efficient estimation of the number of clusters," in *Proceedings of the 7th International Conference on Machine Learning (ICML '00)*, Stanford, Calif, USA, June-July 2000.

- [127] Y. W. Teh, M. I. Jordan, M. J. Beal, and D. M. Blei, "Hierarchical Dirichlet processes," *Journal of the American Statistical Association*, vol. 101, no. 476, pp. 1566–1581, 2006.
- [128] C.-Y. Wang, Y. Chen, and K. Liu, "Sequential Chinese restaurant game," *IEEE Transactions on Signal Processing*, vol. 61, no. 3, pp. 571–584, 2013.
- [129] M. D. Escobar and M. West, "Bayesian density estimation and inference using mixtures," *Journal of the American Statistical Association*, vol. 90, no. 430, pp. 577–588, 1995.
- [130] M. D. Escobar, "Estimating normal means with a dirichlet process prior," *Journal of the American Statistical Association*, vol. 89, no. 425, pp. 268–277, 1994.
- [131] J. Mitola, *Cognitive radio: an integrated agent architecture for software defined radio [Ph.D. thesis]*, KTH, 2000.
- [132] V. Stavroulaki, A. Bantouna, Y. Kritikou et al., "Knowledge management toolbox: machine learning for cognitive radio networks," *IEEE Vehicular Technology Magazine*, vol. 7, no. 2, pp. 91–99, 2012.
- [133] L. Gavrilovska, V. Atanasovski, I. Macaluso, and L. DaSilva, "Learning and reasoning in cognitive radio networks," *IEEE Communications Surveys and Tutorials*, vol. 15, no. 4, pp. 1761–1777, 2013.
- [134] Y. Li, S. K. Jayaweera, M. Bkassiny, and C. Ghosh, "Learning-aided sub-band selection algorithms for spectrum sensing in wide-band cognitive radios," *IEEE Transactions on Wireless Communications*. In press.
- [135] Y. Li, S. K. Jayaweera, C. Ghosh, and M. Bkassiny, "Learning-aided sensing scheduling for wide-band cognitive radios," in *Proceedings of the IEEE 78th Vehicular Technology Conference (VTC Fall '13)*, pp. 1–5, Las Vegas, Nev, USA, September 2013.
- [136] C. J. C. H. Watkins and P. Dayan, "Q-learning," *Machine Learning*, vol. 8, no. 3-4, pp. 279–292, 1992.
- [137] M. L. Puterman, *Markov Decision Processes: Discrete Stochastic Dynamic Programming*, John Wiley & Sons, New York, NY, USA, 1994.
- [138] L. Buşoniu, R. Babuška, and B. de Schutter, "Multi-agent reinforcement learning: a survey," in *Proceedings of the 9th International Conference on Control, Automation, Robotics and Vision (ICARCV '06)*, pp. 1–6, Singapore, December 2006.

Research Article

Frequency-Tunable and Pattern Diversity Antennas for Cognitive Radio Applications

A. H. Ramadan,¹ J. Costantine,¹ Y. Tawk,² C. G. Christodoulou,³ and K. Y. Kabalan¹

¹ The ECE Department, American University of Beirut, Beirut 1107 2020, Lebanon

² The ECCE Department, Notre Dame University-Louaize, P.O. Box 72, Zouk Michael, Lebanon

³ The Configurable Space Microsystems Innovations & Applications Center (COSMIAC), University of New Mexico, Albuquerque, NM 87131-0001, USA

Correspondence should be addressed to A. H. Ramadan; ramadan@ieee.org

Received 5 December 2013; Accepted 23 January 2014; Published 6 March 2014

Academic Editor: Mario Bkassiny

Copyright © 2014 A. H. Ramadan et al. This is an open access article distributed under the Creative Commons Attribution License, which permits unrestricted use, distribution, and reproduction in any medium, provided the original work is properly cited.

Frequency-tunable microstrip antennas, for cognitive radio applications, are proposed herein. The approach is based on tuning the operating frequency of a bandpass filter that is incorporated into a wideband antenna. The integration of an open loop resonator (OLR-) based adjustable bandpass filter into a wideband antenna to transform it into a tunable filter-antenna is presented. The same technique is employed to design a cognitive radio pattern diversity tunable filter-antenna. A good agreement between the simulated and measured results for the fabricated prototypes is obtained. The radiation characteristics of each designed tunable filter-antenna are included herein.

1. Introduction

The broad frequency allocation with the variety of the existing standards calls for reconfigurable and frequency agile microwave circuits to pave the way toward reconfigurable radio front-end architectures [1]. The “spectrum overcrowding” arising issue, which is due to the coexisting telecommunication standards in overlapping frequency bands, calls for flexible receiver architectures to efficiently share wireless resources [2]. Cognitive radios are expected to sense the occupancy or target any available channel in the entire spectrum and tolerate interferers at any frequency as well. These requirements put constraints on the antenna design to efficiently sense the frequency spectrum [3].

A wideband front-end may not necessarily be the optimum solution for software-defined/cognitive radio as it leads to a compromise in the transceiver performance, caused by limitations in the front-end components. Therefore, techniques of introducing flexible frequency discrimination, which include tunable bandpass, tunable bandstop filters,

and tunable narrowband antennas, help reduce spurious spectral content in the transmitter and limit out-of-band interference in the receiver [4]. Besides the inherent gain-bandwidth product limitations and fluctuations of wideband antennas, their outputs can be heavily corrupted by wideband noise and thus result in a low signal-to-noise (SNR) ratio. Wideband antennas require high-speed ADCs, which are power intensive and have higher quantization errors. Finally, the design for wideband operation leads to compromise in the transceiver performance, caused by limitations in the RF front-end components such as amplifiers, oscillators, and mixers. All the above issues bring in narrowband frequency-tunable antennas, or tunable filter-antennas, as good candidates for use to sense the frequency spectrum. This is because tunable bandpass filtering provides flexible frequency discrimination, wideband suppression of unwanted interference, gain flatness over the operating frequency band, less disruption of the antenna’s radiation characteristics, better processing of down-converted signals, ease of implementation, and good performance. Hence, the new cognitive radio

antenna, for overlay spectrum operation, may be a single-port antenna system, which can be appropriately controlled to efficiently sense the frequency spectrum.

In [5], the concept of multidimensional spectrum sensing is introduced. Herein, the spectrum sensing term involves obtaining spectrum usage characteristics across multiple dimensions such as time, space, frequency, and code. It is not simply based on measuring the spectral content or measuring the radio frequency energy over the spectrum, as traditionally understood. The conventional definition of the spectrum opportunity, which is often defined as a band of frequencies that are not being used by the primary user of that band at a particular time in a particular geographic area, only exploits the frequency, time, and space dimensions of the spectrum. However, other dimensions, such as location, angle of arrival, and code need to be explored. For the angle of arrival dimension, secondary users can alter their transmission direction without creating any interference if they know the location or direction of primary users. The potential of dynamical beam-forming and simultaneous frequency/polarization reconfiguration of reflectarray structures for use in cognitive radio application to achieve multiplexing in frequency, angular, and polarization domains is reported in [6]. Therefore, frequency tuning is one dimension to exploit in cognitive radio antennas. However, tunable filter-antennas with a pattern diversity attribute add on the efficiency of spectrum sensing in cognitive radio networks. For instance, pattern diversity tunable filter-antennas help combat multipath fading and cochannel interference, while sensing the frequency spectrum.

In this paper, tunable filter-antennas for overlay cognitive radio applications are presented. A design approach, which is based on converting the wideband operation of an antenna into a tunable narrowband one via preselect filtering is discussed. A varactor-tuned bandpass filter is integrated into a wideband antenna to achieve frequency tunability without disturbing the radiation pattern. The SMV1405 varactor is utilized in this work [7]. The same technique is employed to design a pattern diversity tunable filter-antenna for cognitive radio applications. The paper is organized as follows. Section 2 discusses the integration of an OLR-based bandpass filter, with a tuning capability, into a wideband antenna. The proposed tunable filter-antenna for cognitive radio applications is presented in Section 3. Section 4 discusses the design of a cognitive radio pattern diversity tunable filter-antenna. Conclusions are presented in Section 5.

2. Integration of an OLR-Based Bandpass Filter into a Wideband Antenna

According to [8], a microstrip transmission line loaded with rectangular-shaped half-wavelength open loop resonators results in an overall structure that behaves as an effective medium with negative-valued permeability. Therefore, a bandstop operation will appear in the vicinity of the OLR's resonant frequency. This bandstop behavior is because of the nonsimultaneous change in the sign of the permeability (μ) and permittivity (ϵ) of the medium. This nonparallel

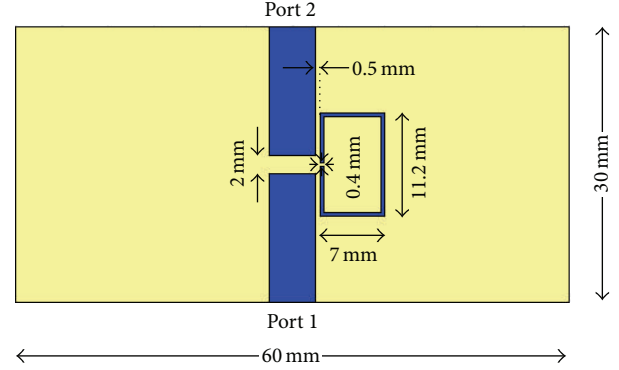


FIGURE 1: An OLR-based bandpass filter.

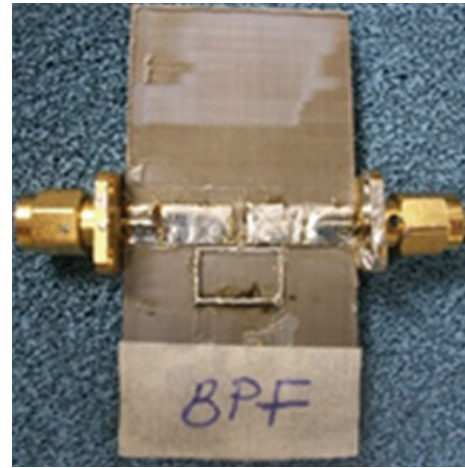


FIGURE 2: A photo of the fabricated bandpass filter prototype.

change affects the squared refractive index (η^2) and yields no wave propagation. A bandpass transformation of the above scenario is obtained by etching a series capacitive gap in the microstrip transmission line, as shown in Figure 1. This combination is considered as a right-handed OLR/gap section and provides forward signal propagation in the frequency band where both the permeability and the permittivity are positive. The series capacitance loaded in the line precludes transmission outside of the OLR's resonant frequency band.

The illustrated OLR-based bandpass filter, which is based on a 1.6 mm thick Taconic TLY substrate, is designed and simulated using Ansoft HFSS [9]. A fabricated prototype of the filter is given in Figure 2. A comparison between the simulated and measured S-parameters is depicted in Figure 3, where a good agreement is attained. The integration of an OLR-based bandpass filter, into a wideband antenna, is discussed herein. A 3.41 GHz-operable OLR-based bandpass filter is firstly designed on a 1.6 mm thick Taconic TLY substrate. The dimensions of the proposed filter are given in Figure 4(a). A $60 \times 60 \times 1.6 \text{ mm}^3$ Taconic TLY based wideband antenna is then designed as shown in Figure 4(b).

The antenna has a 30 mm long partial ground plane flushed with the feed line. A tapered matching section is incorporated between the rectangular patch of the antenna

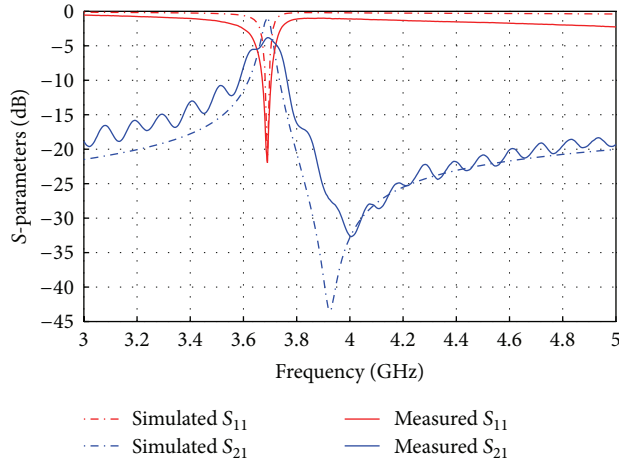


FIGURE 3: Simulated and measured S-parameters of the OLR-based bandpass filter.

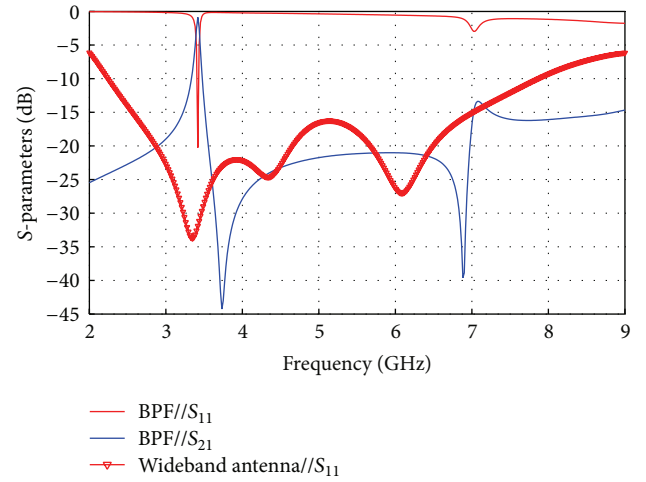


FIGURE 5: Computed S-parameters of the OLR-based bandpass filter and the wideband antenna.

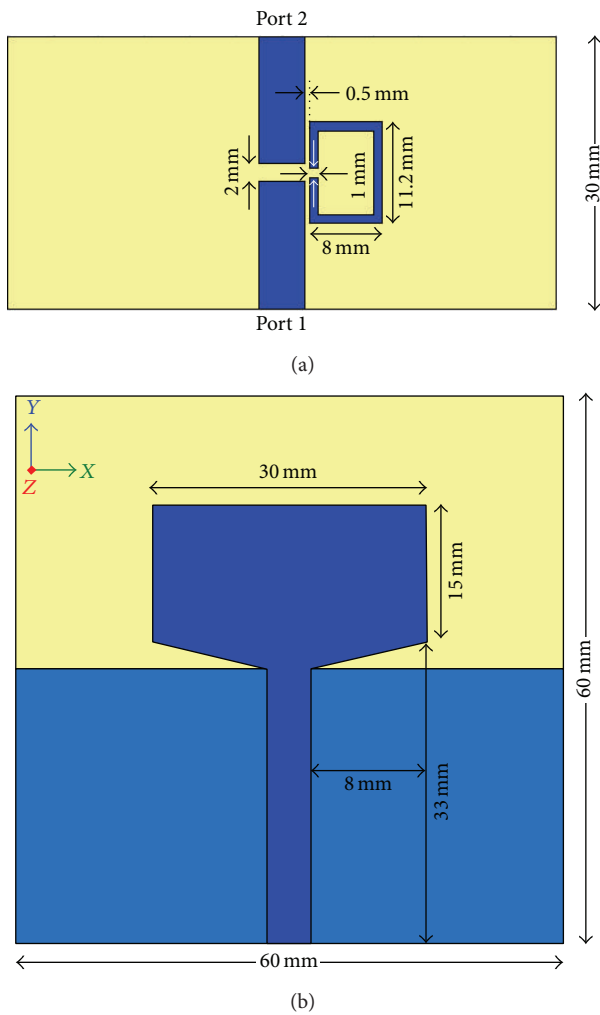


FIGURE 4: Geometry of (a) the OLR-based bandpass filter and (b) wideband antenna.

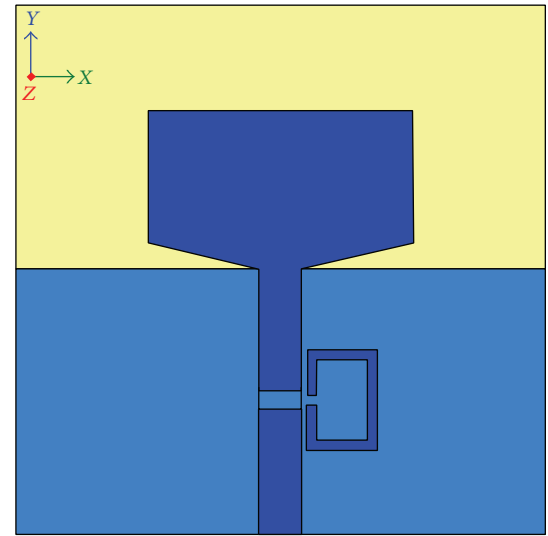


FIGURE 6: Integration of the OLR-based bandpass filter into the wideband antenna.

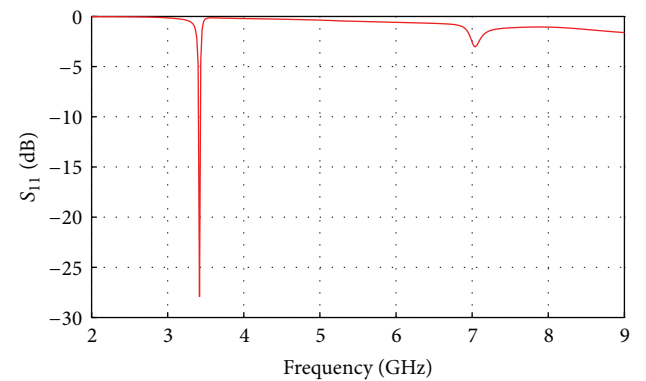


FIGURE 7: Simulated reflection coefficient of the assembled structure.

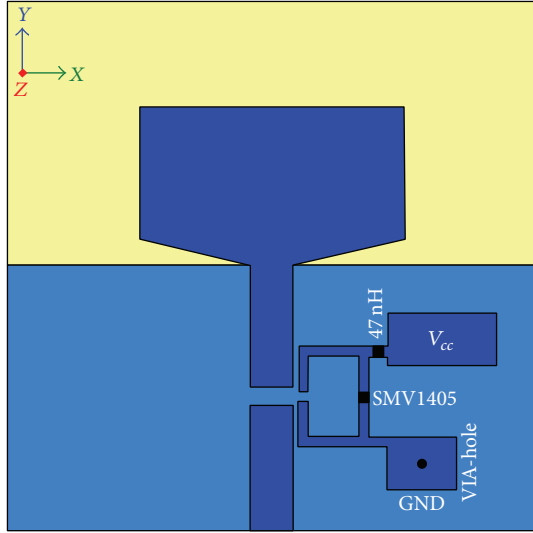


FIGURE 8: Configuration of the proposed tunable filter-antenna.

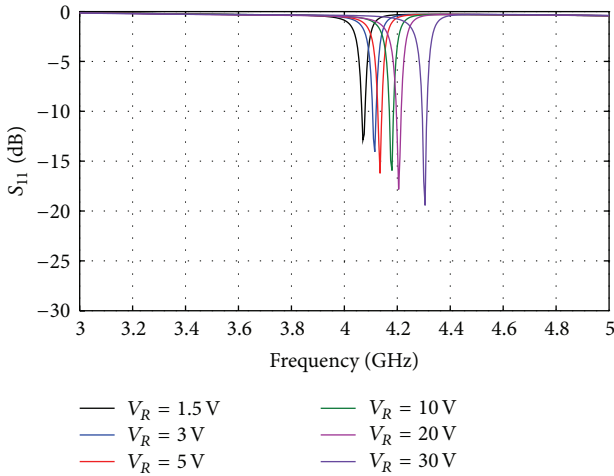


FIGURE 9: Simulated reflection coefficient of the proposed tunable filter-antenna.

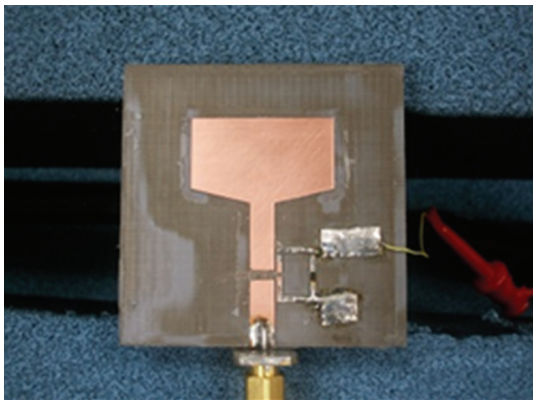


FIGURE 10: A fabricated prototype of the proposed tunable filter-antenna.

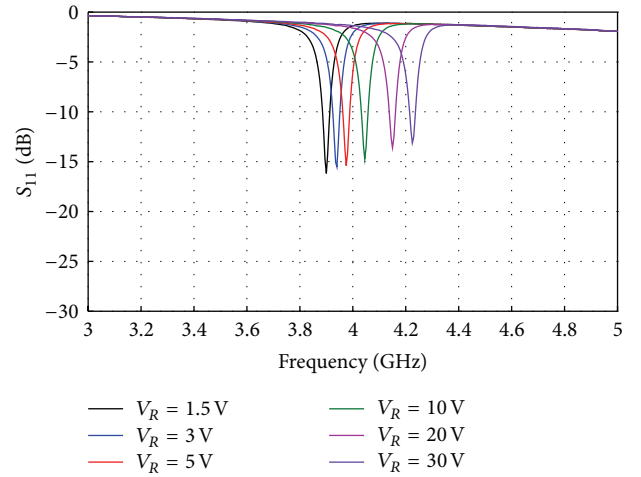


FIGURE 11: Measured reflection coefficient of the proposed tunable filter-antenna.

and its feed line in order to achieve better impedance matching. The computed S-parameters of the bandpass filter and the wideband antenna, in the 2–9 GHz frequency range, are shown in Figure 5. The reflection coefficient of the antenna is ≤ -10 dB in the 2.24–7.86 GHz frequency range. Finally, both the OLR-based bandpass filter and the wideband antenna are assembled in a single structure, as illustrated in Figure 6. The proposed filter-antenna is found to resonate, as shown in Figure 7, at the same operating frequency of the contained bandpass filter.

3. A Narrowband Frequency-Tunable Antenna for Cognitive Radio Applications

In order to achieve narrowband frequency tuning for the proposed 1.6 mm thick Taconic based filter-antenna, given that its radiation characteristics are not distracted, an SMV1405 varactor is mounted on the OLR contained in the bandpass filter to adjust its resonant frequency. According to [10], varactor-loaded half-wavelength OLRs witness longer electrical lengths and thus resonate at lower frequencies, as the loading capacitance is increased. In other words, the adjustment of the reverse voltage across the bridging varactor will result in tuning the resonant frequency of the filter-antenna. The configuration of the proposed tunable filter-antenna, along with its biasing network, is given in Figure 8. A 47 nH RF choke is incorporated to prevent any RF leakage to the DC supply. The other terminal of the tunable OLR is grounded through a via-hole. Accordingly, the Vcc and GND pads are used to adjust the reverse voltage across the mounted varactor.

The computed reflection coefficient for different reverse voltages is shown in Figure 9. It is worth mentioning that as the reverse voltage increases, the tunable filter-antenna resonates at higher frequencies. This is because the value of the loading capacitance is inversely proportional to the applied reverse voltage, and this yields a resonance at higher frequencies. A prototype of the designed tunable

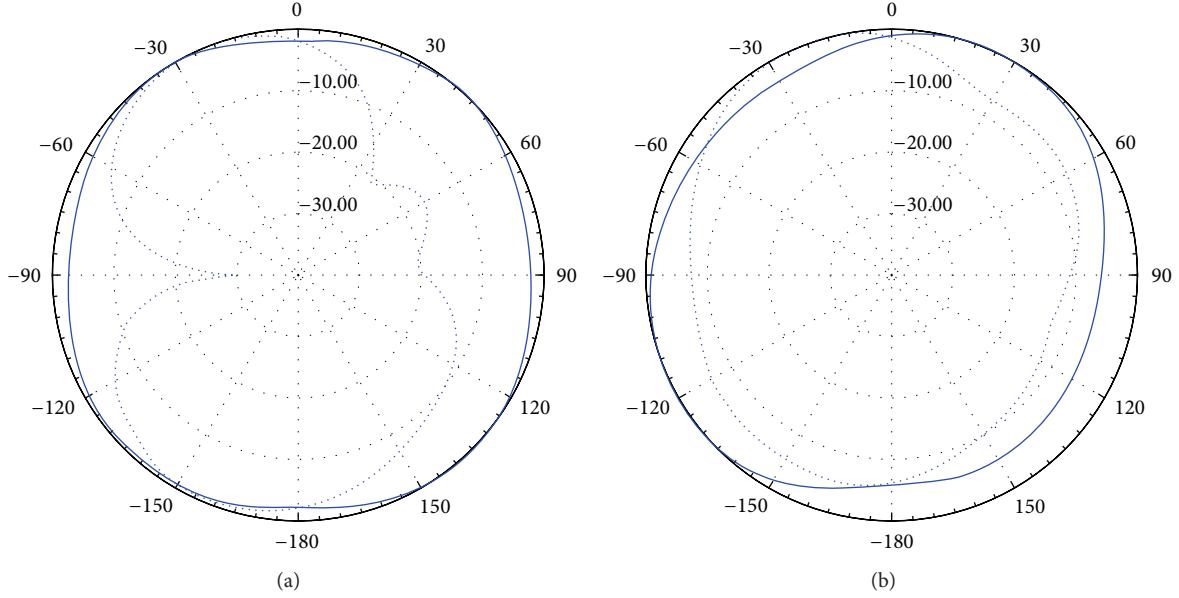


FIGURE 12: Normalized radiation pattern of (a) the wideband antenna and (b) the proposed tunable filter-antenna at 4.18 GHz (X-Z/Y-Z plane: solid/dotted line).

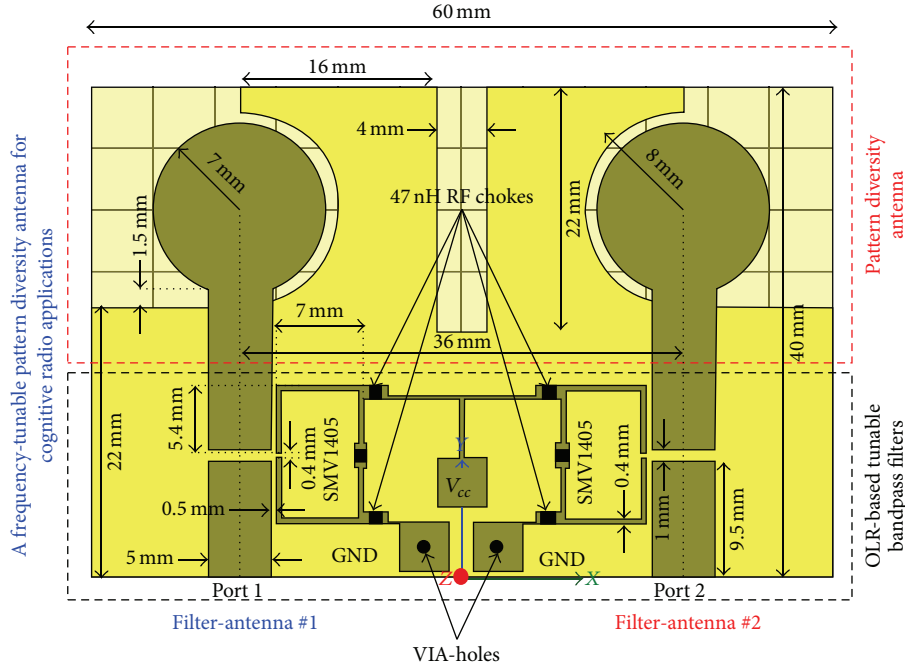


FIGURE 13: Configuration of the proposed pattern diversity tunable filter-antenna.

filter-antenna, as illustrated in Figure 10, is fabricated and measured. A good analogy between simulated and measured plots, as given in Figure 11, is revealed. However, a slight shift is witnessed due to Ansoft-HFSS varactor modeling issues and milling effects. The normalized radiation patterns, of the wideband antenna and the proposed tunable filter-antenna, at 4.18 GHz are depicted in Figure 12. It is pretty obvious that the radiation pattern of the tunable filter-antenna, in the X-Z plane, is still omnidirectional and minimally distracted.

Moreover, the gain of the tunable filter-antenna at 4.18 GHz is 4 dB, which is 1.86 dB higher than that of the wideband antenna at the same frequency.

4. A Frequency-Tunable Pattern Diversity Antenna for Cognitive Radio Applications

In a communication system implementing diversity, the same data is sent over independent fading paths. The signals

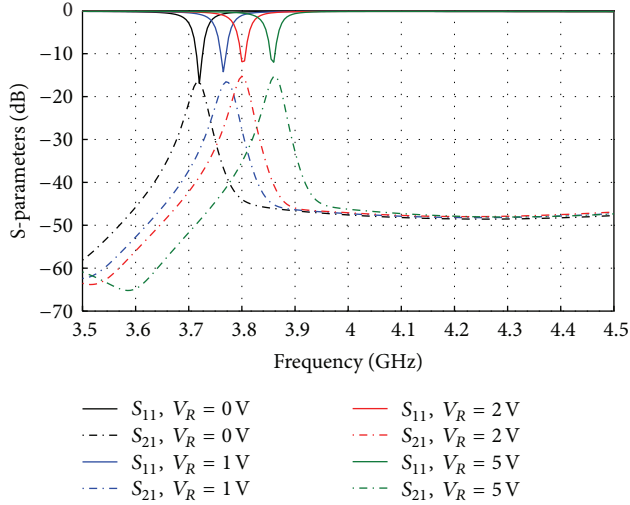


FIGURE 14: Simulated S-parameters of the proposed pattern diversity tunable filter-antenna.

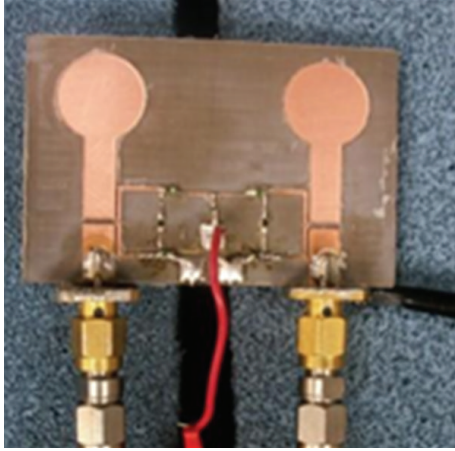


FIGURE 15: A fabricated prototype of the proposed pattern diversity tunable filter-antenna.

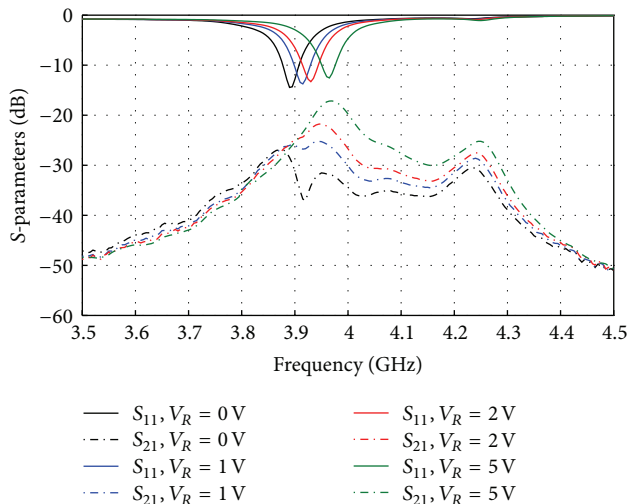


FIGURE 16: Measured S-parameters of the proposed pattern diversity tunable filter-antenna.

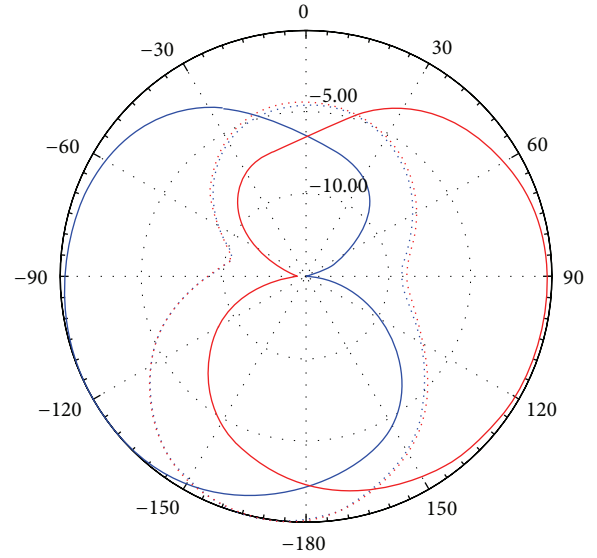


FIGURE 17: Normalized radiation pattern of the proposed pattern diversity tunable filter-antenna at 3.72 GHz (X-Z/Y-Z plane: solid/dotted line).

received over the independent paths are then combined in such a way that the fading of the resultant signal is reduced. A wireless communication system equipped with diversity antennas leads to improved capacity and quality of the wireless channel. In this section, a pattern diversity antenna with a frequency tuning feature is presented. This will help combat multipath fading and cochannel interference, while sensing the frequency spectrum.

The proposed 1.6 mm thick Taconic TLY based pattern diversity tunable filter-antenna comprises two microstrip-line fed monopoles that are based on the same circular patch. Two symmetrically curved slots are etched in the ground plane. First, a circular slot with a radius of 8 mm is introduced below each patch, and then a $10 \times 18 \text{ mm}^2$ rectangular slot is made at each of two corners. The etched curved slots direct the beams of the two monopoles in opposite azimuth directions, leading to pattern diversity. A $2 \times 20 \text{ mm}^2$ rectangular slot placed halfway between the monopoles is used to increase the isolation and adjust the antenna's operating frequency range. Two varactor-tuned half-wavelength OLR-based bandpass filters are then integrated into the pattern diversity antenna to achieve frequency tuning. The detailed structure of the proposed pattern diversity tunable filter-antenna is illustrated in Figure 13.

The computed S-parameters for each reverse voltage of the bridging varactor are shown in Figure 14. The simulations results reveal a narrowband frequency tuning and a better than 18 dB isolation. A fabricated prototype of the proposed design is depicted in Figure 15. The measured results are shown in Figure 16. A slight shift between the simulated and measured data is found due to SMV1405 modeling and milling issues. Figure 17 shows the normalized radiation patterns of the presented tunable filter-antenna at 3.72 GHz. It is seen that the patterns in the X-Z plane are symmetric

TABLE 1: Diversity parameters of the proposed tunable filter-antenna.

| Frequency (GHz) | $\rho_e \ll 0.5$ | MEG1/MEG2 ≈ 1 |
|-----------------|-----------------------|-----------------------|
| 3.72 | 6214×10^{-7} | 0.9952 |
| 3.765 | 101×10^{-4} | 1.0066 |
| 3.8 | 7489×10^{-7} | 0.9915 |
| 3.86 | 3144×10^{-6} | 0.9899 |

and tend to cover complementary space region. With these patterns, the proposed design can provide pattern diversity over the operating frequencies. At 3.72 GHz, each monopole provides a peak gain of approximately 5 dB.

The diversity performance of an antenna system, as reported in [11], can be assessed by calculating the envelope correlation coefficient (ρ_e) and the mean effective gain (MEG). The correlation coefficient shows the influence of the different propagation paths on the RF signals reaching the antenna elements. In a diversity system, a good gain can be obtained when $\rho_e < 0.5$. ρ_e relates to the mutual coupling between the antennas' ports as follows:

$$\rho_e = \frac{|S_{11}^* S_{12} + S_{21}^* S_{22}|^2}{(1 - |S_{11}|^2 - |S_{12}|^2)(1 - |S_{22}|^2 - |S_{21}|^2)}. \quad (1)$$

The mean effective gain is a parameter that includes antenna radiation power pattern, antenna efficiency, and the propagation effects. Equal power branches mean better condition for achieving high diversity gain. To guarantee that the signal strengths of the two monopoles are approximately equal, the ratio MEG1/MEG2 should be close to unity. For the proposed tunable filter-antenna, the conditions $\rho_e < 0.5$ and MEG1/MEG2 ≈ 1 are both met, per operating frequency, as given in Table 1. As a result, a high diversity gain for the presented tunable filter-antenna is achieved:

$$\text{MEG} = \frac{1}{2\pi} \cdot \int_0^{2\pi} \left[\frac{\Gamma \cdot G_\theta((\pi/2), \varphi) + G_\varphi((\pi/2), \varphi)}{1 + \Gamma} \right] d\varphi. \quad (2)$$

5. Conclusion

In this paper, tunable filter-antennas for overlay cognitive radio applications are presented. The exploitation of OLR to design a bandpass filter and its integration into a wideband antenna are discussed. The proposed approach is based on integrating varactor-tuned half-wavelength OLR-based bandpass filter(s) to electronically adjust the resonant frequency of the reported filter-antennas. Accordingly, a narrowband frequency-tunable microstrip antenna is firstly designed and tested. The same methodology is employed to design a pattern diversity tunable filter-antenna for overlay cognitive radio applications.

Conflict of Interests

The authors declare that there is no conflict of interests regarding the publication of this paper.

Acknowledgments

The authors gratefully acknowledge the support of the AUB Alumni Association Dubai & Northern Emirates to the Electromagnetic and Radio Frequency Group (EMRF) at the American University of Beirut (AUB).

References

- [1] E. Lourandakis, R. Weigel, H. Mextorf, and R. Knoechel, "Circuit agility," *IEEE Microwave Magazine*, vol. 13, no. 1, pp. 111–121, 2012.
- [2] A. Acampora, A. Collado, and A. Georgiadis, "Nonlinear analysis and optimization of a distributed voltage controlled oscillator for cognitive radio," in *Proceedings of the IEEE International Microwave Workshop Series on RF Front-Ends for Software Defined and Cognitive Radio Solutions (IMWS '10)*, pp. 1–4, Aviero, Portugal, February 2010.
- [3] B. Razavi, "Challenges in the design of cognitive radios," in *Proceedings of the IEEE Custom Integrated Circuits Conference (CICC '09)*, pp. 391–398, San Jose, Calif, USA, September 2009.
- [4] B. E. Carey-Smith, P. A. Warr, P. R. Rogers, M. A. Beach, and G. S. Hilton, "Flexible frequency discrimination subsystems for reconfigurable radio front ends," *EURASIP Journal on Wireless Communications and Networking*, vol. 2005, no. 3, pp. 354–363, 2005.
- [5] T. Yücek and H. Arslan, "A survey of spectrum sensing algorithms for cognitive radio applications," *IEEE Communications Surveys and Tutorials*, vol. 11, no. 1, pp. 116–130, 2009.
- [6] J. Perruisseau-Carrier, "Versatile reconfiguration of radiation patterns, frequency and polarization: a discussion on the potential of controllable reflectarrays for software-defined and cognitive radio systems," in *Proceedings of the IEEE International Microwave Workshop Series on RF Front-Ends for Software Defined and Cognitive Radio Solutions (IMWS '10)*, pp. 1–4, Aviero, Portugal, February 2010.
- [7] SMV1405-SMV1419, Hyperabrupt Junction Tuning Varactors from Skyworks Solutions.
- [8] R. Marques, F. Martin, and M. Sorolla, *Metamaterials with Negative Parameters: Theory, Design and Microwave Applications*, John Wiley & Sons, Hoboken, NJ, USA, 2008.
- [9] Ansoft HFSS, Pittsburg, Pa 15219, USA.
- [10] J.-S. Hong, "Theory and experiment of novel microstrip slow-wave open-loop resonator filters," *IEEE Transactions on Microwave Theory and Techniques*, vol. 45, no. 12, pp. 2358–2365, 1997.
- [11] M. Al-Husseini, A. Ramadan, C. G. Christodoulou, K. Y. Kabalan, and A. El-Hajj, "A novel printed diversity antenna for WiMAX applications," in *Proceedings of the IEEE International Symposium on Antennas and Propagation and USNC/URSI National Radio Science Meeting (APSURSI '11)*, pp. 2212–2214, Spokane, Wash, USA, July 2011.

Research Article

A Miniaturize Bandpass Filter with Harmonic Suppression Using Meandered Quarter-Wavelength Resonators

Yun-Long Lu,^{1,2} Shun Wang,³ Tingting Gu,¹ Ping Cao,¹ and Kai Li¹

¹ Department of Information Science & Electronic Engineering, Zhejiang University, Hangzhou 310027, China

² Hangzhou RFID Research Center, Chinese Academy of Sciences, Hangzhou 310011, China

³ Institute of Electronics, Chinese Academy of Sciences, Beijing 100190, China

Correspondence should be addressed to Shun Wang; swang@mail.ie.ac.cn

Received 3 November 2013; Accepted 12 December 2013; Published 18 February 2014

Academic Editor: Said E. El-Khamy

Copyright © 2014 Yun-Long Lu et al. This is an open access article distributed under the Creative Commons Attribution License, which permits unrestricted use, distribution, and reproduction in any medium, provided the original work is properly cited.

A miniaturized bandpass filter with harmonics suppression is presented. The proposed filter consists of two quarter-wavelength microstrip resonators, which are meandered for circuit size reduction. An interdigital capacitor, loading at zero-voltage point, is employed to provide the desired coupling between the resonators at operating frequency, whereas the coupling coefficient at the third harmonic is realized to be zero. Besides, the second and fourth harmonics are suppressed since $\lambda/4$ resonators are adopted. Benefiting from these properties, a miniaturized bandpass filter with the second, third, and fourth harmonics suppression was designed and implemented. The final measured and simulated results show good consistence with the theoretical counterparts.

1. Introduction

The bandpass filter is one of the most important components in modern RF/microwave systems [1–3]. Unfortunately, without special measures, most of the filters exhibit harmonic responses, which degrade the system performance [4–9]. On the other hand, most mobile devices become smaller and leave limited space for the placement of filters. It is also of importance to miniaturize the required filter size. Therefore, bandpass filters with miniaturized size and harmonics suppression become more and more attractive [10–16]. To reduce the circuit size, the designed filters with lower orders are preferred once the passband selectivity and out-of-band rejection can reach the design requirements. One important method to improve the selectivity of the filters is to realize transmission zeros at finite frequencies. Moreover, the additional transmission zeros at harmonics can reject unwanted signals without sacrificing the performance of the passband [17, 18]. Therefore, a low-order filter with the help of transmission zeros may meet the stopband requirement that is usually achieved by higher-order filters. It still has challenges to design a lower order miniature bandpass filter with harmonic suppression. Various structures are proposed

in [19–31], such as meandered parallel coupled-line structure [19–26], coupled/slot spur lines [27, 28], fractal-shaped coupled lines [29], and triple-mode stub-loaded resonator [30, 31]. Recently, a novel coupling schematic is proposed in [32–34] that exhibits one transmission zero at a harmonic frequency. Thus, with this coupling scheme, one more transmission zero is added to the filter, which helps to improve the upper stopband performance. However, most of the filters mentioned above still occupy a fairly large space.

In this letter, a miniature two-order harmonic-suppressed microstrip bandpass filter using meandered quarter-wavelength resonators is presented. An interdigital coupling capacitor is placed on the zero-voltage point of the third harmonic along the resonators. With this benefit, a transmission zero appears at the third harmonic frequency. Besides, two additional transmission zeros located at the lower and upper skirts of the passband are obtained to enhance the selectivity. The circuit size reduction is realized by using two meandered quarter-wavelength resonators. With this structure, the proposed filter not only miniaturizes the circuit size but also extends the rejection band. To verify the performance, the proposed filter is implemented and measured. The active area of the filter is

TABLE 1: Dimensions of the proposed filter (unit: mm).

| | | |
|-------------------|-------------------|-----------------|
| $L_1 = 8.9$ mm | $L_2 = 5.3$ mm | $L_3 = 3.8$ mm |
| $L_4 = 4$ mm | $L_5 = 3$ mm | $L_6 = 3.55$ mm |
| $L_7 = 2.85$ mm | $L_8 = 1.45$ mm | $L_9 = 1.5$ mm |
| $L_{10} = 5.4$ mm | $L_{11} = 1.2$ mm | $W_1 = 0.5$ mm |
| $W_2 = 1.8$ mm | $g = 0.6$ mm | $g_1 = 2.2$ mm |
| $d = 0.6$ mm | $L_i = 1$ mm | $W_i = 0.2$ mm |
| $g_i = 0.2$ mm | $g_2 = 1.1$ mm | $s = 1.4$ mm |

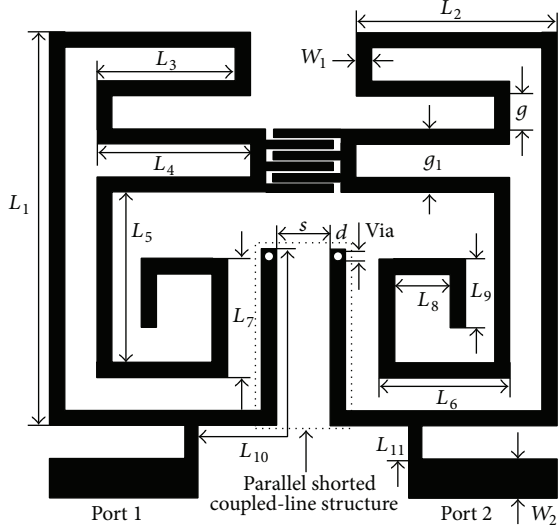


FIGURE 1: Schematic of the proposed miniaturized bandpass filter.

only $8.9 \text{ mm} \times 12.2 \text{ mm}$ ($0.052\lambda_g \times 0.071\lambda_g$; λ_g is the guided wavelength at operating frequency), and the rejection band is extended to $4.2f_0$.

2. Filter Design and Analysis

Figure 1 depicts the geometrical schematic of the proposed miniature harmonic-suppressed microstrip bandpass filter, which is operating at $f_0 = 1.13 \text{ GHz}$. This is a two-order bandpass filter. The quarter-wavelength resonators are meandered and separated enough, as shown in Figure 1. The substrate in this design is the Rogers4350 substrate with a relative dielectric constant of 3.48 and a thickness of 0.762 mm. The physical dimensions are shown in Table 1. The coupling of the proposed bandpass filter is achieved only by the interdigital coupling capacitor, and the coupling coefficient is mainly determined by the location and value of interdigital coupling capacitor. With the meandered quarter-wavelength resonators, the circuit size can be reduced effectively. The input and output ports are connected with the resonators directly. The relation between the external quality and taper position of input/output port has been investigated in [35].

The interdigital coupling capacitor and its equivalent circuit are shown in Figure 2. C_s and C_p represent the series and shunt capacitors of interdigital coupling capacitor, respectively [36]. The value of interdigital coupling capacitor

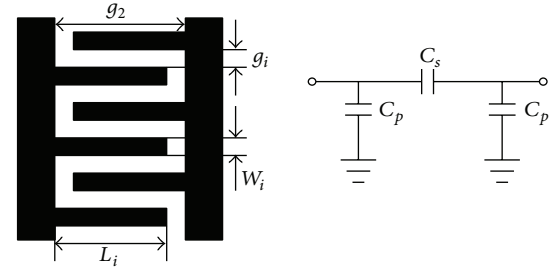


FIGURE 2: Interdigital coupling capacitor and its equivalent circuit.

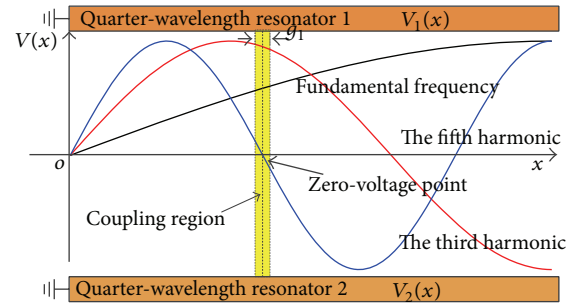


FIGURE 3: Voltage wave functions along the quarter-wavelength resonators.

C_{int} can be adjusted by changing the parameters W_i , L_i , and g_i . As the resonators separate away from each other, the coupling between them can be ignored when the interdigital coupling capacitor does not exist. Thus, the coupling is mainly realized by the interdigital capacitor, and the coupling coefficients can be calculated by [37]

$$|k| = p \times C_{\text{int}} \times |v_1(x) \times v_2(x)|, \quad (1)$$

where $v_1(x)$ and $v_2(x)$ are normalized voltage wave functions along the two quarter-wavelength resonators and p represents a constant. As we know, the even-mode harmonics cannot be excited at the quarter-wavelength resonators. And thus, only the odd-mode harmonics existed, as shown in Figure 3.

When the center of coupling region is at the zero-voltage point of the third harmonic, $v_1(x)$ and $v_2(x)$ are nearly to zero for the third harmonic. With the very small length of coupling region g_1 , the coupling coefficient k is close to 0. As a result, the third harmonic signals cannot pass through the coupling region and thus is suppressed. Therefore, combining the quarter-wavelength resonators and proper position of

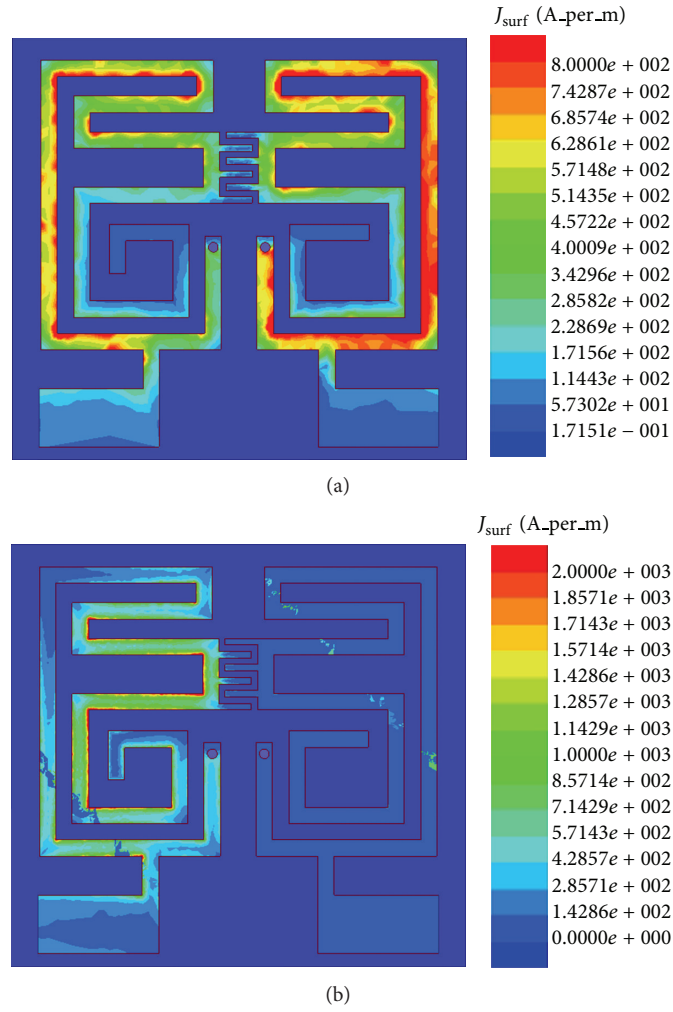


FIGURE 4: Current distribution: (a) fundamental frequency and (b) the third harmonic.

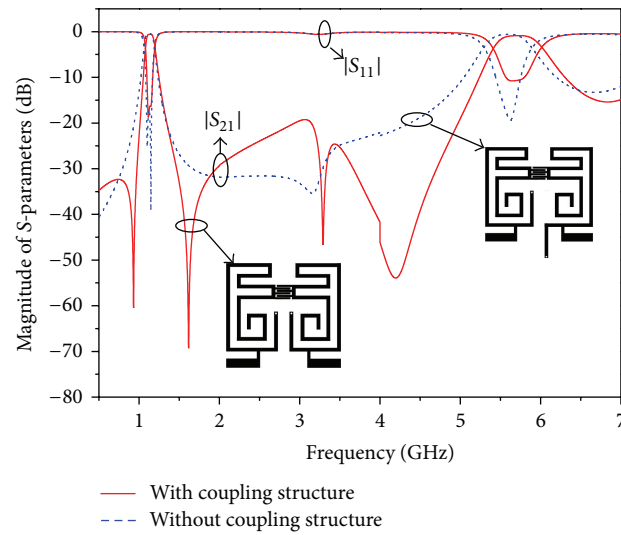


FIGURE 5: Response of proposed bandpass filter of different types.

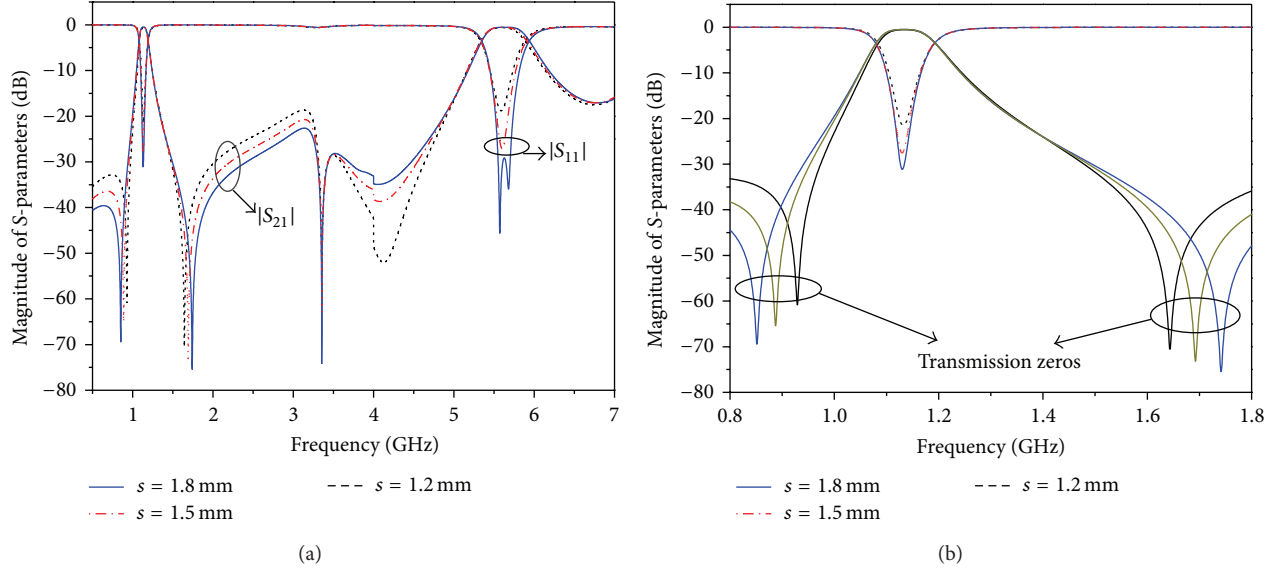


FIGURE 6: (a) Transmission characteristics and (b) location of transmission zeros.

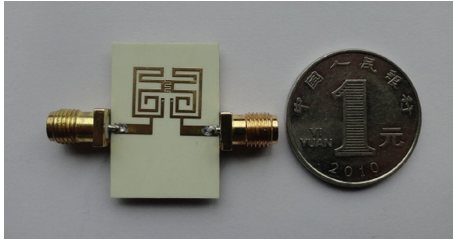


FIGURE 7: Photograph of the fabricated filter.

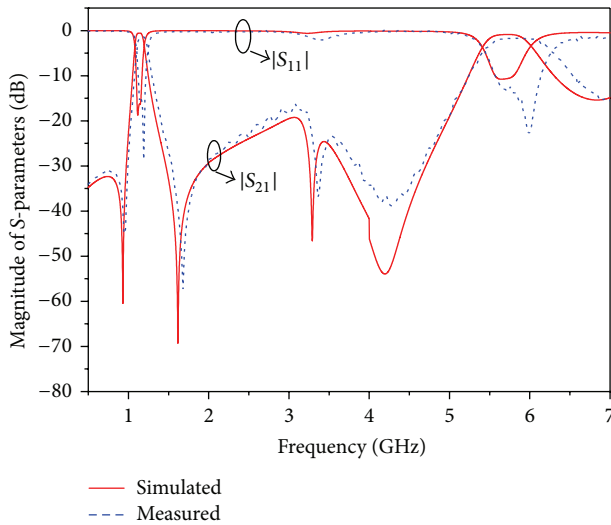


FIGURE 8: Simulated and measured S-parameters.

the interdigital coupling capacitor, the rejection band can be extended to the fifth harmonic.

The proposed filter is simulated by the commercially available electromagnetic (EM) simulator of Ansoft HFSS.

Current distributions of the fundamental and third harmonic of the proposed filter are shown in Figure 4. It clearly shows how the fundamental frequency current is coupled from the input port to the output port, whereas the third harmonic is suppressed. This verifies the theoretical analysis stated above.

A parallel shorted coupled-line structure, shown in Figure 1, is adopted to enhance the selectivity. As shown in Figure 5, two additional transmission zeros are realized by the parallel shorted coupled-line structure. This structure is similar to the source-load coupling. Meanwhile, the location of transmission zeros is determined by the gap s . The higher selectivity is achieved with the smaller gap s , which is shown in Figure 6.

3. Experiments

The proposed microstrip bandpass filter is fabricated using printed circuit-board (PCB) process and the photograph is given in Figure 7. The active area of the proposed filter is only $8.9 \text{ mm} \times 12.2 \text{ mm}$, which is about $0.052\lambda_g \times 0.071\lambda_g$, where λ_g is the guided wavelength at operating frequency. Agilent network analyzer 8358E is used to test the performance. The simulated and measured results are illustrated in Figure 8 and show good agreements. The centre frequency of the passband is measured at 1.17 GHz against that of the simulated results at 1.13 GHz. Furthermore, the measured passband has a 3 dB bandwidth of 111 MHz or 10.6%. The insertion loss, including the loss from subminiature A (SMA) connectors, is only 1.3 dB compared to the simulated loss of 0.59 dB. From Figure 8, it is noted that there are two transmission zeros on the lower and upper skirts of the passband at 0.9 GHz and 1.61 GHz. Besides, another transmission zero is located at 3.1 GHz. Thus, the third harmonic is efficiently suppressed. It agrees with the theoretical analysis. Therefore, the 20 dB rejection band is extended to 4.96 GHz, which is about $4.2f_0$.

TABLE 2: Comparison with some previously published designs.

| | IL @ f_0 | 3 dB FBW | Harmonic suppression* | Size (λ_g^2) |
|-----------|------------|----------|-----------------------|------------------------|
| [26] | 2.0 dB | 26.5% | $3.9f_0$ | $0.189 * 0.438$ |
| [27] | 3.3 dB | 12.5% | $>3.75f_0$ | $0.166 * 0.141$ |
| [28] | 1.93 dB | 4% | — | $0.175 * 0.175$ |
| [29] | 2.1 dB | 5.1% | $>2f_0$ | $1.03 * 0.171$ |
| [30] | 1.2 dB | 13.2% | $>2f_0$ | $0.21 * 0.15$ |
| [31] | 0.78 dB | 15.8% | $4f_0$ | $0.23 * 0.17$ |
| [32] | 2.2 dB | 6.0% | $2.5f_0$ | $0.557 * 0.124$ |
| This work | 1.3 dB | 10.6% | $4.2f_0$ | $0.052 * 0.071$ |

* 20 dB rejection bandwidth.

The proposed filter is compared with some previously published designs [26–32] in Table 2. Obviously from the table, the proposed filter has identical or even improved in-band performances. In addition, this work exhibits the smallest circuit size.

4. Conclusion

A miniature microstrip bandpass filter with harmonic suppression is presented in this paper. By utilizing the quarter-wavelength and position of interdigital coupling capacitor, the second, third, and fourth harmonics are suppressed. The miniaturization characteristic is achieved based on the meandered quarter-wavelength resonator. Compared with the conventional approaches on designing miniature bandpass filter with harmonic suppression, the work in this paper exhibits a smaller circuit size and wider rejection band.

Conflict of Interests

The authors declare that there is no conflict of interests regarding the publication of this paper.

Authors' Contribution

Yun-Long Lu contributed with the original idea, simulation, writing, and revising the paper; Shun Wang supplied the test equipment, did the test for the filter, figured out the mistake in the early PCB layout to improve the filter performance, and gave the significant suggestion to revise the paper; Tingting Gu and Ping Cao assisted the authors to simulate and optimize the proposed filter; Kai Li discussed the design and helped the authors complete the original idea.

Acknowledgments

This work was partly supported by the National Natural Science Foundation of China (NSFC) under Projects 61201072, 61271086 and the National High Technology Research and Development Program of China (863 Program) under Grant SS2012AA120505.

References

- [1] J. S. Hong and M. J. Lancaster, *Microstrip Filters for RF/Microwave Applications*, Wiley-Interscience, New York, NY, USA, 2004.
- [2] C.-C. Yang and C.-Y. Chang, "Microstrip cascade trisection filter," *IEEE Microwave and Wireless Components Letters*, vol. 9, no. 7, pp. 271–273, 1999.
- [3] A. B. Frazier, R. O. Warrington, and C. Friedrich, "Miniaturization technologies: past, present, and future," *IEEE Transactions on Industrial Electronics*, vol. 42, no. 5, pp. 423–430, 1995.
- [4] S.-G. Mo, Z.-Y. Yu, and L. Zhang, "Compact dual-mode bandpass filters using hexagonal meander loop resonators," *Journal of Electromagnetic Waves and Applications*, vol. 23, no. 13, pp. 1723–1732, 2009.
- [5] J.-T. Kuo and E. Shih, "Microstrip stepped impedance resonator bandpass filter with an extended optimal rejection bandwidth," *IEEE Transactions on Microwave Theory and Techniques*, vol. 51, no. 5, pp. 1554–1559, 2003.
- [6] Y. W. Kong and S. T. Chew, "EBG-based dual mode resonator filter," *IEEE Microwave and Wireless Components Letters*, vol. 14, no. 3, pp. 124–126, 2004.
- [7] L. Zhu and W. Menzel, "Compact microstrip bandpass filter with two transmission zeros using a stub-tapped half-wavelength line resonator," *IEEE Microwave and Wireless Components Letters*, vol. 13, no. 1, pp. 16–18, 2003.
- [8] T. Lopetegui, M. A. G. Laso, J. Hernández et al., "New microstrip 'wiggly-line' filters with spurious passband suppression," *IEEE Transactions on Microwave Theory and Techniques*, vol. 49, no. 9, pp. 1593–1598, 2001.
- [9] L.-H. Hsieh and K. Chang, "Piezoelectric transducer tuned bandstop filter," *Electronics Letters*, vol. 38, no. 17, pp. 970–971, 2002.
- [10] H. W. Liu, J. H. Lei, Y. L. Zhao, W. Y. Xu, Y. C. Fan, and T. T. Wu, "Tri-band microstrip bandpass filter using dual-mode stepped-impedance resonator," *ETRI Journal*, vol. 35, no. 2, pp. 344–347, 2013.
- [11] J.-S. Hong and M. J. Lancaster, "Design of highly selective microstrip bandpass filters with a single pair of attenuation poles at finite frequencies," *IEEE Transactions on Microwave Theory and Techniques*, vol. 48, no. 7, pp. 1098–1107, 2000.
- [12] Q.-X. Chu, F.-C. Chen, Z.-H. Tu, and H. Wang, "A novel crossed resonator and its applications to bandpass filters," *IEEE Transactions on Microwave Theory and Techniques*, vol. 57, no. 7, pp. 1753–1759, 2009.

- [13] S. W. Ren, H. L. Peng, J. F. Mao, and A. M. Gao, "Compact quasielliptic wideband bandpass filter using cross-coupled multiple-mode resonator," *IEEE Microwave and Wireless Components Letters*, vol. 22, pp. 397–399, 2012.
- [14] Y. P. Zhang and M. Sun, "Dual-band microstrip bandpass filter using stepped-impedance resonators with new coupling schemes," *IEEE Transactions on Microwave Theory and Techniques*, vol. 54, no. 10, pp. 3779–3785, 2006.
- [15] C.-Y. Chen, C.-Y. Hsu, and H.-R. Chuang, "Design of miniature planar dual-band filter using dual-feeding structures and embedded resonators," *IEEE Microwave and Wireless Components Letters*, vol. 16, no. 12, pp. 609–611, 2006.
- [16] P. K. Singh, S. Basu, and Y.-H. Wang, "Miniature dual-band filter using quarter wavelength stepped impedance resonators," *IEEE Microwave and Wireless Components Letters*, vol. 18, no. 2, pp. 88–90, 2008.
- [17] M. A. El-Tanani and G. M. Rebeiz, "Corrugated microstrip coupled lines for constant absolute bandwidth tunable filters," *IEEE Transactions on Microwave Theory and Techniques*, vol. 58, no. 4, pp. 956–963, 2010.
- [18] S. Sun and L. Zhu, "Periodically nonuniform coupled microstrip-line filters with harmonic suppression using transmission zero reallocation," *IEEE Transactions on Microwave Theory and Techniques*, vol. 53, no. 5, pp. 1817–1822, 2005.
- [19] L. K. Yeung and K.-L. Wu, "A compact second-order LTCC bandpass filter with two finite transmission zeros," *IEEE Transactions on Microwave Theory and Techniques*, vol. 51, no. 2, pp. 337–341, 2003.
- [20] J.-T. Kuo, C.-Y. Fan, and S.-C. Tang, "Dual-wideband bandpass filters with extended stopband based on coupled-line and coupled three-line resonators," *Progress in Electromagnetics Research*, vol. 124, pp. 1–15, 2012.
- [21] M. Á. Sánchez-Soriano, E. Bronchalo, and G. Torregrosa-Penalva, "Parallel-coupled line filter design from an energetic coupling approach," *IET Microwaves, Antennas & Propagation*, vol. 5, no. 5, pp. 568–575, 2011.
- [22] M. Á. Sánchez-Soriano, G. Torregrosa-Penalva, and E. Bronchalo, "Multispurious suppression in parallel-coupled line filters by means of coupling control," *IET Microwaves, Antennas & Propagation*, vol. 6, no. 11, pp. 1269–1276, 2012.
- [23] P. Cheong, S.-W. Fok, and K.-W. Tam, "Miniaturized parallel coupled-line bandpass filter with spurious-response suppression," *IEEE Transactions on Microwave Theory and Techniques*, vol. 53, no. 5, pp. 1810–1815, 2005.
- [24] J.-H. Park, S. Lee, and Y. Lee, "Extremely miniaturized bandpass filters based on asymmetric coupled lines with equal reactance," *IEEE Transactions on Microwave Theory and Techniques*, vol. 60, no. 2, pp. 261–269, 2012.
- [25] S.-M. Wang, C.-H. Chi, M.-Y. Hsieh, and C.-Y. Chang, "Miniaturized spurious passband suppression microstrip filter using meandered parallel coupled lines," *IEEE Transactions on Microwave Theory and Techniques*, vol. 53, no. 2, pp. 747–753, 2005.
- [26] Y.-S. Lin and C.-C. Cheng, "Miniature CPW parallel-coupled bandpass filter based on inductive loaded coupled-lines and lumped-element J-inverters," *IEEE Microwave and Wireless Components Letters*, vol. 17, no. 5, pp. 343–345, 2007.
- [27] C.-W. Tang and S.-F. You, "Miniaturised wide stopband rejected microstrip filter with coupled spur-lines," *Electronics Letters*, vol. 42, no. 5, pp. 286–288, 2006.
- [28] H. Liu, J. Lei, J. Wan, Y. Wang, F. Yang, and S. Peng, "A miniaturized dual-mode bandpass filter using slot spurline technique," *International Journal of Antennas and Propagation*, vol. 2013, Article ID 853594, 6 pages, 2013.
- [29] W.-L. Chen and G.-M. Wang, "Effective design of novel compact fractal-shaped microstrip coupled-line bandpass filters for suppression of the second harmonic," *IEEE Microwave and Wireless Components Letters*, vol. 19, no. 2, pp. 74–76, 2009.
- [30] M. Zhou, X. Tang, and F. Xiao, "Miniature microstrip bandpass filter using resonator-embedded dual-mode resonator based on source-load coupling," *IEEE Microwave and Wireless Components Letters*, vol. 20, no. 3, pp. 139–141, 2010.
- [31] A. Torabi and K. Forooraghi, "Miniature harmonic-suppressed microstrip bandpass filter using a triple-mode stub-loaded resonator and spur lines," *IEEE Microwave and Wireless Components Letters*, vol. 21, no. 5, pp. 255–257, 2011.
- [32] X. Y. Zhang and Q. Xue, "Harmonic-suppressed bandpass filter based on discriminating coupling," *IEEE Microwave and Wireless Components Letters*, vol. 19, no. 11, pp. 695–697, 2009.
- [33] G. le Dai, X. Y. Zhang, C. H. Chan, Q. Xue, and M. Y. Xia, "An investigation of open- and short-ended resonators and their applications to bandpass filters," *IEEE Transactions on Microwave Theory and Techniques*, vol. 57, no. 9, pp. 2203–2210, 2009.
- [34] Y. L. Lu, G. L. Dai, and K. Li, "Dual band bandpass filter using coupled and series capacitors with controllable bandwidths," *Microwave and Optical Technology Letters*, vol. 55, no. 7, pp. 1543–1546, 2013.
- [35] G.-L. Dai and M.-Y. Xia, "An investigation of quarter-wavelength square-spiral resonator and its applications to miniaturized bandpass filters," *Journal of Electromagnetic Waves and Applications*, vol. 24, no. 10, pp. 1303–1313, 2010.
- [36] L. Zhu and K. Wu, "Accurate circuit model of interdigital capacitor and its application to design of new quasi-lumped miniaturized filters with suppression of harmonic resonance," *IEEE Transactions on Microwave Theory and Techniques*, vol. 48, no. 3, pp. 347–356, 2000.
- [37] Y. L. Lu and G. L. Dai, "An investigation of novel capacitor-based coupling scheme and its applications to microstrip bandpass filters," *Journal of Electromagnetic Waves and Applications*, vol. 27, no. 5, pp. 659–669, 2013.